THE UNIVERSITY of ADELAIDE

The impact of hydrodynamic coupling on the performance of multi-mode wave energy converters

Ngan Tran

School of Mechanical Engineering
The University of Adelaide
Adelaide, Australia

Thesis submitted in partial fulfillment of the requirements for the degree of Doctor of Philosophy in December, 2021.

Ph. D. Thesis

20th May 2022

School of Mechanical Engineering
The University of Adelaide
Adelaide, Australia

Typeset by the author using LaTeX.
Printed in Australia.

Abstract

Recently, research interest has deepened in developing technologies that are capable of generating electricity from renewable sources. Ocean wave energy is one such source, and is gaining attention due to its high energy density and favourable variability properties compared to other sources such as solar and wind. Although many Wave Energy Converter (WEC) prototypes have been proposed over the years, there is still no convergence on the best design.

An emerging subset of WEC designs are *'multi-mode converters'*, which are capable of absorbing power from multiple hydrodynamic modes. This allows them to generate more energy from incoming waves compared to most other WECs, which typically use only one Degree-of-Freedom (DOF) for power absorption. However, one of the key challenges in the design and control of multi-mode WECs is the strong coupling between hydrodynamic modes, which can potentially lead to sub-optimal performance. The effect of this coupling on the device performance may also be further exacerbated when nonlinear hydrodynamic effects are considered.

This thesis is dedicated to building an understanding of the impact of nonlinear coupling between hydrodynamic modes on the power absorption efficacy of a submerged, multi-mode, point absorber WEC with a flat cylindrical geometry. From this, the project also intends to provide general recommendations regarding the control and design of multi-mode WECs for increased performance. Three specific research questions were investigated: (i) what is the effect of nonlinear hydrodynamic coupling forces, caused by the change in projected surface area with large pitch motions, on the performance of multi-mode WECs, (ii) how should the surge, heave and pitch hydrodynamic modes be tuned to enhance the performance of WECs subjected to nonlinear coupling forces and (iii) what design parameters can be implemented to passively tune the hydrodynamic modes in a nonlinear, under-actuated WEC device. To address these questions, various numerical models were developed and compared, ranging from low fidelity models in the frequency-domain based on linear hydrodynamic models, to a weakly

nonlinear hydrodynamic code based on the weak-scatterer approximation.

Initially, it was necessary to gain a fundamental understanding of the nonlinear hydrodynamic forces acting on a device forced to undergo large pitch motions and oscillate in multiple hydrodynamic modes simultaneously. To this end, initial investigations assumed a simple WEC system with fully idealised kinematic control, wherein the pitch and surge motions could be explicitly defined. It was found that simultaneous surge and pitch motions changed the radiation forces acting on the WEC, resulting in significant reductions to the maximum power that could be absorbed by the device.

Different approaches for adjusting the dynamics and resonance behaviour of the multi-mode WEC through tuning of the hydrodynamic modes were then investigated. Under the effects of nonlinear coupling between hydrodynamic modes, tuning the surge, heave and pitch modes to the same natural frequency was demonstrated to result in significant reductions in power absorbed, especially when the pitch amplitude was high. Recommendations were therefore made to decouple these modes when developing multi-mode WECs in the case where the design does not limit large pitch amplitudes. From the models investigated, this tuning approach also demonstrated a potential for improving the broadband power absorption efficacy of the device in irregular waves.

In the final stage of this project, the impact of nonlinear coupling in an under-actuated system was investigated. A sensitivity study was conducted to investigate the effect of adjusting the geometric design of a three-tethered WEC on the resonance behaviour of each hydrodynamic mode. It was concluded that for maximum power absorption, two out of three of the device's planar rigid body modes should be utilised to harvest energy from incident waves. Furthermore, for this WEC geometry and design, these rigid body modes should contain predominantly surge and heave motions. Subharmonic excitations caused by nonlinear forces arising from the tether arrangement and hydrodynamic interactions were also found to significantly reduce the performance of the device compared to the predictions from linear theory. It was determined that the power absorbed by the device was most sensitive to the arrangement of the tethers, while adjusting parameters related to the mass distribution resulted in little benefit to the overall device performance.

Declaration

Declaration

I certify that this work contains no material which has been accepted for the award of any other degree or diploma in my name, in any university or other tertiary institution and, to the best of my knowledge and belief, contains no material previously published or written by another person, except where due reference has been made in the text. In addition, I certify that no part of this work will, in the future, be used in a submission in my name, for any other degree or diploma in any university or other tertiary institution without the prior approval of the University of Adelaide and where applicable, any partner institution responsible for the joint-award of this degree.

The author acknowledges that copyright of published works contained within the thesis resides with the copyright holder(s) of those works.

I also give permission for the digital version of my thesis to be made available on the web, via the University's digital research repository, the Library Search and also through web search engines, unless permission has been granted by the University to restrict access for a period of time.

I acknowledge the support I have received for my research through the provision of an Australian Government Research Training Program Scholarship.

Ngan Tran

Acknowledgements

Firstly, I would like to thank all of my supervisors for their support throughout the course of my research journey. I owe a very special thanks to my principle supervisor Professor Benjamin Cazzolato for accepting me into this project, providing me with his immense expertise and for guiding me to become an independent researcher of integrity. Next, I am deeply grateful to Dr Nataliia Sergiienko for consistently aspiring me to perform high-quality research with her invaluable advice, honest critique and firm encouragement. A big thank you also to Professor Maziar Arjomandi for his mentorship and for always looking out for both my personal and professional development in all my time of research. And finally, I would like to also thank Dr Mergen Ghayesh, the last member of my supervisory panel, for his energetic support and advice since the very beginning of my candidature.

I also wish to thank my PhD colleagues, friends and other members of the Wave Energy Group for contributing to an enjoyable working environment during these years. In particular Benjamin Schubert, for his willingness to provide help, ideas and encouragement during roadblocks in my research. I would also like to acknowledge Dr Boyin Ding and Dr Pierre-Yves Wuillaume for their expertise and support with the weak-scatterer model which formed a major part of my research project.

Finally, I would like to thank my parents and brothers, who have been great source of unconditional support and encouragement. Whether it be a surprise gift on my desk, or a humorous message in my inbox, thank you for always being there for me throughout this whole adventure.

Authors' Comments

The articles included in Chapters 4 and 5 of this Thesis have been reproduced with identical content as the published articles. While the content is identical, the typesetting and formatting have been adapted to ensure consistency with the remainder of this thesis. As such, the

- placement and size of figures;
- placement and size of tables; and
- numbering of figures, tables, and references

may differ from the original article. In addition, the published articles may use American English spelling, but this thesis uses the Australian English spelling preferred by the author. Footnotes have been included where clarifications to the text have been made in response to examiner comments.

While the article included in Chapter 6 of this Thesis has been reproduced with similar content as the submitted manuscript, several changes have been made in response to examiner comments. The material included in this Chapter therefore contains a number of differences compared to the published version of this article.

Contents

List of Figures

List of Tables

Acronyms

BEM	Boundary element method
BVP	Bounder value problem
CFD	Computation fluid dynamics
DOF	Degree of freedom
FD	Frequency domain
FK	Froude-Krylov
HPA	Heaving pitch absorber
LCoE	Levelised cost of electricity
MIMO	Multiple-input multiple-output
MPC	Model predictive control
NWT	Numerical wave tank
OPC	Oscillating pitch converter
OSC	Oscillating surge converter
OWC	Oscillating water column
PA	Point absorber
PM	Pierson-Moscowitz
P-NL	Partially nonlinear
PTO	Power take-off
RAO	Response amplitude operator
RK4	Fourth-order Runge-Kutta
SGP	Stewart-Gough platform
SPH	Smoothed-particle hydrodynamics
TD	Time domain
VTC	Velocity tracking control
WEC	Wave energy converter
WS	Weak-scatterer

Chapter 1

Introduction

1.1 Background and motivation

In recent years, there has been an unprecedented momentum for developing sustainable technologies which are capable of harvesting energy from renewable sources to generate electricity. Around the world, governments, industries and research communities are devoting considerable resources into establishing reliable, affordable and renewable energies to address the problems of rising world energy consumption and the damaging effects of climate change.

Global energy demand continues to grow every year as a result of emerging markets and developing economies, such as China and India. In 2021, it was estimated that this demand increased by 4.6%, surpassing even pre-Covid-19 levels [12]. However, the global energy mix is currently dominated by fossil fuels, which contributed approximately 83% to the total energy produced in 2020 [3]. Their continuous and widespread use has led to serious environmental issues, namely global warming, i.e. an increase in the Earth's mean surface temperature. In response to this growing problem, nearly 200 countries adopted the Glasgow Climate Pact at COP26, all pledging to the goal of limiting global warming to less than 1.5° above pre-industrial levels and achieving net-zero CO_2 emissions by 2050. There is a broad consensus that renewable sources and technologies are the only viable solutions for meeting this target [14].

Among the available resources, ocean wave energy is emerging as a viable contributor to the renewable energy mix. Compared to other renewable sources such as solar and wind, ocean wave power has one of the highest energy densities and more predictable variability properties [22]. Wave energy has also been considered as a potential solution for providing off-grid

electricity in places where solar and wind energies may not be feasible, such as small remote island communities or offshore industrial projects [18]. As a result, ocean wave power is attracting significant attention from the research community and industry sectors alike.

1.2 Ocean wave energy resource

Ocean wave energy can be considered as a concentrated form of solar energy. Heat from the sun results in temperature differences across the globe, which in turn causes winds to blow across the surface of the ocean [5]. Even with relatively small solar energy input rates of 0.01-0.1 W/m^2, ocean waves can build up to energy densities averaging over 100 kW/m [1]. Once fully developed, these waves can travel for thousands of kilometres with virtually no loss of energy.

The distribution of average annual wave energy around the globe is illustrated in Figure 1.1. Previous estimates from a decade ago placed the global annual mean power of wave energy at around 21,100 to 37,000 TWh/yr [8, 17], although recent studies have suggested that the current value could be even greater [21]. It has been estimated that approximately 10-25% of this energy can be feasibly extracted [1]. For perspective, the total world consumption of electricity in 2019 was 25,027 TWh [13]. Ocean wave energy therefore has the potential to contribute a significant amount towards the worldwide present-day electricity requirements.

As can be seen in Figure 1.1, Australia has one of the best wave energy

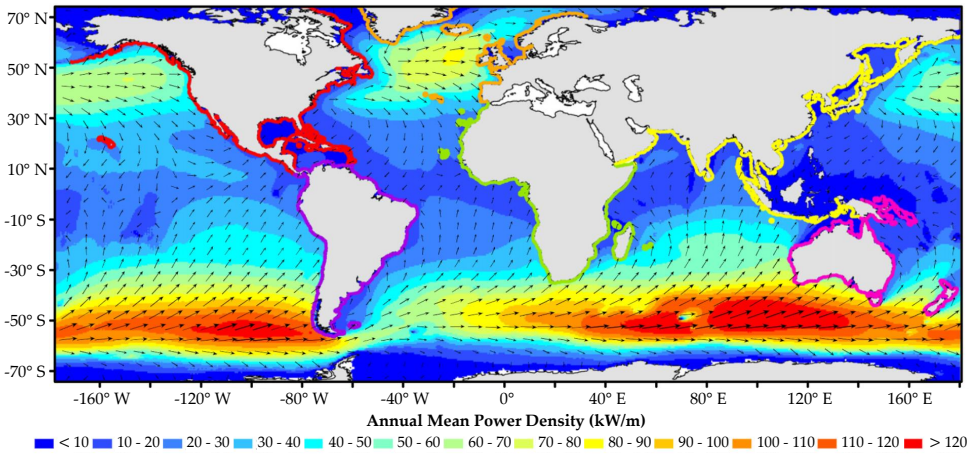

Figure 1.1: Distribution of average annual wave energy density and direction around the globe, based on [8].

resources in the world, particularly along its southern coastline. This has been credited to strong westerly winds blowing over large uninterrupted distances, or fetch, across the Southern Ocean [11]. The resource along Australia's southern margin alone has been estimated to be 1455 TWh/yr, as taken at a 25 m depth contour [10]. It has been estimated that extracting only 10% of this energy could be sufficient to satisfy roughly half of Australia's current electricity demands [2]. However, this requires significant investments; a more modest estimate predicts that wave energy could provide up to 10% of Australia's total energy needs by 2050, after taking into account external factors such as capital costs and projected uptake [9].

1.3 Wave energy converter development and modelling

To date, over a thousand Wave Energy Converter (WEC) prototypes have been proposed, covering a wide variety of designs and operating principles [15]. Despite this, there is still no consensus on the best design. Most devices are still in the early stages of development, with only a few having been tested at full scale in a real sea environment. There are also currently no devices which are economically viable for large-scale deployment. The challenge lies in not only increasing the energy conversion efficiency of the device but also reducing the Levelised Cost of Electricity (LCoE) delivered. This is a particularly complex problem with WECs due to their harsh operating environments, which results in increased development times and costs.

Of the total number of prototypes available, the Point-Absorber (PA) design is the most common, accounting for over half of all designs [16]. Most PAs are designed to absorb energy from one hydrodynamic mode only. However, in this category of WECs, there is an emerging subset of devices which can be classified as 'multi-mode converters' due to their ability to absorb energy from multiple hydrodynamic modes simultaneously. This allows for increased power absorption compared to single Degree-of-Freedom (DOF) systems, which typically only rely on one hydrodynamic mode for power absorption [6, 7].

Due to the high cost and lengthy time-frames required for physical experiments and testing, numerical simulations are typically employed for the design, optimisation and performance assessment of WECs in the early stages of development. Traditionally, numerical models based on linear hydrodynamic theory have been widely used for these purposes [19]. Linear hydrodynamics can be modelled in Frequency Domain (FD), allowing for fast and efficient computations of the system response. Much of the theory

regarding the behaviour and performance of WECs has been formulated based on these linear models [7].

Recently, there has been an increased research interest in utilising higher fidelity models for performance assessment of WECs. In order to achieve maximum power absorption, it is often desired for the WEC to be mechanically resonant with the incoming waves. This can be achieved through the geometric design (e.g. if the device size allows it to resonate naturally with the incoming waves) or through the application of control strategies which modify the device response in order to achieve resonance. However, operating at resonance can lead to several problems with regards to WEC modelling. Resonance amplifies the system response, which can consequently invalidate the fundamental assumptions of linear hydrodynamic theory, the most relevant being the assumption of small WEC and wave motions. Applying linear models in these cases can result in inaccurate estimates of the WEC performance [20]. Employing higher fidelity models could therefore provide a more accurate understanding of the system behaviour in these conditions.

1.4 Thesis

1.4.1 Aims and scope

This project focuses specifically on developing an understanding of the performance and behaviour of a submerged, disk-like, multi-mode PA WEC when subjected to nonlinear hydrodynamic forces. The WEC design featured in this project is inspired by the CETO-6 device developed by Carnegie Clean Energy in Perth, Western Australia [4]. One of the key design features of the CETO-6 is the use of three tethers which allow it to capture energy from the full orbital motion of the waves. While this multi-mode design has demonstrated better power absorption compared to an equivalent single-tether device [23], it has also introduced many challenges associated with the control of the WEC.

For multi-mode converters, due to coupling between hydrodynamic modes, it is not always possible to achieve an optimal power absorption by applying the typical control strategies designed for single-DOF devices. This problem can be further exacerbated by nonlinear hydrodynamic effects when the device oscillates in multiple modes simultaneously. This is particularly true for the flat cylindrical buoy employed by the CETO-6 device, which may also induce further coupling effects between hydrodynamic modes. Compared to other buoy geometries, the flat cylindrical design has demonstrated improved WEC performance with regards to LCoE [23]. However,

the chosen geometry also means that the projected surface area of the buoy can change significantly with pitching motions. Consequently, the magnitude of the hydrodynamic forces acting on the WEC in the other translational directions are also affected, resulting in enhanced and nonlinear coupling between hydrodynamic modes. The exact impact of this nonlinear coupling on the performance of multi-mode WECs is not well understood, with very few studies addressing these effects in the existing literature.

The overall aim of this thesis is to therefore investigate the behaviour of multi-mode WECs in the presence of significant nonlinear coupling between hydrodynamic modes. This knowledge is intended to aid in development of appropriate control strategies for multi-mode WECs in order to maximise their power absorption capabilities. The specific project objectives can be summarised as:

(i) to investigate the effect of nonlinear forces caused by coupling between hydrodynamic modes on the performance of multi-mode converters,

(ii) to investigate the resonance behaviour of the coupled surge, heave and pitch modes in a device with hydrodynamic nonlinearities present,

(iii) to develop recommendations for tuning each hydrodynamic mode in multi-mode systems where nonlinear coupling effects are significant,

(iv) to identify design parameters which can be adjusted to achieve the optimal tuning conditions in an under-actuated three-tethered device,

(v) to assess the potential advantages of tuning the hydrodynamic modes in a multi-mode system to different frequencies for increased broadband power absorption in real sea states.

The initial project objectives are dedicated to building a fundamental understanding of the response and behaviour of a general multi-mode WEC system when significant hydrodynamic coupling effects are present. To this end, simplified cases with idealised control are initially considered. With each subsequent objective, the complexity of the systems and corresponding models are increased, with the final step involving a specific case with an under-actuated three-tethered system. The progression of the project objectives is shown graphically in Figure 1.2. The analysis performed in this Thesis is limited to pure numerical modelling, using hydrodynamic models based on both linear potential flow theory and the Weak-Scatterer (WS) approximation (with more details given in Chapter 3).

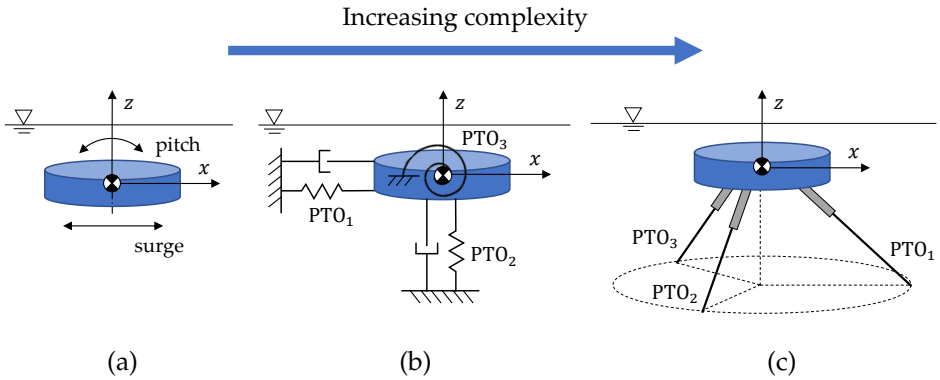

Figure 1.2: With each project objective, additional complexities are added to the WEC system, beginning with (a) kinematic control of each hydrodynamic mode, followed by (b) independent spring-damper control of each mode and finally to (c) a more realistic case with an under-actuated three-tether system. This is done to progressively build up a fundamental and generalised understanding of nonlinear multi-mode systems.

1.4.2 Outline

The main chapters of this thesis are a collection of manuscripts and conference proceedings that have been published or are currently under review. This is prefaced by a literature review and a chapter outlining the background theory relevant to ocean waves and modelling of WECs.

The literature review is presented in Chapter 2. Existing WEC prototypes and classifications are briefly outlined, with the main discussion devoted to the review of multi-mode prototypes. This chapter also addresses the importance of high-fidelity hydrodynamic modelling for wave energy applications.

Chapter 3 covers the background theory relevant to the work performed in this Thesis. Topics covered include the linear potential flow theory and the WS approximation. The mathematical theory behind the main modelling approaches used in this project are also presented.

In Chapter 4, the nonlinear hydrodynamic forces acting on a submerged cylindrical WEC oscillating in multiple directions simultaneously are investigated. The main assumption here is the use of a fully idealised controller where the WEC motions in surge and pitch can be explicitly defined, as illustrated in Figure 1.2(a). The resultant nonlinear hydrodynamic forces and their subsequent impact on power absorbed is assessed and compared to the predicted results obtained from the linear theory.

The effect of nonlinear coupling between hydrodynamic modes on the resonance behaviour of multi-mode WECs is explored in Chapter 5. The

role of the surge, heave and pitch natural frequencies on the response of a WEC with a simple Power Take-Off (PTO) system modelled with spring-damper control is analysed. This is illustrated graphically in Figure 1.2(b). The potential broadband performance of a multi-mode WEC in real waves when the modes are tuned to different natural frequencies is also explored.

Chapter 6 considers a passive approach for tuning of an under-actuated WEC system subjected to nonlinear coupling forces. A sensitivity study is performed to investigate the effect of various design parameters on the power absorbed and resonance behaviour of a three-tethered WEC, as shown in Figure 1.2(c). This study also analyses the effect of nonlinear forces caused by the tether arrangement and hydrodynamic coupling on the response of the three-tethered device.

Finally, chapter 7 summarises the main conclusions and contributions of this research. A number of recommended areas for future work are also provided.

1.4.3 List of publications included as part of the thesis

1. Tran, N., Sergiienko, N. Y., Cazzolato, B. S., Ding, B., Ghayesh, M. H. and Arjomandi, M. (2020). "The impact of pitch-surge coupling on the performance of a submerged cylindrical wave energy converter". In: *Applied Ocean Research* 104, p. 102377

2. Tran, N., Sergiienko, N. Y., Cazzolato, B. S., Ding, B., Wuillaume, P.-Y., Ghayesh, M. H. and Arjomandi, M. (2021). "On the importance of nonlinear hydrodynamics and resonance frequencies on power production in multi-mode WECs". In: *Applied Ocean Research* 117, p. 102924

3. Tran, N., Sergiienko, N. Y., Cazzolato, B. S., Ghayesh, M. H. and Arjomandi, M. (2022). "Design considerations for a three-tethered point absorber wave energy converter with nonlinear coupling between hydrodynamic modes", Manuscript submitted to *Ocean Engineering*

1.4.4 Additional publications relevant to the thesis but not forming part of it

1. Tran, N., Sergiienko, N. Y., Cazzolato, B. S., Ghayesh, M. H. and Arjomandi, M. (Oct. 2020). "The effect of nonlinear pitch-surge coupling on the performance of multi-DOF submerged WECs". In: *Proceedings of the 30th International Ocean and Polar Engineering Conference*, pp. 144–151.

References

[1] Barstow, S., Mørk, G., Mollison, D. and Cruz, J. (2008). "The Wave Energy Resource". In: *Ocean Wave Energy: Current Status and Future Prespectives*. Ed. by J. Cruz. Berlin, Heidelberg: Springer Berlin Heidelberg, pp. 93–132.

[2] Behrens, S., Hayward, J., Hemer, M. and Osman, P. (2012). "Assessing the wave energy converter potential for Australian coastal regions". In: *Renewable Energy* 43, pp. 210–217.

[3] BP p.l.c (2021). *BP Statistical Review of World Energy 2021*. Tech. rep.

[4] Carnegie Clean Energy (2020). *CETO Technology - Carnegie Clean Energy*. URL: https://www.carnegiece.com/ceto-technology/.

[5] Cruz, J. (2008). *Ocean Wave Energy: Current Status and Future Prespectives*. Green Energy and Technology. Springer.

[6] Evans, D. V. (1976). "A theory for wave-power absorption by oscillating bodies". In: *Journal of Fluid Mechanics* 77.1, 1–25.

[7] Falnes, J. (2002). *Ocean waves and oscillating systems: Linear interactions including wave-energy extraction*. Cambridge University Press, p. 220.

[8] Gunn, K. and Stock-Williams, C. (2012). "Quantifying the global wave power resource". In: *Renewable Energy* 44, pp. 296–304.

[9] Hayward, J., Behrens, S., McGarry, S. and Osman, P. (2012). "Economic modelling of the potential of wave energy". In: *Renewable Energy* 48, pp. 238–250.

[10] Hemer, M. A., Zieger, S., Durrant, T., O'Grady, J., Hoeke, R. K., McInnes, K. L. and Rosebrock, U. (2017). "A revised assessment of Australia's national wave energy resource". In: *Renewable Energy* 114, pp. 85–107.

[11] Hughes, M. G. and Heap, A. D. (2010). "National-scale wave energy resource assessment for Australia". In: *Renewable Energy* 35.8, pp. 1783–1791.

[12] IEA (2021a). *Global Energy Review 2021*. Tech. rep. Paris.

[13] IEA (2021b). *Key world energy statistics 2021*. Tech. rep. Paris.

[14] IRENA (2021). *World Energy Transitions Outlook: 1.5°C Pathway*. Tech. rep. Abu Dhabi: International Renewable Energy Agency.

[15] López, I., Andreu, J., Ceballos, S., Martínez De Alegría, I. and Kortabarria, I. (2013). "Review of wave energy technologies and the necessary power-equipment". In: *Renewable and Sustainable Energy Reviews* 27, pp. 413–434.

[16] Mofor, L., Goldsmith, J. and Jones, F. (2014). *Ocean Energy: Technology Readiness, Patents, Deployment Status and Outlook*. Tech. rep. August, p. 76.

[17] Mørk, G., Barstow, S., Kabuth, A. and Pontes, M. T. (June 2010). *Assessing the Global Wave Energy Potential*.

[18] Ocean Energy Systems (2020). *Ocean Energy in Islands and Remote Coastal Areas: Opportunities and Challenges*. Tech. rep. International Energy Agency (IEA).

[19] Penalba, M., Giorgi, G. and Ringwood, J. V. (2017). "Mathematical modelling of wave energy converters: A review of nonlinear approaches". In: *Renewable and Sustainable Energy Reviews* 78, pp. 1188–1207.

[20] Penalba, M., Merigaud, A., Gilloteaux, J.-c. and Ringwood, J. (Sept. 2015). "Nonlinear Froude-Krylov force modelling for two heaving wave energy point absorbers". In: *Proceedings of the 11th European Wave and Tidal Energy Conference EWTEC*. Nantes, France.

[21] Reguero, B. G., Losada, I. J. and Méndez, F. J. (2019). "A recent increase in global wave power as a consequence of oceanic warming". In: *Nature Communications* 10.1, p. 205.

[22] Ringwood, J. V., Bacelli, G. and Fusco, F. (2014). "Energy-maximizing control of wave-energy converters: The development of control system technology to optimize their operation". In: *IEEE Control Systems* 34.5, pp. 30–55.

[23] Sergiienko, N. Y., Cazzolato, B. S., Ding, B. and Arjomandi, M. (2016). "Three-tether axisymmetric wave energy converter: estimation of energy delivery". In: *Proceedings of the 3rd Asian Wave and Tidal Energy Conference AWTEC*. Singapore: Singapore: Research Publishing, pp. 163–171.

Chapter 2

Literature Review

The overall aim of this Thesis is to build understanding on the impact of nonlinear coupling between hydrodynamic modes on the performance and control of multi-mode WECs. To provide context and justification for this research, this chapter will review the following topics:

(i) a broad overview of WEC development to date,
(ii) oscillating body converters and factors impacting their performance,
(iii) nonlinear hydrodynamic modelling for WEC applications.

Particular emphasis is placed on developments specific to the design, control and modelling of *multi-mode* converters. In this project, the term '*multi-mode*' refers specifically to devices that are designed to absorb power from multiple hydrodynamic modes (i.e., surge, heave or pitch) simultaneously during normal operation. This is distinct from other converters which may oscillate in multiple directions or have more than one rigid body mode, but still rely only on one dominant hydrodynamic mode for power absorption (e.g. heave).

2.1 Categories of wave energy converters

Since the conception of wave energy harvesting in the late 18th century, and its subsequent dissemination to the broader research community in the 1970s [97], it has been estimated that over one thousand patented wave energy devices have been developed [37]. However, despite the many years of development, there is still no consensus on the best design with regards to power absorption efficiency or economic viability. As a result, there is a considerable variation across all the different available prototypes, from

the method of energy extraction, to the size, shape and intended operating location of the device.

Several studies have attempted to categorise the different wave energy technologies [25, 31, 64, 98]. However, this can be a challenge in itself since there are also many possible methods of classifying converters [107]. For example, it is possible to sort converters according to [72, 98]:

- Operating principle, or interface with the sea,
- Orientation relative to the incident wave direction,
- Reaction source,
- PTO mechanisms,
- Location relative to the water, sea-bed or land.

Of these options, the two most commonly used methods for classifying WECs in the literature appear to be [9]: (i) orientation and (ii) operating principle.

Orientation

Initially, WECs were typically classified according to their dimensions and orientation relative to the incoming waves [107]. The different device types are shown schematically in Figure 2.1. These labels are still often used as additional qualifiers when describing WECs.

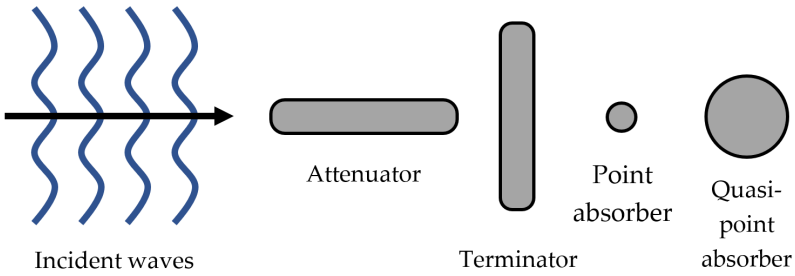

Figure 2.1: Schematic of WEC types by dimensions and orientation relative to the incoming wave, based on [107]

Attenuators, or line absorbers, are large devices with lengths comparable to or larger than the incident wavelength. They are aligned to the direction of wave propagation, allowing them to progressively absorb more energy from the wave as it travels down the length of the device.

Terminators are similar to attenuators in that they are also long structures. However, these devices are orientated perpendicular to the direction of wave propagation.

Point absorber (PA) WECs have dimensions that are significantly smaller than the incident wavelength. More precisely, a device can be classified as a PA if its characteristic length is smaller than 1/20th of the wavelength [18]. Compared to terminators and attenuators, they are insensitive to the direction of wave propagation.

Quasi-point absorbers are devices that are also insensitive to the wave direction. However, they do not fit within the formal definition of PAs due to their large dimensions relative to the wavelength. This classification was introduced by Falnes and Hals [36] to describe devices with operating conditions between PAs and line absorbers.

A study performed by the International Renewable Energy Agency suggests that PAs (including quasi-PAs) are the most common technology among existing WEC designs [72]. The breakdown of device types according to orientation is shown in Figure 2.2, based on a shortlist of 36 active, commercial WEC technologies.

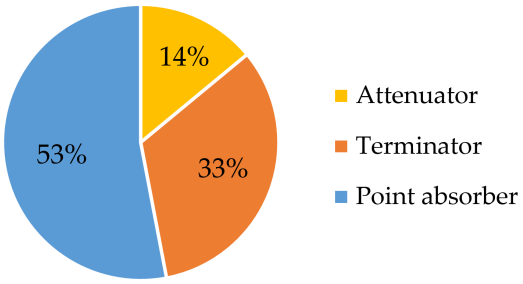

Figure 2.2: Breakdown of WEC types by orientation, based on [72]

Operating principle

Currently, it is more common to categorise the various WEC technologies based on operating principle. A widely referenced example, originally proposed by Falcão [31], is shown in Figure 2.3. Using this classification method, WEC prototypes can be divided into three main categories: oscillating water columns, oscillating bodies and overtopping converters.

Oscillating water columns (OWCs) use a moving air-water interface to capture energy from waves. These are partially immersed hollow structures with the lower end open to the sea. Passing waves cause the pressure of the air trapped inside the structure to oscillate, compressing the air at the upper end and forcing it through a turbine coupled to a generator [28, 32].

Oscillating body WECs transfer the energy of the waves to the motion of a structure, or group of structures. A PTO system connected to the structures

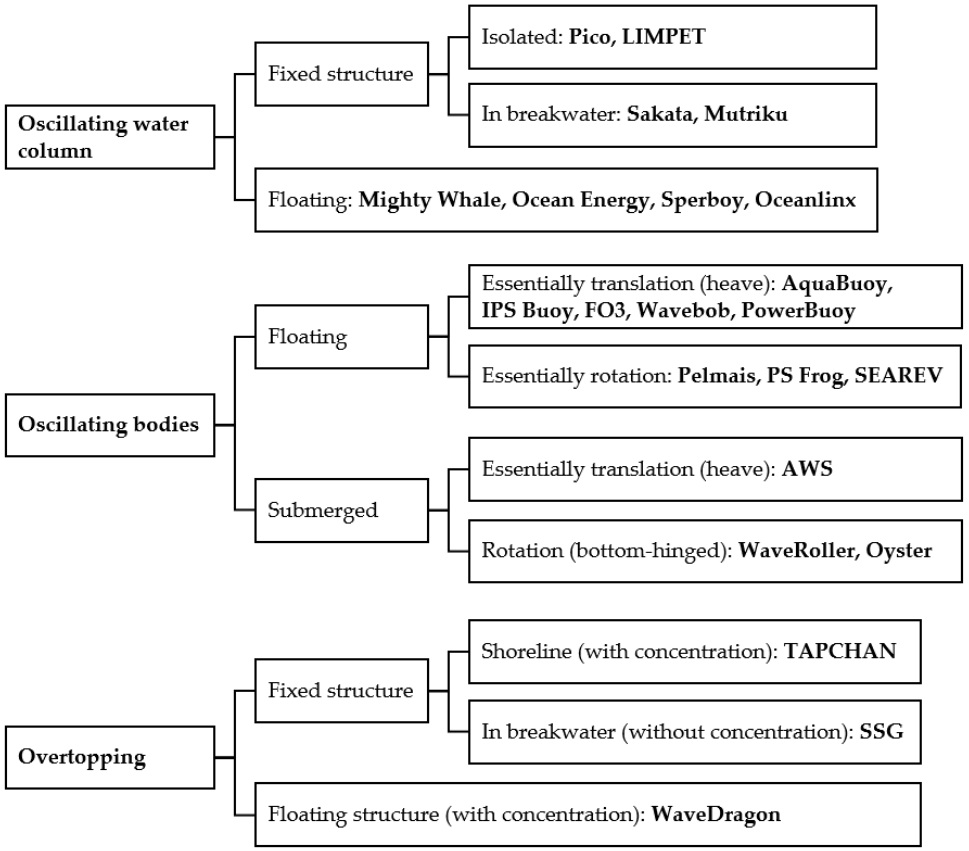

Figure 2.3: Wave energy converter classification by operating principle with examples, based on [31].

is used to convert the mechanical motion into electricity. The devices in this class of converters are more complex compared to those in the other categories, and hence it has only been mainly in the past decade that many oscillating body prototypes have reached the full-scale testing stages [31].

Overtopping devices use the action of the waves to capture and deposit water into a reservoir located above the mean free-surface level of the surrounding sea. The water is then returned to the sea via a low head turbine, converting the potential energy of the stored water into electricity [31, 72].

Using this classification of WECs, Babarit [3] attempted to compile a database to compare the hydrodynamic efficiency (defined as the capture width ratio), of devices in each of these three categories. Although performance differed significantly between devices in the same category, the approximate mean efficiency of each category of converters is listed in Table 2.1. In this study, the oscillating body class of WECs was further divided into subcat-

egories to differentiate between heaving and surging devices (referred to as 'essentially translation' and 'essentially rotation' in Figure 2.3, respectively). A distinction was also made between surging devices with fixed and floating references. Note that the only 'multi-mode' WEC in the database, according to the definition used in this Thesis - the Bristol Cylinder - was included as a variant of the 'fixed surging converter' subcategory of oscillating bodies.

Table 2.1: Mean hydrodynamic efficiency of various WEC technologies, as categorised by operating principle, based on [3].

WEC type	Efficiency %
OWC	29
Oscillating body	
- heave	16
- surge (fixed)	37
- surge (floating)	12
Overtopping	17

From this brief overview, it is clear that it would be much beyond the scope of single project to explore all possible WEC categories, given the wide variety of existing designs. Therefore, this Thesis will focus solely on oscillating body type WECs, specifically multi-mode devices which include power absorption from surge as a key aspect of their design. This is based on their potential for the highest power absorption efficiency compared to other WEC types, as suggested in Table 2.1. Accordingly, the following sections will be dedicated primarily to the review of oscillating body-type converters.

2.2 Oscillating bodies

2.2.1 Wave energy absorption principles

The law of conservation of energy entails that, to successfully absorb energy from waves, a converter must act in such a way that reduces the amount of wave energy present in the surrounding sea. For an oscillating body device, this is achieved by generating a wave that interferes destructively with the incident sea waves [11]. A good wave absorber must therefore also be a good wave generator [35].

Any body oscillating in the water will produce waves. However, to effectively cancel and therefore absorb energy from an incident wave, the radiated wave generated by the oscillating body must also have the correct amplitude and phase [34]. The amplitude of the radiated waves is dependent on both the size of the body and the amplitude of its oscillations. A small body can

radiate equally large waves as a bigger body, provided that it oscillates with a larger amplitude.

The pattern of the radiated wave also affects the ability of an oscillating body to absorb power from the waves, which in turn is dependent on the mode of motion of the body [27, 36, 108]. The motion of a WEC is usually decomposed into six hydrodynamic modes, as shown in Figure 2.4. However, for simplicity, future discussions will assume that the wave is travelling purely in the xz-plane, meaning only motions in the surge, heave and pitch modes will be considered. An axisymmetric body oscillating in heave will produce symmetrical monopole, or source-type, waves which radiate away in a circular pattern as shown in Figure 2.5(a). Motions in surge or pitch will radiate asymmetric dipole-type waves, as shown in Figure 2.5(b).

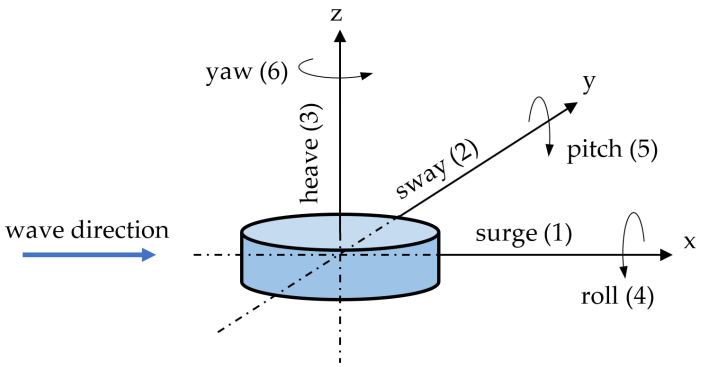

Figure 2.4: Modes of motion of an oscillating body. The numbers in parenthesis are often used as indexes for each mode.

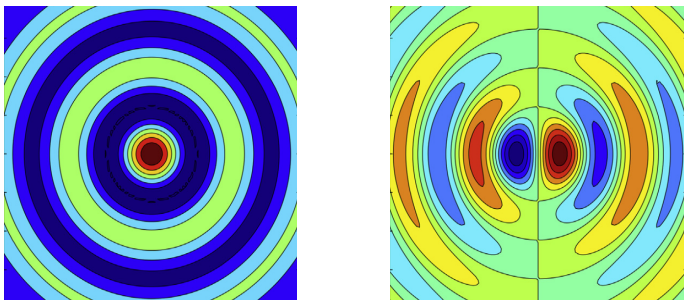

Figure 2.5: Pattern of the radiated waves produced by an axisymmetric body oscillating in (a) heave (monopole waves) and (b) surge or pitch (dipole waves), adapted from [3].

The principle of wave energy absorption by an oscillating body is visually summarised in Figure 2.6. It can be seen that, by moving in both the heave and surge/pitch modes together at the correct amplitude and phase, it is

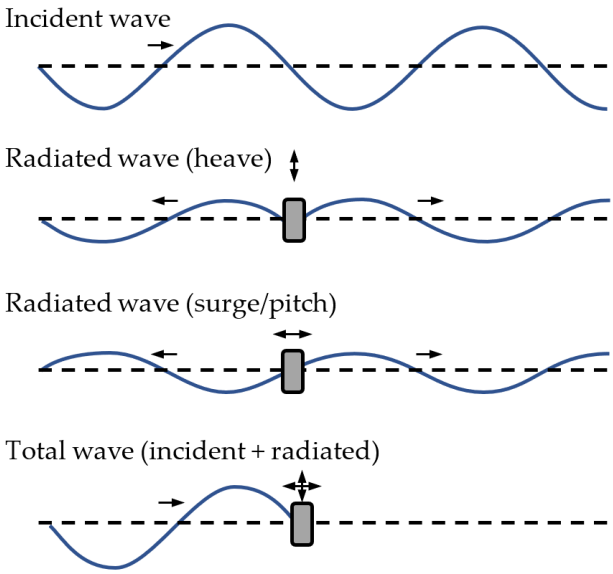

Figure 2.6: Wave absorption principle of an oscillating body, adapted from [34]. The total wave is a superposition of the incident and radiated waves.

possible for a device to achieve highly efficient power absorption from the incident wave. An infinitely elongated body with the same cross section as shown in Figure 2.6 (i.e. an infinitely long terminator-type device) could even theoretically achieve 100% absorption from the wave by oscillating in this manner [27, 76]. This is the primary motivation behind the development of the Bristol cylinder, one of the first 'multi-mode' oscillating body WEC prototypes (more details will be given in Section 2.2.2).

For point absorbers, although it is not possible to achieve 100% absorption from waves, there is still a clear benefit to using a combination of modes for energy extraction. Assuming no motion constraints, the maximum power that can be absorbed by an axisymmetric body is given by [27, 34]:

$$P_{\max} = \alpha \frac{J}{k} \tag{2.1}$$

where J is the wave-energy transport per unit frontage of the incident wave and k is the wave number. The coefficient α is related to the radiated wave patterns generated by the body, and hence depends on the mode of oscillation:

- $\alpha = 1$ for heave,
- $\alpha = 2$ for surge or pitch,
- $\alpha = 3$ for a combination of surge-heave, or heave-pitch.

A multi-mode axisymmetric PA converter utilising a combination of surge and heave, or heave and pitch, can therefore theoretically absorb up to three times more power compared to a device operating in heave only. The relationship given in Eq. (2.1) also explains why surging and pitching converters are reported to have, on average, higher power absorption efficiencies compared to heaving devices [6], as observed in Table 2.1.

It is important to note that since surge and pitch both radiate dipole-type waves, it is not possible to increase the efficiency of a device by using both modes simultaneously for power absorption [34]. Instead, the two modes are coupled hydrodynamically, and the optimal motion in one mode will depend on the motion of the other. For example, if a WEC pitches arbitrarily and radiates waves, the surge motion should be adjusted accordingly to ensure that the total dipole-type waves radiated by the device still interferes optimally with the incident wave.

2.2.2 Multi-mode converter prototypes

Although multi-mode converters have a clear advantage over single-DOF converters in terms of power absorption efficiency, the number of existing prototypes is still relatively limited. This is likely due to the increased complexity of multi-mode systems, especially in the design of the controller and actuators. These challenges will be discussed in more detail with respect to specific multi-mode WEC prototypes in the following subsection.

One of the first multi-mode concepts was the Bristol cylinder, which was proposed in 1979 by Evans et al. [29]. This device features a fully submerged, long horizontal cylinder that undergoes both heave and surge motions to absorb power from the waves, similar to the principle illustrated in Figure 2.6 and following the theory originally derived in [76, 109]. As shown in Figure 2.7, the original design featured a 75 m long cylinder with a 15 m diameter, with a total of six hydraulic PTO systems for energy conversion. Despite predicted efficiencies of up to 65%, the project was deemed economically unfeasible due to the high costs of installation and power take-off, and hence was abandoned in 1982 [87].

In another early concept, Srokosz [105] suggested applying multi-mode motion for energy extraction in a point absorber device. The design featured a fully submerged spherical buoy attached to three inclined tethers, which were used to anchor the device to the sea floor. Each inclined tether was also attached to a power generator, allowing the device to capture wave energy from all translational motion modes. Various tether angles were also investigated as part of the study. Results showed that for certain angles, the

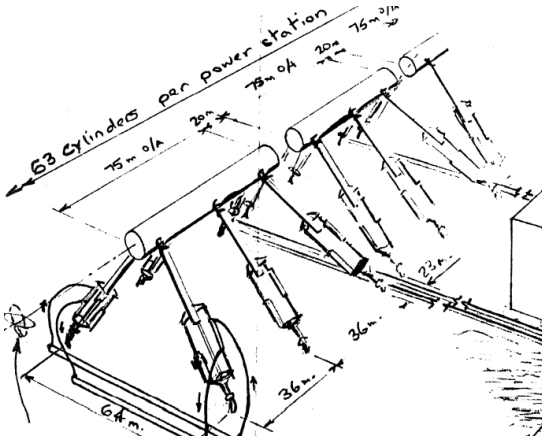

Figure 2.7: Sketch of the Bristol Cylinder concept from [87]

three tethered configuration was able to absorb power from a crest length of incident wave greater than its diameter, implying a hydrodynamic efficiency higher than 100% which was not possible with an equivalent single-tether heave-only configuration. However, the study was purely conceptual and, like the Bristol cylinder, this device was never tested in real seas.

More recently, several commercial multi-mode prototypes have been developed by various wave energy companies around the world. One such device is the CETO-6 by Carnegie Clean Energy, Australia [13]. The device is fully submerged and anchored directly to the sea floor by three inclined tethers connected to an individual PTO unit. The design is therefore similar to the concept proposed by Srokosz, although the CETO-6 uses a flat, cylinder buoy instead of a sphere, as shown in Figure 2.8. Additionally, given the proposed dimensions of the device, it is more accurate to describe the CETO-6 as a quasi-PA type WEC. The buoy shape was chosen based on studies

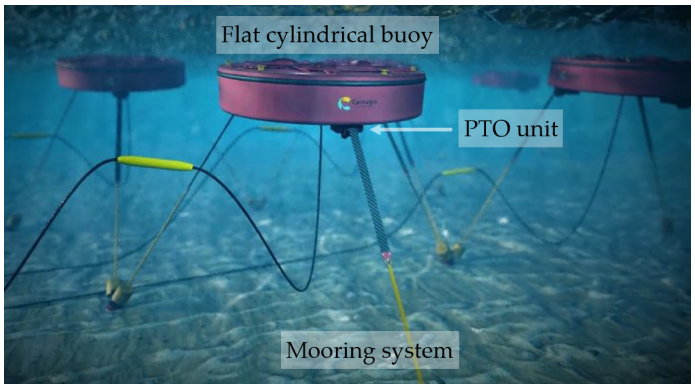

Figure 2.8: CETO-6 WEC by Carnegie Clean Energy [13]

which demonstrated a better performance with regards to LCoE compared to other possible geometries [86, 103]. However, this shape also introduces complications due to increased hydrodynamic coupling between surge and pitch, which can negatively impact power absorption [101].

The WaveSub [68] is another fully submerged multi-mode device, developed by Marine Power Systems in collaboration with the University of Bath, UK. In contrast to the CETO-6 device, the WaveSub uses the relative motion between a submerged moored inertia platform (the 'reactor' body) and a submerged buoy (termed the 'float') to generate energy. Initial designs for the WaveSub featured only a single spherical PA-type float. Subsequent modelling, experimental and optimisation studies [38, 39, 40] explored the use of multi-float arrays, with an example shown in Figure 2.9(a), placed in various orientations relative to the wave direction. The most current design features a horizontal cylinder float which appears to operate similar to the Bristol cylinder, as shown in Figure 2.9(b). The original single float concept has been tested at 1/4 Froude scale in real seas [68], while the multi-float concept has been tested at 1/25 scale in wave basin experiments [39]. However, given that the WaveSub is a commercial product, no further information regarding its efficiency is publicly available.

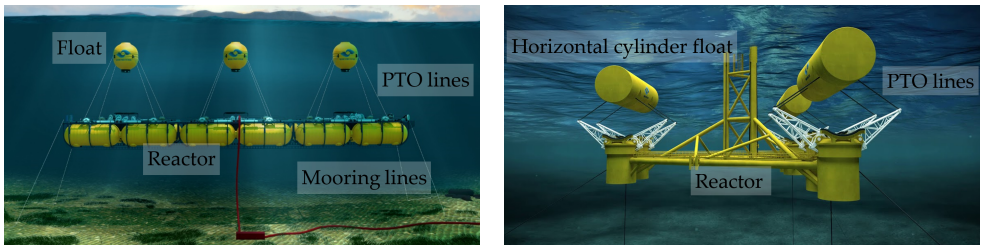

(a) (b)

Figure 2.9: Design concepts of the WaveSub device by Marine Power Systems, (a) multi-float design, adapted from [38] and (b) current design, adapted from [68].

The Triton WEC by Oscilla Power [78] is a quasi-PA device featuring a floating buoy with an optimised asymmetric geometry [96]. The device uses a submerged reactor body, similar to the WaveSub. In this case, the floating buoy is attached to a ring-shaped reactor body via three flexible tethers (termed 'tendons'), as shown in Figure 2.10 [17]. Despite having multiple tethers, they are arranged almost vertically between the buoy and the reactor body. This means the device relies predominantly on heave for power absorption, while energy converted from surge and sway motions is limited. Since relative rotational motions are difficult to achieve with

non-rigidly fixed reference structures [3], pitch and roll are also unlikely to contribute much to power. This may explain why the efficiency of the device, calculated as 23.5% based on 1/20 scale testing results in irregular sea states [110], is only slightly higher than the mean efficiency of an oscillating body-type WEC operating primarily in heave (as given in Table 2.1).

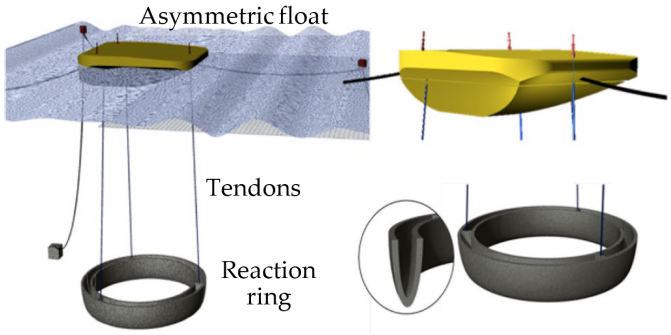

Figure 2.10: Triton WEC by Oscilla Power, adapted from [17]

The NEMOS device is another commercial, floating multi-tethered WEC prototype, developed by NEMOS GmbH [74]. This device consists of an elongated terminator-like buoy which follows a curved trajectory upon the surface of the water. Initially, the device was designed to be anchored directly to the sea floor using three tethers, with a fixed tower above the mean water level to store the winches and generators used to convert the buoy motion into electrical energy. This initial design was capable of a hydrodynamic efficiency of up to 60% in real sea states, based on testing at 1/5 scale [84]. In the most current design iteration, the floating body is instead connected to a submerged reactor body via an inclined spring-loaded belt drive. Unlike the initial concept, this design does not require a fixed structure and can

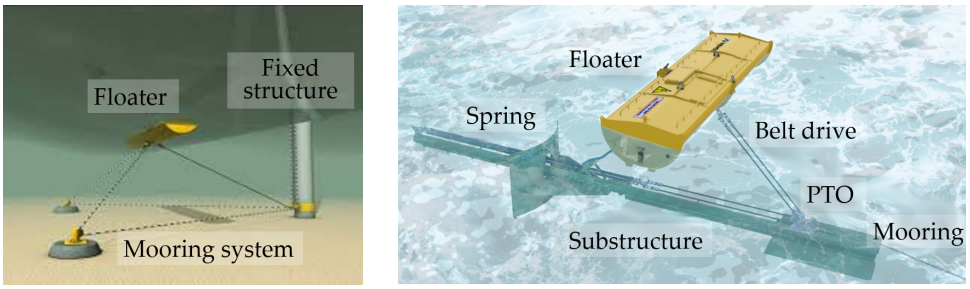

(a) (b)

Figure 2.11: Design concepts of the NEMOS wave device by NEMOS GmbH, (a) original design, adapted from [84] and (b) current design, adapted from [74].

be deployed as a standalone floating unit [75]. Full-scale testing of this new prototype in the Belgian North Sea was completed in 2019; however, no information on the efficiency of this new design is publicly available.

Wave energy converter devices with full six-DOF control have also been proposed by various research groups, as shown in Figure 2.12. These devices operate using a similar principle to the Stewart-Gough Platform (SGP), which is a parallel mechanism with six independent actuators and was first proposed for use in a wave energy device by Lofti and Huang [66]. The concept shown in Figure 2.12(a) features an upper floating component consisting of three rigidly interconnected floats, connected by six legs to a lower fixed base which acts as a reaction platform. Cases where the floats operate in heave-surge-sway were found to result in up to 10% more power absorbed than cases where only heave motions were allowed [43]. Conversely, in the concept proposed by Gao and Yu [44] shown in Figure 2.12(b), the upper platform is instead fixed while the movement of the floating lower platform is used to generate energy. The effect of various buoy parameters on the power absorbed by the surge, heave and pitch modes were analysed, leading to an optimised cone-cylinder geometry which the authors claim can achieve roughly 48% power absorption in irregular seas [44].

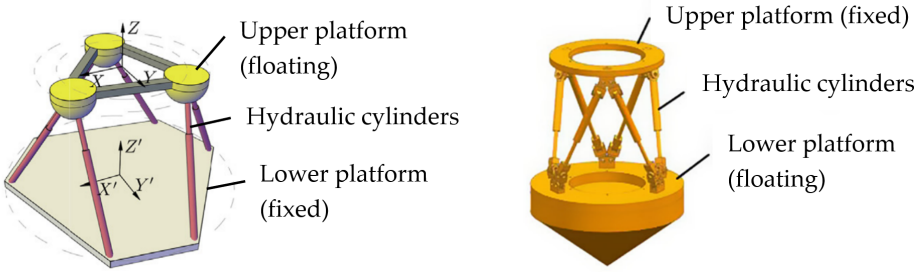

Figure 2.12: WEC concepts with six-DOF control, such as the (a) WEC-SGP concept, adapted from [43] and (b) floating cone-cylinder concept proposed by Gao and Yu [44]

In contrast to previous concepts, which all feature multi-tethered devices, Meng et al. [69] proposed a single-tether, multi-mode submerged spherical point absorber with an asymmetric mass distribution. Multi-mode power absorption is achieved with the introduction of an offset mass, allowing the surge, heave and pitch motions of the device to all couple strongly with the tether elongation and PTO unit, as shown in Figure 2.13. Improved performance was observed for offset mass locations which resulted in strong motion coupling between surge and heave, resulting in a power output of

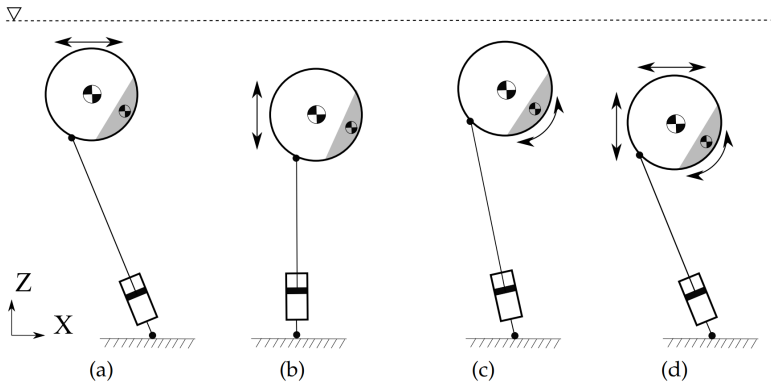

Figure 2.13: Schematic of the spherical point absorber with asymmetric mass distribution, showing motions in (a) surge, (b) heave, (c) pitch and (d) all three DOFs combined, adapted from [70].

up to 3 times higher than a generic heaving spherical point absorber when optimised, even with nonlinear surface piercing effects [70]. However, control of the device is complex since there is only one tether for actuation. While the resonance behaviour of the heave mode can be adjusted through the PTO control parameters, the surge natural frequency is primarily sensitive to the initial tether length which cannot be easily changed during operation.

The CECO wave converter, currently in development at the University of Porto, Portugal [41], is another multi-mode device that does not use multiple moorings for power capture. Instead, a single inclined DOF is used to capture energy from both the surge and heave motions of the waves, based

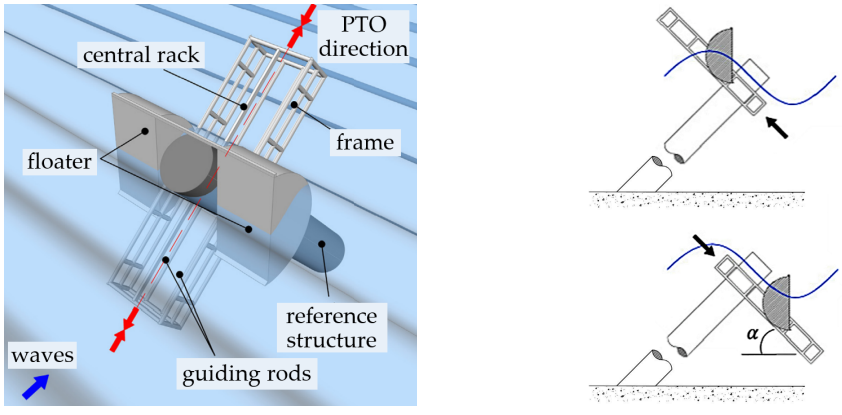

Figure 2.14: Original CECO design (a) schematic, adapted from [65] and (b) motion under wave action, adapted from [95].

on concepts initially proposed by the University of Edinburgh in the 1990s [81, 82, 83, 99]. The CECO concept is illustrated in Figure 2.14(a). The main floating structure consists of two floaters rigidly attached to a sliding frame, which moves along an inclined axis relative to the vertical under the action of the waves, as shown in Figure 2.14(b). Since its inception, improvements to the device have included optimisation of the the PTO inclination angle, damping parameters and floater geometry [65, 92]. Experimental testing of the initial CECO design reported absorption efficiencies of up to 30% in irregular seas [91], although it is claimed that the new optimised floater geometry can achieve efficiencies of more than twice this amount in certain sea states [93].

A number of other scale multi-mode WEC devices have also been featured in experimental tests performed by independent studies [104, 116]. While these studies confirm that using multiple modes results in greater power absorption than a single mode, the featured WECs appear to be designed purely for testing rather than full-scale deployment. Furthermore, control of these devices was limited only to passive damping control.

Concluding remarks for multi-mode WEC prototypes

Despite the comparatively small number of multi-mode prototypes, it can be seen from this review that there is still considerable variation between the available designs. It is difficult to make an objective comparison between the performance of all the various designs, especially given that several are commercial in confidence and information regarding their development is limited. However, it is clear overall that multi-mode devices offer improved efficiency over their traditional, heave-only counterparts.

One commonality between designs is the use of inclined DOFs to achieve power absorption from multiple modes simultaneously, with the degree of inclination affecting the relative contribution to power from each mode. However, the number of moored tethers or actuators varies between designs. While more tethers and PTO units can increase the controllability of the device, the cost of the system can also be expected to increase accordingly. Conversely, reducing the number of actuators leads to under-actuated systems where there are fewer control inputs than the number of operational degrees of freedom. In such systems, some DOFs may not be fully controllable, requiring more complex control solutions such as passively tuning certain DOFs through the geometric design of the device.

It is noted that most designs appear to favour the surge and heave modes for power absorption, while the pitch mode is either not utilised or neglected

in these cases. While this is acceptable for spherical buoys, this may not be the case for WECs with non-spherical geometries. For these geometries, hydrodynamic coupling between pitch and the other modes may introduce challenges with regards to the control of the system. There also appears to be a trend towards larger devices, especially for the commercial prototypes, which may also have implications for the hydrodynamic modelling of these devices.

2.2.3 Control of wave energy converters

All WECs require a PTO to convert the energy from waves into useful electrical power, which can be controlled to maximise the energy absorption of the device during its operation. It is expected that control systems and technology will be critical for improving the LCoE of WECs [14, 90]. However, while the principles behind the control of oscillating body WECs have been known for decades [11, 27], there are still many challenges regarding their implementation in real devices.

As previously described in Section 2.2.1, an effective oscillating body converter must act in such a way that it generates waves that interfere destructively with the incoming waves. The main goals of a control system are to therefore ensure that [34]:

1. the body oscillates at an amplitude such that the radiated waves are of an optimum amplitude relative to the incident wave,
2. the velocity of the body has the correct phase relationship relative to the dynamic pressure (and hence excitation force) of the incoming wave, including the diffraction forces.

Ideally, these conditions are met by tuning the resonance frequency of the device to the incident wave frequency. This can theoretically be achieved through providing an optimal stiffness and damping that matches the intrinsic impedance of the system, also known as *complex-conjugate control* [34, 57]. However, optimal control is often difficult to apply in practice due to several issues [90]:

- The system impedance is dependent on the incident wave frequency, making application in real seas difficult since they contain a broad spectrum of frequencies,
- The control force required to achieve the optimality conditions is acausal (or non-causal) [33], meaning it relies on future knowledge of the excitation force,

- The PTO may need to supply power to the system during some parts of its oscillation cycle, meaning that storage and release of energy is required over the cycle when tuning for different frequencies,
- Physical constraints, such as limits on the maximum WEC displacement or PTO forces, are not taken into account in this control strategy,
- High transmitted loads and control forces can restrict physical implementation in real-life PTO system.

Many alternative control strategies have therefore been proposed in the literature for WEC applications. Some recent reviews can be found in [67, 79, 111], while comparisons of a select number of strategies can be found in [16, 57]. In general, most control strategies can be sorted into two broad categories: (i) passive and (ii) reactive control [111].

Passive control strategies only require the PTO to extract energy; power does not need to be supplied back into the system. The simplest strategies are purely *resistive*, where the PTO system only provides a velocity-dependent damping force to the device. While simple to optimise for regular waves, this strategy has extremely reduced effectiveness in real sea waves, which are irregular [67].

An alternative passive control strategy is *latching control*, which involves locking the motion of the device during a part of its oscillation cycle to ensure that its velocity remains roughly in phase with the excitation force [4]. A similar strategy is *declutching control*, which operates using a similar principle except that the PTO is alternatively switched on and off instead [7].

Reactive control strategies require the PTO to store and then return some energy back into the system during parts of the oscillation cycle to maintain the optimal amplitude and phase conditions. In this strategy, the PTO provides a stiffness force which is proportional to the WEC displacement as well as a damping force to control the WEC system. The complex-conjugate control described previously is an example of a reactive control strategy.

Other reactive control strategies have been proposed to address the various problems related to complex-conjugate control. *Model Predictive Control* (MPC) is one such strategy, which can be used to take into account the physical constraints of the device [56]. However, MPC is computationally intensive and sensitive to modelling errors, which makes its physical implementation difficult [30, 88]. Another strategy is *Velocity Tracking Control* (VTC), which was proposed by Fusco and Ringwood [42] to address the problem of

acausality. In this strategy, only the current (as opposed to future) value of the excitation forces are required, from which a reference velocity signal is computed and tracked by the PTO machineries using a feedback control loop.

An illustrative comparison between the effectiveness of reactive and passive (including latching) control strategies in regular waves is shown in Figure 2.15. Radiation limits, as defined by Eq. (2.1), and volume stroke limits imposed by motion constraints and WEC size [12] are also indicated in the figure. It can be seen that reactive control is the most efficient strategy, since it ensures that the amplitude and phase optimality conditions are satisfied during all parts of the the oscillation cycle. While slightly sub-optimal, latching control satisfies the phase optimality condition and hence also has a relatively high efficiency. Purely resistive passive control, when not optimised for the incoming wave, is insufficient to ensure the phase optimality conditions and hence results in very poor efficiency compared to the other strategies.

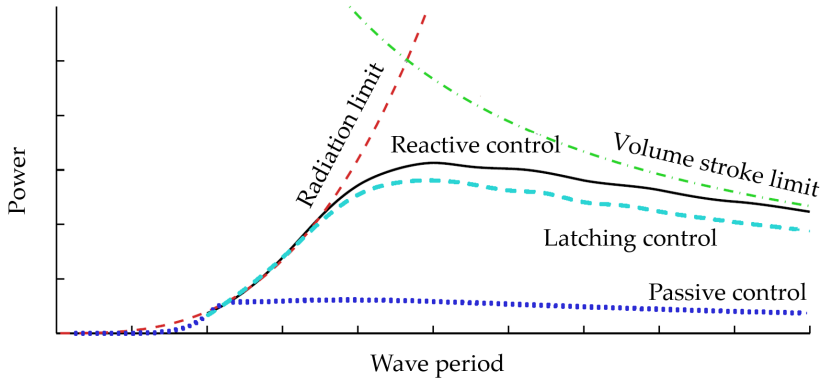

Figure 2.15: Example of power that can be absorbed by an oscillating body-type converter in regular waves using reactive and passive (including latching) control strategies, adapted from [36].

Multi-mode control problem

The vast majority of control strategies proposed to date predominantly focus on single-DOF WECs. Comparatively, the existing literature focusing specifically on the control of multi-mode WECs is relatively limited. One of the key challenges in the design of multi-mode WECs is the issue of coupling between hydrodynamic modes. This can arise due to various factors, such as through the geometric design of the device or hydrodynamic interactions between modes (e.g. surge and pitch). Depending on the design of the device,

failing to take into account such effects can result in noticeably reduced performance and power absorption efficiency [101].

In one of the first studies to address the effects of hydrodynamic coupling on control, Yavuz [115] suggested that coupling between surge and pitch could be potentially beneficial for enhancing the performance of a floating WEC device with active control. This was later contradicted in a study by Abdelkhalik et al. [2], who considered the Multiple-Input-Multiple-Output (MIMO) control of a floating WEC operating in surge, heave and pitch simultaneously. Instead, the authors recommended using only either surge or pitch for power absorption - but not both - to decrease the number of actuators required. It was proposed to take advantage of hydrodynamic coupling to shift power from one mode to the other to maintain the same maximum available power, which supports the discussion regarding diople-modes in Section 2.2.1. Several other theoretical MIMO controllers have also been developed for similar floating WEC devices operating in heave, surge and pitch [1, 61, 117]. Experimental testing of a MIMO controller for a floating 3-DOF WEC in a more realistic ocean environment has also been conducted [15]. However, in all of the aforementioned studies, independent control inputs were assumed for each degree of freedom, which is very difficult to realise in practice.

Regarding under-actuated systems, an optimal MIMO controller for a three-tethered floating buoy was initially considered in a study by Scruggs et al. [100]. Following this, Sergiienko et al. also considered the control of a three-tethered cylindrical WEC based on the CETO-6 device [101, 102], using a VTC strategy which was extended to the MIMO system. An interesting conclusion from both [100] and [101] was that some of the tethers may be required to operate as actuators at all times during the operation of the device. Another important conclusion from [101] was that the pitch mode, over which the device had poor control authority, was responsible for losses of up to 15% of the total power absorbed in certain cases due to coupling with the surge mode. VTC was also considered for a multi-DOF system based on the WaveSub device in a separate study by Hillis et al. [59]. In this study, a significant attempt was made to consider the controller performance in realistic operating conditions, including nonlinear kinematic and viscous forces and irregular sea states. The controller was demonstrated to have improved device performance by up to 80% compared to a well-tuned, passively damped system.

Overall, the importance of proper control in WEC systems cannot be overlooked. Some notable progress has been made towards developing MIMO controllers specifically for multi-mode WECs. Several studies have high-

lighted the importance of surge-pitch hydrodynamic coupling in the design of the controller in particular [2, 115]. Further studies have pointed out the need to better understand the effect of this coupling on device performance, especially in the case of under-actuated systems [101]. It is also noted that most controllers have been designed using linear hydrodynamic models. This is an important consideration, given that control strategies developed based on linear hydrodynamic models have consistently led to overestimations of power when compared to results from higher fidelity models [20, 23, 48]. It is therefore necessary to consider any relevant nonlinear effects when designing controllers for multi-mode WECs, in order to avoid potentially misleading results.

2.3 Nonlinear hydrodynamics for wave energy applications

The development of wave energy converters relies heavily on numerical modelling to accurately estimate the behaviour and performance of the system during its operation. Modelling of WECs has typically been based on linear theory and tools previously developed for various marine applications, such as ships or offshore structures [52, 85]. These linear models have been used to formulate much of the fundamental theory regarding wave energy absorption [34].

One of the complications of employing traditional linear models is that, unlike ships or other marine applications, most WECs are instead designed to undergo relatively large motions to maximise power absorption. A WEC may therefore encounter nonlinear dynamics not only in survival mode and extreme wave conditions, but also during its normal operation in power production mode as shown in Figure 2.16. Higher fidelity models are therefore recommended in these instances to capture any important nonlinear effects and provide a more accurate assessment of WEC behaviour and performance.

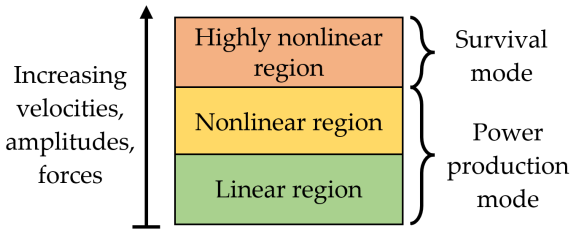

Figure 2.16: Operating regions of wave energy converters, adapted from [90].

In this section, the importance of nonlinear effects for modelling of WECs will be discussed. A number of available numerical modelling approaches will also be briefly reviewed. The scope of the discussion will primarily focus on hydrodynamic nonlinearities associated with the interactions between the device and the surrounding fluid, rather than those caused purely by the wave itself, geometric nonlinearities or the PTO system. The highly nonlinear operating region associated with extreme waves and survival mode, as indicated in Figure 2.16, is also considered outside the scope of this study.

2.3.1 Nonlinear hydrodynamic effects

There are several hydrodynamic forces which can act on a WEC during its operation and result in nonlinear dynamics. The main forces that are relevant for the modelling of oscillating body-type WECs are [85]:

- **Froude-Krylov (FK) force** - generated by the unsteady pressure field of an undisturbed wave in the absence of any bodies in the fluid,
- **Diffraction force** - caused by the disturbance of an incident wave due to the presence of a body in the fluid. In linear models, this is combined together with the FK force to form the total **excitation force** acting on the body.
- **Radiation force** - the load associated with waves radiated by a moving body, assuming no incident waves are present,
- **Viscous forces** - comprising both form and skin friction drag, and oppose the relative motion between the body and fluid,
- **Parametric excitations** - are an amplification of motions caused by the nonlinear coupling between the DOFs of a moving body. This usually occurs when the incident wave frequency is approximately twice the resonant frequencies of the roll, pitch or yaw modes, or when hydrodynamic modes have resonances which are multiples of other modes.
- **Slamming** - occurs when the body impacts the sea surface. This may occur when a converter rises above the free surface, followed by an impact as it falls.

The relevance of these hydrodynamic nonlinearities for various oscillating-body WEC devices is summarised in Table 2.2, based on a review by Penalba et al. [85]. The types of WECs featured in Table 2.2 are categorised based on size and mode of oscillation:

- Heaving point absorbers (HPA),
- Oscillating pitch converters (OPC),
- Oscillating surge converters (OSC).

Table 2.2: Relevance of nonlinear hydrodynamic forces for various WEC types, based on [85].

		Relevance of nonlinear effects			
WEC type	**Particular effects**	**Froude-Krylov**	**Diffraction**	**Radiation**	**Viscous**
HPA	Parametric excitation	High	Low	Low	Low
OPC	Parametric excitation Slamming	High	-	-	High
OSC	Slamming	Low	Not proven	Not proven	High

Particular nonlinear effects or phenomena that are important only for certain device types are also outlined in Table 2.2. For example, OPC and OSC devices may encounter slamming effects during operation if large pitching motions raise part of the device above the free surface. Parametric excitations have also been observed during experimental testing of HPAs and OPCs, leading to amplified pitch, roll and yaw motions of the device [77, 106].

Regarding the remaining forces listed in Table 2.2, Giorgi et al. [47, 50] have demonstrated in a number of studies that nonlinear FK forces can significantly influence the performance of HPAs. OPCs may also benefit from nonlinear modelling of FK forces for the prediction of parametric excitations [5]. For diffraction and radiation forces, their importance has only been considered for HPAs and OSCs [47, 50], as shown in Figure 2.17.

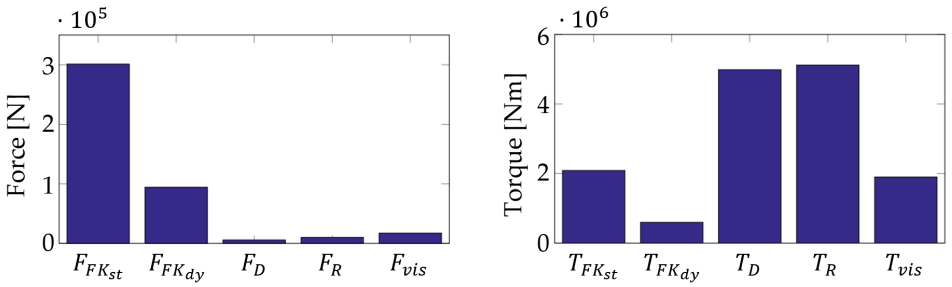

(a) (b)

Figure 2.17: Contribution of various forces to the total hydrodynamic force acting on an (a) HPA and (b) OSC under controlled conditions in regular waves. The total hydrodynamic force (F) and torque (T) have been decomposed into their static FK (FK_{st}), dynamic FK (FK_{dy}), diffraction (D), radiation (R) and viscous drag (vis) components. Adapted from [47].

While Figure 2.17(b) suggests that they are the dominant forces in OSCs, the impact of nonlinear diffraction and radiation effects on the performance of these devices has not been definitively investigated in any of the existing literature. Additionally, despite the reportedly low importance of diffraction and radiation effects for HPAs [71], this is more likely due to the size of the device as opposed to the mode of oscillation [34]. It is unknown if nonlinear diffraction and radiation forces have a greater impact on larger quasi-PA devices. Finally, out of the oscillating body-type devices, nonlinear viscous forces are most important for modelling of OPCs and OSCs [5, 10].

It is critical to note that most of the available literature has only considered the relevance of nonlinear effects for WEC devices which oscillate primarily in one hydrodynamic mode. There is almost no literature addressing the importance of nonlinear forces acting on multi-mode devices which oscillate in multiple modes at the same time. Table 2.2 suggests that most of the nonlinear hydrodynamic forces listed above may be relevant for their modelling and performance assessment. While a number of studies have applied fully nonlinear modelling approaches to spherical [19, 70] and long horizontal cylinder [54] WECs moving in surge, heave and pitch simultaneously, the geometries investigated in these studies are only minimally affected by pitch motions. For other geometries, some literature exists addressing the nonlinear hydrodynamic forces acting on vertical cylinders [58, 114] and rectangular boxes [94] oscillating in multiple directions simultaneously; however, these cover various marine applications unrelated to WECs, such as ships and cargo. It is unknown how these nonlinear forces may affect the performance and control of multi-mode WECs with similar, non-spherical geometries.

2.3.2 Modelling approaches

With the increase in computational capabilities in recent years, various mathematical and computational tools are now available for modelling of nonlinear wave-body interactions. According to Penalba et al. [85], modelling approaches can be divided into three main categories: (i) Navier-Stokes Computational Fluid Dynamics (CFD) and Smoothed-Particle Hydrodynamics (SPH), (ii) potential flow models and (iii) models from data.

CFD and SPH are fully nonlinear modelling approaches based on solving the Navier-Stokes equations [85]. CFD models use a mesh to discretise the numerical domain, while SPH models are mesh-free and use an array of particles instead. Meshed domains used to generate waves in CFD codes are also known as Numerical Wave Tanks (NWT). When validated against

experimental results, CFD and SPH are among the most accurate of all the available modelling techniques [112]. However, their main drawbacks are high computational time and costs, as well as the considerable experience required by the analysts.

In **potential flow models**, the fluid velocity is described as a gradient of the velocity potential. By solving for this velocity potential, typically using boundary element methods (BEM), the pressure and hydrodynamic forces acting on a body can then be computed. The potential flow formulation can be applied in various ways:

- In **fully linear models**, the hydrodynamic parameters are calculated using only the mean free-surface level and nominal position of body. This may lead to reduced accuracy in cases with steep incident waves, large device motions or significant changes to the wetted surface during operation [113].
- **Partially nonlinear** potential flow models extend the linear model by including some additional nonlinear effects. A common extension involves recalculating the nonlinear FK forces at each time step using the instantaneous wetted surface area of the body [45, 46, 49, 55].
- **Weakly nonlinear** models consider both the nonlinear free surface and body-exact conditions, while simplifying some aspects of the potential flow formulation. For example, using the weak-scatterer (WS) approximation [80], the incident component of the velocity potential becomes a model input so only the diffracted and radiated components need to be determined [62]. Another approach is to assume shallow-water conditions and eliminate the vertical component of the velocity terms in the potential flow equations, thereby reducing the computational domain to 2D [21, 26, 89].
- **Fully-nonlinear** models apply the complete potential flow formulation with no simplifications [8, 53, 54].

Viscous losses can also be included into potential flow models through an additional damping term or through the Morison equation [73]. More detail regarding potential flow theory will also be given in Chapter 3, Section 3.2.

Models from data can be applied in instances where the physical system is too complex or computationally demanding to model in its entirety. The

data for these models can be obtained from real-life wave tank experiments [51, 60] or NWT simulations [22]. However, the accuracy of these models is dependent on the validity of the data that it was built from. Data from experiments may be subjected to measurement errors or reflection effects, while data from NWTs may be unreliable unless previously validated against experimental results [85].

Computation versus fidelity

In order to select the most suitable modelling approach, it is important to consider both the device and whether the dominant requirement of the model is either: (i) high fidelity (accuracy) or (ii) low computation (speed). A comparison of the relative fidelity and computational costs of the different modelling approaches is illustrated in Figure 2.18.

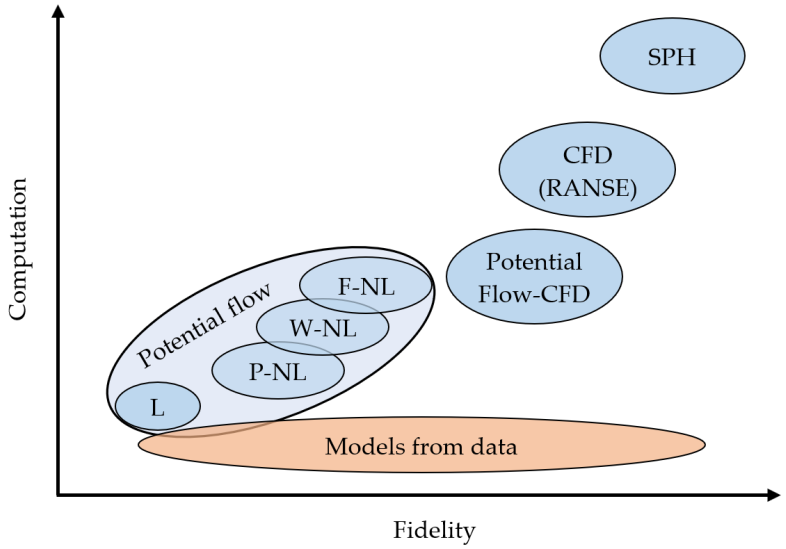

Figure 2.18: Relative computational cost and fidelity of various modelling approaches, adapted from [85]. L refers to linear, P-NL is partially-nonlinear, W-NL is weakly-nonlinear, F-NL is fully-nonlinear.

Based on these considerations, Penalba et al. [85] made a number of recommendations for suitable modelling approaches for various oscillating body-type WECs, which are given in Table 2.3. Overall, when the main model requirement is low computation, potential flow models with viscous drag effects are the recommended approach for all devices. Since FK forces are responsible for most of the nonlinear effects in HPAs, partially nonlinear potential flow models with viscous drag are recommended for higher fidelity modelling of these devices, having demonstrated good agreement with

Table 2.3: Suggested modelling approaches for different WEC types and model purposes, based on [85]. F_{visc} refers to viscous forces, which can be externally included in potential flow models.

WEC type	**High fidelity (accuracy)**	**Low computation (speed)**
HPA	P-NL potential theory with F_{visc}	P-NL potential theory with F_{visc}
OPC	P-NL potential theory with CFD	P-NL potential theory with F_{visc}
OSC	CFD	Linear potential theory with F_{visc}

experimental results [106]. If higher fidelity is required for OPCs and OSCs, CFD approaches were suggested due to the higher relevance of radiation and diffraction effects [50].

Concerning suitable modelling approaches for multi-mode WECs, while partially nonlinear potential flow models appear to be the most versatile approach from Table 2.3, they may be unable to capture all the relevant nonlinearities for devices oscillating in heave, surge and pitch simultaneously. As previously discussed, most partially nonlinear potential flow models in the literature only consider the nonlinear FK forces. While suitable for small or heaving buoys, it is unknown whether this is sufficient to accurately model larger, surging or pitching devices where diffraction and radiation forces are more significant [50]. CFD may also be prohibitive for performance assessment and design optimisation purposes which have low computation requirements. Weakly or fully nonlinear approaches may therefore be suitable alternatives in this case. There are also many prospective avenues of research using these modelling approaches, since they are still in the early stages of development and have not been widely considered in the literature. The weak-scatterer approach is particularly promising, with early studies showing good agreement with fully nonlinear potential flow models [63] and CFD [24], whilst still achieving faster computational times.

2.4 Concluding remarks and perspectives

In this chapter, some relevant literature pertaining to the work done in this Thesis was presented. From the broad overview of existing prototypes, it can be seen that the design of WECs is extremely diverse. Compared to other WEC types, multi-mode WECs have the potential to be the most hydrodynamically efficient, resulting in more power absorbed from waves. However, given that many existing prototypes are designed as single-mode devices, there are many aspects of multi-mode converters that are not well understood, such as those related to their design, control, and the effect of

nonlinear hydrodynamics on performance.

As discussed in Section 2.2.2, most multi-mode prototypes appear to favour surge and heave as the main modes of absorption, while the effect of pitch is often overlooked. While this may be suitable for smaller or spherical WECs, the assumption of negligible pitch may not be valid for larger converters with non-spherical geometries. The nonlinear hydrodynamics and control of such devices may also be consequently affected. Furthermore, Section 2.3 indicated a large gap in the literature regarding the impact of nonlinear hydrodynamic effects on the performance of multi-mode WECs which oscillate in multiple directions simultaneously. Additionally, the effect of nonlinear diffraction and radiation forces on pitching and surging converters is also not well understood. These gaps are therefore addressed in Chapter 4, which considers the impact of nonlinear hydrodynamic forces on the performance of a flat cylindrical quasi-PA WEC oscillating in surge and pitch simultaneously. Special emphasis is placed on the nonlinear diffraction and radiation forces resulting from both surge and pitch motions.

An effective controller is critical for increasing the efficiency of wave energy devices. While a number of controllers have been developed specifically for multi-mode WECs, it was identified in Section 2.2.3 that these controllers have all been designed under the assumption of linear hydrodynamics. Given that most WEC controllers aim to increase power absorption through resonance and large amplitude motions, linear hydrodynamic models may be inadequate and overestimate power absorption. Therefore, Chapter 5 considers the spring-damper control of a multi-mode WEC in surge, heave and pitch, and compares the performance of the device between a fully linear and weakly nonlinear potential flow model. From the results of this investigation, an alternative approach where the natural frequencies of each hydrodynamic mode are tuned to different frequencies is also examined to explore the potential for increased broadband performance in real seas.

In addition to coupling between hydrodynamic modes, another complication related to the design and control of multi-mode WECs is the issue of under-actuation. While controllability can be increased with the number of actuators, this comes at the expense of increased capital and operational costs. The three-tethered configuration appears to provide a good compromise between both controllability and cost, as evidenced by its use in a number of different multi-mode WEC designs. As identified in Section 2.2.3, many control strategies for multi-mode WECs have only considered ideal or independent control for each oscillation mode. Studies that consider physical devices with proper actuation systems only include hydrodynamic forces based on linear potential theory. Therefore, to address this gap, Chapter

6 studies a multi-mode WEC with an under-actuated three-tether configuration subjected to various nonlinear forces, including those caused by hydrodynamic coupling between modes. Several device parameters, such as the tether angles, location of the centre of gravity and rotational moment of inertia, are also examined for passive tuning of the pitch mode in particular, given that the three-tethered configuration does not have full control authority over this mode.

References

[1] Abdelkhalik, O. and Zou, S. (2018). "Control of Wave Energy Converters Using A Simple Dynamic Model". In: *IEEE Transactions on Sustainable Energy* 10.2, pp. 579–585.

[2] Abdelkhalik, O., Zou, S., Robinett, R. D., Bacelli, G., Wilson, D. G., Coe, R. and Korde, U. (2017). "Multiresonant feedback control of a three-degree-of-freedom wave energy converter". In: *IEEE Transactions on Sustainable Energy* 8.4, pp. 1518–1527.

[3] Babarit, A. (2015). "A database of capture width ratio of wave energy converters". In: *Renewable Energy* 80, pp. 610–628.

[4] Babarit, A and Clément, A. H. (2006). "Optimal latching control of a wave energy device in regular and irregular waves". In: *Applied Ocean Research* 28.2, pp. 77–91.

[5] Babarit, A, Mouslim, H., Clément, A. H. and Laporte-Weywada, P. (May 2009a). "On the numerical modelling of the non-linear behaviour of a wave energy converter". In: *ASME 2009 28th International Conference on Ocean, Offshore and Arctic Engineering*, pp. 1045–1053.

[6] Babarit, A. and Delhommeau, G. (2015). "Theoretical and numerical aspects of the open source BEM solver NEMOH". In: *Proceedings of the 11th European Wave and Tidal Energy Conference EWTEC* September 2015, pp. 1–12.

[7] Babarit, A., Guglielmi, M. and Clément, A. H. (2009b). "Declutching control of a wave energy converter". In: *Ocean Engineering* 36.12, pp. 1015–1024.

[8] Bai, W and Taylor, R. E. (2006). "Higher-order boundary element simulation of fully nonlinear wave radiation by oscillating vertical cylinders". In: *Applied Ocean Research* 28.4, pp. 247–265.

[9] Behrens, S., Griffin, D., Hayward, J., Hemer, M., Knight, C., McGarry, S., Osman, P. and Wright, J. (2016). *Ocean renewable energy: 2015-2050:*

An analysis of ocean energy in Australia. Tech. rep. July 2012. CSIRO, pp. 1095–1097.

[10] Bhinder, M. A., Babarit, A., Gentaz, L. and Ferrant, P. (2012). "Effect of viscous forces on the performance of a surging wave energy converter". In: *Proceedings of the 22nd International Offshore and Polar Engineering Conference ISOPE* 4, pp. 545–549.

[11] Budal, K and Falnes, J (1975). "A resonant point absorber of ocean-wave power". In: *Nature* 256.5517, pp. 478–479.

[12] Budal, K and Falnes, J (1980). "Interacting point absrobers with controlled motion". In: *Power from sea waves*. Ed. by B. M. Count. London, UK: Academic Press, pp. 381–399.

[13] Carnegie Clean Energy (2020). *CETO Technology - Carnegie Clean Energy*. URL: https://www.carnegiece.com/ceto-technology/.

[14] Coe, R., Bacelli, G. and Forbush, D. (May 2021). "A practical approach to wave energy modeling and control". In: *Renewable and Sustainable Energy Reviews* 142, p. 110791.

[15] Coe, R., Bacelli, G., Spencer, S. J., Forbush, D. and Dullea, K. (2019a). *MASK3 for Advanced WEC Dynamics and Controls*. Tech. rep.

[16] Coe, R. G., Bacelli, G., Wilson, D. G., Abdelkhalik, O., Korde, U. A. and Robinett III, R. D. (2017). "A comparison of control strategies for wave energy converters". In: *International Journal of Marine Energy* 20, pp. 45–63.

[17] Coe, R. G., Rosenberg, B. J., Quon, E. W., Chartrand, C. C., Yu, Y.-H., Rij, J. van and Mundon, T. R. (2019b). "CFD design-load analysis of a two-body wave energy converter". In: *Journal of Ocean Engineering and Marine Energy* 5.2, pp. 99–117.

[18] Count, B. M. (1980). "Wave power: a problem searching for a solution". In: *Power from sea waves*. Ed. by B. Count. London, England: Academic Press, pp. 11–27.

[19] Dafnakis, P., Bhalla, A. P. S., Sirigu, S. A., Bonfanti, M., Bracco, G. and Mattiazzo, G. (Sept. 2020). "Comparison of wave–structure interaction dynamics of a submerged cylindrical point absorber with three degrees of freedom using potential flow and computational fluid dynamics models". In: *Physics of Fluids* 32.9, p. 93307.

[20] Davidson, J, Genest, R and Ringwood, J. V. (2018a). "Adaptive control of a wave energy converter". In: *IEEE Transactions on Sustainable Energy* 9.4, pp. 1588–1595.

[21] Davidson, J. and Costello, R. (2020). "Efficient Nonlinear Hydrodynamic Models for Wave Energy Converter Design—A Scoping Study". In: *Journal of Marine Science and Engineering* 8.1.

[22] Davidson, J., Giorgi, S. and Ringwood, J. V. (2015). "Linear parametric hydrodynamic models for ocean wave energy converters identified from numerical wave tank experiments". In: *Ocean Engineering* 103, pp. 31–39.

[23] Davidson, J., Windt, C., Giorgi, G., Genest, R. and Ringwood, J. (Feb. 2018b). "Evaluation of energy maximising control systems for wave energy converters using OpenFOAM". In: *OpenFOAM - Selected papers from the 11th workshop*. Ed. by J. M. Nóbrega; and H. Jasak. Springer International Publishing, pp. 157–171.

[24] Ding, B., Wuillaume, P, Meng, F., Babarit, A., Schubert, B., Sergiienko, N. Y. and Cazzolato, B. S. (2019). "Comparison of wave-body interaction modelling methods for the study of reactively controlled point absorber wave energy converter". In: *Proceedings of the 34th International Workshop on Water Waves and Floating Bodies*. Newcastle.

[25] Drew, B., Plummer, A. R. and Sahinkaya, M. N. (2009). "A review of wave energy converter technology". In: *Proceedings of the Institution of Mechanical Engineers, Part A: Journal of Power and Energy* 223.8, pp. 887–902.

[26] Eskilsson, C., Palm, J., Engsig-Karup, A., Bosi, U. and Ricchiuto, M. (Sept. 2015). "Wave induced motions of point-absorbers: a hierarchical investigation of hydrodynamic models". In: *Proceedings of the 12th European Wave and Tidal Energy Conference EWTEC*. Nantes,France.

[27] Evans, D. V. (1976). "A theory for wave-power absorption by oscillating bodies". In: *Journal of Fluid Mechanics* 77.1, 1–25.

[28] Evans, D. V. (1978). "The oscillating water column wave-energy device". In: *IMA Journal of Applied Mathematics* 22.4, pp. 423–433.

[29] Evans, D. V., Jeffrey, D. C., Salter, S. H. and Taylor, J. R. M. (1979). "Submerged cylinder wave energy device: theory and experiment". In: *Applied Ocean Research* 1.1, pp. 3–12.

[30] Faedo, N., Olaya, S. and Ringwood, J. V. (2017). "Optimal control, MPC and MPC-like algorithms for wave energy systems: An overview". In: *IFAC Journal of Systems and Control* 1, pp. 37–56.

[31] Falcão, A. F. d. O. (2010). "Wave energy utilization: A review of the technologies". In: *Renewable and Sustainable Energy Reviews* 14.3, pp. 899–918.

[32] Falcão, A. F. O. and Henriques, J. C. C. (2016). "Oscillating-water-column wave energy converters and air turbines: A review". In: *Renewable Energy* 85, pp. 1391–1424.

[33] Falnes, J. (1995). "On non-causal impulse response functions related to propagating water waves". In: *Applied Ocean Research* 17.6, pp. 379–389.

[34] Falnes, J. (2002). *Ocean waves and oscillating systems: Linear interactions including wave-energy extraction*. Cambridge University Press, p. 220.

[35] Falnes, J. (2007). "A review of wave-energy extraction". In: *Marine Structures* 20.4, pp. 185–201.

[36] Falnes, J. and Hals, J. (2012). "Heaving buoys, point absorbers and arrays". In: *Philosophical Transactions of the Royal Society A: Mathematical, Physical and Engineering Sciences* 370.1959, pp. 246–277.

[37] Falnes, J. and Løvseth, J. (1991). "Ocean wave energy". In: *Energy Policy* 19.8, pp. 768–775.

[38] Faraggiana, E, Chapman, J. C., Williams, A. J. and Masters, I (2020a). "Genetic based optimisation of the design parameters for an array-on-device orbital motion wave energy converter". In: *Ocean Engineering* 218, p. 108251.

[39] Faraggiana, E, Whitlam, C, Chapman, J, Hillis, A, Roesner, J, Hann, M, Greaves, D, Yu, Y.-H., Ruehl, K, Masters, I, Foster, G and Stockman, G (2020b). "Computational modelling and experimental tank testing of the multi float WaveSub under regular wave forcing". In: *Renewable Energy* 152, pp. 892–909.

[40] Faraggiana, E., Masters, I. and Chapman, J. (Sept. 2019). *Multidirectional waves and time domain perturbed field visualization of the WaveSub device*.

[41] Finnegan, W., Rosa-Santos, P., Taveira-Pinto, F. and Goggins, J. (2021). "Development of a numerical model of the CECO wave energy converter using computational fluid dynamics". In: *Ocean Engineering* 219, p. 108416.

[42] Fusco, F. and Ringwood, J. (Jan. 2013). "A simple and effective real-time controller for wave energy converters". In: *Sustainable Energy, IEEE Transactions on* 4, pp. 21–30.

[43] Galván-Pozos, D. E. and Ocampo-Torres, F. J. (2020). "Dynamic analysis of a six-degree of freedom wave energy converter based on the concept of the Stewart-Gough platform". In: *Renewable Energy* 146, pp. 1051–1061.

[44] Gao, H. and Yu, Y. (2018). "The dynamics and power absorption of cone-cylinder wave energy converters with three degree of freedom in irregular waves". In: *Energy* 143, pp. 833–845.

[45] Gilloteaux, J.-C., Babarit, A., Ducrozet, G., Durand, M. and Clément, A. (June 2007a). "A non-linear potential model to predict

large-amplitudes-motions: application to the SEAREV wave energy converter". In: *ASME 2007 26th International Conference on Offshore Mechanics and Arctic Engineering*. San Diego, California, USA, pp. 529–535.

[46] Gilloteaux, J.-C., Ducrozet, G., Babarit, A. and Clément, A. (Jan. 2007b). "Non-linear model to simulate large amplitude motions: application to wave energy conversion". In: *Proceedings of the 22nd International Workshop on Water Waves and Floating Bodies IWWFB*. Plitvice, Croatia.

[47] Giorgi, G., Penalba, M. and Ringwood, J. (2016). "Nonlinear hydrodynamic force relevance for heaving point absorbers and oscillating surge converters". In: *Proceedings of the 3rd Asian Wave and Tidal Energy Conference AWTEC*. Singapore.

[48] Giorgi, G. and Ringwood, J. V. (2016). "Implementation of latching control in a numerical wave tank with regular waves". In: *Journal of Ocean Engineering and Marine Energy* 2.2, pp. 211–226.

[49] Giorgi, G. and Ringwood, J. V. (2018a). "Analytical representation of nonlinear Froude-Krylov forces for 3-DoF point absorbing wave energy devices". In: *Ocean Engineering* 164, pp. 749–759.

[50] Giorgi, G. and Ringwood, J. V. (Feb. 2018b). "Comparing nonlinear hydrodynamic forces in heaving point absorbers and oscillating wave surge converters". In: *Journal of Ocean Engineering and Marine Energy* 4.1, pp. 25–35.

[51] Giorgi, S., Davidson, J., Jakobsen, M., Kramer, M. and Ringwood, J. V. (2019). "Identification of dynamic models for a wave energy converter from experimental data". In: *Ocean Engineering* 183, pp. 426–436.

[52] Greaves, D. (Mar. 2018). "Wave Energy Technology". In: *Wave and Tidal Energy*. Wiley Online Books, pp. 52–104.

[53] Grilli, S. T., Guyenne, P. and Dias, F. (Apr. 2001). "A fully non-linear model for three-dimensional overturning waves over an arbitrary bottom". In: *International Journal for Numerical Methods in Fluids* 35.7, pp. 829–867.

[54] Guerber, E., Benoit, M., Grilli, S. and Buvat, C. (June 2010). "Modeling of fully nonlinear wave interactions with moving submerged structures". In: *Proceedings of the 20th International Offshore and Polar Engineering Conference ISOPE*. Vol. 3. Beijing, China.

[55] Guerinel, M., Alves, M. and Sarmento, A. (Sept. 2011). "Nonlinear modelling of the dynamics of a free floating body". In: *Proceedings of the 9th European Wave and Tidal Energy Conference EWTEC*. Southampton, UK.

[56] Hals, J., Falnes, J. and Moan, T. (Nov. 2010). "Constrained optimal control of a heaving buoy wave-energy converter". In: *Journal of Offshore Mechanics and Arctic Engineering* 133.1, pp. 11401–11415.

[57] Hals, J., Falnes, J. and Moan, T. (Mar. 2011). "A comparison of selected strategies for adaptive control of wave energy converters". In: *Journal of Offshore Mechanics and Arctic Engineering* 133.3, pp. 31101–31112.

[58] Hannan, M. A., Bai, W and Ang, K. K. (Mar. 2014). "Modeling of fully nonlinear wave radiation by submerged moving structures using the higher order boundary element method". In: *Journal of Marine Science and Application* 13.1, pp. 1–10.

[59] Hillis, A. J., Whitlam, C, Brask, A, Chapman, J and Plummer, A. R. (2020). "Active control for multi-degree-of-freedom wave energy converters with load limiting". In: *Renewable Energy* 159, pp. 1177–1187.

[60] Iturrioz, A., Guanche, R., Armesto, J. A., Vidal, C. and Losada, i. J. (June 2013). "Experimentally calibrated time-domain numerical model for a fixed OWC device". In: *ASME 2013 32nd International Conference on Ocean, Offshore and Arctic Engineering*.

[61] Korde, U. A., Lyu, J., Robinett, R. D., Wilson, D. G., Bacelli, G. and Abdelkhalik, O. (2017). "Constrained near-optimal control of a wave energy converter in three oscillation modes". In: *Applied Ocean Research* 69, pp. 126–137.

[62] Letournel, L., Chauvigné, C., Gelly, B., Babarit, A., Ducrozet, G. and Ferrant, P. (2018). "Weakly nonlinear modeling of submerged wave energy converters". In: *Applied Ocean Research* 75, pp. 201–222.

[63] Letournel, L., Ferrant, P., Babarit, A., Ducrozet, G., Harris, J. C., Benoit, M. and Dombre, E. (June 2014). "Comparison of fully nonlinear and weakly nonlinear potential flow solvers for the study of wave energy converters undergoing large amplitude motions". In: *ASME 2014 33rd International Conference on Ocean, Offshore and Arctic Engineering*. San Francisco, California.

[64] López, I., Andreu, J., Ceballos, S., Martínez De Alegría, I. and Kortabarria, I. (2013). "Review of wave energy technologies and the necessary power-equipment". In: *Renewable and Sustainable Energy Reviews* 27, pp. 413–434.

[65] López, M, Ramos, V, Rosa-Santos, P and Taveira-Pinto, F (2018). "Effects of the PTO inclination on the performance of the CECO wave energy converter". In: *Marine Structures* 61, pp. 452–466.

[66] Lotfi, B. and Huang, L. (2013). "A novel wave energy converter using the Stewart platform". In: *Journal of Green Engineering* 4.1, pp. 33–48.

[67] Maria-Arenas, A., Garrido, A. J., Rusu, E. and Garrido, I. (2019). "Control strategies applied to wave energy converters: state of the art". In: *Energies* 12.16.

[68] Marine Power Systems (2018). *WaveSub - The Future of Energy*. URL: http://marinepowersystems.co.uk/.

[69] Meng, F., Cazzolato, B., Li, Y., Ding, B., Sergiienko, N. and Arjomandi, M. (2019). "A sensitivity study on the effect of mass distribution of a single-tether spherical point absorber". In: *Renewable Energy* 141, pp. 583–595.

[70] Meng, F., Rafiee, A., Ding, B., Cazzolato, B. and Arjomandi, M. (Mar. 2020). "Nonlinear hydrodynamics analysis of a submerged spherical point absorber with asymmetric mass distribution". In: *Renewable Energy* 147, pp. 1895–1908.

[71] Merigaud, A., Gilloteaux, J.-C. and Ringwood, J. (July 2012). "A nonlinear extension for linear boundary element methods in wave energy device modelling". In: *ASME 2012 31st International Conference on Offshore Mechanics and Arctic Engineering*. Vol. 4. Rio de Janeiro, Brazil.

[72] Mofor, L., Goldsmith, J. and Jones, F. (2014). *Ocean Energy: Technology Readiness, Patents, Deployment Status and Outlook*. Tech. rep. August, p. 76.

[73] Morison, J., Johnson, J. and Schaaf, S. (1950). "The force exerted by surface waves on piles". In: *Journal of Petroleum Technology* 2.05, pp. 149–154.

[74] NEMOS GmbH (2021). *Wave Energy - NEMOS*. URL: https://nemos.de/en/wave-energy.

[75] OES (2020). *Annual Report: An Overview of Ocean Energy Activities in 2020*. Tech. rep. Ocean Energy Systems.

[76] Ogilvie, T. F. (1963). "First- and second-order forces on a cylinder submerged under a free surface". In: *Journal of Fluid Mechanics* 16.3, 451–472.

[77] Orszaghova, J., Wolgamot, H., Draper, S. and Rafiee, A. (2018). "Motion instabilities in tethered buoy WECs". In: *Proceedings of the 4th Asian Wave and Tidal Energy Conference AWTEC*. Taipei.

[78] Oscilla Power (2020). *Triton WEC - Oscilla Power*. URL: https://oscillapower.com/triton-wec/.

[79] Ozkop, E. and Altas, I. H. (2017). "Control, power and electrical components in wave energy conversion systems: A review of the technologies". In: *Renewable and Sustainable Energy Reviews* 67, pp. 106–115.

[80] Pawlowski, J. S. and Bass, D. W. (1991). *A theoretical and numerical model of ship motions in heavy seas*. Tech. rep.

[81] Payne, G. S., Pascal, R. and Vaillant, G. (Oct. 2015). "On the concept of sloped motion for free-floating wave energy converters". In: *Proceedings of the Royal Society A: Mathematical, Physical and Engineering Sciences* 471.2182, p. 20150238.

[82] Payne, G. S., Taylor, J. R. M., Bruce, T. and Parkin, P. (2008a). "Assessment of boundary-element method for modelling a free-floating sloped wave energy device. Part 1: Numerical modelling". In: *Ocean Engineering* 35.3, pp. 333–341.

[83] Payne, G. S., Taylor, J. R. M., Bruce, T. and Parkin, P. (2008b). "Assessment of boundary-element method for modelling a free-floating sloped wave energy device. Part 2: Experimental validation". In: *Ocean Engineering* 35.3, pp. 342–357.

[84] Peckolt, J., Runkel, T., Baumann, S., Pütz, J., Peckolt, J., Schneider, N., Wegner, J., Lucas, J. and Friedhoff, B. (2015). *1:5 scale tests of the NEMOS wave energy converter in natural waves at Nissum Bredning Test Site*. Tech. rep. Marine Renewables Infrastructure Network.

[85] Penalba, M., Giorgi, G. and Ringwood, J. V. (2017). "Mathematical modelling of wave energy converters: A review of nonlinear approaches". In: *Renewable and Sustainable Energy Reviews* 78, pp. 1188–1207.

[86] Rafiee, A. and Valizadeh, A. (2018). *Multi-moored CETO and results from Plymouth 2018 test campaign*. Tech. rep. Carnegie Clean Energy.

[87] Rendel Palmer & Tritton and Kennedy & Donkin (1982). *United Kingdom wave energy programme - Consultant's 1981 assessment*. Tech. rep. UK Department of Energy.

[88] Richter, M., Magaña, M., Sawodny, O. and Brekken, T. (2013). "Nonlinear model predictive control of a point absorber wave energy converter". In: *Sustainable Energy, IEEE Transactions on* 4, pp. 118–126.

[89] Rijnsdorp, D. P., Hansen, J. E. and Lowe, R. J. (2018). "Simulating the wave-induced response of a submerged wave-energy converter using a non-hydrostatic wave-flow model". In: *Coastal Engineering* 140, pp. 189–204.

[90] Ringwood, J. V., Bacelli, G. and Fusco, F. (2014). "Energy-maximizing control of wave-energy converters: The development of control system technology to optimize their operation". In: *IEEE Control Systems* 34.5, pp. 30–55.

[91] Rodríguez, C. A., Rosa-Santos, P. and Taveira-Pinto, F. (2018). "Assessment of the power conversion of wave energy converters based

on experimental tests". In: *Energy Conversion and Management* 173, pp. 692–703.

[92] Rodríguez, C. A., Rosa-Santos, P. and Taveira-Pinto, F. (2019). "Assessment of damping coefficients of power take-off systems of wave energy converters: A hybrid approach". In: *Energy* 169, pp. 1022–1038.

[93] Rodríguez, C. A., Rosa-Santos, P. and Taveira-Pinto, F. (2020). "Hydrodynamic optimization of the geometry of a sloped-motion wave energy converter". In: *Ocean Engineering* 199, p. 107046.

[94] Rodriguez, M., Spinneken, J. and Swan, C. (2016). "Nonlinear loading of a two-dimensional heaving box". In: *Journal of Fluids and Structures* 60, pp. 80–96.

[95] Rosa-Santos, P., Taveira-Pinto, F., Rodríguez, C. A., Ramos, V. and López, M. (2019). "The CECO wave energy converter: Recent developments". In: *Renewable Energy* 139, pp. 368–384.

[96] Rosenberg, B. J. and Mundon, T. R. (2016). "Numerical and physical modeling of a flexibly-connected two-body wave energy converter". In: *Proceedings of the 4th Marine Energy Technology Symposium*. Washington D.C., USA, pp. 5–8.

[97] Salter, S. H. (1974). "Wave power". In: *Nature* 249.5459, pp. 720–724.

[98] Salter, S. H. (Jan. 1989). "World progress in wave energy—1988". In: *International Journal of Ambient Energy* 10.1, pp. 3–24.

[99] Salter, S. H. and Lin, C.-P. (1998). "Wide tank efficiency measurments on a model of the sloped IPS buoy". In: *Proceedings of the 3rd European Wave and Tidal Energy Conference EWTEC*. Nantes, France.

[100] Scruggs, J. T., Lattanzio, S. M., Taflanidis, A. A. and Cassidy, I. L. (2013). "Optimal causal control of a wave energy converter in a random sea". In: *Applied Ocean Research* 42, pp. 1–15.

[101] Sergiienko, N. Y., Cazzolato, B. S., Arjomandi, M, Ding, B and Silva, L. S. P. da (2019). "Considerations on the control design for a three-tether wave energy converter". In: *Ocean Engineering* 183, pp. 469–477.

[102] Sergiienko, N. Y., Cazzolato, B. S., Hardy, P., Arjomandi, M. and Ding, B. (2017). "Internal-model-based velocity tracking control of a submerged three-tether wave energy converter". In: *Proceedings of the 12th European Wave and Tidal Energy Conference EWTEC*, pp. 1–8.

[103] Sergiienko, N. Y., Neshat, M., Silva, L. S. P. da, Alexander, B. and Wagner, M. (2020). "Design optimisation of a multi-mode wave energy converter". In: *ASME 2020 39th International Conference on Ocean, Offshore & Arctic Engineering*. Vol. 9. International Conference on Offshore Mechanics and Arctic Engineering.

[104] Shi, H., Huang, S. and Cao, F. (2019). "Hydrodynamic performance and power absorption of a multi-freedom buoy wave energy device". In: *Ocean Engineering* 172, pp. 541–549.

[105] Srokosz, M. A. (1979). "The submerged sphere as an absorber of wave power". In: *Journal of Fluid Mechanics* 95.4, pp. 717–741.

[106] Tarrant, K. and Meskell, C. (2016). "Investigation on parametrically excited motions of point absorbers in regular waves". In: *Ocean Engineering* 111, pp. 67–81.

[107] Thomas, G. P. (2008). "The Theory Behind the Conversion of Ocean Wave Energy: a Review". In: *Ocean Wave Energy*. Berlin, Heidelberg: Springer.

[108] Todalshaug, J. H. (2017). "Hydrodynamics of WECs". In: *Handbook of Ocean Wave Energy*. Ed. by A. Pecher and J. P. Kofoed. Cham: Springer International Publishing, pp. 139–158.

[109] Ursell, F (1950). "Surface waves on deep water in the presence of a submerged circular cylinder. I". In: *Mathematical Proceedings of the Cambridge Philosophical Society* 46.1, 141–152.

[110] US Department of Energy (2017). *Wave Energy Prize - 1/20th Testing - Oscilla Power*. URL: `https://mhkdr.openei.org/submissions/200`.

[111] Wang, L., Isberg, J. and Tedeschi, E. (2018). "Review of control strategies for wave energy conversion systems and their validation: the wave-to-wire approach". In: *Renewable and Sustainable Energy Reviews* 81.October 2016, pp. 366–379.

[112] Windt, C., Davidson, J. and Ringwood, J. V. (2018). "High-fidelity numerical modelling of ocean wave energy systems: A review of computational fluid dynamics-based numerical wave tanks". In: *Renewable and Sustainable Energy Reviews* 93, pp. 610–630.

[113] Wolgamot, H. A. and Fitzgerald, C. J. (2015). "Nonlinear hydrodynamic and real fluid effects on wave energy converters". In: *Proceedings of the Institution of Mechanical Engineers, Part A: Journal of Power and Energy* 229.7, pp. 772–794.

[114] Wu, G. X. (1993). "Hydrodynamic forces on a submerged circular cylinder undergoing large-amplitude motion". In: *Journal of Fluid Mechanics* 254, 41–58.

[115] Yavuz, H. (July 2011). "On control of a pitching and surging wave energy converter". In: *International Journal of Green Energy* 8.5, pp. 555–584.

[116] Zhang, D., George, A., Wang, Y., Gu, X., Li, W. and Chen, Y. (2015). "Wave tank experiments on the power capture of a multi-axis wave

energy converter". In: *Journal of Marine Science and Technology* 20.3, pp. 520–529.

[117] Zou, S., Abdelkhalik, O., Robinett, R., Korde, U., Bacelli, G., Wilson, D. and Coe, R. (2017). "Model Predictive Control of parametric excited pitch-surge modes in wave energy converters". In: *International Journal of Marine Energy* 19, pp. 32–46.

Chapter 3

Background theory

The purpose of this chapter is to introduce and provide details on the main methods used throughout this Thesis to model ocean waves and fluid-structure interactions. This includes a brief discussion on methods of characterising ocean waves and the overarching concepts behind potential flow theory, which all the hydrodynamic models used in this Thesis are based upon. Considerations specific to linear wave theory are then presented, followed by an overview of a modelling approach based on the Weak-Scatterer (WS) approximation.

3.1 Ocean waves

Regular waves

Despite the large amount of variation between different types of ocean waves, the simplest waves can be represented by a monochromatic, sinusoidal function. There are a number of basic parameters that can be used to characterise such a wave [13, 36]:

- λ - wavelength,
- T - wave period,
- H - wave height,
- h - water depth,
- $s = H/\lambda$ - wave steepness,
- $k = 2\pi/\lambda$ - wave number,
- $\omega = 2\pi/T$ - wave frequency,
- $A_w = H/2$ - wave amplitude.

Of these parameters, the wave steepness and water depth can affect the nonlinearity of the wave profile. This consequently affects the suitability of various modelling approaches that can be used to represent the waves. Generally, waves in deep water ($h > \lambda/2$) and with low steepness ($s < 0.01$) can be adequately approximated using sinusoidal functions and linear wave

theory. For shallower water depths and steeper waves, the wave profile becomes more nonlinear due to sharper crests and flatter troughs, which necessitates the use of higher-order wave models. An example of increasing nonlinearity in the wave profile with decreasing water depth is shown in Figure 3.1. It is worth noting that linear wave theory is often used even for nonlinear wave profiles, since higher-order wave models can be extremely difficult to apply to anything other than regular waves [13].

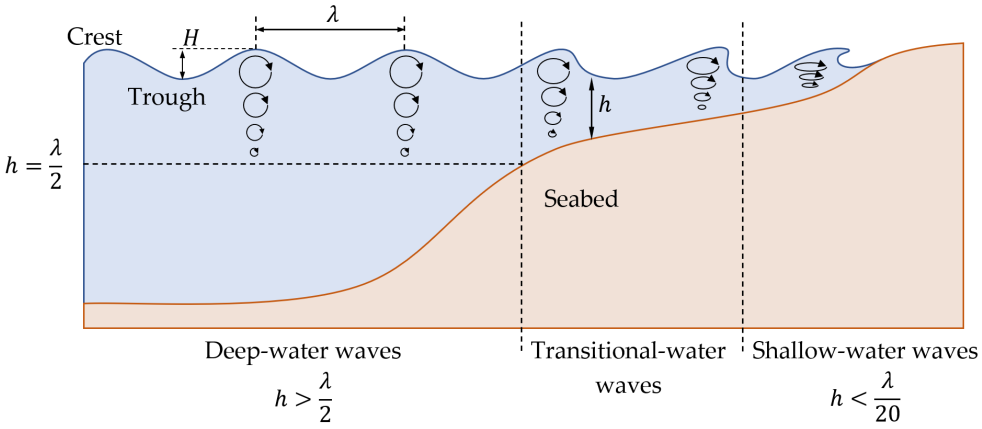

Figure 3.1: Examples of linear and nonlinear wave profiles with varying water depth, adapted from [14]. Deep-water waves with low steepness can be approximated as a sinusoidal function, while shallow-water and higher steepness waves have more nonlinear profiles.

Irregular waves

In reality, most ocean waves cannot be fully represented by a single sinusoidal function. Instead, they often have irregular shapes since waves are constantly overtaking and crossing each other on the surface of the sea [36].

For a more accurate, short-term description of a sea-state, a spectrum can be used to characterise the waves. In this case, the surface waves are represented as a linear superposition of many sinusoidal waves of different frequencies, amplitudes and phases. A wave spectrum may be defined by two main parameters: (i) the spectral peak period T_p and (ii) the significant wave height H_s, which is defined as the average height of the third highest waves in the spectrum.

One of the most commonly used spectra for ocean waves was developed by Pierson and Moskowitz [29]. Termed the Pierson-Moskowitz (PM) spectrum, this can be used to describe fully developed seas where the wind has blown across the surface of the water for a sufficiently long time, such that

the energy input is balanced and the waves no longer grow. An example of the PM spectrum is shown in Figure 3.2(a). The spectral variance density is given by [29]:

$$S_\eta(\omega) = \frac{A_{PM}}{f^5} \exp\left(-\frac{B_{PM}}{f^4}\right), \tag{3.1}$$

where f is the wave frequency in Hz, and A_{PM} and B_{PM} may be parameterised in terms of T_p and H_s [35]:

$$A_{PM} = \frac{5}{16}\frac{H_s^2}{T_p^4}, \qquad B_{PM} = \frac{5}{4T_p^4}. \tag{3.2}$$

For long-term descriptions of a sea site, it is common to use a scatter diagram to illustrate the probability of encountering an irregular wave with a particular peak frequency and wave height at a given location. An example of a scatter diagram is shown in Figure 3.2(b).

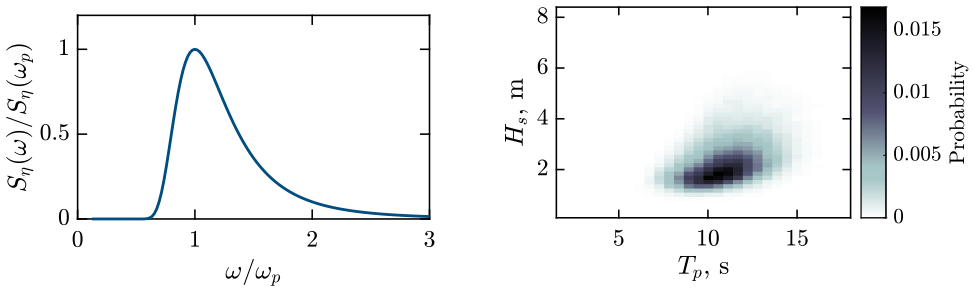

(a) (b)

Figure 3.2: Examples of characterisation of irregular waves using (a) PM spectrum for short-term sea states and (b) scatter diagram for a long-term description of the wave climate at a particular location.

In this Thesis, Chapters 4 to 6 feature regular wave analysis. Irregular wave analysis involving a PM spectrum and scatter diagram is also applied in Chapters 5 and 6 to consider the performance of a multi-mode WEC system in a more realistic sea state. Having defined the wave input, the next step in the modelling process is to consider the interactions between the wave and the body of the converter itself.

3.2 Potential flow theory

Potential flow theory is a mathematical formulation that can be used to model fluid-structure interactions based on the assumption of an ideal fluid. In other words, the flow is assumed to be inviscid, irrotational and incompressible. In

this section, the main considerations and equations which form the basis of all potential flow models will be presented.

Laplace equation

The Laplace equation forms the basis for the potential flow problem, and is derived from the conservation of mass, i.e. the continuity equation [10]:

$$\frac{\partial \rho}{\partial t} + \nabla \cdot (\rho \boldsymbol{v}) = 0, \tag{3.3}$$

where ρ is the mass density of the fluid and $\boldsymbol{v}(x, y, z, t)$ is a the velocity of the fluid particles. Since the flow is assumed to be incompressible, Eq. (3.3) becomes:

$$\nabla \cdot \boldsymbol{v} = 0. \tag{3.4}$$

Next, the assumption of irrotational flow requires that the curl of $\boldsymbol{v}$ is zero [1], hence:

$$\nabla \times \boldsymbol{v} = 0. \tag{3.5}$$

At this point, a scalar property of the fluid is then introduced, known as the velocity potential $\phi(x, y, z, t)$. Using the fact that the curl of a gradient vanishes, described by the vector identity $\nabla \times \nabla\phi = 0$, and equating this to Eq. (3.5) gives:

$$\boldsymbol{v} = \nabla\phi. \tag{3.6}$$

Substituting Eq. (3.6) into (3.4) then results in the Laplace equation:

$$\nabla^2\phi = 0, \tag{3.7}$$

which must be satisfied throughout the fluid domain.

Boundary conditions

The solution for the velocity potential must also satisfy a number of boundary conditions in the fluid domain, which are defined at:

- The free surface (i.e. the air-water interface),
- Body surface,
- On the sea floor.

The fluid domain and boundaries are illustrated in Figure 3.3. The xyz Cartesian coordinate system is used to describe the domain, with the z-axis pointing upwards and $z = 0$ located at the undisturbed free surface level. Any elevation of the free surface relative to this level is defined as $z = \eta(x, y, t)$.

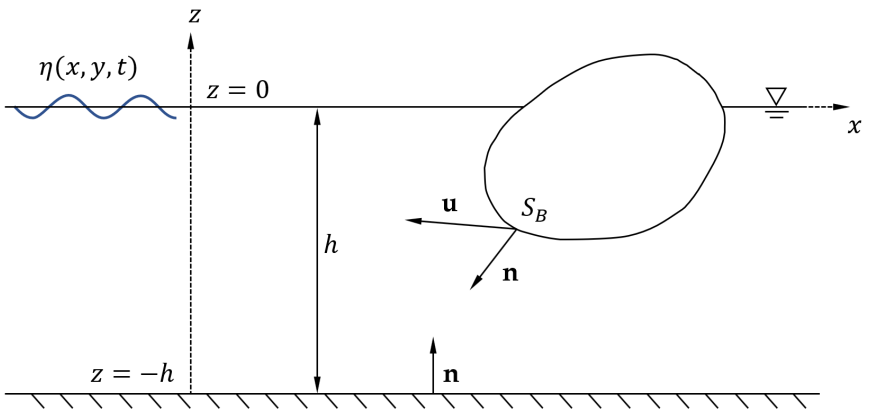

Figure 3.3: Fluid domain for potential flow theory, adapted from [10]. Unit normal vectors on wetted surfaces (i.e. interfaces between water and rigid bodies) are denoted by **n**, while **u** denotes the velocity vector of a particular point on the body wetted surface S_B.

It is assumed that the fluid domain has a constant depth h and that waves propagate in the xy-plane.

Two conditions are applied on the free surface: a (i) dynamic and (ii) kinematic boundary condition. The dynamic free surface boundary condition can be found by considering the Bernoulli equation, which reflects the principle of conservation of energy for an ideal fluid flow. When applied on the exact free surface position at $z = \eta$, where the pressure in the fluid is assumed equal to the air pressure, this becomes [10]:

$$\frac{\partial \phi}{\partial t} + \frac{v^2}{2} + g\eta = C - \frac{p_a}{\rho} \qquad \text{on} \quad z = \eta, \tag{3.8}$$

where C is an integration constant and p_a is the atmospheric pressure. Given that the right-hand side of Eq. (3.8) must vanish in still water conditions (i.e. $C = p_a/\rho$), and using the expression in Eq. (3.6), the dynamic free surface boundary condition can therefore be written as:

$$\frac{\partial \phi}{\partial t} + \frac{1}{2}\nabla\phi \cdot \nabla\phi + g\eta = 0 \qquad \text{on} \quad z = \eta. \tag{3.9}$$

The kinematic free surface boundary condition requires that a fluid particle on the air-water interface will always remain on the free surface and follow the motion of the waves. Mathematically, this is expressed by having the substantial derivative of $(z - \eta)$ vanish on the free surface [12, 26]:

$$\frac{D}{Dt}(z - \eta) = \frac{\partial \eta}{\partial t} - \frac{\partial \phi}{\partial z} + \nabla\phi \cdot \nabla\eta = 0 \qquad \text{on} \quad z = \eta, \tag{3.10}$$

where D/Dt is the substantial derivative.

Since there is no fluid flow through the solid body, any fluid particles on its wetted surface must also have the same normal component of velocity as the body itself. The boundary condition on the wetted surface of the body S_B is therefore:

$$\frac{\partial \phi}{\partial n} = \mathbf{u} \cdot \mathbf{n} \qquad \text{on} \quad S_B, \tag{3.11}$$

where $\mathbf{u}$ denotes the velocity vector of a particular point on S_B, while $\mathbf{n}$ denotes the unit normal vector on the wetted surface.

Finally, there is a no flow condition on the sea floor at $z = -h$, which gives the seabed boundary condition:

$$\frac{\partial \phi}{\partial z} = 0 \qquad \text{on} \quad z = -h. \tag{3.12}$$

The above conditions in Eqs. (3.9) to (3.12), along with the Laplace equation in Eq. (3.7), form a Boundary Value Problem (BVP) which can then be solved for the velocity potential $\phi = \phi(x, y, z, t)$. From this, a number of other important properties can subsequently be derived, such as the fluid velocity, pressure and wave elevation.

The total hydrodynamic forces acting on the body can also be determined by integrating the pressure exerted by the surrounding fluid over the wetted surface area of the body:

$$\mathbf{F}_{\text{hyd}} = -\iint_{S_B} p\mathbf{n} \mathrm{d}S_B. \tag{3.13}$$

It can be seen that the nonlinear free surface boundary conditions in Eqs. (3.9) and (3.10) contain nonlinear terms and are expressed using the exact position of the free surface $z = \eta$. However, this is also one of the unknowns, which makes the fully nonlinear potential flow problem difficult to solve. Various assumptions can therefore be applied to simplify the formulation.

3.3 Linear potential flow models

3.3.1 Linear wave theory

In linear theory, the free surface conditions may be linearised by assuming that the dynamic variables such as ϕ and η and all their derivatives are small. Consequently, the nonlinear terms in Eqs. (3.9) and (3.10) can be neglected. The boundary conditions are also imposed on the undisturbed position of the free surface $z = 0$, rather than the instantaneous position. As a result,

the linearised form of the free surface boundary conditions in Eqs. (3.9) and (3.10) become, respectively [1]:

$$\frac{\partial \phi}{\partial t} + g\eta = 0 \qquad \text{on} \quad z = 0, \tag{3.14}$$

and

$$\frac{\partial \eta}{\partial t} + \frac{\partial \phi}{\partial z} = 0 \qquad \text{on} \quad z = 0. \tag{3.15}$$

The time derivative of the linearised dynamic boundary condition in Eq. (3.14) can be combined with the kinematic condition in Eq. (3.15) to give a single free surface boundary condition:

$$\frac{\partial^2 \phi}{\partial t} + g\frac{\partial \phi}{\partial z} = 0 \qquad \text{on} \quad z = 0. \tag{3.16}$$

Once a solution for the velocity potential is obtained, the velocity of the fluid can then be determined from Eq. (3.6). The linearised hydrodynamic pressure can be found using the dynamic part of the Bernoulli equation, disregarding any nonlinear terms [10]:

$$p = -\rho\frac{\partial \phi}{\partial t}. \tag{3.17}$$

The wave elevation can also be determined using the linearised dynamic free surface boundary condition in Eq. (3.14):

$$\eta = -\frac{1}{g}\frac{\partial \phi}{\partial t}. \tag{3.18}$$

3.3.1.1 Harmonic waves

As previously discussed in Section 3.1, the assumption of small wave amplitudes in deep-water allows the use of sinusoidal functions to represent the motion of the fluid. The velocity potential can therefore be separated into spatial and temporal variables to further simplify the fluid-body interaction problem [10]:

$$\phi = \phi(x, y, z, t) = \text{Re}\left\{\hat{\phi}(x, y, z)e^{i\omega t}\right\}, \tag{3.19}$$

where ^ denotes the complex amplitude.

The linear BVP can therefore be re-written as:

$$\begin{cases} \nabla^2\hat{\phi} = 0 & \text{in the fluid domain} \\ -\omega^2\hat{\phi} + g\dfrac{\partial\hat{\phi}}{\partial z} = 0 & \text{on} \quad z = 0 \\ \dfrac{\partial\hat{\phi}}{\partial n} = \hat{u}_n & \text{on} \quad S_0 \\ \dfrac{\partial\hat{\phi}}{\partial z} = 0 & \text{on} \quad z = -h, \end{cases} \tag{3.20}$$

where $u_n = \mathbf{u} \cdot \mathbf{n}$ is the component of $\mathbf{u}$ along the normal to the body surface and S_0 is the mean wetted surface area of the body in its equilibrium position. Additionally, a fluid domain extending out to infinity must also satisfy a 'radiation condition', which will be discussed further in Section 3.3.1.2.

Other physical variables, such as the fluid velocity, pressure and wave elevation, can also be re-written in terms of complex amplitudes [10]:

$$\hat{\boldsymbol{v}} = \nabla\hat{\phi}, \tag{3.21}$$

$$\hat{p} = -i\omega\rho\hat{\phi}, \tag{3.22}$$

$$\hat{\eta} = -\frac{i\omega}{g}\hat{\phi} \qquad \text{on} \quad z = 0. \tag{3.23}$$

3.3.1.2 Hydrodynamic force decomposition

To determine the hydrodynamic forces acting on a body in linear theory, the pressure is integrated over the mean wetted body surface area. Using Eqs. (3.13) and (3.22), the complex amplitude of the linear hydrodynamic force acting on an immersed body can be expressed as:

$$\hat{F}_{\mathrm{hyd},j} = i\omega\rho \iint_{S_0} \hat{\phi} n_j \mathrm{d}S_0, \tag{3.24}$$

where the subscript j (j =1, 2, ..., 6) denotes the j-th hydrodynamic mode and n_j is the j-th component of $\mathbf{n}$.

The linearity assumption also allows the total wave field and forces acting on an immersed body to be decomposed into several components [1]:

$$\hat{\phi} = \hat{\phi}_i + \hat{\phi}_d + \hat{\phi}_r, \tag{3.25}$$

where ϕ_i, ϕ_d and ϕ_r are the incident, diffraction and radiation components, respectively. The incident and diffraction components can be considered together to describe the total excitation force acting on the body.

Excitation problem

The excitation force is defined as the incident wave load acting on a fixed body with no motion (and hence no radiated waves). Since the body is assumed to be fixed, the boundary condition on the body wetted surface in Eq. (3.20) becomes:

$$\frac{\partial \hat{\phi}_0}{\partial n} + \frac{\partial \hat{\phi}_d}{\partial n} = 0 \qquad \text{on} \quad S_0, \tag{3.26}$$

which the incident and diffracted velocity potentials must then satisfy.

As previously discussed, there is also a 'radiation condition' for diffracted waves propagating away from the body at infinite distance, given by [22]:

$$\lim_{kx \to \pm\infty} \left(\frac{\partial \hat{\phi}_d}{\partial x} \mp ik\hat{\phi}_d \right) = 0. \tag{3.27}$$

The excitation force in the j-th mode due to the incident and diffraction loads is then given by [10]:

$$\hat{F}_{\text{exc},j} = i\omega\rho \iint_{S_0} (\hat{\phi}_i + \hat{\phi}_d) n_j \mathrm{d}S_0. \tag{3.28}$$

In cases where the body is sufficiently small compared to the wavelength, it is acceptable to neglect the diffracted component of the wave field when considering the excitation force. This means that the diffracted velocity potential $\hat{\phi}_d$ does not have to be solved in the BVP, which can help reduce computational costs [1, 10].

Radiation problem

The radiated component $\hat{\phi}_r$ is the result of waves generated by a body's motion in the absence of an incident wave. The total radiated velocity potential is the superposition of potentials caused by oscillations in all six hydrodynamic modes [10]:

$$\hat{\phi}_r = \sum_{j=1}^{6} \varphi_j \hat{u}_j, \tag{3.29}$$

where u_j is the j-th component of $\mathbf{u}$ and $\varphi_j = \varphi_j(x, y, z)$ is the coefficient of proportionality, which corresponds to the radiation potential amplitude caused by a unit velocity in mode j. The coefficient of proportionality must satisfy the body condition:

$$\frac{\partial \varphi_j}{\partial n} = n_j \qquad \text{on} \quad S_0, \tag{3.30}$$

as well as the Laplace equation, along with all the other free surface and seabed boundary conditions.

The radiation force in the j'-th mode due to oscillations in mode j can then be written as [10]:

$$\hat{F}_{\text{rad},j'} = i\omega\rho \iint_{S_0} \varphi_j \hat{u}_j n_{j'} \mathrm{d}S_0, \tag{3.31}$$

or alternatively:

$$\hat{F}_{\text{rad},j'} = -Z_{j'j}\hat{u}_j, \tag{3.32}$$

where $Z_{j'j}$ represents the radiation impedance and is given by:

$$Z_{j'j} = -i\omega\rho \iint_{S_0} \varphi_j n_{j'} \mathrm{d}S_0. \tag{3.33}$$

The radiation impedance is complex, and so $Z_{j'j}$ can be written in terms of its real and imaginary parts:

$$Z_{j'j} = B_{j'j} + i\omega A_{j'j}, \tag{3.34}$$

where $B_{j'j}$ and $A_{j'j}$ are coefficients of the radiation damping $\mathbf{B}_{\text{rad}}$ and added mass $\mathbf{A}_{\text{rad}}$ matrices, respectively. The real part of the radiation impedance $B_{j'j}$ represents a resistive or dissipative effect due to energy from the body's motion being transferred into the water and propagating away. By itself, the term $A_{j'j}$ can be interpreted as an additional mass of surrounding fluid that is displaced and accelerated along with the body as it moves [26]. As a result of this fluid motion, kinetic and potential energy is stored in the water, which is then added to the mechanical system before flowing back into the water again. This reactive effect is reflected in the imaginary part of Eq. (3.34).

3.3.1.3 Solving the boundary value problem

The BVP given by the Laplace equation and various boundary conditions can be solved using either analytical or numerical approaches. Generally, analytical solutions are limited mainly to very simple geometries, such as spheres [23] or cylinders [15, 16]. For numerical approaches, this usually involves Boundary Element Methods (BEM), wherein a boundary integral equation satisfying all the conditions of the linear BVP is applied to the discretised mean wetted surface of the body. Widely known BEM solvers based on this approach include WAMIT [17], ANSYS AQWA [3] and NEMOH [5]. Separate computations are performed for the excitation problem to obtain the incident wave loads on the fixed body, as well as in each individual

hydrodynamic mode for the radiation problem. The solutions are then used to output the relevant hydrodynamic parameters, such as the excitation force, added mass and radiation damping coefficients [1].

3.3.2 Modelling approaches for WECs

In order to model an oscillating body WEC, the forces acting on the system must be considered together. Using linear wave theory, it is convenient to decompose the total hydrodynamic forces acting on a body into various components. Using Newton's second law, the governing equation describing the dynamic motion of the WEC can therefore be written in the time-domain as:

$$\mathbf{M}\ddot{\mathbf{x}}(t) = \mathbf{F}_{\text{exc}}(t) + \mathbf{F}_{\text{rad}}(t) + \mathbf{F}_{\text{buoy}}(t) + \mathbf{F}_{\text{visc}}(t) + \mathbf{F}_{\text{PTO}}(t), \tag{3.35}$$

where $\mathbf{M}$ is the mass matrix and $\ddot{\mathbf{x}}$ is the acceleration at the centre of gravity of the buoy. The main forces acting on the buoy, $\mathbf{F}_{\text{exc}}$, $\mathbf{F}_{\text{rad}}$, $\mathbf{F}_{\text{buoy}}$, $\mathbf{F}_{\text{visc}}$ and $\mathbf{F}_{\text{PTO}}$ are the excitation, radiation, buoyancy, viscous drag and PTO forces, respectively.

The corresponding equation in the frequency-domain can be written as:

$$\begin{aligned}\mathbf{M}\hat{\mathbf{a}}(\omega) = \hat{\mathbf{F}}_{\text{exc}}(\omega) + \underbrace{[-\mathbf{A}_{\text{rad}}(\omega)\hat{\mathbf{a}}(\omega) - \mathbf{B}_{\text{rad}}(\omega)\hat{\mathbf{u}}(\omega)]}_{\hat{\mathbf{F}}_{\text{rad}}(\omega)} + \underbrace{[-\mathbf{K}_s\hat{\mathbf{x}}(\omega)]}_{\hat{\mathbf{F}}_{\text{buoy}}(\omega)} \\ + \underbrace{[-\mathbf{B}_{\text{visc}}(\omega)\hat{\mathbf{u}}(\omega)]}_{\hat{\mathbf{F}}_{\text{visc}}(\omega)} + \hat{\mathbf{F}}_{\text{PTO}}(\omega),\end{aligned} \tag{3.36}$$

where $\hat{\mathbf{a}}$, $\hat{\mathbf{u}}$ and $\hat{\mathbf{x}}$ denote the complex body acceleration, velocity and displacement vectors, respectively, while $\mathbf{B}_{\text{visc}}$ and $\mathbf{K}_s$ denote the linearised viscous damping and hydrostatic stiffness matrices, respectively.

In certain cases, such as when determining the optimal control requirements, it is more convenient to write Eq. (3.36) in terms of the intrinsic impedance $\mathbf{Z}_i$ of the system [10]. Using $\hat{\mathbf{a}}(\omega) = i\omega\hat{\mathbf{u}}(\omega) = -\omega^2\hat{\mathbf{x}}(\omega)$, this gives:

$$\begin{aligned}\left\{i\omega(\mathbf{M} + \mathbf{A}_{\text{rad}}(\omega)) + (\mathbf{B}_{\text{rad}}(\omega) + \mathbf{B}_{\text{visc}}(\omega)) - \frac{i}{\omega}\mathbf{K}_s\right\}\hat{\mathbf{u}}(\omega) \\ \equiv \mathbf{Z}_i(\omega)\hat{\mathbf{u}}(\omega) = \hat{\mathbf{F}}_{\text{exc}}(\omega) + \hat{\mathbf{F}}_{\text{PTO}}(\omega).\end{aligned} \tag{3.37}$$

More detail regarding modelling of the various forces in Eqs. (3.35) and (3.36) will be provided in the subsequent discussions.

3.3.2.1 Excitation force

Having obtained the excitation force coefficients from the solution of the BVP, as discussed in Section 3.3.1.3, the complex excitation force vector can be calculated as [10]:

$$\hat{\mathbf{F}}_{\text{exc}}(\omega) = \hat{\mathbf{f}}_{\text{exc}}(\omega)\hat{\eta}(x_0, y_0, \omega), \tag{3.38}$$

where $\hat{\mathbf{f}}_{\text{exc}}$ is the complex excitation force coefficient vector, representing the excitation loads per unit wave elevation, and $\hat{\eta}$ is the wave elevation measured at the reference position (x_0, y_0), which usually taken as the projection of the centre of the body on the water surface.

In the time domain, assuming regular, monochromatic waves, the wave elevation and excitation force in the j-th mode can be expressed as [30]:

$$\eta(t) = A_w \cos(\omega t), \tag{3.39}$$

$$F_{\text{exc},j}(t) = |\hat{f}_{\text{exc},j}(\omega)| A_w \cos(\varphi_{\text{exc}}(\omega) + \omega t), \tag{3.40}$$

where $|\hat{f}_{\text{exc},j}|$ and φ_{exc} are the amplitude and phase of the frequency dependent excitation force coefficient, respectively.

For irregular waves, the complex wave elevation for each frequency component in a spectrum can be calculated as [2]:

$$\hat{\eta}(\omega_k) = \sqrt{2S_\eta(\omega_k)\Delta\omega_k}\, e^{i\varphi_\eta(\omega_k)}, \tag{3.41}$$

where the subscript $k (k = 1, 2, ..., N)$ denotes the k-th frequency component and φ_η is a phase angle, which can be taken from real life data or randomly generated assuming a uniform distribution between $[0, 2\pi)$.

Eq. (3.41) is substituted into Eq. (3.38) to find the complex excitation force amplitude for each frequency. The resultant irregular excitation force time-series containing N frequency components can then be calculated as:

$$\mathbf{F}_{\text{exc}}(t) = \sum_{k=1}^{N} \text{Re}\left\{\hat{\mathbf{F}}_{\text{exc}}(\omega_k) e^{i\omega_k t}\right\}. \tag{3.42}$$

3.3.2.2 Radiation force

As previously shown in Eq. (3.36), the radiation force in the frequency domain is often expressed in terms of the added mass $\mathbf{A}_{\text{rad}}$ and radiation damping $\mathbf{B}_{\text{rad}}$ matrices.

In the time-domain, another common method of expressing the radiation force is by means of Cummins' equation [7]:

$$\mathbf{F}_{\text{rad},j}(t) = -A_{jj',\infty}\ddot{x}_{j'} - \int_{-\infty}^{t} k_{jj'}(t-\tau)\dot{x}_{j'}(\tau)\mathrm{d}\tau, \tag{3.43}$$

where $A_{jj',\infty} = \lim_{\omega \to \infty} A_{jj'}(\omega)$ is the added mass at infinite frequency and $k_{jj'}(t)$ is the radiation impulse response, obtained from the inverse Fourier transform [30]:

$$k_{jj'}(t) = \frac{1}{2\pi} \int_{-\infty}^{\infty} \left(B_{jj'}(\omega) + i\omega(A_{jj'}(\omega) - A_{jj',\infty}) \right) e^{i\omega t} \mathrm{d}\omega. \tag{3.44}$$

The convolution integral term in Eq. (3.43) is also known as a memory function. Physically, this means that part of the radiation force acting on the body at a particular time instant is caused by changes in the fluid which remain from a previous motion of the body [2]. Directly evaluating the convolution integral can be computationally expensive, so an alternative approach is to approximate this term using a state-space representation:

$$\begin{aligned} \dot{\mathbf{p}}(t) &= \mathbf{A}_r \mathbf{p}(t) + \mathbf{B}_r \dot{x}_{j'}(t) \\ \int_0^t k_{jj'}(t-\tau)\dot{x}_{j'}(\tau)\mathrm{d}\tau &= \mathbf{C}_r \mathbf{p}(t), \end{aligned} \tag{3.45}$$

where $\mathbf{A}_r$, $\mathbf{B}_r$ and $\mathbf{C}_r$ are state space matrices and $\mathbf{p}(t)$ is an intermediate state vector. The MATLAB MSS FDI toolbox developed by Perez and Fossen [28] can be used to obtain the coefficients for the state space matrices, based on pre-calculated values of the added mass $A_{jj'}$ and radiation damping $B_{jj'}$ coefficients.

3.3.2.3 Hydrostatic restoring force

For fully submerged bodies, the hydrostatic restoring force (or buoyancy force) is constant since the volume of displaced water and gravitational forces acting on the body remain the same. This force acts purely in the heave direction and can be calculated as:

$$F_{\text{buoy},3}(t) = g(\rho V - m_b), \tag{3.46}$$

where V and m_b are the volume and mass of the body, respectively. A body less dense than the water will be positively buoyant and will require tension from the PTO mechanisms to remain submerged.

In cases where the centre of buoyancy does not coincide with the centre of gravity, the buoyancy force may also result in a spring-like hydrostatic restoring moment which acts in the rotational modes. Care should be taken to ensure that the static stability of the system is not negatively impacted in such cases [24].

3.3.2.4 Viscous force

Apart from the radiation damping, viscous effects of the fluid flow will also lead to energy being dissipated from the system. Although these effects are neglected in the potential flow formulation due to the assumption of inviscid flow, they can be included in the WEC model as an additional viscous force or moment term. In the time domain, the Morison [4, 25] equation can be applied to obtain:

$$F_{\text{visc},j}(t) = -\frac{1}{2}\rho C_{d,j} A_{\perp,j} |\dot{x}_j(t) - v_j(t)| \left(\dot{x}_j(t) - v_j(t)\right), \tag{3.47}$$

$$M_{\text{visc},j}(t) = -\frac{1}{2} B_{Q,j} |\dot{\theta}_j| \dot{\theta}_j, \tag{3.48}$$

where $A_{\perp,j}$ is the cross sectional area of the body perpendicular to the flow and $\dot{\theta}$ is the angular velocity. The drag and quadratic roll damping coefficients, denoted $C_{d,j}$ and $B_{Q,j}$ respectively, are dependent on the properties of both the body and the fluid. For simple shapes such as spheres, cylinders and flat plates, these coefficients can be obtained from published test results in the literature.

The relative velocity $(\dot{x}_j(t) - v_j(t))$ between the body and fluid flow is also required for the viscous force calculations. Assuming only planar motions in the xz-plane, the undisturbed fluid velocity components in the horizontal and vertical directions can determined as [26]:

$$u(t) = \frac{\partial \phi}{\partial x} = \frac{g A_w k}{\omega} \frac{\cosh k(z + d_s)}{\cosh k d_s} \cos(kx - \omega t), \tag{3.49}$$

$$v(t) = \frac{\partial \phi}{\partial z} = \frac{g A_w k}{\omega} \frac{\sinh k(z + d_s)}{\cosh k d_s} \sin(kx - \omega t), \tag{3.50}$$

where d_s is the submergence depth of the body.

In order to include viscous loads in the frequency domain, the quadratic terms in Eq. (3.47) and (3.48) must be linearised. The Lorentz linearisation approach [34] can be applied to obtain an approximate expression for the viscous drag forces and moments, which was shown previously in Eq. (3.36). The matrix containing the linearised viscous damping coefficients $\mathbf{B}_{\text{visc}}$ must be calculated for each wave height and frequency condition.

3.4 Weak-scatterer model

In this Thesis, a weakly nonlinear potential flow model based on the WS approximation was employed to study the effect of nonlinear hydrodynamic forces acting on a multi-mode WEC. This approach was implemented using

the *WS_CN* solver developed by the *LHEEA* laboratory of École Centrale de Nantes [18, 37]. The fundamental theory and numerical implementation used in the WS model is presented in this section.

3.4.1 Weak-scatterer approximation

First introduced by Pawlowski [27], the WS approximation is an alternative approach to simplifying the fully nonlinear potential flow formulation. Here, the velocity potential and free surface wave elevation are decomposed into an incident ϕ_i and perturbed ϕ_p component:

$$\begin{cases} \phi = \phi_i + \phi_p \\ \eta = \eta_i + \eta_p. \end{cases} \tag{3.51}$$

It is assumed that the effect of the perturbed component, which consists of radiation and diffraction effects, is small compared to the incident component:

$$\begin{cases} \phi_p = \mathcal{O}(\phi_i) \\ \eta_p = \mathcal{O}(\eta_i) \end{cases} \tag{3.52}$$

This approximation allows the free surface boundary conditions to be linearised about the instantaneous incident wave elevation $z = \eta_i(x, y, t)$, which is explicitly known and used as a model input. Therefore, only the perturbed components need to be solved in the BVP. The hydrodynamic forces are also evaluated using the instantaneous position of the body.

Compared to linear wave theory, the WS approach provides an improved modelling accuracy in cases with steep incident waves and large body motions. Regarding numerical simulations, the approximation in Eq. (3.52) means that incident waves do not have to be propagated throughout the entire fluid domain and perturbed waves do not have to be meshed, resulting in shorter computation times compared to CFD solvers [19].

It is necessary to note that for a WEC operating with reactive control, the assumption in Eq. (3.52) may not always be satisfied due to large radiated waves caused by significant body motions. Despite this, the WS method is still likely to be more accurate than linear wave theory in these cases. This was demonstrated for heaving PA WEC operating in steep waves with large body motions, where the WS solver remained capable of producing results comparable to CFD with only small errors of within 8%, compared to discrepancies of up to 37% from the linear solver [9].

3.4.1.1 Boundary value problem

Within the framework of the WS approximation, the free surface boundary conditions need to be transposed onto the position of the incident free surface. The WS decomposition in Eq. (3.51) is therefore introduced to the dynamic free surface boundary condition in Eq. (3.9) [18]:

$$\begin{aligned}\frac{\partial}{\partial t}(\phi_i+\phi_p)+\frac{1}{2}\nabla(\phi_i+\phi_p)\cdot\nabla(\phi_i+\phi_p)\\ +g(\eta_i+\eta_p)=0, \qquad \text{on} \quad z=\eta.\end{aligned} \tag{3.53}$$

A Taylor expansion on the perturbation component is then applied at the incident free surface position. The higher order terms of the perturbation components can be neglected using the WS assumption in Eq. (3.52). This gives the WS dynamic free surface boundary condition [18, 37]:

$$\begin{aligned}\frac{\partial\phi_p}{\partial t}=&-\frac{\partial\phi_i}{\partial t}-\frac{1}{2}\nabla\phi_i\cdot\nabla\phi_i-\nabla\phi_i\cdot\nabla\phi_p-g(\eta_i+\eta_p)\\ &-\eta_p\left(\frac{\partial^2\phi_i}{\partial z\partial t}+\frac{\partial\nabla\phi_i}{\partial z}\cdot\nabla\phi_i\right), \qquad \text{on} \quad z=\eta_i.\end{aligned} \tag{3.54}$$

A similar decomposition and expansion process is applied to Eq. (3.10) to obtain the WS kinematic free surface boundary condition:

$$\begin{aligned}\frac{\partial\eta_p}{\partial t}=&-\frac{\partial\eta_i}{\partial t}+\frac{\partial}{\partial z}(\phi_i+\phi_p)-\nabla\phi_i\cdot\nabla\eta_i-\nabla\phi_i\cdot\nabla\eta_p-\nabla\phi_p\cdot\nabla\eta_i\\ &+\eta_p\left(\frac{\partial^2\phi_i}{\partial z^2}-\frac{\partial\nabla\phi_i}{\partial z}\cdot\nabla\eta_i\right), \qquad \text{on} \quad z=\eta_i.\end{aligned} \tag{3.55}$$

The WS decomposition in Eq. (3.51) is also applied to the other equations in the BVP, giving [19, 37]:

$$\nabla^2\phi_p=-\nabla^2\phi_i=0, \qquad \text{in the fluid domain,} \tag{3.56}$$

on the surface body:

$$\frac{\partial\phi_p}{\partial n}=-\frac{\partial\phi_i}{\partial n}+\mathbf{u}\cdot\mathbf{n} \qquad \text{on} \quad S_B, \tag{3.57}$$

and finally, on the sea floor:

$$\frac{\partial\phi_p}{\partial z}=-\frac{\partial\phi_i}{\partial z} \qquad \text{on} \quad z=-h. \tag{3.58}$$

3.4.1.2 Fluid-structure interaction

Since the force decomposition used in linear wave theory cannot be applied, the governing body motion equation used in the WS model takes a slightly different form:

$$\mathbf{M}\ddot{\mathbf{x}}(t) = \mathbf{F}_{\text{hyd}}(t) + \mathbf{M}\mathbf{g} + \mathbf{F}_{\text{ext}}(t), \tag{3.59}$$

where $\mathbf{F}_{\text{hyd}}$ is the total hydrodynamic force (including hydrostatic), $\mathbf{g} = [0, 0, -g]$ is the vector acceleration due to gravity and $\mathbf{F}_{\text{ext}}$ denotes external forces, which in the WS model includes viscous drag, PTO and mooring effects.

The WS model uses the instantaneous wetted surface of the body and includes the nonlinear terms in the Bernoulli equation when determining the hydrodynamic forces. Therefore, from Eq. (3.13), the nonlinear hydrodynamic force acting on the body is:

$$\mathbf{F}_{\text{hyd}} = \rho \iint_S \left(\frac{\partial \phi}{\partial t} + \frac{1}{2}\nabla\phi \cdot \nabla\phi + \mathbf{g}z \right) \mathbf{n} \mathrm{d}S_B. \tag{3.60}$$

Most of the terms in Eq. (3.60) can be evaluated from the velocity potential and boundary conditions. The only exception is the time derivative of the velocity potential $\partial\phi/\partial t$, which can be determined using either of two methods depending on whether the body is:

(i) 'forced' to undergo a prescribed motion, or
(ii) left 'free' to respond to the incident wave excitation.

If the body is undergoing 'forced' prescribed motion, Eqs. (3.59) and (3.60) do not need to be solved to continue the simulation. Instead, $\partial\phi/\partial t$ and the subsequent hydrodynamic loads at each time step can be calculated at the end of the simulation using a finite difference scheme [19].

For a body undergoing 'free' motion, the problem is more complex. The body motion in Eq. (3.59) is dependent on the hydrodynamic force, which in turn requires knowledge of the motion of the body. In this case, an implicit boundary method [8, 33] is applied in the *WS_CN* solver. This introduces a second BVP involving the time derivative of the velocity potential [19, 37]:

$$\begin{cases} \nabla^2 \dfrac{\partial \phi_p}{\partial t} = 0 & \text{in the fluid domain} \\ \dfrac{\partial \phi_p}{\partial t} = -\dfrac{\partial \phi_i}{\partial t} - \dfrac{1}{2}\nabla\phi_i \cdot \nabla\phi_i - \nabla\phi_i \cdot \nabla\phi_p \\ \qquad\qquad - g(\eta_i + \eta_p) - \eta_p \left(\dfrac{\partial^2 \phi_i}{\partial z \partial t} + \dfrac{\partial \nabla \phi_i}{\partial z} \cdot \nabla\phi_i \right) & \text{on} \quad z = \eta_i \\ \dfrac{\partial^2 \phi_p}{\partial n \partial t} = -\dfrac{\partial^2 \phi_i}{\partial n \partial t} + \ddot{\mathbf{x}} \cdot \mathbf{n} + q & \text{on} \quad S_B \\ \dfrac{\partial^2 \phi_p}{\partial z \partial t} = -\dfrac{\partial^2 \phi_i}{\partial z \partial t} & \text{on} \quad z = -h, \end{cases} \tag{3.61}$$

where q is an advection term (more details can be found in [20]).

The coupled nature of the fluid-structure problem is apparent through the appearance of $\ddot{\mathbf{x}}$ in the body condition in Eq. (3.61). The second BVP is then extended to include Eqs. (3.59) and (3.60) to solve for the body motion and hydrodynamic forces simultaneously.

3.4.2 Numerical implementation

3.4.2.1 Incident wave modelling

In the WS decomposition in Eq. (3.51), the incident components are assumed to be known and can therefore be used as a model inputs. Two methods are used in the *WS_CN* solver to model the incoming wave field:

1. The Airy wave theory:

$$\eta_i(x, y, t) = A_w \cos(kx - \omega t + \varphi), \tag{3.62}$$

2. The stream function theory of Rienecker and Fenton [31]:

$$\eta_i(x, y, t) = \sum_{n=1}^{N_{RF}} B_n \cos(n(k_{RF}x - \omega_{RF}t) + \varphi_{RF}), \tag{3.63}$$

   where N_{RF} is the order and B_n is the n-th coefficient of the Fourier series, while k_{RF}, ω_{RF} and φ_{RF} are the wave number, frequency and phase of the Rienecker and Fenton's regular wave.

Both theories use the dispersion relation, which is given as:

$$\omega^2 = gk\tanh(kh), \tag{3.64}$$

where g is the gravitational acceleration.

At the start of the simulation, a ramp function is also applied to the incident components of the body conditions given in Eqs. (3.57) and (3.61). This prevents any non-physical waves from being generated by the abrupt appearance of the body in the flow. The ramp function is given by the expression:

$$f(t) = \begin{cases} 0 & \text{when } t \leq T_1 \\ 1 & \text{when } t \geq T_2 \\ \frac{1}{2}\left[1 - \cos\left(\pi \frac{t - T_1}{T_2 - T_1}\right)\right] & \text{otherwise} \end{cases}, \tag{3.65}$$

where T_1 and T_2 are the start and final time for the application of the ramp function, respectively.

3.4.2.2 Discretisation

A collocation BEM is applied in the WS model to solve the BVPs given in Section 3.4.1. The numerical domain is discretised and a boundary integral equation is applied to a set of nodes on the surfaces of the domain. Green's second identity is used to transform the perturbed velocity potential condition in Eq. (3.56) into the following boundary integral equation [6, 38]:

$$\Omega(\mathbf{x}_l)\phi_p(\mathbf{x}_l) - \iint_{S_j} \left[\frac{\partial \phi_p}{\partial n}(\mathbf{x})G(\mathbf{x}, \mathbf{x}_l) - \phi_p(\mathbf{x})\frac{\partial G}{\partial n}(\mathbf{x}, \mathbf{x}_l)\right] \mathrm{d}S_j = 0, \tag{3.66}$$

where the subscript l denotes a point on the mesh element j, G is the Rankine source and Ω is the solid angle at the point with coordinates $\mathbf{x}_l$.

Triangular elements are used to discretise the fluid domain surfaces in the *WS_CN* solver. Linear approximations are assumed over each element for the velocity potential and its normal derivative. This method was chosen over other constant panel and higher order discretisation approaches, such as those used in NEMOH, to achieve shorter computation times. The approximation results in a linear system of equations that can be represented as [21]:

$$\mathbf{G}_{lj}\frac{\partial \boldsymbol{\phi}_p}{\partial n} - \mathbf{H}_{lj}\boldsymbol{\phi}_p, \tag{3.67}$$

where $\mathbf{G}_{lj}$ and $\mathbf{H}_{lj}$ are influence matrices. The matrix $\mathbf{G}$ contains all integrals of the Green's function while $\mathbf{H}$ contains all integrals of the normal derivative of the Green's function, as well as all solid angle terms Ω. An iterative Generalised minimal residual method [32] is used to solve the system of equations in Eq. (3.67).

A number of techniques are employed in the *WS_CN* solver to reduce the computational load required to calculate the influence matrices [19]:

- Partial calculation - influence matrices are only updated on boundaries which have changed in the previous time step,
- Symmetries - halves the number of required mesh elements. For example, for purely planar motions in surge, heave and pitch, symmetry can be applied along the xz-plane,
- Numerical beach - dissipates perturbed waves before they reach the domain walls, allowing for open domain simulations (i.e. involving only the body and free surface) and avoiding reflection effects.

3.4.2.3 Mesh generation

Since the geometry of the fluid domain changes with the incident free surface elevation and body motions, the mesh needs to be updated accordingly at each time step. To avoid remeshing the domain at each time step, which is computationally slow and expensive, mesh deformation algorithms are implemented instead. However, over long simulations, this can cause the mesh to become highly distorted. The free surface and body wetted surfaces must therefore be completely remeshed in these cases to avoid numerical errors.

The *WS_CN* solver is able to use an advance front method to automatically generate an unstructured mesh for the fluid domain [6]. A grid is first generated on the edges of a surface to form an initial front, which is then advanced out into the field, forming new triangular elements until the entire surface is covered [37]. The shape and size of the mesh elements can be controlled in the *WS_CN* solver by quality metric functions, allowing for the mesh to be refined closer to the free surface and body. An example of a mesh generated using this method in the WS model is shown in Figure 3.4.

3.4.2.4 Time marching scheme

A modified fourth-order Runge-Kutta (RK4) scheme, known as geometry-locked-RK4 [11], is used for time marching in the *WS_CN* solver. The normal RK4 method requires the BVP to be solved for four different mesh configurations at each time step, which in turn implies four calculations of the influence matrices. To reduce computation times, the free surface and body geometries are kept fixed during each of the four RK4 substeps. Therefore, the influence matrices only need to be calculated once for each time step.

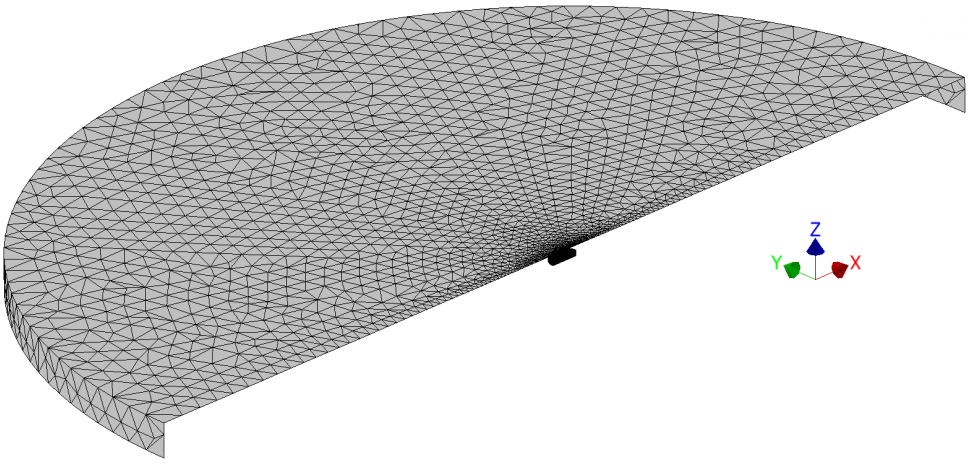

Figure 3.4: Example of a mesh used to discretise the numerical domain in the WS model.

3.5 Concluding remarks

In this chapter, a number of common modelling approaches in the wave energy sector were presented, with a particular focus on potential flow theory for modelling of fluid-structure interactions. It was shown that fully linearised potential flow theory can be used to develop simplified hydrodynamic models which may be applied in both the frequency- and time-domain. Linear wave theory assumes small wave elevations, calculates the forces about the nominal position of the device and allows the hydrodynamic forces acting on a wave converter device to be conveniently decomposed into its various components. In comparison, the weakly-nonlinear potential flow model based on the WS approximation linearises the free-surface boundary conditions about the incident wave elevation only, and calculates the hydrodynamic forces about the instantaneous position of the device. Hydrodynamic models based on the WS approximation can therefore provide higher accuracy in cases with steep incident waves and large body motions, which may not be sufficiently modelled using linear wave theory alone.

References

[1] Alves, M. (Jan. 2016). “Frequency-Domain Models”. In: *Numerical Modelling of Wave Energy Converters*. Academic Press, pp. 11–30.

[2] Alves, M. (2017). "Wave-to-Wire Modelling of WECs". In: *Handbook of Ocean Wave Energy*. Ed. by A. Pecher and J. P. Kofoed. Cham: Springer International Publishing, pp. 261–287.

[3] ANSYS Inc. (2012). *AQWA User Manual*. ANSYS, Inc.

[4] Babarit, A, Hals, J, Muliawan, M. J., Kurniawan, A, Moan, T and Krokstad, J (2011). *Numerical estimation of energy delivery from a selection of wave energy converters*. Tech. rep., pp. 1–37.

[5] Babarit, A. and Delhommeau, G. (2015). "Theoretical and numerical aspects of the open source BEM solver NEMOH". In: *Proceedings of the 11th European Wave and Tidal Energy Conference EWTEC* September 2015, pp. 1–12.

[6] Chauvigné, C., Letournel, L., Babarit, A., Ducrozet, G., Bozonnet, P., Gilloteaux, J.-C. and Ferrant, P. (May 2015). "Progresses in the development of a weakly-nonlinear wave body interaction model based on the weak-scatterer approximation". In: *ASME 2015 34th International Conference on Ocean, Offshore and Arctic Engineering*.

[7] Cummins, W. E. (1962). *The impulse response function and ship motions*. Tech. rep. Washington DC, USA.

[8] Daalen, E. F. G. van (1993). "Numerical and theoretical studies of water waves and floating bodies". PhD thesis. University of Twente.

[9] Ding, B., Wuillaume, P, Meng, F., Babarit, A., Schubert, B., Sergiienko, N. Y. and Cazzolato, B. S. (2019). "Comparison of wave-body interaction modelling methods for the study of reactively controlled point absorber wave energy converter". In: *Proceedings of the 34th International Workshop on Water Waves and Floating Bodies*. Newcastle.

[10] Falnes, J. (2002). *Ocean waves and oscillating systems: Linear interactions including wave-energy extraction*. Cambridge University Press, p. 220.

[11] Ferrant, P. (1993). "Three-dimensional unsteady wave-body interactions by a Rankine boundary element method". In: *Ship Technology Research* 40.4, pp. 165–175.

[12] Fitzgerald, C. J. (2016). "Chapter 5 - Nonlinear Potential Flow Models". In: *Numerical Modelling of Wave Energy Converters*. Ed. by M. Folley. Academic Press, pp. 83–104.

[13] Folley, M., Whittaker, T. and Hoff, J. van't (2007). "The design of small seabed-mounted bottom-hinged wave energy converters". In: *Proceedings of the 7th European Wave and Tidal Energy Conference EWTEC*. Porto, Portugal.

[14] Garrison, T. (2002). *Oceanography : an invitation to marine science*. 4th ed. Pacific Grove, USA: Thomson Learning.

[15] Jiang, S.-C., Gou, Y. and Teng, B. (May 2014a). "Water wave radiation problem by a submerged cylinder". In: *Journal of Engineering Mechanics* 140.5, p. 6014003.

[16] Jiang, S.-C., Gou, Y., Teng, B. and Ning, D.-Z. (Jan. 2014b). "Analytical solution of a wave diffraction problem on a submerged cylinder". In: *Journal of Engineering Mechanics* 140.1, pp. 225–232.

[17] Lee, C.-H. and Newman, J. N. (2013). *WAMIT User Manual, Version 7.0*. Chestnut Hill, MA: WAMIT, Inc.

[18] Letournel, L. (Mar. 2015). "Développement d'un outil de simulation numérique basé sur l'approche "Weak-Scatterer" pour l'étude des systèmes houlomoteurs en grands mouvements". PhD thesis. École Centrale de Nantes (ECN).

[19] Letournel, L., Chauvigné, C., Gelly, B., Babarit, A., Ducrozet, G. and Ferrant, P. (2018). "Weakly nonlinear modeling of submerged wave energy converters". In: *Applied Ocean Research* 75, pp. 201–222.

[20] Letournel, L., Ducrozet, G., Babarit, A. and Ferrant, P. (2017). "Proof of the equivalence of Tanizawa–Berkvens' and Cointe–van Daalen's formulations for the time derivative of the velocity potential for non-linear potential flow solvers". In: *Applied Ocean Research* 63, pp. 184–199.

[21] Letournel, L., Ferrant, P., Babarit, A., Ducrozet, G., Harris, J. C., Benoit, M. and Dombre, E. (June 2014). "Comparison of fully nonlinear and weakly nonlinear potential flow solvers for the study of wave energy converters undergoing large amplitude motions". In: *ASME 2014 33rd International Conference on Ocean, Offshore and Arctic Engineering*. San Francisco, California.

[22] Linton, C. and McIver, P. (2001). *Handbook of Mathematical Techniques for Wave/Structure Interactions*. CRC Press.

[23] Linton, C. M. (1991). "Radiation and diffraction of water waves by a submerged sphere in finite depth". In: *Ocean Engineering* 18.1-2, pp. 61–74.

[24] Meng, F., Ding, B., Cazzolato, B. and Arjomandi, M. (Jan. 2019). "Modal analysis of a submerged spherical point absorber with asymmetric mass distribution". In: *Renewable Energy* 130, pp. 223–237.

[25] Morison, J., Johnson, J. and Schaaf, S. (1950). "The force exerted by surface waves on piles". In: *Journal of Petroleum Technology* 2.05, pp. 149–154.

[26] Newman, J. N. (1977). *Marine Hydrodynamics*. MIT Press Cambridge, Mass.

[27] Pawlowski, J. S. and Bass, D. W. (1991). *A theoretical and numerical model of ship motions in heavy seas*. Tech. rep.

[28] Perez, T. and Fossen, T. I. (2009). "A Matlab toolbox for parametric identification of radiation-force models of ships and offshore structures". In: *Modeling, Identification and Control* 30.1, pp. 1–15.

[29] Pierson, W. J. and Moskowitz, L. (1964). "A proposed spectral form for fully developed wind seas based on the similarity theory of S. A. Kitaigorodskii". In: *Journal of Geophysical Research* 69.24, pp. 5181–5190.

[30] Ricci, P. (Dec. 2016). "Time-Domain Models". In: *Numerical Modelling of Wave Energy Converters*. Ed. by M. Folley. Academic Press. Chap. 3, pp. 31–66.

[31] Rienecker, M. M. and Fenton, J. D. (1981). "A Fourier approximation method for steady water waves". In: *Journal of Fluid Mechanics* 104, 119–137.

[32] Saad, Y. and Schultz, M. H. (July 1986). "GMRES: a generalized minimal residual algorithm for solving nonsymmetric linear systems". In: *SIAM Journal on Scientific and Statistical Computing* 7.3, pp. 856–869.

[33] Tanizawa, K. (1995). "A nonlinear simulation method of 3-D body motions in waves (1st report)". In: *Journal of the Society of Naval Architects of Japan* 1995.178, pp. 179–191.

[34] Terra, G. M., Berg, W. J. van de and Maas, L. R. M. (2005). "Experimental verification of Lorentz' linearization procedure for quadratic friction". In: *Fluid Dynamics Research* 36.3, pp. 175–188.

[35] The Specialist Committee on Waves (2002). "Final report and recommendations to the 23 rd ITTC". In: *Proceedings of the 23rd International Towing Tank Conference*. Vol. 2, pp. 505–736.

[36] World Meteorological Organization (1998). *Guide to wave analysis and forecasting*. 2nd ed. WMO (Series) ; no. 702. Geneva, Switzerland: WMO.

[37] Wuillaume, P.-Y. (Jan. 2019). "Numerical simulation of installation operations for offshore wind farms". PhD thesis. École Centrale de Nantes.

[38] Wuillaume, P.-Y., Babarit, A., Rongère, F., Lynch, M., Combourieu, A. and Ferrant, P. (June 2018). "Comparison between experiments and a multibody weakly nonlinear potential flow approach for modelling of marine pperations". In: *ASME 2018 37th International Conference on Offshore Mechanics and Arctic Engineering*. Madrid, Spain.

Chapter 4

The impact of nonlinear pitch-surge hydrodynamic coupling on multi-mode WEC performance

The focus of this Thesis is on oscillating-body type WECs which utilise multiple modes simultaneously for improved power absorption. From the literature review presented in Chapter 2, it was identified that most existing multi-mode prototypes are designed to absorb power primarily from heave and surge, while the effect of the pitch mode is often neglected, even for larger non-spherical converters where there is strong hydrodynamic coupling with surge. It was also unclear from the existing literature how nonlinear hydrodynamic forces may further affect the behaviour and performance of WECs which oscillate in multiple directions at the same time.

This chapter aims to address these gaps by investigating the effect of nonlinear hydrodynamic forces and coupling on a multi-mode WEC forced to oscillate simultaneously in surge and pitch. Taking inspiration from the CETO-6 design, a submerged flat cylindrical geometry is used in the analysis to highlight the effect of pitch on the device response, which may not be apparent in more spherical geometries. From this, the following research question is explored: *What is the effect of nonlinear hydrodynamic coupling forces, caused by the change in projected surface area with large pitch motions, on the performance of multi-mode WECs?*

The analysis in this chapter assumes full kinematic control of the WEC (as shown in Figure 1.2(a)) according to an explicitly prescribed motion while ignoring coupling with other hydrodynamic modes, such as heave, as well

as the influence of PTO and viscous drag forces. This was done in order to simplify the problem in the case of a plane incident wave and to isolate the effects of hydrodynamic pitch-surge coupling on performance. Numerical models based on the linear potential flow theory and WS approximation, as previously introduced in Chapter 3, are developed and compared in order to emphasise the importance of the nonlinear forces on the performance of the device. By developing a fundamental understanding of the effects of the nonlinear hydrodynamic forces acting on a multi-mode WEC during its operation, the knowledge developed in this study forms the basis for the analysis performed in the subsequent Chapters 5 and 6 of this Thesis.

This chapter consists of the published journal article:
Tran, N., Sergiienko, N. Y., Cazzolato, B. S., Ding, B., Ghayesh, M. H. and Arjomandi, M. (2020). "The impact of pitch-surge coupling on the performance of a submerged cylindrical wave energy converter". In: ***Applied Ocean Research*** **104, p. 102377**

The article in its published format is available at `https://doi.org/10.1016/j.apor.2020.102377`.

Statement of Authorship

Title of Paper	The impact of pitch-surge coupling on the performance of a submerged cylindrical wave energy converter
Publication Status	☑ Published ☐ Accepted for Publication ☐ Submitted for Publication ☐ Unpublished and Unsubmitted w ork w ritten in manuscript style
Publication Details	Tran, N., Sergiienko, N. Y., Cazzolato, B. S., Ding, B., Ghayesh, M. H. and Arjomandi, M. (2020). "The impact of pitch-surge coupling on the performance of a submerged cylindrical wave energy converter". In: *Applied Ocean Research* 104, p. 102377

Principal Author

Name of Principal Author (Candidate)	Ngan Tran
Contribution to the Paper	Developed ideas and concepts, conducted literature review Performed modelling • Developed weak-scatterer (WS) model of the multi-mode WEC using WS_CN code • Modified WS_CN code to allow for 'forced' motion in multiple hydrodynamic modes • Conducted convergence tests to verify WS model in linear conditions with small wave amplitudes and body motions • Developed protocols for running WS model on the HPC • Developed fully linearised model of the system based on hydrodynamic parameters obtained using potential flow solver NEMOH • Performed optimisations of the surge and pitch motions for maximum power absorbed using both the linear and WS models • Performed simulations where the phase of the surge and pitch velocities were systematically varied to study effect on power • Performed radiation-only simulations in the WS model to obtain the nonlinear hydrodynamic forces Interpreted results • Collected and stored data from simulations • Post processed data using Matlab • Applied processes to extract the nonlinear radiation coefficients • Analysed and compared results between the linear and WS models • Generation of plots to visualise results Writing • Wrote first full draft of manuscript • Applied comments and feedback provided by co-authors • Acted as corresponding author • Revised manuscript following review
Overall percentage (%)	85%
Certification:	This paper reports on original research I conducted during the period of my Higher Degree by Research candidature and is not subject to any obligations or contractual agreements with a third party that would constrain its inclusion in this thesis. I am the primary author of this paper.
Signature	Date: 01/12/21

Co-Author Contributions

By signing the Statement of Authorship, each author certifies that:

i. the candidate's stated contribution to the publication is accurate (as detailed above);

ii. permission is granted for the candidate in include the publication in the thesis; and

iii. the sum of all co-author contributions is equal to 100% less the candidate's stated contribution.

Name of Co-Author	Nataliia Y. Sergiienko		
Contribution to the Paper	Supervised the work, participated in developing ideas and concepts, shaped research and direction of manuscript, provided parts of code for modelling, helped analyse and interpret results, provided revision of manuscript		
Signature		Date	07/12/21

Name of Co-Author	Benjamin S. Cazzolato		
Contribution to the Paper	Supervised the work, participated in developing ideas and concepts, encouraged to pe, helped analyse and interpret results, provided revision of manuscript		
Signature		Date	01/12/21

Name of Co-Author	Boyin Ding		
Contribution to the Paper	Provided expertise and advice on numerical model used in the work, provided data for verification of models, discussed results, contributed table comparing different modelling approaches in the manuscript, provided revision of manuscript		
Signature		Date	08/12/2021

Name of Co-Author	Mergen H. Ghayesh		
Contribution to the Paper	Supervised work, provided revision of manuscript		
Signature		Date	22/12/2021

Name of Co-Author	Maziar Arjomandi		
Contribution to the Paper	Supervised work, helped in developing ideas, provided revision of manuscript		
Signature		Date	7/12/2021

The impact of pitch-surge coupling on the performance of a submerged cylindrical wave energy converter

N. Tran, N. Y. Sergiienko, B. S. Cazzolato, B. Ding, M.H. Ghayesh, M. Arjomandi

Abstract

Multi-mode wave energy converters are able to generate power from multiple degrees-of-freedom, typically delivering increased power absorption from ocean waves compared to devices operating in heave or surge only. However, the control of such systems is complex due to strong coupling between different degrees-of-freedom. This study aims to understand the effect of both linear and nonlinear pitch-surge hydrodynamic coupling on the performance of a submerged cylindrical wave energy converter. Results showed that when nonlinear coupling effects were considered, pitch had a much larger effect on device performance than what was predicted from a linear model. The maximum power that could be absorbed by the device at lower frequencies was significantly reduced as pitch amplitude increased. In terms of control, from linear theory, for any given pitch amplitude and phase, only the surge amplitude and phase was required to tune the device for maximum power absorption from the wave. However, when a nonlinear model was used, results showed that proper tuning of the pitch phase was also required to achieve maximum power absorption. As the pitch amplitude increased, nonlinear hydrodynamic effects caused by the combined pitch-surge motions became more significant, which in turn affected power estimates. Care should therefore be taken, since linear hydrodynamic models could potentially provide misleading predictions regarding the performance and control of multi-mode wave energy converters.

4.1 Introduction

Recently, there has been an increased focus on developing technologies for harvesting energy from renewable sources, one of which is wave energy. Compared to other renewable energy sources, such as solar or wind, wave has one of the highest energy densities and good variability properties [22]. As a result, many Wave Energy Converter (WEC) prototypes have been

proposed to date. Despite this, there is still no convergence on the best design for a WEC and many still remain in the pre-commercial stage of development.

Point Absorbers (PAs) feature most commonly in WEC prototypes and account for more than half of the existing designs [18]. However, many of these PAs are intended to operate in heave only, which theoretically limits the power that can be absorbed to one third of what is possible from an incident wave [17][1]. Therefore, to improve the efficiency of these devices, several multi-mode PA designs have been proposed that are capable of harvesting power from more than one Degree-of-Freedom (DOF).

One of the challenges with multi-mode WEC design is the coupling between DOFs, which can pose a challenge in terms of control. For a single DOF WEC, it is well known that power absorption is maximised when the device operates at resonance and the conditions of optimum phase and amplitude are satisfied. However, the strong hydrodynamic coupling between the surge and pitch DOFs means these conditions may not result in maximum power absorption for multi-mode WECs [9]. For example, in a study of a multi-mode, three-tethered submerged WEC by Sergiienko et al. [23], a Multiple-Input Multiple-Output (MIMO) controller was applied to optimise the heave and surge motions, while hydrodynamic coupling effects between surge and pitch were neglected. As a result, it was found that up to 15% of the total power was lost through the pitch DOF. Although these considerations suggest that the best design choice would be to constrain either surge or pitch, this can be very difficult to achieve in practice. It is therefore necessary to consider optimum control of both surge and pitch simultaneously, such that the power losses caused by pitch-surge coupling can be minimised or alternatively, in an ideal situation, utilised to further enhance the power absorption efficacy of the system.

The vast majority of designs feature devices operating in only one DOF and, consequently, comparatively little work has been done on the control of multi-mode WECs [6]. The existing literature related specifically to the simultaneous control of pitch and surge is even more limited. In an early study by Yavus [29], the performance of a floating WEC with and without coupling between pitch and surge was compared. Here, the author claimed that coupling between the pitch and surge modes could be used to improve the performance of the WEC, especially if active control was applied. In a later study by Abdelkhalik et al. [1], simultaneous control of surge, pitch and heave for a floating three-DOF WEC was considered. The behaviour of the WEC in surge and pitch was considered separately from heave. When

[1] Assuming that the WEC has available only the six rigid body modes of a single body.

the energy absorbed by the surge DOF alone was compared with the total energy harvested from the pitch and surge DOFs combined, there appeared to be configurations where the energy from surge was greater than the total energy absorbed. The results suggest that the addition of the pitch DOF was therefore detrimental to power absorption in these cases. Korde et al. [14] also considered the three-DOF control of a floating multi-mode WEC, but due to the geometry of the buoy considered the effect of surge and pitch on the total power absorbed was relatively minimal. It is also important to note that in all these studies, only linear hydrodynamics were considered in the performance assessment of the WEC. A more recent study featured experimental testing of a MIMO controller for a floating 3-DOF WEC in a more realistic ocean environment [5]. Although the coupling between surge and pitch was considered in the controller design, the impact of this coupling on performance was not studied in detail.

This study aims to provide an understanding of pitch-surge coupling on the performance and control of a flat, cylindrical multi-mode submerged WEC. The shape of the WEC is inspired by Carnegie Clean Energy's CETO-6 device, which is a submerged quasi-PA with a three-tether mooring configuration. The flat, disk-like design is used to achieve the best performance with regards to the cost of electricity associated with the Power Take-Off (PTO) forces and actuation [24]. However, the choice of shape also means that pitching motions can significantly change the projected surface of the WEC in surge, which will result in enhanced and nonlinear hydrodynamic coupling between these two DOFs. Similar hydrodynamic nonlinearities have been observed previously in a number of studies [3, 11, 30]; however, their effects on WEC efficiency have not been investigated. Furthermore, in these studies, only nonlinearities in the hydrodynamic forces due to combined pitch-heave motions were discussed, while combined pitch-surge motions were not addressed. Considering that there is already a strong hydrodynamic coupling between surge and pitch, even in the linear models, the effect of the enhanced coupling due to changes in projected surface area on the performance of multi-mode WECs also needs to be determined. The results have important implications for the design of an appropriate control strategy, since the majority of the literature to date has only considered control of WECs with the assumption of linear hydrodynamics.

The current research therefore attempts to provide a comparison of the performance of the flat cylindrical WEC based on both linear theory and results from a weakly nonlinear potential flow model [15]. Specifically, this study focuses on the nonlinear hydrodynamic coupling effects caused by oscillations in the surge and pitch DOFs exclusively, in order to decouple and

simplify the problem in the case of a plane incident wave. The knowledge built in this study can therefore be considered a preliminary step towards building a complete understanding of important nonlinear coupling effects in a full 6-DOF system. The analysis assumes full kinematic control of the buoy in both surge and pitch according to an explicitly prescribed motion, so that the hydrodynamic forces resulting from this motion can be examined. Nonlinear hydrodynamic coupling of surge and pitch with other DOFs, such as heave, and the influence of other forces on the submerged buoy, such as PTO and viscous drag forces, were not considered in order to isolate the effects of hydrodynamic pitch-surge coupling on performance. Additionally, nonlinearities associated with wave breaking and surface piercing were also considered outside the scope of this study.

The rest of the paper will be structured as follows. The WEC system considered in this study is discussed in more detail in Section 4.2. Section 4.3 briefly describes and compares the linear and nonlinear hydrodynamic models used in this study. The impact of pitch-surge coupling on the maximum power is presented in Section 4.4, while its effects on the required control parameters are presented in Section 4.5. Differences between the linear and nonlinear surge and pitch hydrodynamics are discussed in Section 4.6. This is then followed by a brief discussion of the findings in Section 4.7 with a conclusion in Section 4.8.

4.2 System description

The WEC used in this study features a flat, cylindrical buoy, with parameters similar to Carnegie Clean Energy's CETO-6 device [4]. In the CETO-6 conceptual design, a three-tether mooring configuration is used to anchor the buoy to the seafloor. The tethers are also directly integrated with the PTO system, allowing the WEC to harvest power from heave, surge and pitch simultaneously. However, in this study, kinematic control of the WEC was applied to focus specifically on understanding the hydrodynamic coupling effects on performance. Therefore, the effect of tethers on the behaviour of the WEC system was not considered in the analysis performed in this paper.

The parameters of the WEC are listed in Table 4.1, while a schematic is shown in Figure 4.1. The buoy is fully submerged, with a submergence depth of d_s = 6.5 m as measured from the buoy centre. Since this study will involve relatively large pitch amplitudes, this submergence depth was used in order to prevent the WEC from breaking the free-surface. As illustrated in Figure 4.1, as the submerged WEC moves in pitch x_5, the instantaneous

Table 4.1: Buoy parameters.

Parameter	Value
Radius, a	12.5 m
Height, H	5 m
Mass, m	1.99 $\times 10^6$ kg
Water depth, d	30 m
Submergence depth, d_s	6.5 m

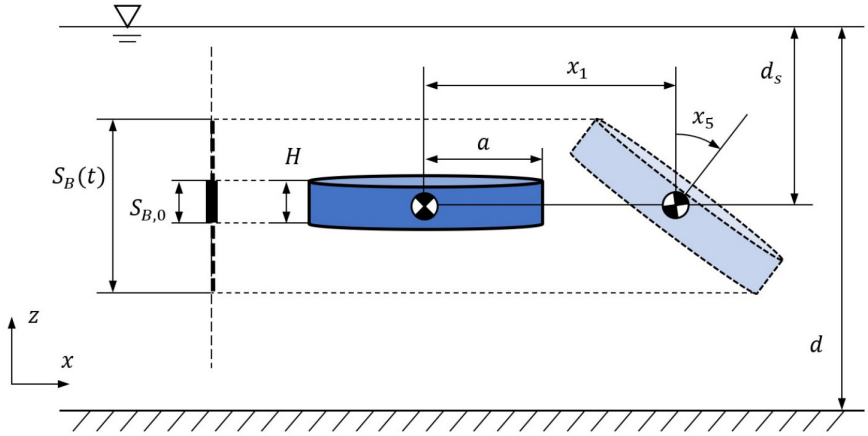

Figure 4.1: Schematic of the flat cylindrical buoy. Increasing the pitch angle x_5 can lead to significant changes in the instantaneous projected surface area of the buoy in surge $S_B(t)$. Not to scale.

projected surface area of the buoy in surge $S_B(t)$ will also change relative to its nominal projected surface area $S_{B,0}$. This will affect the instantaneous hydrodynamic forces acting on the buoy in surge and lead to an increased coupling between the surge and pitch DOFs.

Although the CETO-6 device is designed for motion in all six DOFs, the focus of this study was on the surge x_1 and pitch x_5 DOFs only. Therefore, for simplicity, only the motion in the xz-plane was considered. Furthermore, in order to isolate the effect of pitch-surge coupling on the nonlinear hydrodynamics, and because the hydrodynamic coupling between surge-heave and pitch-heave is not as significant, the heave DOF was also fully constrained in this study. The buoy was excited by linear, monochromatic waves which propagate along the positive X-direction. A constant wave amplitude of 0.5 m was used for all cases considered. The wave amplitude was selected to be large enough such that nonlinearities in the hydrodynamic forces could be observed, while still being reasonable as to avoid compromising the validity of the weakly nonlinear potential flow model used in this study.

4.3 Hydrodynamic modelling

When assessing the performance of WECs, linear analysis based on potential flow theory is the most commonly used modelling technique. However, linear analysis is not always accurate and, for the cases presented in this paper, were unable to fully capture the hydrodynamic interactions between surge and pitch. Therefore, nonlinear analysis was also required in this study to provide a more accurate assessment of the WEC performance.

Nonlinear analysis can be done in several ways. Experiments best approximate full-scale real-world performance, but can be expensive and time consuming to set up, making it difficult to perform sensitivity studies because design parameters cannot be easily changed. Another increasingly common method used in wave energy is Computational Fluid Dynamics (CFD). However, the high computational requirements of this technique also limits its usefulness for the purposes of performance assessment and optimisation, where many cases need to be studied [21].

An alternative approach to modelling nonlinear hydrodynamics is the use of weakly nonlinear potential flow solvers [21]. In this study, one such numerical model based on the Weak-Scatterer (WS) approximation and developed by École Centrale de Nantes was used [15]. Although this modelling technique is also based on potential flow theory, unlike in the linear models, the hydrodynamic forces are calculated about the exact position of the WEC at each time step in a meshed numerical tank, allowing it to capture more complex hydrodynamic interactions than the linear models. The model has been shown capable of providing a good match with CFD results, even under nonlinear conditions with large motion amplitudes [8]. In another comparison between the WS model and a fully nonlinear numerical wave tank, the WS model was found to be approximately one order of magnitude faster in terms of computational time [16]. The faster simulation times therefore made the WS model a more appropriate choice for conducting sensitivity studies and investigating the effect of different parameters on the performance of the WEC in this study.

As a result, the WEC hydrodynamics and its effect on the power production was studied using two different approaches: (i) a linear frequency domain (FD) model based on analytical equations [12, 13] and (ii) a nonlinear WS numerical model developed by École Centrale de Nantes. Since linear models are commonly adopted in literature for performance assessment and design optimisation, it is important to understand how nonlinear hydrodynamic pitch-surge coupling may affect the actual behaviour of the WEC compared to the results predicted by linear theory. By comparing these two

modelling approaches, the limitations of the linear model and the impact of these nonlinear coupling effects on the performance of the multi-mode WEC can be clearly highlighted. More detail about the modelling theory and assumptions of these two techniques, which are both based on potential flow theory, are presented below.

4.3.1 Potential flow theory

From potential flow theory, assuming that the fluid is irrotational, incompressible and inviscid, there is a velocity potential ϕ, a scalar quantity that can be used to compute the velocity of the flow.

In linear wave theory, in order to calculate the hydrodynamic forces, this velocity potential can be decomposed into several components [2]:

$$\phi = \phi_i + \phi_d + \phi_r \tag{4.1}$$

where ϕ_i, ϕ_d and ϕ_r are the incident, diffraction and radiation components, respectively. The incident and diffraction components are considered together to describe the total excitation force acting on the buoy, while the radiation force can be expressed in terms of the added mass and radiation damping coefficients. These forces are dependent on both the wave frequency and the geometry of the buoy. The excitation and radiation forces can then be added together to determine the total hydrodynamic force acting on the WEC:

$$F_{\text{hyd}} = F_{\text{exc}} + F_{\text{rad}} \tag{4.2}$$

where F_{hyd}, F_{exc} and F_{rad} are the total hydrodynamic, excitation and radiation forces, respectively.

In this study, the linear excitation force and radiation coefficients for a submerged cylindrical body were determined using analytical expressions [12, 13]. For the WEC considered in this study, values of the linear excitation force amplitude $|F_{\text{exc}}|$ (Fig. 4.2(a)) and phase $\angle F_{\text{exc}}$ (Fig. 4.2(b)) are shown in Figure 4.2. The added mass and radiation damping coefficients are usually expressed in terms of matrices **A** and **B**, respectively, with individual matrix elements for this WEC shown in Figure 4.3. Note that due to reciprocity relation, $A_{15} = A_{51}$ and $B_{15} = B_{51}$ [9].

In the WS approximation, the velocity potential and free-surface wave elevation are decomposed into incident ϕ_i and perturbed ϕ_p components. It is assumed that the effect of the perturbed component, which consists of radiation and diffraction effects, is relatively small compared to the incident

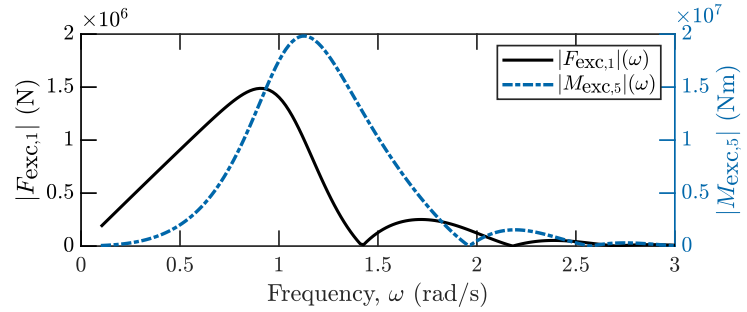

(a)

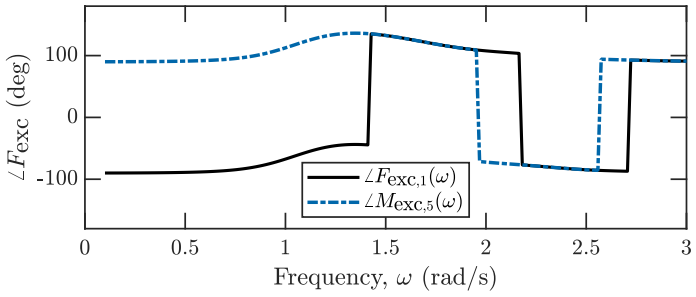

(b)

Figure 4.2: Surge excitation force and pitch excitation moment (a) amplitude and (b) phase

component [19]:

$$\begin{cases} \phi = \phi_i + \phi_p \\ \phi_p = \mathcal{O}(\phi_i) \end{cases} \tag{4.3}$$

This approximation allows the free-surface conditions to be linearised about the instantaneous incident wave elevation $z = \eta_i(x, y, t)$, which is explicitly known and applied as an input to the system. Only the perturbed components need to be solved in the boundary value problem. These assumptions mean that the incident waves do not have to be propagated throughout the entire numerical domain and the perturbed waves do not have to be meshed, which reduces computation time when compared to CFD solvers [15]. The total hydrodynamic forces are then obtained by integrating the pressure p of the surrounding fluid over the instantaneous wetted surface of the body $S_B(t)$.

It is necessary to note that for a WEC operating with reactive control, there will likely be cases where the assumption in Eq. (4.3) may not be satisfied due to large body motions. However, results from the WS model are still likely to be more accurate than those obtained from linear theory, which also requires

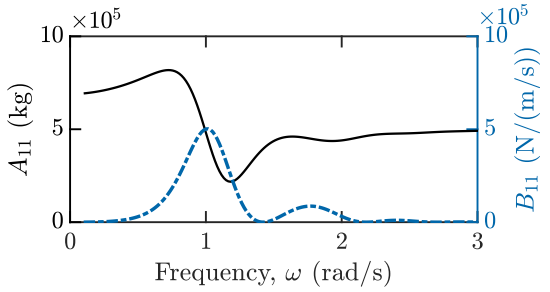

(a) Surge-surge

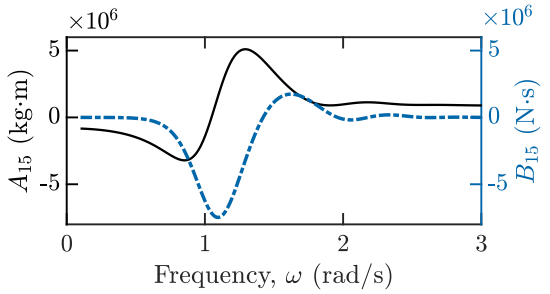

(b) Surge-pitch

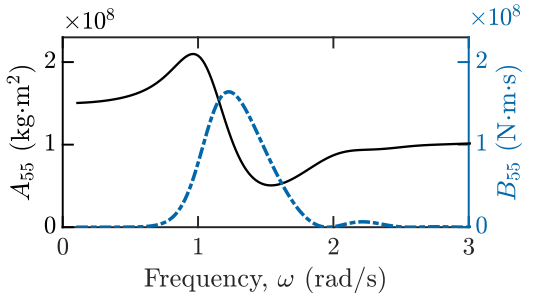

(c) Pitch-pitch

Figure 4.3: Added mass and radiation damping coefficients

additional assumptions of small amplitude motions and wave steepness that are often not fulfilled in these cases either. It has also been shown that even when the assumption in Eq. (4.3) is broken, such as in the case of a heaving PA WEC operating in steep waves with large body motions [15], the WS model remained capable of producing results comparable to CFD with only small errors of within 8% [8]. This gives confidence that WS model can still be expected to provide a reasonably accurate representation of the actual WEC system, especially in comparison to linear theory when large motion amplitudes are considered.

The key differences between the WS, linear potential flow and CFD models with regards to the computation of hydrodynamics are summarised

in Table 4.2. More detail about the WS model can be found in [15, 27, 28], while a more detailed comparison of the different modelling methods can be found in [8].

Table 4.2: Differences between linear, WS and CFD hydrodynamic modelling, from [8]

	Linear potential flow model	Weak-scatterer model	Navier-Stokes based CFD models
Hydrodynamics decomposition	$\phi = \phi_i + \phi_d + \phi_r$	$\phi = \phi_i + \phi_p$	N/A
Meshed free surface	$z = 0$	$z = \eta_i(x, y, t)$	$z = \eta(x, y, t)$
Meshed body surface	$S_{B,0}$	$S_B(t)$	$S_B(t)$
Hydrodynamic force computation	$F_{\text{exc}} + F_{\text{rad}}$	Integration of p over $S_B(t)$	Integration of total stress over $S_B(t)$
Drag force	Morison term can be added	Morison term can be added	yes
Fluid vortices	no	no	yes
Wave breaking	no	no	yes
Surface piercing	no	yes	yes
Computational speed	fast	medium	slow

4.3.2 Verification in linear conditions

The two models used in this study were first verified in linear conditions with small wave amplitudes and body motions. A comparison of the hydrodynamic forces and moments obtained from both models is shown in Figure 4.4 for a selected number of incident wave frequencies. The incident wave and surge amplitude were both set to 0.1 m, while the pitch amplitude was set to 1°. For all cases, the WEC was forced to oscillate in surge and pitch at the same frequency as the incident wave, or $\omega_{\text{exc}} = \omega_1 = \omega_5$. The phases of both the surge and pitch oscillations were 0° relative to the incident wave.

Recommendations for the time step and size of the smallest mesh elements given in [15] were initially applied to the WS model. In order to follow the numerical set-up suggested in the aforementioned study, a 1:50 scale was applied to the WEC system detailed in Table 4.1 due to the difference in buoy sizes used. The choice of scale should not affect results since the model is based on potential theory and the effects of viscous drag were neglected.

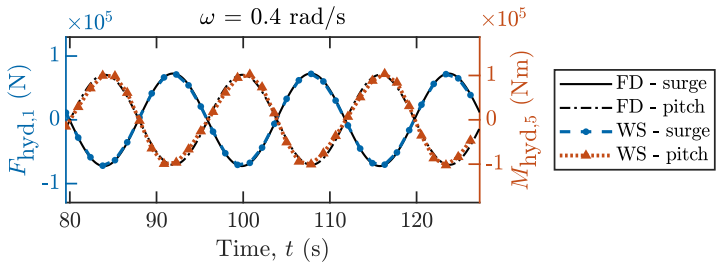

(a)

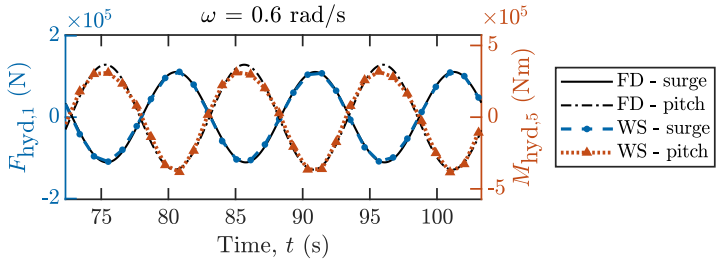

(b)

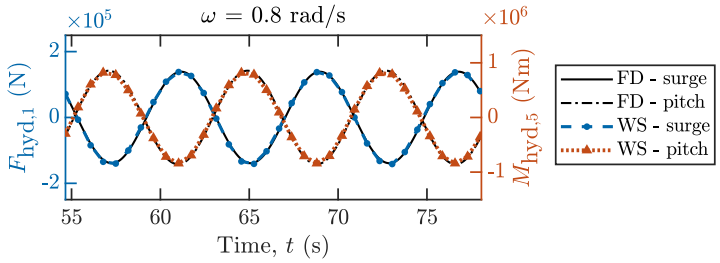

(c)

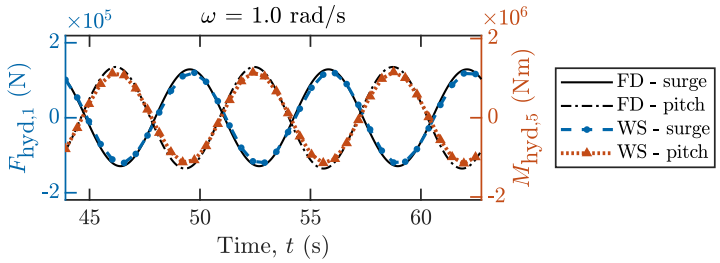

(d)

Figure 4.4: Comparison of the hydrodynamic forces and moments from the FD and WS models for relatively small incident wave and surge motion amplitudes of 0.1m and a pitch amplitude of 1°. Validation cases are shown for frequencies ω of (a) 0.4 rad/s, (b) 0.6 rad/s, (c) 0.8 rad/s and (d) 1.0 rad/s.

The small-scale values obtained from the WS model were then converted to full-scale using Froude scaling laws as given in [20].

Since the set-up in [15] was only for oscillations in a single DOF, it was found that the recommended time and mesh settings led to inaccurate power estimates when the WEC was moving in surge and pitch simultaneously. It was determined that a time step of $\Delta t < \tau/115$ was more appropriate for the cases required in this study, where τ is the wave period, which is only slightly less than the recommended value given in [15]. In contrast, it was found that the size of the smallest mesh element should be approximately four times smaller than the recommendation in [15], or $d_x < \lambda/80$, where λ is the incident wavelength. This setting was required for cases with large pitching motions, which caused the edges of the WEC to move very close to the free surface.

Overall, in Figure 4.4, a good match was achieved between the hydrodynamic forces and moments obtained from the two models, hence the WS model was considered successfully verified for linear conditions.

4.4 Effect of pitch on available power

In order to determine the effect of pitch-surge hydrodynamic coupling on the power absorption efficacy of the flat, cylindrical WEC, its dynamic motion must first be considered:

$$\mathbf{M}\ddot{\mathbf{x}}(t) = \mathbf{F}_{\text{hyd}}(t) + \mathbf{F}_{\text{buoy}}(t) + \mathbf{F}_{\text{PTO}}(t) + \mathbf{F}_{\text{ext}}(t) \tag{4.4}$$

where $\mathbf{M}$ is the mass matrix and $\ddot{\mathbf{x}}$ is the acceleration at the centre of gravity of the buoy. The main forces acting on the buoy, $\mathbf{F}_{\text{hyd}}$, $\mathbf{F}_{\text{buoy}}$, $\mathbf{F}_{\text{PTO}}$ and $\mathbf{F}_{\text{ext}}$ are the hydrodynamic, buoyancy, power take-off (PTO) and external (such as viscous drag, mooring, etc.) forces, respectively. In both the FD and WS models, it was possible to prescribe the motion of the buoy explicitly in order to implement the kinematic control assumption used in this study. As a result, it was not necessary to directly calculate the exact PTO forces required in the models. Instead, the PTO controller was simply assumed to be fully ideal, including being able to account for any coupling present between surge and pitch (both linear and nonlinear). Additionally, since the focus of this paper was specifically on the effect of hydrodynamic pitch-surge coupling on power, the buoy was assumed to be neutrally buoyant (achieved through explicit and kinematic control of the buoy) and external forces were not considered ($\overline{\mathbf{F}}_{\text{buoy}} = \overline{\mathbf{F}}_{\text{ext}} = \mathbf{0}$, where the overbar denotes the long term average).

Therefore, to calculate the power that can be absorbed by the system, only the WEC motions and hydrodynamic forces were required:

$$P = \mathbf{F}_{\text{hyd}}^{T}\dot{\mathbf{x}}. \tag{4.5}$$

For the linear model, since there are no control or mooring forces, a frequency domain analysis is sufficient. The motion of the buoy can therefore be kinematically controlled by specifying a complex displacement for surge and pitch:

$$\hat{\mathbf{x}} = \begin{pmatrix} |x_1|\mathrm{e}^{-i\angle x_1} \\ |x_5|\mathrm{e}^{-i\angle x_5} \end{pmatrix} \tag{4.6}$$

where ^ denotes the complex amplitude and $|x_1|$ and $|x_5|$ are the surge and pitch amplitudes, respectively. The phases of the surge and pitch displacement relative to the incident wave elevation are denoted by $\angle x_1$ and $\angle x_5$, respectively. The heave DOF is assumed to be fully constrained.

Similarly in the WS model, the buoy can be controlled by simply specifying the amplitude and phase of surge and pitch modes:

$$\mathbf{x}(t) = \begin{pmatrix} |x_1|\cos(-\omega t + \angle x_1) \\ |x_5|\cos(-\omega t + \angle x_5) \end{pmatrix} \tag{4.7}$$

From this, Eq. (4.5) can then be re-written to give the time-averaged power absorbed by the WEC in the FD domain [9]:

$$\overline{P} = \frac{1}{4}(\hat{\mathbf{F}}_{\text{exc}}^{*}\hat{\mathbf{u}} + \hat{\mathbf{u}}^{*}\hat{\mathbf{F}}_{\text{exc}}) - \frac{1}{2}\hat{\mathbf{u}}^{*}\mathbf{B}\hat{\mathbf{u}}. \tag{4.8}$$

where $\hat{\mathbf{u}}$ refers to the velocity in of the WEC in the frequency domain and * refers to the complex conjugate transpose. The total power in the FD model can also be decomposed into the individual surge and pitch components using:

$$\begin{aligned} \overline{P}_1 = {} & \frac{1}{4}\left(\hat{F}_{\text{exc},1}^{*}\hat{u}_1 + \hat{u}_1^{*}\hat{F}_{\text{exc},1}\right) \\ & -\frac{1}{2}\left(B_{11}|\hat{u}_1|^2 + B_{15}|\hat{u}_1||\hat{u}_5|\cos(\angle\hat{u}_1 - \angle\hat{u}_5)\right), \end{aligned} \tag{4.9a}$$

$$\begin{aligned} \overline{P}_5 = {} & \frac{1}{4}\left(\hat{F}_{\text{exc},5}^{*}\hat{u}_5 + \hat{u}_5^{*}\hat{M}_{\text{exc},5}\right) \\ & -\frac{1}{2}\left(B_{55}|\hat{u}_5|^2 + B_{51}|\hat{u}_5||\hat{u}_1|\cos(\angle\hat{u}_5 - \angle\hat{u}_1)\right). \end{aligned} \tag{4.9b}$$

where $|u_1|$ and $|u_5|$ are the surge and pitch velocity amplitudes, respectively, while $\angle u_1$ and $\angle u_5$ denote the phases of the surge and pitch velocity relative to the incident wave elevation, respectively.

In the WS model, the average total surge and pitch power over each cycle is given by:

$$\overline{P} = \frac{1}{\tau}\int_0^\tau \mathbf{F}_{\text{hyd}}^T(t)\dot{\mathbf{x}}(t)\mathrm{d}t, \tag{4.10a}$$

$$\overline{P}_1 = \frac{1}{\tau}\int_0^\tau F_{\text{hyd},1}(t)\dot{x}_1(t)\mathrm{d}t, \tag{4.10b}$$

$$\overline{P}_5 = \frac{1}{\tau}\int_0^\tau F_{\text{hyd},5}(t)\dot{x}_5(t)\mathrm{d}t. \tag{4.10c}$$

4.4.1 Optimal power absorption from linear theory

From linear theory, it is possible to find the optimal surge and pitch motions required to achieve maximum power absorption from the incident waves. To do so, the WEC velocity must fulfil both the amplitude and phase optimality conditions, also known as the complex conjugate control criteria [9]. If these conditions are met, for a single body oscillating in one DOF and assuming no motion constraints, the maximum power that can be absorbed by the WEC is [9]:

$$P_{\text{max}} = \frac{1}{4}\hat{\mathbf{F}}_{\text{exc}}^*\hat{\mathbf{u}}_{\text{opt}} = \frac{1}{2}\hat{\mathbf{u}}_{\text{opt}}^*\mathbf{B}\hat{\mathbf{u}}_{\text{opt}}. \tag{4.11}$$

The following condition must therefore be met:

$$\mathbf{B}\hat{\mathbf{u}}_{\text{opt}} = \frac{1}{2}\hat{\mathbf{F}}_{\text{exc}}. \tag{4.12}$$

For a body operating in only surge in the absence of pitch, the optimal velocity can then be determined using the following equation:

$$\hat{u}_{1,\text{opt}}(\omega) = \frac{\hat{F}_{\text{exc},1}(\omega)}{2B_{11}(\omega)} \tag{4.13}$$

However, when both surge and pitch motions are combined, the radiation damping matrix $\mathbf{B}$ becomes singular, meaning that Eq. (4.12) cannot be solved for both $\hat{u}_1$ and $\hat{u}_5$ simultaneously. As a result, the optimal velocity in surge becomes dependent on the velocity in pitch, and vice versa. In practice, it is often difficult to control or constrain the pitching motions of the WEC. Therefore, the surge motions required to compensate for the presence of

pitch in the system were considered. Given any arbitrary pitch velocity, the surge velocity required for maximum power absorption becomes [9, 23]:

$$\hat{u}_{1,\text{opt}}(\omega) = \frac{\hat{F}_{\text{exc},1}(\omega) - 2B_{15}(\omega)\hat{u}_5(\omega)}{2B_{11}(\omega)} \tag{4.14}$$

This relationship can be explained physically by considering the fact that both surge and pitch motions radiate dipole-type waves. In order to absorb maximum power, the WEC must radiate waves to interfere destructively with the incident wave [9]. If pitch is moving arbitrarily and radiating waves, the surge motion can be adjusted accordingly to ensure that the total dipole-type wave radiated by the WEC still interferes optimally with the incident wave. Hence according to linear theory, for any given pitching motion, it is always possible to absorb the maximum possible power from the incident wave, provided that the conditions given in Eq. (4.14) are fulfilled. The only requirement is for the surge amplitude and phase to be correctly tuned, in order to compensate for the amount of pitch present in the system.

To fulfil the conditions in Eq. (4.14), the required optimal surge amplitude $|x_1|_{\text{opt}}$ must also change as pitch amplitude increases. This relationship is illustrated in Figure 4.5. Note that in reality, the exact value of $|x_1|_{\text{opt}}$ will also vary with pitch phase; however, for clarity only the required surge amplitudes

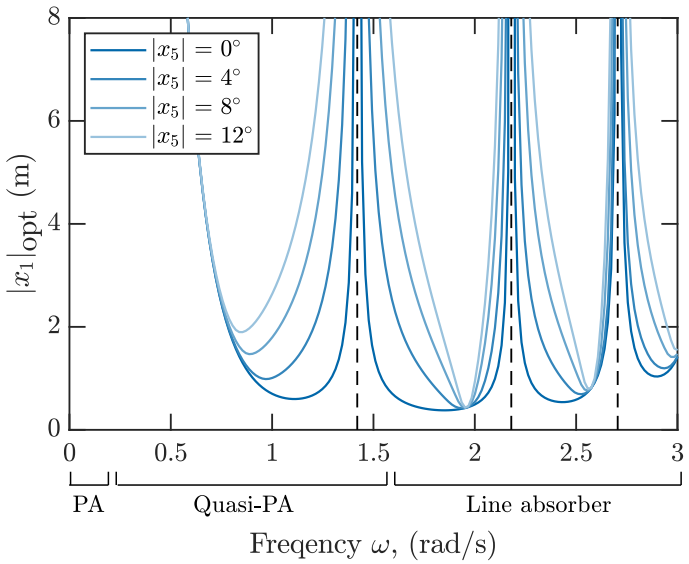

Figure 4.5: Optimal surge amplitude from the linear FD model for a range of incident wave frequencies and pitch amplitudes. Note that these amplitudes were obtained assuming no viscous drag forces or motion constraints.

for a pitch phase of $\angle x_5 = 0°$ are shown. The major trends discussed here are also consistent across all pitch phases.

It is also important to note that the CETO-6 WEC used in this study is classified as a quasi-PA due to its size relative to the incident wavelength. Proposed by Falnes and Hals [10], this category of WECs is used to describe devices with operating frequencies between PAs and line absorbers. The different operating ranges of these WEC categories is also indicated in Figure 4.5. For a WEC to be classified as a PA, its size must be very small relative to the incident wavelength λ. If the length of the WEC is given as $2a$, then for a PA it is required that $2a << \lambda$, or more precisely $2a < \lambda/20$ [7]. In contrast, a line absorber is defined as a structure with a dominant lengtLah that is comparable to at least one wavelength, or $2a \geq \lambda$. Hence, given that the wavelength can also be defined as $\lambda = 2\pi/k$, where k is the wavenumber, the intended operating range of quasi-PA is between $\pi/20 < ka < \pi$. The cases investigated in this study were therefore limited to within this range of frequencies.

From Figure 4.5, it can be seen that the required surge amplitude from Eq. (4.14) grew significantly at particular frequencies. At these frequencies, both the surge radiation damping B_{11} and pitch-surge coupling B_{15} terms dropped close to zero, hence from Eq. (4.14), the required surge amplitude increased to infinity. In reality, however, there are several external factors that limit the maximum surge amplitude of the WEC. In the case of surge motions, the PTO machinery, mooring systems and viscous drag effects are most likely to limit the maximum allowable amplitude, which in turn may affect the amount of power that can be absorbed [25]. As this increase in surge amplitude occurs within the intended operating range for this WEC, these amplitude limitations are also required when assessing performance.

When pitch was added to the system, the sharp increase in surge amplitude occurred across a much wider range of frequencies. In Figure 4.5, this is most evident in the range of frequencies between $\omega = 1.2$-1.7 rad/s. This is because the magnitude of the coupling term B_{15} reached its peak values at these frequencies. As a result, the system was much more sensitive to changes in pitch for these cases, resulting in large increases in surge amplitude as pitch increases. From a practical viewpoint, this means that the effect of the surge amplitude limitations on maximum power is experienced across a wider range of frequencies than for the case without pitch. In contrast, at frequencies where the pitch damping term B_{55} was small, such as below $\omega < 0.7$ rad/s, the optimal surge amplitude $|x_1|_{\text{opt}}$ was unaffected by pitch amplitude.

In addition to the surge amplitude, the surge phase was also dependent

on pitch. The relationship between the phases of these two DOFs for different frequencies is shown in Figure 4.6. Note that the phases of the surge and pitch velocities are shown, to better relate the results back to the well-known complex control criteria. Initially, when there was no pitch in Figure 4.6(a), the optimal phase of the surge velocity matched the phase of the excitation force, which was expected from the conjugate control criteria. As the WEC began to pitch, the optimal surge phase also changed depending on the phase of the pitching motions. At higher incident wave frequencies, the surge phase could shift significantly from its initial value, compared to the results at lower wave frequencies which only showed a small variation in surge phase. Again, from linear theory, it appeared that the WEC was not as strongly affected by pitch when operating at lower frequencies.

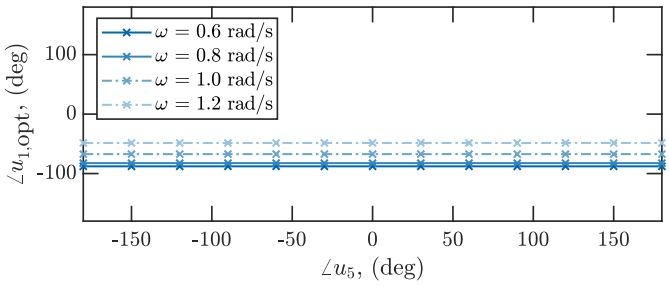

(a)

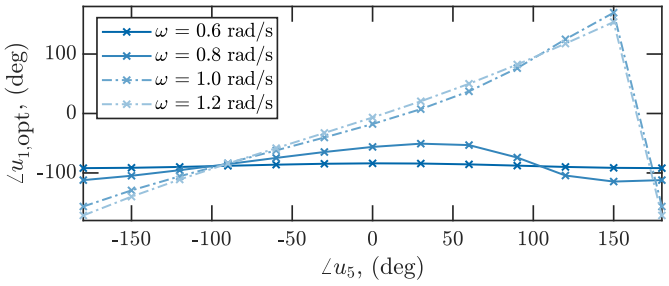

(b)

Figure 4.6: Relationship between optimal surge and pitch phases in the linear FD model, as pitch amplitude increases from (a) 0° to (b) 8°.

4.4.2 Effect of pitch on power absorption with hydrodynamic nonlinearities

The effect of pitch on maximum power available with nonlinear hydrodynamic coupling was then considered. The WEC was forced in both surge and pitch simultaneously in the presence of an incident wave in the WS

model and neglecting viscous drag forces. Assuming kinematic control, the power that could be absorbed by the WEC was a function of the surge and pitch amplitudes and phases, or $P(|x_1|, |x_5|, \angle x_1, \angle x_5)$. By varying these parameters in the WS model, it was possible to find the optimal surge and pitch motions which resulted in the maximum power absorbed by the WEC at each incident wave frequency. Two key steps were used to optimise the WS results, which are outlined in the following sections.

4.4.2.1 Step 1 - Optimisation of surge amplitude and phase

From linear theory, for any combination of pitch amplitude and phase, maximum available power is always possible provided that the surge amplitude and phase are correctly tuned. However, it was unknown whether this condition will remain the same when nonlinear hydrodynamics are considered. Therefore, to check this hypothesis and as a first step, the pitch amplitudes and phases were varied incrementally in the WS model while values of the surge amplitude and phase were optimised using the inbuilt Matlab function *fminsearch*.

For each set value of frequency, pitch amplitude and pitch phase, Eq. (4.14) was used to calculate the linear estimates for the optimal surge amplitude and phase, which were then used as initial values for the optimisation function. The optimisation was then repeated for multiple incident wave frequencies, pitch amplitudes and pitch phases. For completeness, the full range of pitch phases across $-180° < \angle x_5 < 180°$ was tested in the WS model. In the real CETO-6 system, the arrangement of the tethers determines the actual range of pitch phases that may be experienced by the device during operation.

At certain frequencies, it was found that the required surge amplitude reached unreasonably large values in excess of 10 m, which would not be possible in reality due to constraints imposed by the PTO equipment and viscous drag effects. Volume stroke limitations, as given in [25], were therefore considered for constraints on the surge amplitude. In the study, the author suggested many practical limitations for body motions in surge; however, these limits were still too large to be feasible in a real-world case. Therefore, an arbitrary limit of $|x_1|_{\max}$ = 5 m was chosen as the maximum allowable surge amplitude. In these cases, a modified version of the function *fminsearch* was used to apply this constraint to the optimisation problem.

The results of this optimisation procedure for a frequencies of ω = 0.4, 0.6, 0.8 and 1.0 rad/s are shown in Figure 4.7. From this step, it was found that the maximum power absorbed by the WEC in the WS model was clearly dependent on pitch phase. However, the exact pitch phase resulting

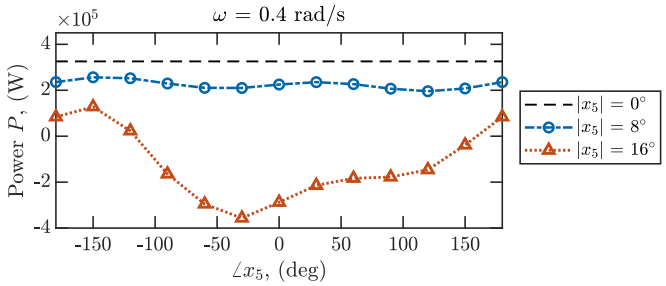

(a)

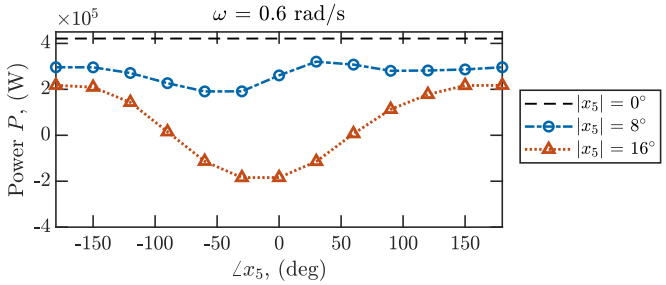

(b)

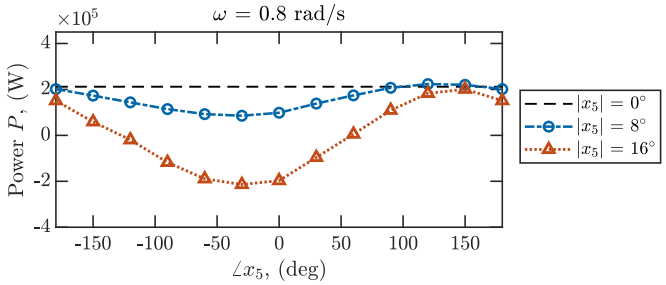

(c)

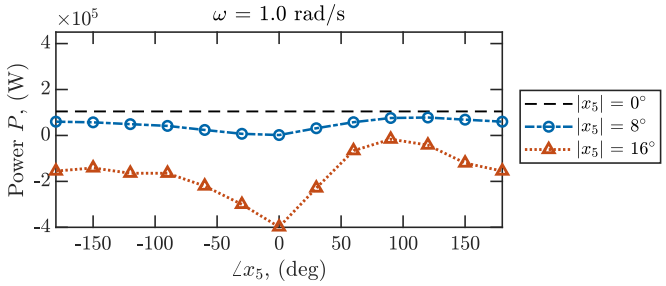

(d)

Figure 4.7: Power available from the WS model at different pitch amplitudes and pitch phases (relative to the incident wave). Results are shown for incident wave frequencies of (a) 0.4 rad/s, (b) 0.6 rad/s, (c) 0.8 rad/s and (d) 1.0 rad/s. Surge amplitude $|x_1|$ and phase $\angle x_1$ are optimised for each set value of pitch amplitude and phase.

in maximum power changed depending on both the incident wave frequency and pitch amplitude. As the pitch amplitude increased, the variation in power with pitch phase became much greater, with some phases resulting in negative net power. This outcome was not consistent with linear theory, whereby the maximum power can always be absorbed from the wave regardless of pitch amplitude or phase. The results from the WS model therefore suggest that the pitch phase has an effect on the nonlinear hydrodynamic coupling between the surge and pitch DOFs. Hence, when nonlinear dynamics are included, the pitch phase must also be tuned in order to achieve maximum power.

4.4.2.2 Step 2 - Optimisation of surge amplitude, surge phase and pitch phase

Following this, the process was then adjusted such that for set values of pitch amplitude, three variables were optimised: (1) surge amplitude, (2) surge phase and (3) pitch phase. To increase the chances of reaching a global maximum, values of (1)-(3) from the previous optimisation step were used as initial values for the optimisation routine at each frequency and pitch amplitude. As such, the first step in this optimisation procedure could be considered analogous to a coarse grid search, while the second optimisation step involved a finer search across all three variables.

The maximum power obtained from the WS after this second optimisation step, with surge amplitude constraints applied, are shown in Figure 4.8. For comparison purposes, the maximum estimated power from the FD model with amplitude constraints are also shown on the same graph.

In the linear FD model, it was observed that adding pitch slightly increased the maximum power absorbed by the system at frequencies $\omega < 0.7$ rad/s. This can be explained by the fact that for $\omega < 0.7$ rad/s, the surge amplitudes required to fulfil the optimality conditions were greater than the applied limit of $|x_1|_{\max} = 5$ m. Physically, this means that the radiated waves generated by the surge DOF alone were not sufficient to cancel out the incident wave due to the applied amplitude constraints. The addition of pitch would aid with the generation of radiated waves; hence the power absorption ability of the WEC increased slightly with pitch amplitude in the linear model for $\omega < 0.7$ rad/s. For $\omega > 1.1$ rad/s and a pitch amplitude of $|x_5| = 16°$, the amplitude limitation completely negated the ability of the WEC to absorb any useful power.

Comparing the FD and WS results, it can be clearly seen that the linear model greatly overestimated the power that could be absorbed, especially as the pitch amplitude increased. It was noted that even without the presence

of pitch, at frequencies of ω = 0.5-0.6 rad/s, differences between the two models could already be observed, with the WS results showing less maximum power absorbed than the values obtained from the FD model. This is likely due to the relatively large wave amplitude and high surge amplitudes required for optimal control in these cases, which can introduce nonlinearities in the hydrodynamic forces even without the addition of pitching motions. When pitch was added, the power available obtained in the WS model for frequencies $\omega \leq 0.7$ rad/s and $\omega \geq 1.0$ rad/s decreased with pitch amplitude. For $\omega \leq 0.7$ rad/s and at a pitch amplitude of $|x_5| = 16°$, this led to approximately 50% less actual power absorbed than the estimates given from the linear model. For $\omega \geq 1.0$ rad/s, the maximum power absorbed became negative in certain cases, indicating that the surging and pitch WEC was actually consuming power rather than generating useful power. Note that total loss of power may possibly be mitigated with the inclusion of the heave DOF for power absorption, leading to better overall performance. However, given the significant power losses observed as pitch was added to the system, it is clear that the effects of nonlinear pitch-surge coupling should not be neglected in the design of multi-mode WECs. Using linear hydrodynamics alone is insufficient for an accurate assessment of performance, since the linear model may be unable to predict the large losses in available power at high pitch amplitudes and wave frequencies. For ω = 0.8 and 0.9 rad/s, a better match was observed between the two models with regards to power available. Provided that the pitch phase was correctly tuned, the maximum absorbed power could still be achieved despite increases in the pitch amplitude.

The power absorbed by the individual surge and pitch DOFs was also compared between the two models. The power available from the surge alone P_1 is shown in Figure 4.9, while the power available in pitch P_5 is shown in Figure 4.10.

For the linear FD results, for each set value of frequency and pitch amplitude, the optimal surge and pitch power resulting in maximum total power varied with pitch phase $\angle x_5$. This variation is therefore shown as a shaded area on the plots. Results correspond to the full range of pitch phases across $-180° < \angle x_5 < 180°$, which again was considered for completeness. In the WS model, there was only one unique and optimal value of $\angle x_5$ that resulted in the maximum power at each frequency and pitch amplitude. The values of P_1 and P_5 shown in the plots are for the WEC which was oscillating at this optimal pitch phase.

It was observed that for most cases, when the motion parameters of the WEC were fully optimised, the surge and pitch power obtained from the WS model lay within or close to the expected bounds given in linear FD

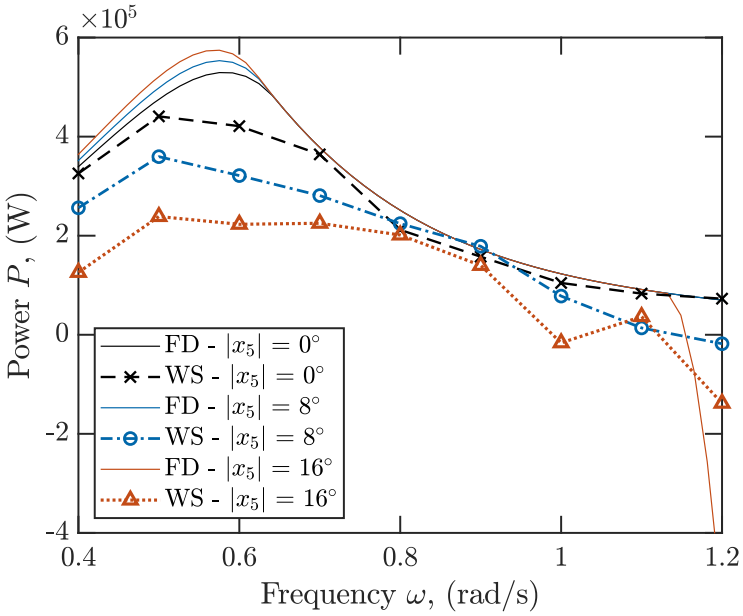

Figure 4.8: Power available at different pitch amplitudes and incident wave frequencies, as obtained from both the FD and WS models. The surge amplitude $|x_1|$, surge phase $\angle x_1$ and pitch phase $\angle x_5$ have been optimised for each set frequency and pitch amplitude.

model. However, some exceptions were noted at $\omega \leq 0.6$ rad/s for $|x_5| = 8°$ and 16°. For $|x_5| = 8°$, the WS pitch power at ω = 0.5-0.6 rad/s was less than the expected values given from the linear FD model, while for $|x_5| = 16°$ the values of surge power from the WS model for $\omega \leq 0.6$ rad/s were all significantly reduced compared to the linear estimates. These differences indicate that there may be some nonlinear effects occurring at these cases which could not be captured by the linear model.

4.5 Effect of pitch on control

In this section, the optimal parameters (surge amplitude, surge phase and pitch phase) obtained from Section 4.4.2 resulting in the maximum power absorbed by the WEC are considered. The sensitivity of the optimally tuned system to variations in surge and pitch phase is also briefly addressed in this section.

4.5.1 Optimal surge amplitude

The optimal surge amplitudes required to absorb the maximum power in both the FD and WS models at different incident wave frequencies and pitch amplitudes are compared in Figure 4.11. In the FD model, for cases where pitch motions were present, the optimal surge amplitude resulting in

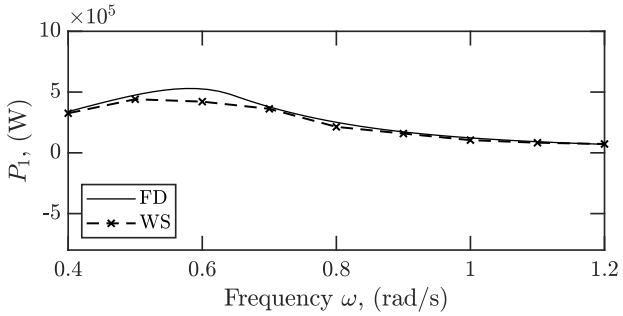

(a) $|x_5|$ = 0 deg

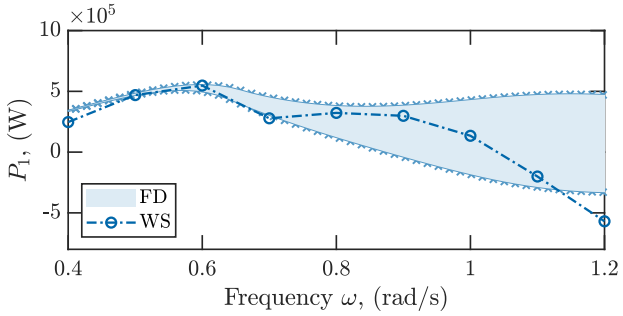

(b) $|x_5|$ = 8 deg

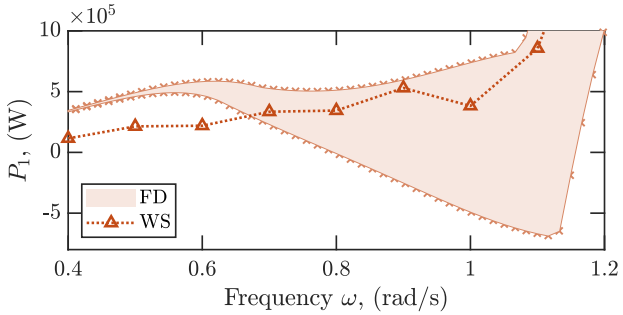

(c) $|x_5|$ = 16 deg

Figure 4.9: Comparison of the power absorbed in the surge DOF at different incident wave frequencies and pitch amplitudes of (a) 0°, (b) 8° and (c) 16°, for cases with maximum power in the FD and WS models. The shaded areas indicate the variation in optimal surge power due to pitch phase in the FD model.

maximum power varied with pitch phase. This variation in optimal amplitude is therefore also shown as a shaded area in the plots.

In Figure 4.11(a), when no pitch was present in system, a relatively good match is achieved between the two models. The only notable exception was at $\omega > 0.6$ rad/s, where the amplitude from the WS model was slightly less than the predicted values from the linear model. This result may explain the

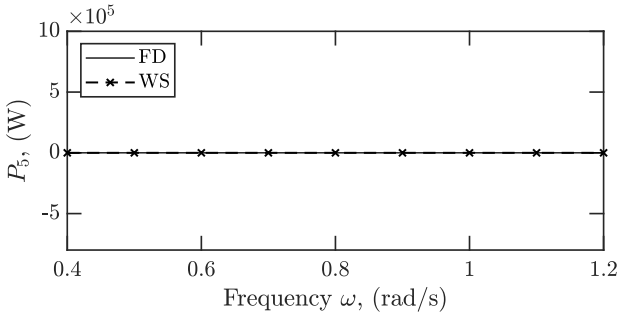

(a) $|x_5|$ = 0 deg

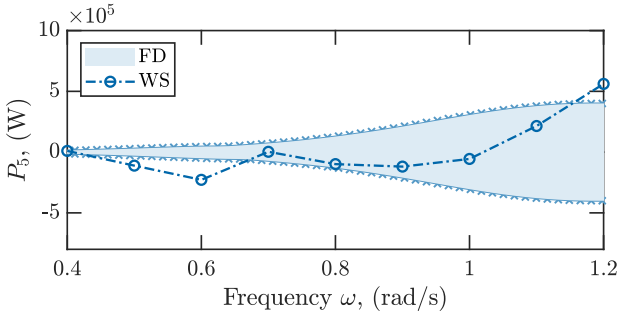

(b) $|x_5|$ = 8 deg

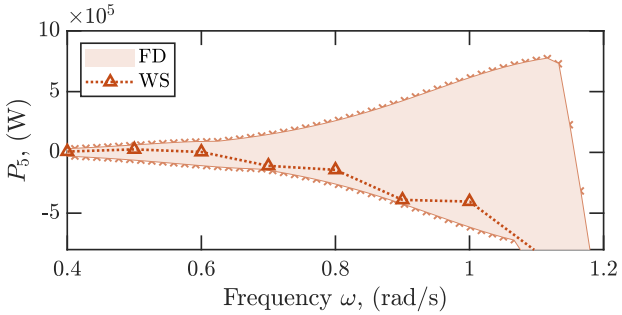

(c) $|x_5|$ = 16 deg

Figure 4.10: Comparison of the power absorbed in the pitch DOF at different incident wave frequencies and pitch amplitudes of (a) 0°, (b) 8° and (c) 16°, for cases with maximum power in the FD and WS models. The shaded areas indicate the variation in optimal surge power due to pitch phase in the FD model.

reduced power observed in Section 4.4.2 for $|x_5| = 0°$.

When pitching motions were added, within the frequency range shown in Figures 4.11(b)-(c), the required surge amplitude initially decreased with frequency before increasing again at higher frequencies. The onset of this decrease in surge amplitude occurred at lower frequencies for a pitch amplitude of $|x_5| = 16°$ than for 8°. This trend was observed in both the FD and WS results.

In most cases, the values of optimal amplitude from the WS model ap-

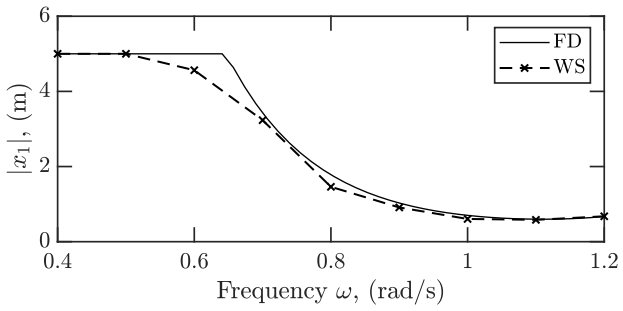

(a) $|x_5| = 0$ deg

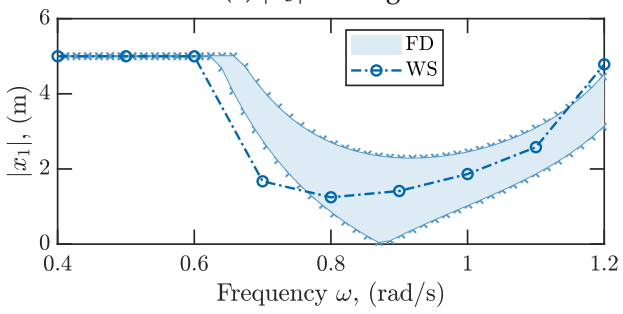

(b) $|x_5| = 8$ deg

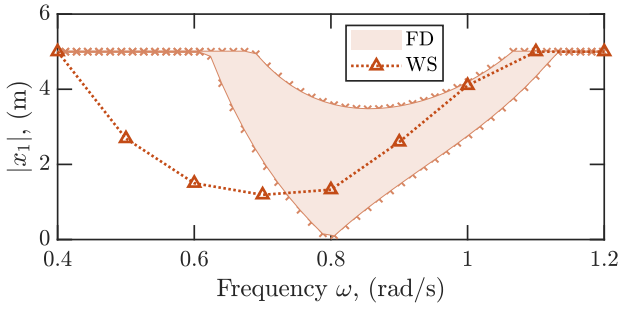

(c) $|x_5| = 16$ deg

Figure 4.11: Optimal surge amplitude from the FD and WS models at different incident wave frequencies and pitch amplitudes of (a) 0°, (b) 8° and (c) 16°. The shaded areas indicate the variation in optimal surge amplitude due to pitch phase in the FD model.

peared to lie within or close to the expected bounds from the FD model. However, exceptions were observed for cases with $\omega \leq 0.7$ rad/s and $|x_5| = 16°$, where the linear model greatly overestimated the surge amplitude required for maximum power absorption. These observations were somewhat consistent with the results regarding power, with the exceptions occurring for similar cases as those noted previously.

4.5.2 Optimal surge phase

Values of optimal surge phase are plotted in Figure 4.12. These values are also compared against the optimal surge phase obtained from the linear model. As previously, shaded areas are used to indicate the variation in optimal surge phase with pitch phase in the FD results.

In the linear FD model, above a certain frequency, the optimal surge phase could take on any value between -180° $< \angle x_5 <$ 180°, depending on the pitch phase. For a pitch amplitude of $|x_5| = 8°$, this occurred at $\omega \geq 0.9$ rad/s, while for $|x_5| = 16°$, this could occur at slightly lower frequencies of $\omega \geq 0.8$ rad/s.

In contrast, when nonlinear hydrodynamics were included, there was only one unique value of optimal surge phase which would result in maximum power. Similar to previous results, these optimal values from the WS model generally lay close or within the expected range from the FD model. For most cases, the optimal surge phase appeared to increase with the incident wave frequency. The optimal surge phases were also slightly higher when pitching motions were present, than when there was no pitch in the system.

4.5.3 Optimal pitch phase

From linear theory, the maximum power that can be absorbed by the WEC from the incident wave is independent of pitch phase. However, it was shown in Section 4.4.2 that this is not true when nonlinear hydrodynamic effects were included. Therefore, values of optimal pitch phase from the WS model are also plotted in Figure 4.13.

For most of the frequency range considered, the optimal pitch phases from the WS model generally appeared to decrease with frequency. Noteworthy exceptions occurred at a frequency of ω = 0.5 and 0.6 rad/s for a pitch amplitude of 8°, where the optimal phase dropped far below the apparent trend from the other results. However, since the existence of a unique value for optimal pitch phase did not align with linear theory, a conclusive statement regarding the trend in optimal pitch phase could not be made by considering linear hydrodynamic forces and coefficients alone.

4.5.4 Sensitivity of optimal power to phase

From the previous sections, it was apparent that an optimal controller for the multi-mode, flat cylindrical WEC will require the simultaneous tuning of surge amplitude, surge phase and pitch phase. However, exact tuning of phase may be difficult to achieve in practice. Hence, the robustness of the proposed control strategy to both the surge and pitch phases also needs to be addressed for cases where perfect tuning cannot be realistically achieved.

Phase plots were therefore produced to illustrate the sensitivity of the available power to surge and pitch phase. For each set value of frequency

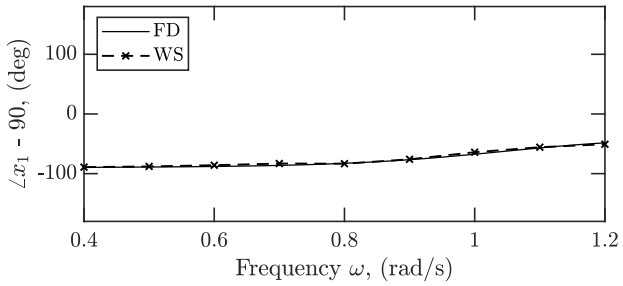

(a) $|x_5|$ = 0 deg

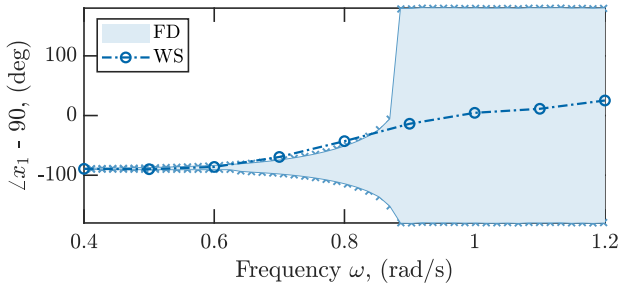

(b) $|x_5|$ = 8 deg

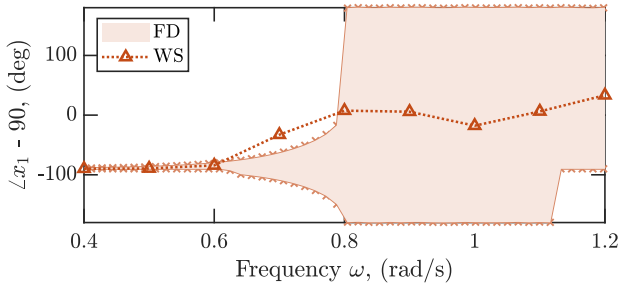

(c) $|x_5|$ = 16 deg

Figure 4.12: Optimal surge phase from the FD and WS models at different incident wave frequencies and pitch amplitudes of (a) 0°, (b) 8° and (c) 16°. The shaded areas indicate the variation in optimal surge phase due to pitch phase in the FD model.

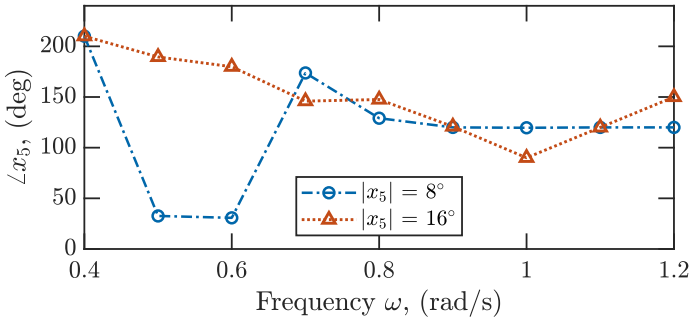

Figure 4.13: Optimal surge phase from the WS models at different incident wave frequencies and pitch amplitudes.

and pitch amplitude, the WEC was kinematically forced at the optimised surge amplitude shown in Section 4.5.1. The surge phase and pitch phase were then varied incrementally, and the power available was determined at each increment. This process was then repeated for multiple incident wave frequencies and pitch amplitudes in both the FD and WS models to generate phase plots showing the variation in total power with surge and pitch phases.

Phase plots produced from the linear FD model are shown in Figure 4.14 for a range of pitch amplitudes and incident wave frequencies of ω = 0.4, 0.6, 0.8 and 1.0 rad/s. Similarly, plots generated using the WS model are shown in Figure 4.15. For all cases, the wave amplitude was kept constant at 0.5 m. On the plots, a solid black line is used to separate areas with positive power available (i.e. when the device is absorbing useful power) from areas where power available is negative (i.e. when the device is consuming power). Phases of the surge and pitch velocities are shown, instead of the displacement phases, to better relate the results to the well-known complex conjugate criteria. For the same reason, the phase of the surge excitation force at each frequency is also shown as a dashed red line on the plots.

When the WEC was forced to oscillate in surge only ($|x_5| = 0°$) in Figure 4.14(a), maximum power occurred for surge velocity phases which matched the phase of the excitation force and aligned with the complex conjugate control criteria. However, when pitch was added to the system, the phase plots were distorted due to the pitch-surge hydrodynamic coupling, with the degree of distortion increasing with pitch amplitude. As a result, the optimal surge and pitch phases required for maximum power also changed with an increase in pitch amplitude, as was discussed earlier in Section 4.4.1. Regarding areas with positive power absorption, combinations of surge and pitch phases resulting in useful power appeared to decrease as incident wave frequency and pitch amplitude increases. Finer tuning will therefore be

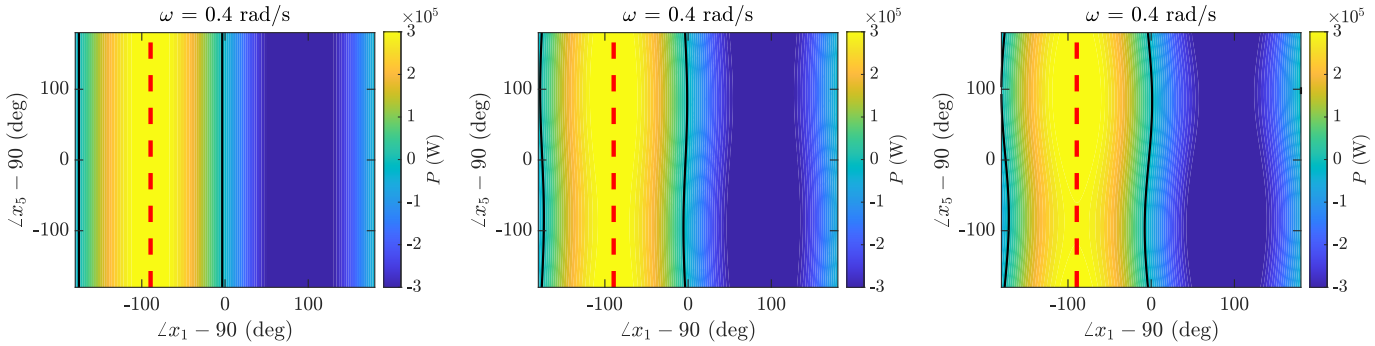

(a) $|x_5| = 0$ deg (b) $|x_5| = 8$ deg (c) $|x_5| = 16$ deg

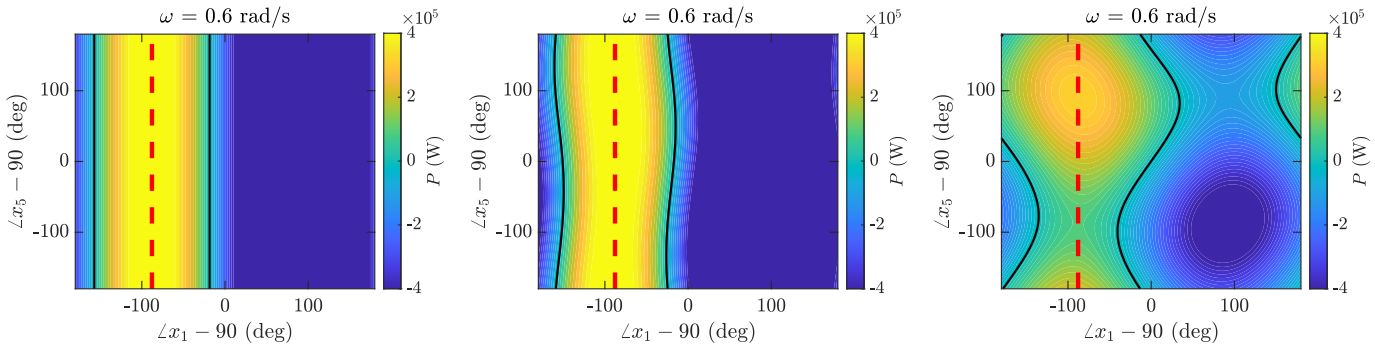

(d) $|x_5| = 0$ deg (e) $|x_5| = 8$ deg (f) $|x_5| = 16$ deg

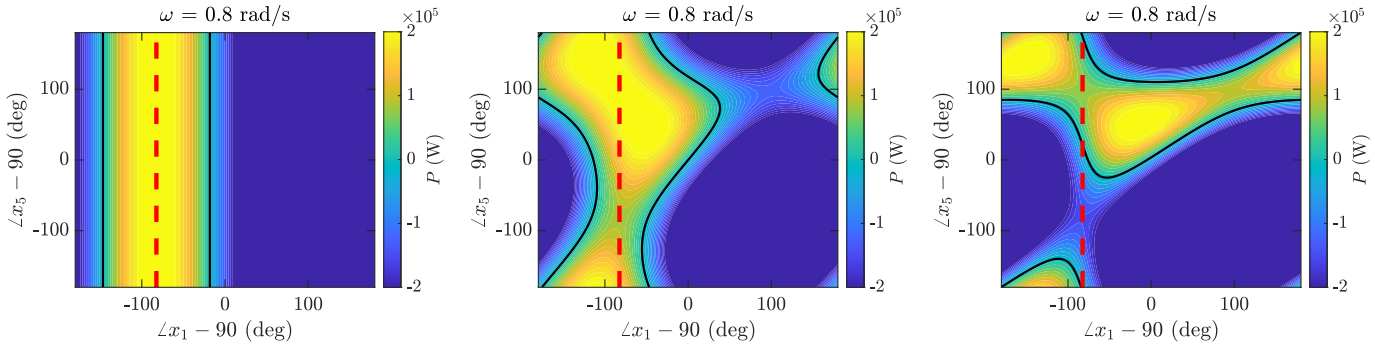

(g) $|x_5| = 0$ deg (h) $|x_5| = 8$ deg (i) $|x_5| = 16$ deg

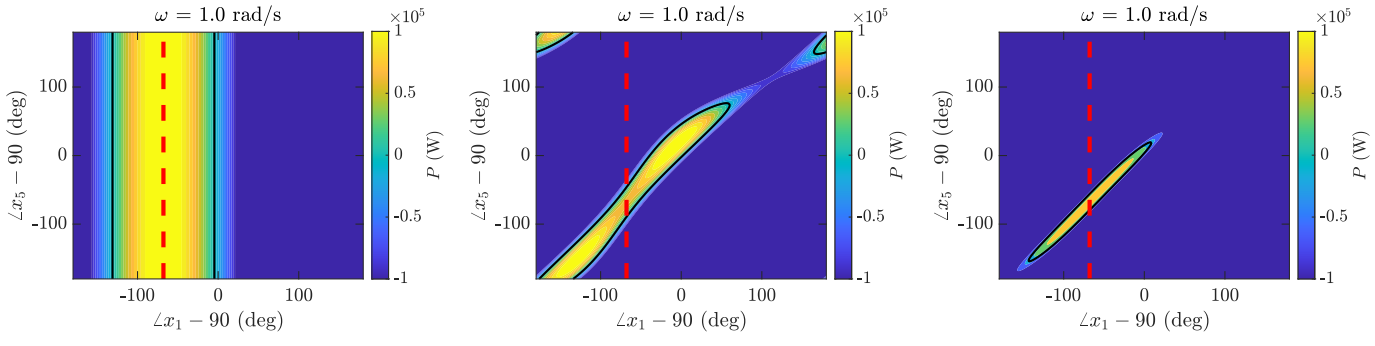

(j) $|x_5| = 0$ deg (k) $|x_5| = 8$ deg (l) $|x_5| = 16$ deg

Figure 4.14: Frequency domain phase plots showing the power available at frequencies ω of (a)-(c) 0.4 rad/s, (d)-(e) 0.6 rad/s, (f)-(h) 0.8 rad/s and (i)-(k) 1.0 rad/s, for different phases of surge and pitch velocity and varying pitch amplitudes. The surge amplitude is constant at each set frequency and pitch amplitude. Wave amplitude is constant at 0.5 m. Areas of positive and negative power are separated by a black line. The dashed red line indicates the phase of the surge excitation force at each frequency. Results show that the phase requirements were clearly higher at high pitch amplitudes and wave frequencies.

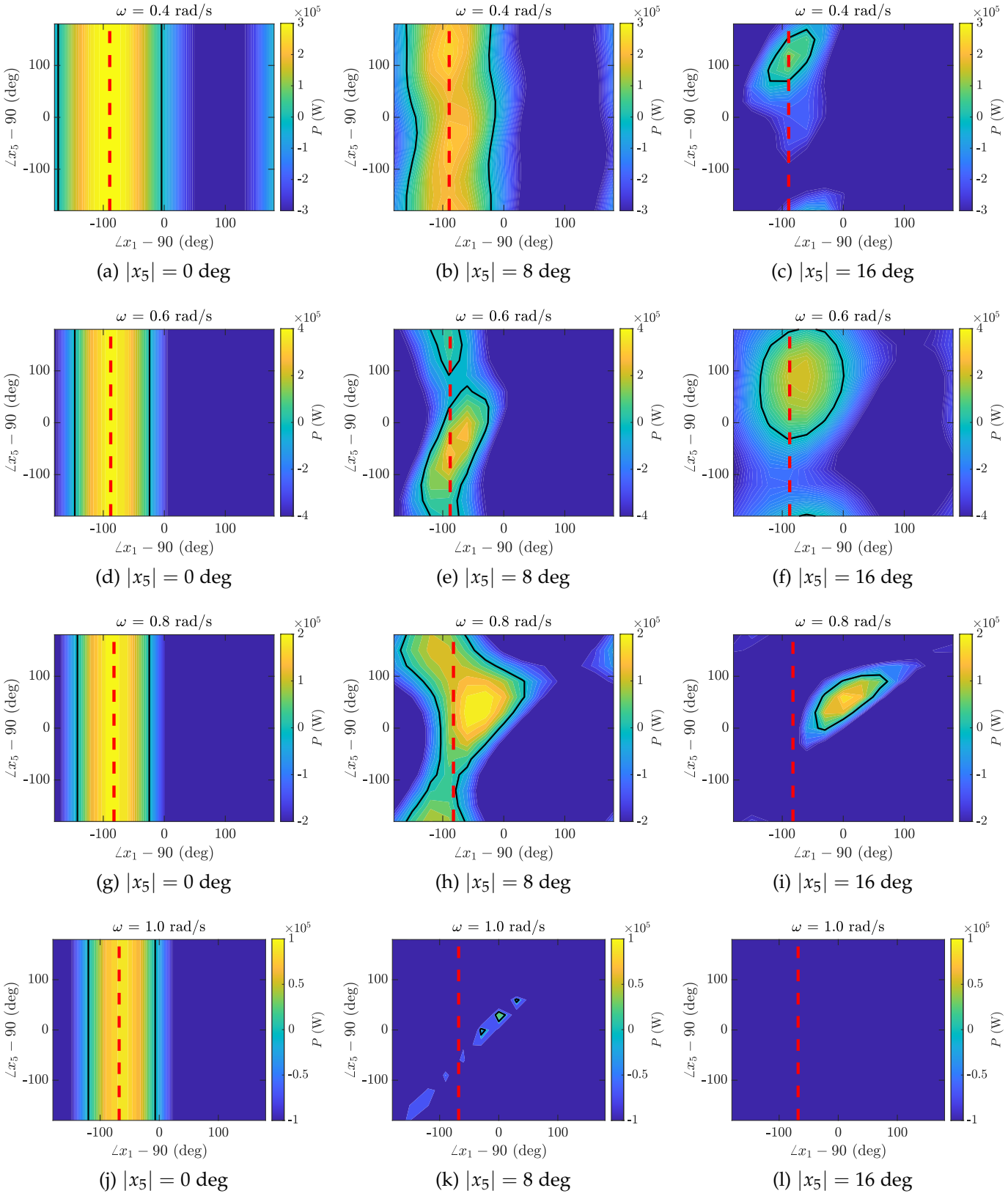

(a) $|x_5| = 0$ deg (b) $|x_5| = 8$ deg (c) $|x_5| = 16$ deg

(d) $|x_5| = 0$ deg (e) $|x_5| = 8$ deg (f) $|x_5| = 16$ deg

(g) $|x_5| = 0$ deg (h) $|x_5| = 8$ deg (i) $|x_5| = 16$ deg

(j) $|x_5| = 0$ deg (k) $|x_5| = 8$ deg (l) $|x_5| = 16$ deg

Figure 4.15: Weak-scatterer phase plots showing the power available at frequencies ω of (a)-(c) 0.4 rad/s, (d)-(e) 0.6 rad/s, (f)-(h) 0.8 rad/s and (i)-(k) 1.0 rad/s, for different phases of surge and pitch velocity and varying pitch amplitudes. The surge amplitude is constant at each set frequency and pitch amplitude. Wave amplitude is constant at 0.5 m. Areas of positive and negative power are separated by a black line. The dashed red line indicates the phase of the surge excitation force at each frequency. Unlike the FD results, it was not possible at all to achieve positive power at high wave frequency and high pitch amplitudes.

required at these frequencies to avoid power losses.

Similar trends were also observed in the phase plots produced from the WS model in Figure 4.15. However, with the inclusion of nonlinear coupling effects, pitch clearly had a much greater impact on the system than what was suggested from the linear model. One of the most noticeable differences between the linear and nonlinear results was the fact that, as pitch amplitude increased, there was a rapid reduction in the operating conditions where positive power could be absorbed. While the linear results seemed to suggest that power could be extracted using a wider range of surge and pitch phases, the nonlinear results showed that in reality, many of these configurations resulted in a net loss of power instead.

Care should therefore be taken since the results from the linear model could potentially be misleading; configurations with positive power absorption in the linear model may actually lead to power losses in the real system. Finer tuning of the surge and pitch phases will be required to avoid dissipating power away from the system when nonlinear hydrodynamic coupling effects are present. Additionally, for the phase plots produced in this study, the wave amplitude was kept constant at 0.5 m; the sensitivity of the system to surge and pitch phase may also change with wave amplitude.

4.6 Effect of pitch on nonlinear hydrodynamics

In this section, the hydrodynamic forces are investigated in more detail in order to find an explanation for the differences observed between the FD and WS results. Particular focus was paid to the total hydrodynamic forces and the radiation forces obtained from the two models. It was not possible to directly obtain the excitation forces for the WEC oscillating simultaneously in surge and pitch, hence these forces were not considered in detail here.

A direct comparison of the total hydrodynamic force signals obtained from the FD and WS models are shown in Figure 4.16. Results for a frequency of $\omega_{\text{exc}} = \omega_1 = \omega_5$ = 0.6 rad/s are shown, since the greatest differences between the two models were observed at this frequency (see Figure 4.8). For each pitch amplitude shown, the WEC was forced at the optimal surge amplitude, surge phase and pitch phase found from Section 4.4.2.

From this comparison, it was seen that hydrodynamic forces from the WS model were clearly nonlinear. These nonlinearities could be observed even without any pitch motions present. Since the surge amplitude required for maximum power at this frequency was quite high ($|x_1| \approx 5$ m), it was not surprising to observe nonlinearities in the WS hydrodynamic force signals.

As the pitch amplitude increased, the amount of nonlinear distortion also increased. At a pitch amplitude of $|x_5|$ = 16°, the nonlinear hydrodynamic force became considerably different to the linear estimation. Apart from the nonlinear distortion, an amplitude and phase difference could be seen between the two signals. This result has significant implications for the control strategy, since the optimality conditions determined from the linear model in Eq. (4.14) will become ineffective and can no longer be applied to the nonlinear system. Overall, the clear mismatch between the linear and nonlinear signals can explain the large difference in power absorbed observed between the two models at this frequency.

The radiation forces could also be directly obtained from the WS model by forcing the WEC to oscillate in the absence of an incident wave. A comparison

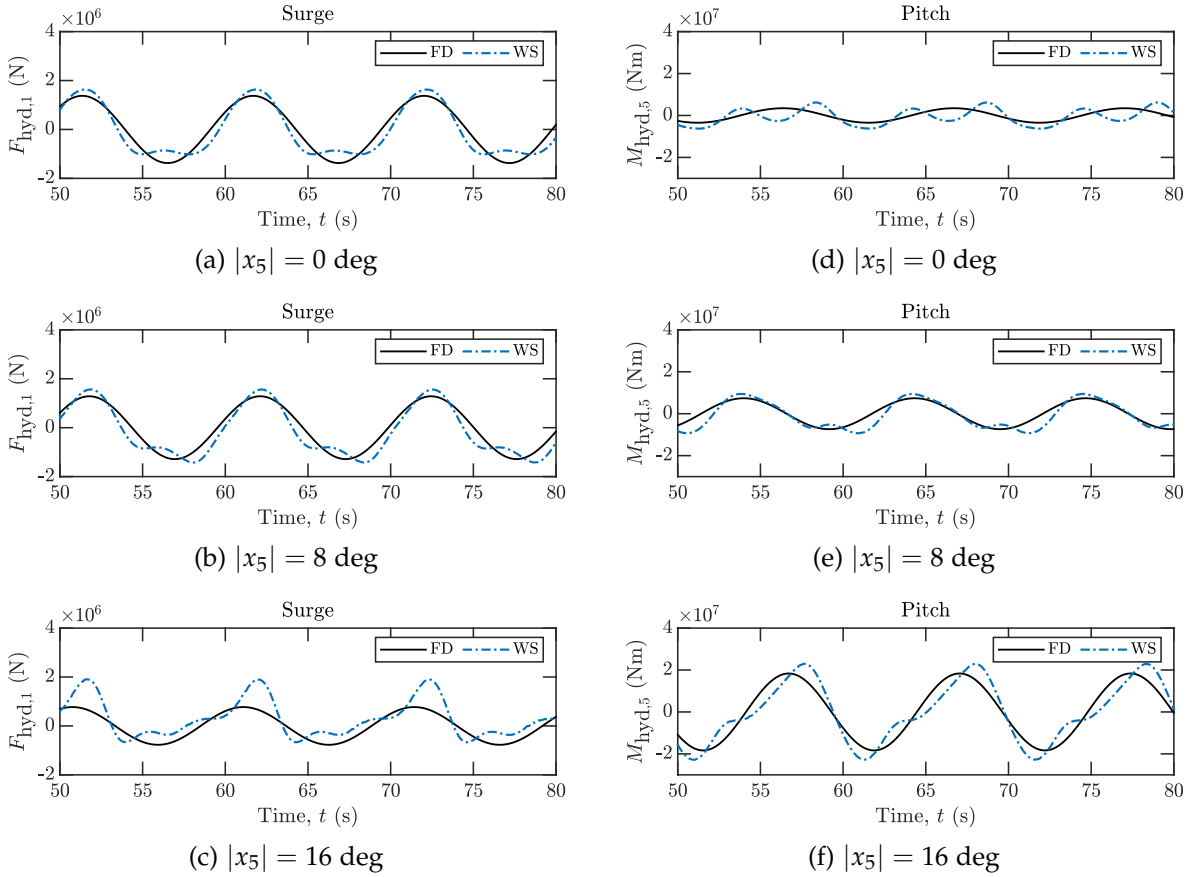

(a) $|x_5| = 0$ deg (d) $|x_5| = 0$ deg

(b) $|x_5| = 8$ deg (e) $|x_5| = 8$ deg

(c) $|x_5| = 16$ deg (f) $|x_5| = 16$ deg

Figure 4.16: Comparison of the total hydrodynamic force time signals from the FD and WS models at different pitch amplitudes, for a set incident and oscillation frequency of ω = 0.6 rad/s. The surge amplitude, surge phase and pitch phase are optimal for each set pitch amplitude shown.

of the radiation forces from the FD and WS models, for a frequency of $\omega_{exc} = \omega_1 = \omega_5$ = 0.6 rad/s, is shown in Figure 4.17. Again, for each pitch amplitude, the WEC was oscillating at the optimal amplitudes and phases found in Section 4.4.2. For the radiation forces, under relatively linear conditions (i.e. when the WEC is only moving in one DOF), there was a good match between the two models. However, as the pitch amplitude increased, the radiation forces from the WS model also experienced an increased degree of nonlinear distortion.

The spectral content of the total hydrodynamic and radiation force signals were then analysed using the in-built MATLAB function *pwelch*. An example of the frequency components and amplitude spectra obtained are shown in Fig. 4.18, corresponding to the surge force time histories shown in

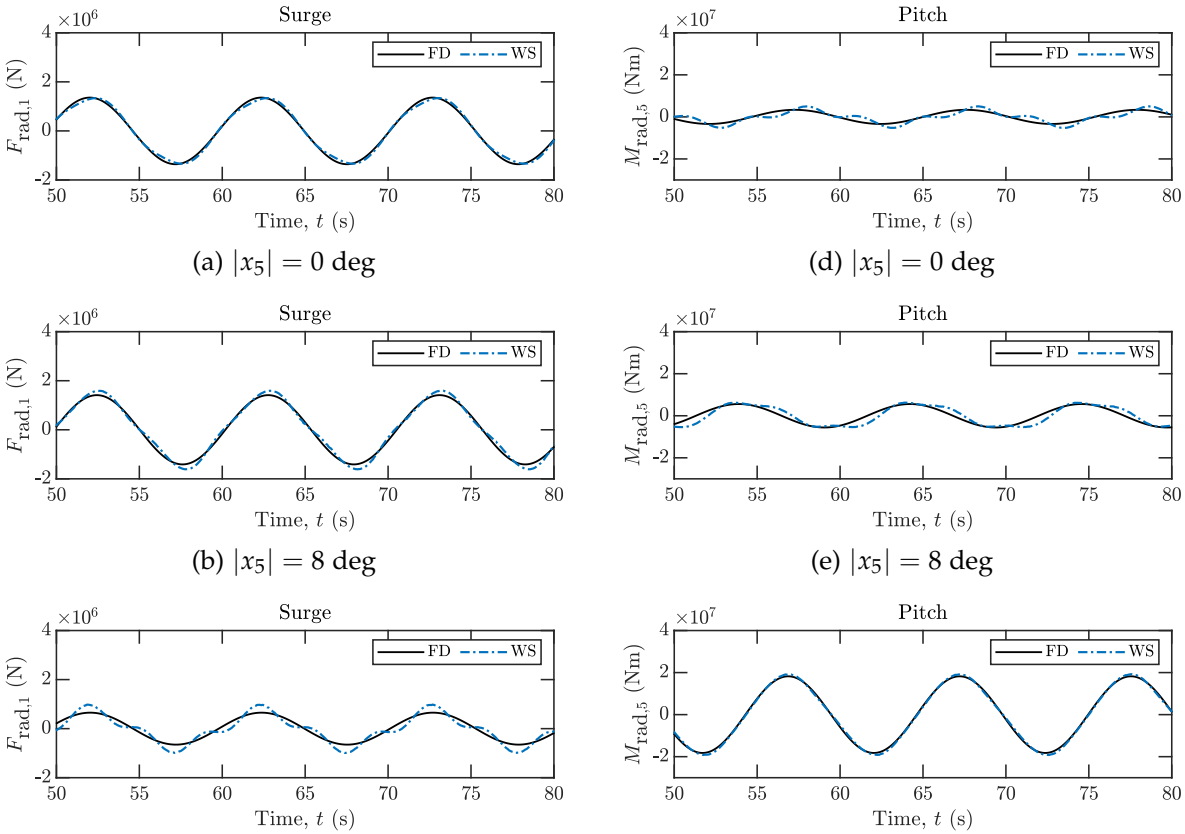

(a) $|x_5| = 0$ deg (d) $|x_5| = 0$ deg

(b) $|x_5| = 8$ deg (e) $|x_5| = 8$ deg

(c) $|x_5| = 16$ deg (f) $|x_5| = 16$ deg

Figure 4.17: Comparison of the radiation force time signals from the FD and WS models at different pitch amplitudes. The frequency of both the surge and pitch oscillations is ω = 0.6 rad/s. The surge amplitude, surge phase and pitch phase are optimal for each set pitch amplitude shown.

Figure 4.16(a)-(c) and Figure 4.17(a)-(c). A flat top window was used in the analysis with a 50% overlap. Note that due to the window type applied and the limited data available for sampling, since long computation times were required for the WS simulations, it was only possible to achieve a relatively low frequency resolution for the amplitude peaks. In spite of this, it could still be clearly seen that the nonlinear distortions in the force signals were caused by the presence of higher-order harmonics. In the results corresponding to the total hydrodynamic forces in Figure 4.18(a), peaks were observed at all higher order harmonics, with decreasing contribution from each subsequent harmonic. The amplitude of each harmonic also varied with pitch amplitude.

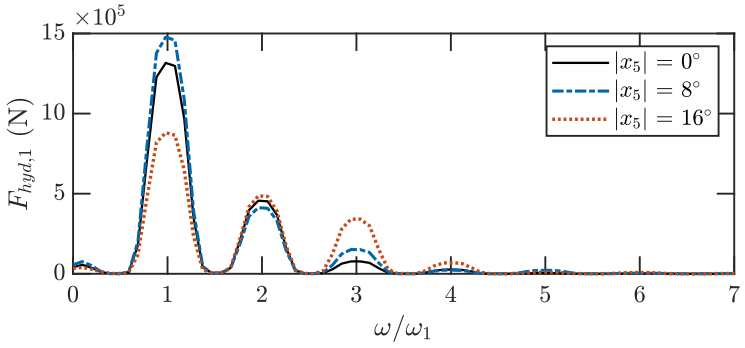

(a)

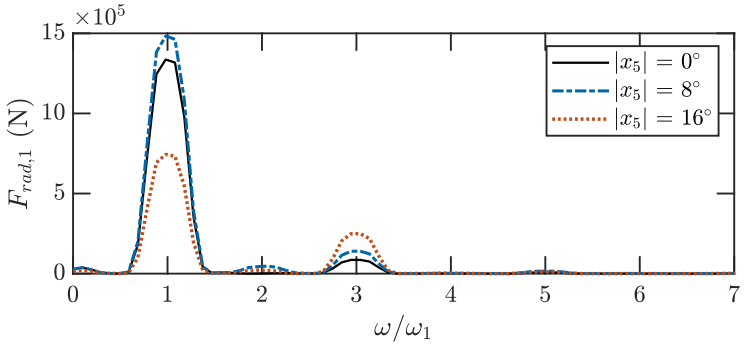

(b)

Figure 4.18: Amplitude spectrum of the surge (a) total hydrodynamic and (b) radiation forces from the WS model for a frequency of ω = 0.6 rad/s. The WEC was oscillating at the optimal surge amplitude, surge phase and pitch phase for each pitch amplitude case shown.

In contrast, from the amplitude spectrum of the radiation forces in Figure 4.18(b), the third-order harmonic appeared to be the most significant component after the fundamental frequency, with other prominent peaks occurring at $(2n+1)\omega$, (n = 0,1,2, ...). Additionally, due to the high surge amplitude at this frequency, slight nonlinearities could also be observed even

when pitch motion was zero. These results seemed to be consistent with the findings reported by Wu [26], who attributed this harmonic behaviour to the asymmetry of the radiated dipole waves created by surging and pitching motions. The prominence of the third harmonic in the radiation force was also different to the results presented for a submerged heaving and pitching cylinder in [11], where the second harmonic was the most significant component instead. Again, the difference can be attributed to the fact that surge motions radiate asymmetric dipole-type waves, while heave motion radiates symmetric source-type waves.

With regards to energy harvesting, despite the strong presence of higher order harmonics in the hydrodynamic forces, the impact of these harmonics on total power absorbed was actually very small. It was found that the first harmonic was responsible for almost all the power absorbed or lost (up to an order of magnitude 3-5 times greater than the subsequent harmonic). This can be explained by the fact that the motion of the device is sinusoidal, and so the first harmonic remains the most important component of the hydrodynamic forces when determining the total amount of power that can be absorbed by the WEC.

Therefore, for energy harvesting purposes, it will be more critical to consider the changes to the fundamental frequency, as a result of the nonlinear pitch-surge coupling. In particular, the amplitude and phase differences observed between the dominant frequency component of the linear and nonlinear pitch hydrodynamic force signals needs to be addressed. These differences suggest a significant mismatch in the force coefficients between the linear and nonlinear cases. Although it was not possible to obtain and directly compare the excitation forces between the two models, the radiation coefficients could still be considered. The analysis and comparison of the radiation force coefficients will therefore be carried out in the consequent section.

4.6.1 Effect of pitch on radiation force

A comparison of the radiation coefficients corresponding to the radiation force obtained in the WS model and those calculated using linear wave theory was then performed. For each set frequency and pitch amplitude, the WEC was forced to oscillate at the corresponding optimal surge amplitude, surge phase and pitch phase, in the absence of an incident wave.

Since maximum power is mainly driven by the first harmonic, the nonlinear radiation forces obtained were first decomposed into their frequency components and only the time-series corresponding to the first harmonic

were used to determine the radiation coefficients.A Fourier transform was performed to extract the required amplitude and phase information from the original nonlinear signal, which was then used to reconstruct the fundamental waveform.

A least mean squares approach was then applied to calculate the radiation coefficients, representing the problem in a form:

$$\mathbf{X}\boldsymbol{\beta} = \mathbf{Y}, \tag{4.15}$$

where

$$\mathbf{X} = \begin{bmatrix} \ddot{x}_1[1] & \ddot{x}_5[1] & \dot{x}_1[1] & \dot{x}_5[1] \\ \ddot{x}_1[2] & \ddot{x}_5[2] & \dot{x}_1[2] & \dot{x}_5[2] \\ \vdots & \vdots & \vdots & \vdots \\ \ddot{x}_1[n] & \ddot{x}_5[n] & \dot{x}_1[n] & \dot{x}_5[n] \end{bmatrix}, \tag{4.16}$$

$$\mathbf{Y} = \begin{bmatrix} F^{(1)}_{rad,1}[1] & M^{(1)}_{rad,5}[1] \\ F^{(1)}_{rad,1}[2] & M^{(1)}_{rad,5}[2] \\ \vdots & \vdots \\ F^{(1)}_{rad,1}[n] & M^{(1)}_{rad,5}[n] \end{bmatrix}, \tag{4.17}$$

and the matrix of unknown radiation coefficients is:

$$\boldsymbol{\beta} = \begin{bmatrix} A_{11} & A_{51} \\ A_{15} & A_{55} \\ B_{11} & B_{51} \\ B_{15} & B_{55} \end{bmatrix}. \tag{4.18}$$

The radiation force coefficients were then computed by minimising the sum of the squared errors between the estimations and the original force signals obtained from the WS model.

The added mass and radiation damping coefficients calculated using the nonlinear results with combined surge-pitch oscillations are shown in Figure 4.19 and 4.20, respectively. Similar to the linear coefficients, it was found that $A_{15} \approx A_{51}$ and $B_{15} \approx B_{51}$; hence only a single graph is illustrated for each of these coupling coefficients.

Initially, at $|x_5| = 0°$, the values from the WS model showed a relatively good match with the linear values obtained from the FD model. However, as the pitch amplitude increased, the values of added mass and radiation damping began to diverge from the values obtained under linear conditions. The coupling terms did not appear to diverge greatly from their linear values. However, some coefficients corresponding to the surge and pitch DOFs

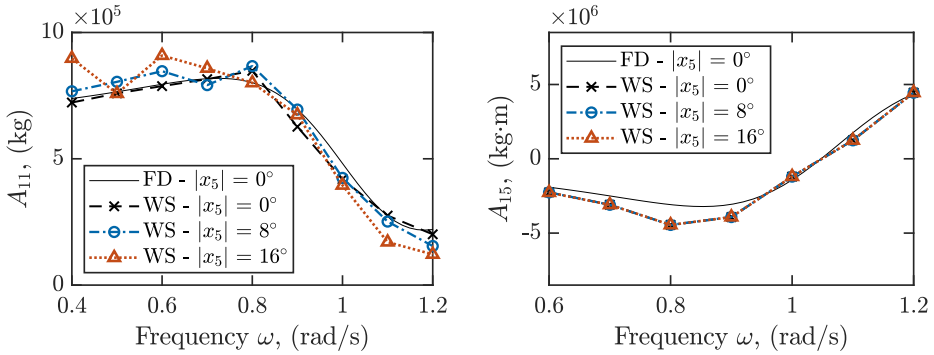

(a) Surge-surge

(b) Surge-pitch

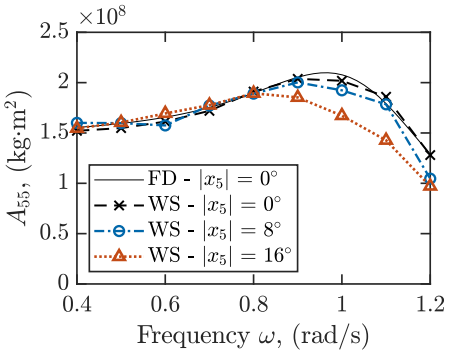

(c) Pitch-pitch

Figure 4.19: Comparison of the added mass coefficients from the FD and WS models, at different pitch amplitudes and incident wave frequencies.

showed notable changes from their expected values, depending on the pitch amplitude.

A noticeable difference was observed for the surge radiation damping values B_{11}, particularly for the case with a pitch amplitude of $|x_5| = 16°$. Focusing on the lower frequencies, where large differences were observed between the FD and WS models, the nonlinear results indicated greater radiation damping in surge than the values obtained from the linear model. This increase in radiation damping explains the reduced power available in surge observed in Figure 4.9(c). In terms of control and optimal WEC motion, the increase in surge damping also explains the large difference in values of optimal surge amplitude seen in Figure 4.11(c). According to Eq. (4.14), an increase in B_{11} corresponds to a reduction in surge motion.

For pitch, noteworthy exceptions were observed for $\omega = 0.5$ and 0.6 rad/s, where the pitch damping term B_{55} was larger than the expected values from linear theory. This increase in radiation damping also appeared to correspond to the losses in pitch power seen in Figure 4.10(b). It was noted previously

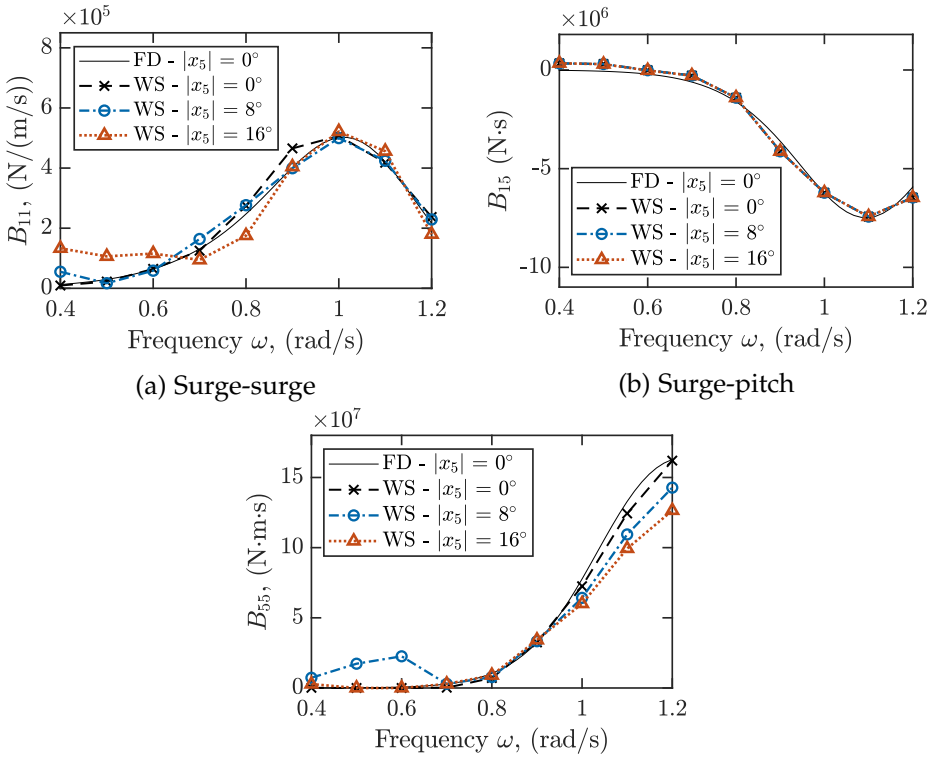

(a) Surge-surge

(b) Surge-pitch

(c) Pitch-pitch

Figure 4.20: Comparison of the radiation damping coefficients from the FD and WS models, at different pitch amplitudes and incident wave frequencies.

in Section 4.5.3 that at these frequencies, the optimal pitch phase did not follow the expected trends as the other cases in Figure 4.13. These results suggest that changes in the radiation coefficients, and subsequently the power absorbed by each individual DOF, were driven by the pitch phase.

Clear differences were also observed for $\omega \geq 1.0$ rad/s in both the pitch added mass A_{55} and radiation damping B_{55} terms as pitch amplitude increased [2]. This may also explain the reduction in total power in the WS results observed in Figure 4.8 at these frequencies.

4.6.2 Effect of harmonics on power

Regarding the contribution of each harmonic to power absorbed, although the higher order harmonics did not have a significant effect on the total power absorbed, they may affect the reactive power required during different parts

[2]The published version of this article incorrectly states that differences were observed for $\omega \leq 1.0$ rad/s. This typographic error has been identified and amended here.

of the power cycle and the quality of the power produced. This is illustrated in Figure 4.21, which compares the instantaneous power over time at different pitch amplitudes. Results are shown for an incident wave frequency of ω = 0.4 rad/s, since the difference in power quality could be seen most clearly for this case.

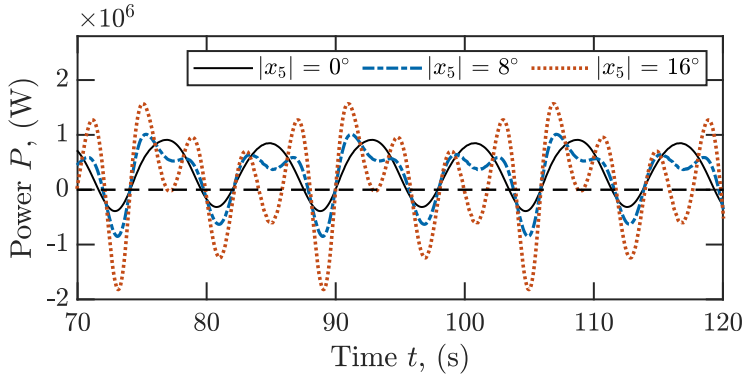

Figure 4.21: Instantaneous power at different pitch amplitudes and for an incident wave frequency of ω = 0.4 rad/s.

The presence of harmonics created by the combined surge and pitching motions may therefore have important practical consequences for the WEC system as a whole. If the power peaks are too large, especially for periods where the power flow is negative, it can introduce unreasonable loads on the power take-off machinery. Furthermore, this power cannot be directly fed into the grid and will need to be smoothed out, potentially reducing the mean useful power that can be delivered by the WEC.

4.7 Discussion

There are a number of uncertainties associated with the analysis used in this paper to assess the performance of the multi-mode WEC system. In this study, it is important to note that the effect of viscous drag forces on the WEC were completely disregarded. Due to the use of kinematic control, in which the WEC was forced to follow an explicitly prescribed motion regardless of external forces, the inclusion of drag forces would not be expected to have a significant impact on the results obtained in this study. Although a reduction in the net power absorbed is possible, the overall effect of nonlinear pitch-surge coupling on the performance of the system should remain largely unaffected, namely a reduction in power absorption efficacy as the pitch oscillation amplitude increases. However, the effect of viscous drag will likely

become an important consideration with regards to the dynamic behaviour of pitch in the actual WEC system, when the kinematic control assumption is removed. In particular, the damping associated with viscous drag is expected to have a major impact on both the pitch amplitude and phase. The inclusion of a viscous drag term will likely reduce the optimal oscillation amplitudes of both surge and pitch, which may in turn lead to a closer match between the results obtained from the linear and nonlinear models. The full impact of nonlinear pitch-surge coupling and the differences between the linear and nonlinear model for the dynamic system will need to be quantified in future work.

The validity of the small perturbation assumption given in Eq. (4.3) for the WS model also needs to be assessed. From the results obtained, obvious discrepancies between the two models occurred mostly for cases involving large displacement amplitudes in both surge and pitch. With these large body motions, the perturbed components of the wave would have been very large, especially in relation to the incident wave. The validity of WS assumption in these cases with large surging and pitching motions will therefore need to be confirmed, especially for when the WEC is oscillating in both DOFs simultaneously. This will require comparisons with fully nonlinear models or experiments.

Additionally, there were several limitations with the optimisation procedure applied, which could have resulted in uncertainties in the final values of optimal surge and pitch amplitude and phase obtained from the WS model. This was especially true for certain frequency and pitch amplitude cases where the results of the optimisation did not exactly follow the expected trend, likely due to the existence of multiple local optima. Due to the long computational times required by the current WS model, there would not be enough time for the optimisation procedure to make the jump from one optima to another and find the global maximum. Hence, there is a need for a simplified model which can sufficiently capture the effect of nonlinear coupling on the hydrodynamic forces while providing faster estimates for the resultant available power. This may allow for a more sophisticated and refined optimisation of the performance of the flat cylindrical WEC considered in this study.

4.8 Conclusion

In this study, the effect of pitch-surge hydrodynamic coupling on the power harvesting capabilities of a submerged flat cylindrical WEC was investigated.

The performance of the WEC oscillating purely in the surge and pitch DOFs, as obtained from both a linear and nonlinear model, was analysed and compared.

Overall, it was apparent that the effect of pitch on the performance of the multi-mode WEC was much larger when nonlinear coupling effects were considered, particularly when compared to the predictions from the linear model. One crucial difference was the fact that, in the linear model, direct control of the pitch DOF itself was not a requirement for maximum power absorption. However, in the nonlinear model, tuning of the pitch phase as well as the surge amplitude and phase was required to absorb the maximum power at each incident wave frequency and pitch amplitude. The inclusion of pitching motions also led to significant reductions in the maximum power from nonlinear model compared to the estimations from the linear model, particularly for frequencies $\omega \leq 0.7$ rad/s and $\omega \geq 1.0$ rad/s. Some differences were also observed regarding the optimal surge amplitudes and phases obtained from the two models, which were more noticeable at lower frequencies where $\omega \leq 0.7$ rad/s. The total power that could be absorbed by the WEC also became more sensitive to surge and pitch phases with the inclusion of nonlinear hydrodynamics.

The differences between the two models could be attributed to changes in the hydrodynamic forces, caused by the nonlinear interactions between surge and pitch. In particular, noticeable changes in both the amplitude and phase of the fundamental frequency component of the hydrodynamic forces were observed when surge and pitch motions were combined. Higher order harmonics were also observed in the nonlinear hydrodynamic forces; although these harmonics did not have a large effect on the overall active power, the impact on the required instantaneous reactive power may have practical implications for the design of the PTO system.

One of the critical assumptions in this work was the ideal and kinematic control of the WEC. Future work should be focused on the dynamic control of a surging and pitching WEC subjected to a nonlinear hydrodynamic forcing. Viscous drag effects, which were neglected in this study, will need to be considered for the dynamically controlled system, especially with regards to the pitch DOF. The work done should also be extended to include nonlinear coupling with the heave DOF as well. The problem of controlling the pitch motion of the WEC in a more realistic and under-actuated system, such as through the use of tethers, will also need to be addressed.

Finally, it may also be worthwhile to investigate the nonlinear hydrodynamic forces caused by the combined pitch-surge motions in more detail, and how to minimise the effect of the superharmonic components on the

performance and efficiency of the WEC. This may require a comparison with fully nonlinear solvers or experiments in order to confirm the validity of the small perturbation assumption used in the WS model for very nonlinear cases involving large surge and pitch displacement amplitudes. If a more simplified model for the calculation of these nonlinear forces can be found, there is also the potential to apply more robust optimisation procedures for the multi-mode WEC considered in this study.

Acknowledgements

The numerical WS_CN model used in this study was developed by École Centrale de Nantes and shared with the University of Adelaide for wave energy harnessing research. The authors would like to thank Pierre-Yves Wuillaume of École Centrale de Nantes for their assistance with getting the WS model running. This work was also supported with supercomputing resources provided by the Phoenix HPC service at the University of Adelaide.

References

[1] Abdelkhalik, O., Zou, S., Robinett, R. D., Bacelli, G., Wilson, D. G., Coe, R. and Korde, U. (2017). "Multiresonant feedback control of a three-degree-of-freedom wave energy converter". In: *IEEE Transactions on Sustainable Energy* 8.4, pp. 1518–1527.

[2] Alves, M. (Jan. 2016). "Frequency-Domain Models". In: *Numerical Modelling of Wave Energy Converters*. Academic Press, pp. 11–30.

[3] Bai, W and Taylor, R. E. (2006). "Higher-order boundary element simulation of fully nonlinear wave radiation by oscillating vertical cylinders". In: *Applied Ocean Research* 28.4, pp. 247–265.

[4] Carnegie Clean Energy (2020). *CETO Technology - Carnegie Clean Energy*. URL: https://www.carnegiece.com/ceto-technology/.

[5] Coe, R., Bacelli, G., Spencer, S. J., Forbush, D. and Dullea, K. (2019). *MASK3 for Advanced WEC Dynamics and Controls*. Tech. rep.

[6] Coe, R. G., Bacelli, G., Wilson, D. G., Abdelkhalik, O., Korde, U. A. and Robinett III, R. D. (2017). "A comparison of control strategies for wave energy converters". In: *International Journal of Marine Energy* 20, pp. 45–63.

[7] Count, B. M. (1980). "Wave power: a problem searching for a solution". In: *Power from sea waves*. Ed. by B. Count. London, England: Academic Press, pp. 11–27.

[8] Ding, B., Wuillaume, P, Meng, F., Babarit, A., Schubert, B., Sergiienko, N. Y. and Cazzolato, B. S. (2019). "Comparison of wave-body interaction modelling methods for the study of reactively controlled point absorber wave energy converter". In: *Proceedings of the 34th International Workshop on Water Waves and Floating Bodies*. Newcastle.

[9] Falnes, J. (2002). *Ocean waves and oscillating systems: Linear interactions including wave-energy extraction*. Cambridge University Press, p. 220.

[10] Falnes, J. and Hals, J. (2012). "Heaving buoys, point absorbers and arrays". In: *Philosophical Transactions of the Royal Society A: Mathematical, Physical and Engineering Sciences* 370.1959, pp. 246–277.

[11] Hannan, M. A., Bai, W and Ang, K. K. (Mar. 2014). "Modeling of fully nonlinear wave radiation by submerged moving structures using the higher order boundary element method". In: *Journal of Marine Science and Application* 13.1, pp. 1–10.

[12] Jiang, S.-C., Gou, Y. and Teng, B. (May 2014a). "Water wave radiation problem by a submerged cylinder". In: *Journal of Engineering Mechanics* 140.5, p. 6014003.

[13] Jiang, S.-C., Gou, Y., Teng, B. and Ning, D.-Z. (Jan. 2014b). "Analytical solution of a wave diffraction problem on a submerged cylinder". In: *Journal of Engineering Mechanics* 140.1, pp. 225–232.

[14] Korde, U. A., Lyu, J., Robinett, R. D., Wilson, D. G., Bacelli, G. and Abdelkhalik, O. (2017). "Constrained near-optimal control of a wave energy converter in three oscillation modes". In: *Applied Ocean Research* 69, pp. 126–137.

[15] Letournel, L., Chauvigné, C., Gelly, B., Babarit, A., Ducrozet, G. and Ferrant, P. (2018). "Weakly nonlinear modeling of submerged wave energy converters". In: *Applied Ocean Research* 75, pp. 201–222.

[16] Letournel, L., Ferrant, P., Babarit, A., Ducrozet, G., Harris, J. C., Benoit, M. and Dombre, E. (June 2014). "Comparison of fully nonlinear and weakly nonlinear potential flow solvers for the study of wave energy converters undergoing large amplitude motions". In: *ASME 2014 33rd International Conference on Ocean, Offshore and Arctic Engineering*. San Francisco, California.

[17] Meng, F., Ding, B., Cazzolato, B. and Arjomandi, M. (Jan. 2019). "Modal analysis of a submerged spherical point absorber with asymmetric mass distribution". In: *Renewable Energy* 130, pp. 223–237.

[18] Mofor, L., Goldsmith, J. and Jones, F. (2014). *Ocean Energy: Technology Readiness, Patents, Deployment Status and Outlook*. Tech. rep. August, p. 76.

[19] Pawlowski, J. S. and Bass, D. W. (1991). *A theoretical and numerical model of ship motions in heavy seas*. Tech. rep.

[20] Payne, G. (Jan. 2008). *Guidance for the experimental tank testing of wave energy converters*. Supergen Marine.

[21] Penalba, M., Giorgi, G. and Ringwood, J. V. (2017). "Mathematical modelling of wave energy converters: A review of nonlinear approaches". In: *Renewable and Sustainable Energy Reviews* 78, pp. 1188–1207.

[22] Ringwood, J. V., Bacelli, G. and Fusco, F. (2014). "Energy-maximizing control of wave-energy converters: The development of control system technology to optimize their operation". In: *IEEE Control Systems* 34.5, pp. 30–55.

[23] Sergiienko, N. Y., Cazzolato, B. S., Arjomandi, M, Ding, B and Silva, L. S. P. da (2019). "Considerations on the control design for a three-tether wave energy converter". In: *Ocean Engineering* 183, pp. 469–477.

[24] Sergiienko, N. Y., Cazzolato, B. S., Ding, B. and Arjomandi, M. (2016). "Three-tether axisymmetric wave energy converter: estimation of energy delivery". In: *Proceedings of the 3rd Asian Wave and Tidal Energy Conference AWTEC*. Singapore: Singapore: Research Publishing, pp. 163–171.

[25] Todalshaug, J. H. (Dec. 2013). "Practical limits to the power that can be captured from ocean waves by oscillating bodies". In: *International Journal of Marine Energy* 3-4, e70–e81.

[26] Wu, G. X. (1993). "Hydrodynamic forces on a submerged circular cylinder undergoing large-amplitude motion". In: *Journal of Fluid Mechanics* 254, 41–58.

[27] Wuillaume, P.-Y. (Jan. 2019). "Numerical simulation of installation operations for offshore wind farms". PhD thesis. École Centrale de Nantes.

[28] Wuillaume, P.-Y., Babarit, A., Rongère, F., Lynch, M., Combourieu, A. and Ferrant, P. (June 2018). "Comparison between experiments and a multibody weakly nonlinear potential flow approach for modelling of marine pperations". In: *ASME 2018 37th International Conference on Offshore Mechanics and Arctic Engineering*. Madrid, Spain.

[29] Yavuz, H. (July 2011). "On control of a pitching and surging wave energy converter". In: *International Journal of Green Energy* 8.5, pp. 555–584.

[30] Zhou, B. Z., Ning, D. Z., Teng, B and Bai, W (2013). "Numerical investigation of wave radiation by a vertical cylinder using a fully nonlinear HOBEM". In: *Ocean Engineering* 70, pp. 1–13.

Chapter 5

Tuning of resonance frequencies in multi-mode WECs subjected to nonlinear hydrodynamics

In the previous chapter, it was found that nonlinear hydrodynamic interactions between the surge and pitch modes can significantly diminish the power absorbed by a flat cylindrical multi-mode WEC. Reducing the effect of this nonlinear coupling required either decreasing the pitch amplitude or adjusting its phase relative to surge where possible. However, while this is easily achievable in an idealised and kinematically controlled system where the WEC motions can be explicitly defined, control of the pitch mode may be more difficult to realise in practise when coupled to the power takeoffs.

In this chapter, the kinematic control assumption is therefore replaced with independent spring-damper control in each of the three degrees-of-freedom, as shown in Figure 1.2(b). The analysis is also expanded to include nonlinear hydrodynamic interactions with the heave mode as well as viscous drag effects, which were omitted in the study presented in Chapter 4. The resonance behaviour of the coupled hydrodynamic modes is then examined in order to investigate the following research question: *How should the surge, heave and pitch hydrodynamic modes be tuned to enhance the performance of multi-mode WECs subjected to nonlinear coupling forces?*

To study the multi-mode WEC device in this chapter, the fully linearised and WS numerical models developed in Chapter 4 are modified to include PTO control forces in each of the surge, heave and pitch modes. Since the control is independent in each mode, the only source of coupling between modes in this case is through the hydrodynamic forces and interactions. This allows the analysis in this chapter to focus on the effect of this hydrodynamic

coupling without the interference of additional tether or mooring forces (which will later be explored in Chapter 6). The results of this study can therefore be applied to any general multi-mode WEC, rather than being limited to a specific design itself.

This chapter consists of the published journal article:
Tran, N., Sergiienko, N. Y., Cazzolato, B. S., Ding, B., Wuillaume, P.-Y., Ghayesh, M. H. and Arjomandi, M. (2021). "On the importance of nonlinear hydrodynamics and resonance frequencies on power production in multi-mode WECs". In: *Applied Ocean Research* 117, p. 102924

The article in its published format is available at `https://doi.org/10.1016/j.apor.2021.102924`.

Statement of Authorship

Title of Paper	On the importance of nonlinear hydrodynamics and resonance frequencies on power production in multi-mode WECs
Publication Status	☑ Published ☐ Accepted for Publication ☐ Submitted for Publication ☐ Unpublished and Unsubmitted work written in manuscript style
Publication Details	Tran, N., Sergiienko, N. Y., Cazzolato, B. S., Ding, B., Wuillaume, P.-Y., Ghayesh, M. H. and Arjomandi, M. (2021). "On the importance of nonlinear hydrodynamics and resonance frequencies on power production in multi-mode WECs". In: *Applied Ocean Research* 117, p. 102924

Principal Author

Name of Principal Author (Candidate)	Ngan Tran
Contribution to the Paper	Developed ideas and concepts, conducted literature review Performed modelling • Developed weak-scatterer (WS) model of the multi-mode WEC with spring-damper control using WS_CN code • Developed fully linearised model of the system based on hydrodynamic parameters obtained using potential flow solver NEMOH • Conducted convergence tests and comparisons with linear model to verify WS model in linear conditions with small wave amplitudes and body motions • Performed simulations with varying surge, pitch and heave natural frequencies in regular waves using both the linear and WS models Analysed results • Collected and stored data from simulations • Post processed data using Matlab • Used simulation results to generate trajectory plots to visualise WEC motion • Used simulation results to perform irregular wave calculations and estimate WEC broadband power absorption • Analysed and compared results between the linear and WS models • Generated plots and tables to compare results between models Writing • Wrote first full draft of manuscript • Applied comments and feedback provided by co-authors • Acted as corresponding author • Revised manuscript following review
Overall percentage (%)	85%
Certification:	This paper reports on original research I conducted during the period of my Higher Degree by Research candidature and is not subject to any obligations or contractual agreements with a third party that would constrain its inclusion in this thesis. I am the primary author of this paper.
Signature	Date 01/12/21

Co-Author Contributions

By signing the Statement of Authorship, each author certifies that:

i. the candidate's stated contribution to the publication is accurate (as detailed above);

ii. permission is granted for the candidate in include the publication in the thesis; and

iii. the sum of all co-author contributions is equal to 100% less the candidate's stated contribution.

Name of Co-Author	Natallia Y. Sergilenko		
Contribution to the Paper	Supervised the work, participated in developing ideas and concepts, shaped research and direction of manuscript, helped analyse and interpret results, provided revision of manuscript		
Signature		Date	07/12/21

Name of Co-Author	Benjamin S. Cazzolato		
Contribution to the Paper	Supervised the work, participated in developing ideas and concepts, shaped research and direction of manuscript, helped analyse and interpret results, provided revision of manuscript		
Signature		Date	01/12/21

Name of Co-Author	Boyin Ding		
Contribution to the Paper	Provided expertise and advice on numerical model used in the work, discussed results, provided revision of manuscript		
Signature		Date	08/12/2021

Name of Co-Author	Pierre-Yves Wuillaume		
Contribution to the Paper	Provided expertise and advice on numerical model used in the work, helped with verification of WS model, discussed results, provided revision of manuscript		
Signature		Date	07/12/21

Name of Co-Author	Mergen H. Ghayesh		
Contribution to the Paper	Supervised work, provided revision of manuscript		
Signature		Date	22/12/2021

Name of Co-Author	Maziar Arjomandi		
Contribution to the Paper	Supervised work, provided revision of manuscript		
Signature		Date	7/12/2021

On the importance of nonlinear hydrodynamics and resonance frequencies on power production in multi-mode WECs

N. Tran, N. Y. Sergiienko, B. S. Cazzolato, B. Ding, P-Y. Wuillaume, M.H. Ghayesh, M. Arjomandi

Abstract

Multi-mode Wave Energy Converters (WECs) are able to harvest energy from multiple Degrees-of-Freedom (DOFs) simultaneously, which increases the power that can be absorbed from the incident wave compared to single-DOF WECs. However, nonlinear coupling between hydrodynamic modes, which occurs when the WEC oscillates simultaneously in multiple directions, means that simply applying the typical control strategies used for single-DOF WECs can lead to sub-optimal performance. This study investigates the multi-DOF dynamic control of a submerged, flat cylindrical WEC subjected to hydrodynamic coupling effects modelled under the weakly nonlinear potential flow theory based on the weak-scatterer approximation. Results show that, at low incident wave frequencies, tuning the surge, heave and pitch modes of the WEC to the same natural frequency can result in power losses of up to 30% in the weakly nonlinear model compared to results obtained from a fully linear model. These discrepancies are attributed to the pitching motions of the WEC, which changes the projected surface area of the device relative to the equilibrium position and hence violates the assumptions of the linear theory. From these findings, a suggested design strategy where the surge, heave and pitch DOFs were all decoupled and tuned to different natural frequencies was therefore proposed. In the presence of weakly nonlinear hydrodynamic coupling, it was found that this design may result in significant improvements in power absorbed for the multi-mode WEC, compared to a case where all DOFs are simply tuned to match the peak frequency of a given sea state.

5.1 Introduction

Wave energy is an attractive source of renewable power due to its high energy density and predictable variability properties [26]. Although many Wave Energy Converters (WECs) have been proposed to date, there is still no convergence on the best design. Almost 80% of existing designs can be

classified as oscillating bodies, making this the most common WEC concept [21]. However, many of these devices are designed to operate in heave only, which in the case of axisymmetric bodies theoretically limits the amount of power that can be absorbed to only one third of what is possible from the incoming wave [10].

An emerging subset of this category are multi-mode WECs which are capable of harvesting energy from multiple Degrees-of-Freedom (DOFs), thereby increasing the amount of power that can be absorbed from the incident wave compared to a single DOF converter [20]. In the context of this paper, the term '*multi-mode converter*' refers to devices that can use multiple hydrodynamic modes (i.e., surge, heave or pitch) simultaneously to absorb power. This is distinct from other WECs which, despite being able to move in multiple directions or having more than one rigid body mode, still absorb wave power predominantly from only one hydrodynamic mode (e.g. heave).

One of the key challenges for multi-mode WECs is the design of the controller. For a device operating in one DOF only, the amplitude and phase optimality conditions required to absorb the maximum power from incident waves is well known and understood [10]. However, in the case of a multi-mode device, strong hydrodynamic coupling between DOFs can affect these optimality conditions. If this coupling is not taken into account, the performance of the device can be drastically compromised. This was shown by [27] for a multi-mode, three-tethered submerged WEC. In the study, a Multiple-Input Multiple-Output (MIMO) controller was designed to optimise the heave and surge DOFs. However, the hydrodynamic coupling with the pitch DOF was neglected in the design of the controller, leading to losses in the pitch DOF of up to 15% of the total power.

Given that most WEC devices are designed to operate predominantly in one DOF only, the existing literature on the control of multi-mode WECs is comparatively limited [6]. An early study by [36] involving a floating WEC suggested that the performance of the device could be improved with the addition of coupling effects between the surge and pitch modes, especially if active control was applied. In contrast, in a later study [1] suggested to only use either the surge or pitch DOF for energy harvesting, in order to reduce the number of required actuators for a three-DOF floating WEC. Instead, the authors proposed shifting the energy from one coupled DOF to the other to maintain roughly the same magnitude of power absorbed compared to when both the surge and pitch DOFs were active simultaneously. Control of heave, surge and pitch for a floating multi-mode WEC was also considered by [16]; however, in this case, the effect of surge and pitch on the total power absorbed was relatively minimal due to the small size of the buoy used in

the study. Experimental testing of a MIMO controller for a floating 3-DOF WEC in a more realistic ocean environment has also been conducted by [5], where coupling between surge and pitch was also considered in the controller design. However, the relative impact of this coupling on performance was not examined.

Another aspect of multi-mode WEC design that is not well understood is the effects of nonlinear coupling between multiple hydrodynamic modes on performance. A recent study by [31] considered the effect of nonlinear pitch-surge hydrodynamic coupling on the behaviour of a submerged cylindrical WEC. The results of the study showed that the nonlinear loads caused by combined surge and pitch oscillations resulted in large losses in power when compared to estimates provided by the linear model, especially when oscillation amplitudes were large. However, one of the main assumptions was the kinematic control of multi-mode WEC, meaning that amplitudes and phases of both the surge and pitch were directly controlled with no controller impedance taken into consideration. It was uncertain whether this nonlinear pitch-surge coupling would have the same effect in a more realistic case when the kinematic control is replaced by dynamic control. Nonlinear effects caused by heaving motions on the power absorbed by the multi-mode WEC were also not considered. Although nonlinear hydrodynamic forces on a submerged cylinder caused by heave-pitch coupling have been reported previously [12], the impact of this interaction on the power that can be absorbed by multi-mode WECs has not been determined.

The current work aims to develop understanding of how the surge, heave and pitch DOFs in a submerged multi-mode WEC, featuring a flat cylindrical buoy, should be designed and tuned when nonlinear coupling between hydrodynamic modes is present. While the relatively flat cylindrical design has been reported to provide better performance with regards to the cost of electricity associated with the Power Take-Off (PTO) forces and actuation [29], the shape also means that the pitch DOF can have a much stronger influence on the behaviour of the device compared to other WEC geometries. It is often difficult to completely constrain the pitch DOF in practice; therefore, in order to minimise the potential power losses, the control of surge, heave and pitch DOFs must be considered simultaneously. Alternatively, if the controller can be properly designed, it may even be possible to utilise the pitch DOF to further enhance the power absorption of the system.

In practice, dynamic control of all three DOFs can be achieved through various mechanisms, such as through the use of tethers. However, in the current work, independent spring-damper control of each DOF was considered to provide a more generalised study of a multi-mode system, rather than

focusing on the dynamics specific to real-life mechanisms used to control WECs. Although similar multi-mode, spring damper systems have been previously investigated [1, 5, 36], the unique contribution of this work is the focus on the effects of pitch and nonlinear hydrodynamic coupling on the WEC performance and controller design. Detailed examinations of the physical causes of these nonlinearities, such as trapped modes or wave breaking, were considered outside the scope of this work.

The paper is organised as follows. A description of the planar WEC system considered in this study is given in Section 5.2. The underlying theory and equations used in the numerical models are presented in Section 5.3. To provide a basis for comparison, the expected behaviour of the multi-mode WEC based on linear theory alone is first discussed in Section 5.4. This is followed by Section 5.5, where the performance of the WEC with nonlinear coupling effects is investigated. Based on this analysis, recommendations for potential multi-mode WEC design strategies are explored in Section 5.6.

5.2 System description

In this study, a multi-mode WEC featuring a fully submerged flat cylindrical buoy was considered. The WEC is inspired by Carnegie Clean Energy's CETO-6 device [4], which is a submerged multi-mode quasi-point absorber with a three-tether mooring configuration. This design allows the device to effectively generate power from surge, heave and pitch motions simultaneously. However, to simplify and generalise the design problem in this study, the PTO system used to control each DOF was modelled as an independent linear spring-damper system. The parameters of the WEC are given in Table 5.1, which are based on values previously proposed by Carnegie Clean Energy for the actual full scale CETO-6 device [24]. A schematic of the WEC system is shown in Fig. 5.1(a). As illustrated in Fig. 5.1(b), due to the flat shape of the WEC, pitching motions change the instantaneous projected surface area of the buoy $S_B(t)$ relative to its nominal projected surface area $S_{B,0}$. This affects

Table 5.1: Buoy parameters.

Parameter	Notation	Value
Radius	a	12.5 m
Height	H	5 m
Mass	m	1.99×10^6 kg
Water depth	d	30 m
Submergence depth	d_s	6.5 m

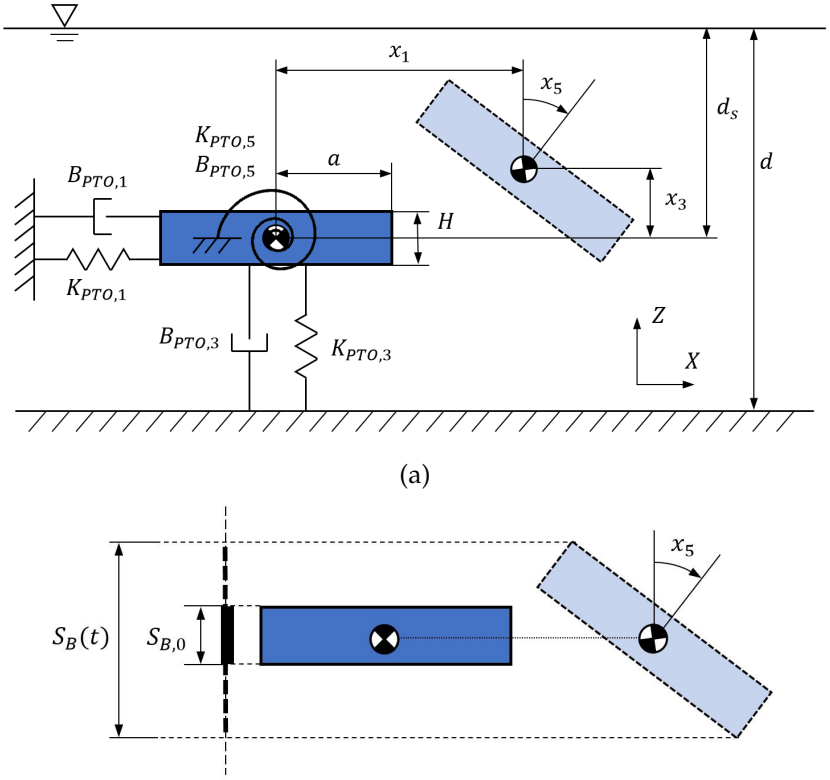

Figure 5.1: (a) Schematic of the flat cylindrical buoy with independent dynamic control of the surge, heave and pitch DOFs. Not to scale. (b) Pitching motions of the flat cylindrical buoy will also change the projected area, leading to enhanced hydrodynamic coupling.

the instantaneous hydrodynamic forces acting on the buoy in both surge and heave, leading to further nonlinear coupling between DOFs.

For simplicity, only motions in the xz-plane were considered. It was also assumed that the buoy was excited by linear, monochromatic plane waves travelling purely in the positive X-direction. Viscous drag effects on the power absorbed by the multi-mode WEC were also considered in this study. However, nonlinearities associated with wave breaking and surface piercing were not modelled, assuming that the buoy operates under normal power generation mode. Hence, a relatively deep submergence depth of d_s = 6.5 m was used in the analysis to prevent the WEC from breaking the free-surface, and to allow a better comparison with the study previously conducted by [31].

5.3 Equations of motion

Assuming an incident wave travelling along the positive X-direction, the planar motion equation describing the dynamic motion of the WEC in surge, heave and pitch can be written as:

$$\mathbf{M}\ddot{\mathbf{x}}(t) = \mathbf{F}_{\text{buoy}}(t) + \mathbf{F}_{\text{PTO}}(t) + \mathbf{F}_{\text{visc}}(t) + \mathbf{F}_{\text{hyd}}(t), \tag{5.1}$$

where $\mathbf{M}$ is the mass matrix and $\ddot{\mathbf{x}} = [\ddot{x}_1 \ \ddot{x}_3 \ \ddot{x}_5]^\mathsf{T}$ is the acceleration at the centre of gravity of the buoy. The main forces acting on the buoy, $\mathbf{F}_{\text{buoy}}$, $\mathbf{F}_{\text{PTO}}$, $\mathbf{F}_{\text{visc}}$ and $\mathbf{F}_{\text{hyd}}$ are the buoyancy, PTO, viscous and hydrodynamic (excitation and radiation) forces, respectively.

For a fully submerged WEC, the buoyancy force is given by:

$$\mathbf{F}_{\text{buoy}}(t) = \begin{bmatrix} 0 & (\rho V - m)g & 0 \end{bmatrix}^\mathsf{T}, \tag{5.2}$$

where ρ is the density of water, V and m are the volume and mass of the buoy, respectively, and g is the acceleration due to gravity. The buoy is positively buoyant, with the PTO unit providing the tension required to keep the device fully submerged.

The PTO system is modelled as:

$$\mathbf{F}_{\text{PTO}} = \mathbf{C}_{\text{PTO}} - \mathbf{B}_{\text{PTO}}\dot{\mathbf{x}} - \mathbf{K}_{\text{PTO}}\mathbf{x}, \tag{5.3}$$

where $\mathbf{B}_{\text{PTO}}$ and $\mathbf{K}_{\text{PTO}}$ are diagonal matrices that include the damping and stiffness coefficients, respectively, of the PTO system in each DOF. The term $\mathbf{C}_{\text{PTO}}$ is a constant force that counteracts the buoyancy force experienced by the WEC in an undisturbed position, given by:

$$\mathbf{C}_{\text{PTO}} = \begin{bmatrix} 0 & -(\rho V - m)g & 0 \end{bmatrix}^\mathsf{T}. \tag{5.4}$$

The viscous drag force can be modelled based on the Morison equation [22]:

$$\mathbf{F}_{\text{visc}} = \begin{bmatrix} -\frac{1}{2}\rho C_{Dx} A_x |\dot{x}_1 - \dot{x}_{f,1}|(\dot{x}_1 - \dot{x}_{f,1}) \\ -\frac{1}{2}\rho C_{Dz} A_z |\dot{x}_3 - \dot{x}_{f,3}|(\dot{x}_3 - \dot{x}_{f,3}) \\ -\frac{1}{2}\rho C_{Dxz} D^4 D |\dot{x}_5| \dot{x}_5 \end{bmatrix}, \tag{5.5}$$

where C_{Dx}, C_{Dz}, C_{Dxz} are the viscous drag coefficients in surge, heave and pitch, respectively. A_x and A_z denote the cross-sectional areas of the buoy in surge and heave, respectively, while D is the diameter of the buoy. The fluid particle velocity in surge and heave at the position of the geometric centre of the buoy is denoted as $\dot{x}_{f,1}$ and $\dot{x}_{f,3}$, respectively. Drag coefficients

of $C_{Dx} = 1$, $C_{Dz} = 1.2$ and $C_{Dxz} = 0.2$ were used for the cylinder in this study, as taken from [13]. The viscous drag forces were calculated assuming fixed cross-sectional areas in each DOF.

In the linear Frequency Domain (FD) model, the nonlinear quadratic terms in Eq. (5.5) were approximated using a Lorentz linearisation approach [30], which has been previously applied in the case of WECs in [11, 20]. The viscous drag forces in the FD model can therefore alternatively be modelled as:

$$\hat{\mathbf{F}}_{\text{visc}}(\omega) = -\mathbf{B}_{\text{visc}}(\omega)\hat{\mathbf{u}}(\omega)\,, \tag{5.6}$$

where ^ denotes the complex amplitude, ω is the wave frequency, $\hat{\mathbf{u}}$ is the velocity of the buoy in the frequency domain and $\mathbf{B}_{\text{visc}}$ is the matrix containing the linearised viscous damping coefficients.

5.3.1 Hydrodynamic modelling

In this study, the hydrodynamic loads on the multi-mode WEC were determined using two potential flow models: (i) a linear FD model based on analytical equations [14, 15] and (ii) in the time domain, a weakly nonlinear potential flow model based on the Weak-Scatterer (WS) approximation [23], developed by École Centrale de Nantes (ECN) [17]. Justification for the use of these modelling techniques was provided previously in [31]; only the main details and assumptions of each modelling theory will be briefly discussed here.

From potential flow theory, assuming an irrotational, incompressible and inviscid fluid, there is a velocity potential ϕ that can be used to compute the velocity of the flow. For linear analysis, the velocity potential is decomposed into several components [2]:

$$\phi = \phi_i + \phi_d + \phi_r\,, \tag{5.7}$$

where ϕ_i, ϕ_d and ϕ_r are the incident, diffraction and radiation components, respectively. The incident and diffraction components are considered together to determine the total excitation force, $\mathbf{F}_{\text{exc}}$. The radiation component can be expressed in terms of an added mass $\mathbf{A}_{\text{rad}}$ and radiation damping $\mathbf{B}_{\text{rad}}$ matrix of coefficients. In the linear FD model, these values are only calculated about the equilibrium position of the WEC. Values of the linear excitation force and radiation coefficients for the submerged cylindrical WEC used in this study are given in Appendix A.

In the WS approximation, the velocity potential is decomposed into incident ϕ_i and perturbed ϕ_p components instead. The perturbed component

consists of radiation and diffraction effects, and is assumed to be relatively small compared to the incident component [23]:

$$\begin{cases} \phi = \phi_i + \phi_p \\ \phi_p = \mathcal{O}(\phi_i)\,. \end{cases} \tag{5.8}$$

The incident component of the wave is explicitly specified as a model input, while only the perturbed components need to be solved in the boundary value problem. The total hydrodynamic forces are then obtained by integrating the pressure of the surrounding fluid over the instantaneous wetted surface of the body $S_B(t)$. More detail about the modelling theory and assumptions of the WS model are presented in [17, 34, 35], while a more detailed comparison of the key differences between the WS, linear potential flow and CFD models with regards to the computation of hydrodynamics for WEC applications are presented in [8].

The analytical equations used for the linear FD model have been previously validated by comparison with published results from a higher-order boundary element method [14, 15]. The numerical WS model developed by ECN has also been previously validated against other available linear, weakly-nonlinear and fully nonlinear hydrodynamic models [33], as well as with experimental data [32]. This same validated WS code has been used in this study.

For the specific multi-mode case considered in this paper, the weakly nonlinear WS was further verified against the FD model by comparing solutions for a linear case with a small wave amplitude of 0.01 m. Mesh and time step convergences were checked, resulting in a good match between the two models for this verification case. It was found that the two most important simulation parameters were: (1) the size of the free-surface mesh directly above the cylinder, which affected displacement offsets, and (2) the time step which affected the accuracy of the motion and force amplitudes. A value of $\Delta dx = \lambda/250$ was used in the WS model for the characteristic dimension of the free-surface mesh, where λ is the wavelength of the incoming wave. For the time step, a value of $\Delta t = T/300$ was used, where T is the period of the incident wave. The cylindrical body was meshed using approximately 4000 panels, while 2800 to 3200 panels were used for the free-surface mesh depending on the incident wavelength.

5.3.2 Power absorbed

The instantaneous power absorbed by the WEC can be calculated by considering the PTO forces and the velocity of the buoy:

$$P = \mathbf{F}_{\mathrm{PTO}}^{\mathsf{T}} \dot{\mathbf{x}} \,. \tag{5.9}$$

In the FD model, Eq. (5.9) can be re-written to give the time-averaged power absorbed by the WEC [10]:

$$\overline{P} = \frac{1}{2} \hat{\mathbf{u}}^{*} \mathbf{B}_{\mathrm{PTO}} \hat{\mathbf{u}} \,. \tag{5.10}$$

where * refers to the complex conjugate transpose.

In the WS model and in regular waves, the average total power from surge, heave and pitch over each cycle is given by:

$$\overline{P} = \frac{1}{T} \int_0^T \mathbf{F}_{\mathrm{pto}}^{\mathsf{T}}(t) \dot{\mathbf{x}}(t) \mathrm{d}t, \tag{5.11}$$

where T is the time period of one complete oscillation cycle.

5.4 WEC performance according to linear theory

From linear theory, it is understood that a WEC operating predominantly in one DOF should be tuned according to the complex conjugate control criteria in order to achieve maximum power absorption from incident waves [10]. This requires the velocity of the buoy to have the same phase as the excitation force, as well as the correct amplitude relative to the incident wave. If these conditions are met, for a single body oscillating in one DOF and assuming no motion constraints, the maximum power that can be absorbed by the WEC is [10]:

$$P_{\max} = \frac{1}{4} \hat{F}_{\mathrm{exc},j}^{*} \hat{u}_{\mathrm{opt},j} = \frac{1}{2} \hat{u}_{\mathrm{opt},j}^{*} B_{\mathrm{tot},j} \hat{u}_{\mathrm{opt},j} \,, \tag{5.12}$$

where j indicates the hydrodynamic mode of power absorption and the total damping in that mode is $B_{\mathrm{tot},j} = B_{\mathrm{rad},jj} + B_{\mathrm{visc},jj}$. The following condition must therefore be met:

$$B_{\mathrm{tot},j} \hat{u}_{\mathrm{opt},j} = \frac{1}{2} \hat{F}_{\mathrm{exc},j} \,. \tag{5.13}$$

For a body operating in one DOF only, the optimal velocity can then be determined using the following equation:

$$\hat{u}_{\mathrm{opt},j}(\omega) = \frac{\hat{F}_{\mathrm{exc},j}(\omega)}{2(B_{\mathrm{rad},jj}(\omega) + B_{\mathrm{visc},jj}(\omega))} \,. \tag{5.14}$$

Assuming a spring-damper control strategy, the optimal PTO damping and stiffness parameters required to achieve this condition at a given frequency are [28]:

$$B_{\mathrm{PTO},j} = B_{\mathrm{rad},jj}(\omega) + B_{\mathrm{visc},jj}(\omega)\,, \tag{5.15a}$$

$$K_{\mathrm{PTO},j} = \omega^2(m + A_{\mathrm{rad},jj}(\omega))\,. \tag{5.15b}$$

However, due to hydrodynamic coupling, the condition in Eq. (5.14) and Eq. (5.15) changes when both surge and pitch motions are combined. The optimal settings in surge become dependent on the motion in pitch, and vice versa. This relationship can be explained physically by the fact that both surge and pitch motions radiate dipole-type waves. To absorb maximum power, the WEC must radiate waves to interfere destructively with the incident wave [10]. If the body is pitching and radiating waves arbitrarily, the surge motion needs to be adjusted accordingly to ensure that the total dipole-type wave radiated by the WEC still interferes optimally with the incident wave.

To demonstrate this relationship, surface plots were generated to show how the power absorbed by the submerged multi-mode WEC varies over a range of natural frequencies of the surge and pitch DOFs, as shown in Fig. 5.2. The surge and pitch natural frequencies are denoted by ω_{n1} and ω_{n5} respectively. A similar analysis was presented previously in [1]; however, a larger number of incident wave frequencies were considered here, with ω_{ex} = 0.6, 0.9 and 1.1 rad/s used for the analysis. These frequencies were chosen based on the hydrodynamic coefficients (see Appendix A) to explore the response of the system when the excitation forces and damping coefficients were low (ω_{ex} = 0.6), or conversely when these parameters were close to their maximum values (ω_{ex} = 0.9 and 1.1 rad/s). The hydrodynamic efficiency, calculated as the sum of power from each DOF divided by the maximum power available for the multi-mode device, is also shown in Fig. 5.3. The total sum of power and the maximum possible power available from the wave are denoted as P_{tot} and P_{max}, respectively.

To produce each plot, the incident wave frequency was kept constant, while the damped natural frequencies of the surge and pitch DOFs were varied by adjusting the value of the PTO stiffness similar to the modal analysis approach presented by [7]. The heave natural frequency was fixed and set equal to the incident wave frequency for all cases shown ($\omega_{n3} = \omega_{ex}$). The PTO damping in all DOFs was set equal to the radiation damping at each frequency, as per Eq. (5.15a). The incident wave amplitude was kept constant at 0.5 m for all cases. Viscous drag effects were not included in these

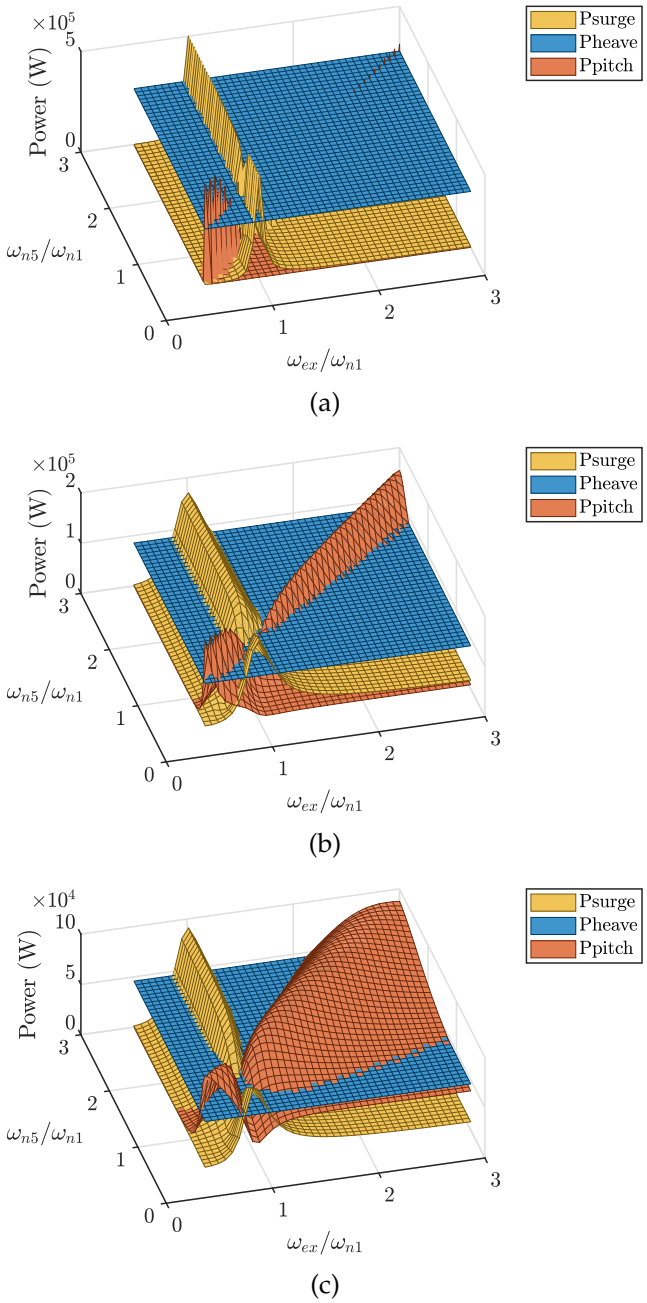

Figure 5.2: Surface plots showing the absolute power absorbed by the surge, heave and pitch DOFs in the linear FD model at incident wave frequencies ω_{ex} of (a) 0.6 rad/s, (b) 0.9 rad/s and (c) 1.1 rad/s, with a wave amplitude of 0.5 m.

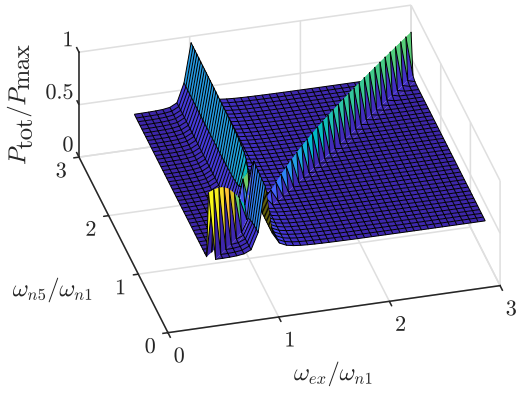

(a)

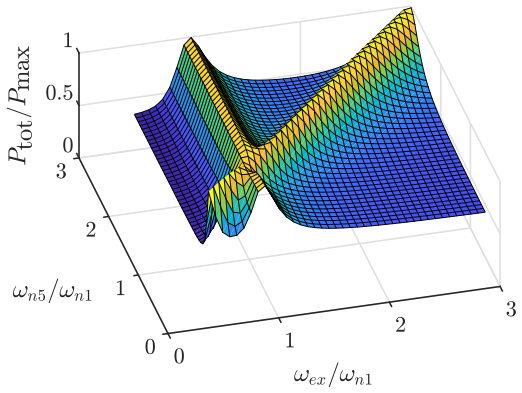

(b)

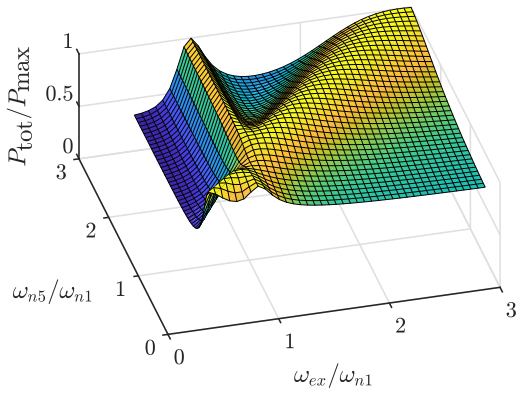

(c)

Figure 5.3: Surface plots showing overall efficiency of the device in the linear FD model at incident wave frequencies ω_{ex} of (a) 0.6 rad/s, (b) 0.9 rad/s and (c) 1.1 rad/s, with a wave amplitude of 0.5 m.

results to further isolate the effects of pitch-surge hydrodynamic coupling on the behaviour of the multi-mode WEC.

In Fig. 5.2, it can be seen that when the surge and pitch natural frequencies were close to one another ($\omega_{n1} = \omega_{n5} = \omega_{ex}$), the power available in each individual DOF dropped as the total power absorbed by the system was divided between them. The pitch DOF was also relatively ineffective at absorbing power in the results for ω_{ex} = 0.6 rad/s in Fig. 5.2(a), due to the low pitch excitation moment amplitude at this frequency (see Fig. 5.13(a) in Appendix A). In contrast, at higher wave frequencies of ω_{ex} = 0.9-1.1 rad/s, when the two modes have well separated natural frequencies and are thus decoupled, the maximum amount of power that can be absorbed from the incident wave is the same regardless of whether surge or pitch are resonant.

From Fig. 5.3, the negative impact of this pitch-surge hydrodynamic coupling on the device's efficiency when both DOFs were tuned to the same natural frequency can also be clearly seen. This was due to the fact that the PTO damping was not optimised to take into account the coupling between these two DOFs, leading to sub-optimal power absorption. It can also be seen that the device was noticeably more affected by this hydrodynamic coupling at ω_{ex}= 0.6 rad/s in Fig. 5.3(a) compared to the higher wave frequencies in Fig. 5.3(b)-(c).

From a design viewpoint, what can be inferred from this relationship is that the surge and pitch DOFs should be decoupled as much as possible to simplify the control problem. If this is the case, Eqs. (5.14)-(5.15) can be directly applied to achieve the maximum power absorption from the system. However, if the two modes are strongly coupled, such as the cases when their natural frequencies were close, simply tuning the system in this manner could result in sub-optimal power absorption instead. Another possible option to maintain the maximum power would be to completely restrain the motions in one DOF by increasing either the controller damping or stiffness. However, tuning the surge and pitch DOFs to target different frequencies may also potentially be advantageous for broadband power absorption.

It is noted that the resonance (or absorption) bandwidth of the device in the pitch DOF is significantly broadened as the wave frequency increases, especially at ω_{ex} = 1.1 rad/s in Fig. 5.2(c) in comparison with Fig. 5.2(a)-(b). This can be explained by considering the radiation damping coefficients, which increases with wave frequency for the range ω_{ex} = 0.6-1.1 rad/s and are also greater in magnitude for pitch than for the surge DOF (see Fig. 5.14 in Appendix A). As a result, the overall efficiency of the device also becomes less sensitive to changes in the surge and pitch natural frequencies as the wave frequency increases, as observed in Fig. 5.3. This is advantageous for

the system, since it reduces the effort required from the controller. Therefore, it may be more suitable to tune the pitch DOF to target the higher incident wave frequencies.

The effect of heave on the system according to the linear model is also shown in Fig. 5.2. From linear theory, there is no hydrodynamic coupling between heave-surge or heave-pitch due to the axisymmetric shape of the buoy. As a result, the power absorbed from heave is insensitive to any changes in the surge or pitch configurations. Hence based on linear hydrodynamics alone, the heave DOF is usually considered independently of the other two DOFs when assessing WEC performance.

5.5 Effect of nonlinear hydrodynamics on power

In this section, the performance and behaviour of the multi-mode WEC system is analysed using the weakly nonlinear WS model.

5.5.1 Power analysis

A similar procedure as described Section 5.4 was used to assess the power absorbed by the WEC in the WS model. However, to reduce computational costs and the number of simulations required, only three fixed ω_{n5}/ω_{n1} pitch and surge natural frequency ratios spanning two octaves were considered in this analysis: (i) $\omega_{n5}/\omega_{n1} = 0.5$, (ii) $\omega_{n5}/\omega_{n1} = 1$ and (iii) $\omega_{n5}/\omega_{n1} = 2$, as shown in Fig. 5.4.

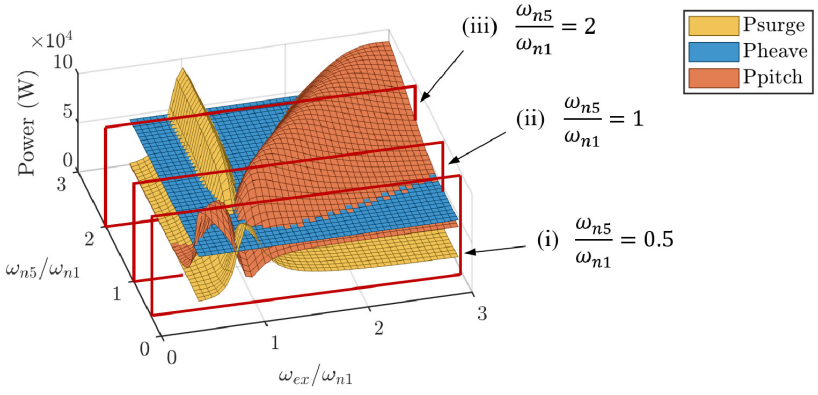

Figure 5.4: Surface plot of power, showing the three pitch-surge natural frequency ratios used in the WS analysis: (i) $\omega_{n5}/\omega_{n1} = 0.5$, (ii) $\omega_{n5}/\omega_{n1} = 1$ and (iii) $\omega_{n5}/\omega_{n1} = 2$

The nonlinear analysis was initially performed for wave frequencies of ω_{ex} = 0.6, 0.9 and 1.1 rad/s, as in Section 5.4. However, it was found the trends in power for ω_{ex} = 0.9 and 1.1 rad/s were very similar. Therefore, only results for $\omega_{ex} = 0.6$ rad/s and 1.1 rad/s are shown in Fig. 5.5 to demonstrate the different responses of the multi-mode WEC at low and high incident wave frequencies, respectively. Each plot shows the power absorbed by the WEC in incident waves with excitation frequencies kept constant, while the pitch and surge natural frequencies were varied[1]. Similar to Section 5.4, the PTO settings in the WS model were also tuned and varied based on Eq. (5.15), using the added mass and radiation damping coefficients obtained from linear theory. Further results showing the amplitudes and phases of the surge, heave and pitch velocities obtained from this analysis can be found in Appendix B.

For all cases shown in Fig. 5.5, the heave natural frequency was set equal to the frequency of the incident wave as was done in Section 5.4 for the linear FD model ($\omega_{n3} = \omega_{ex}$). For the cases with an incident wave frequency of ω_{ex} = 1.1 rad/s, an incident wave amplitude of 1 m was used in the analysis. With this frequency and amplitude, the wave steepness was approximately 12.3%, which was sufficiently large for any potential nonlinear effects to be observed. For ω_{ex} = 0.6 rad/s, the displacement amplitudes of the WEC were much greater, therefore the wave amplitude was reduced to 0.5 m to prevent the WEC breaching the free surface and invalidating the assumptions of the WS model. This wave amplitude was still sufficiently large for nonlinear effects to be observed; the higher displacement amplitudes meant that body nonlinearities, associated with the change in WEC position relative to the free surface, were more important for performance assessment at this frequency [17].

Viscous drag forces were also included in this analysis in order to take into account their effects on the motion amplitudes of the WEC. Given that the presence of nonlinearities only becomes noticeable with large motion amplitudes, this reduction in motion also needs be factored if the importance of nonlinear effects in a more realistic WEC system is to be determined.

5.5.1.1 Low frequency response

Overall, both models indicate that the pitch DOF is relatively ineffective at absorbing power from the waves when the incident wave frequency is low, as illustrated in Fig. 5.5(a)-(c). At an incident wave frequency of ω_{ex} =

[1]Note that the results in (a)-(c) correspond to a wave amplitude of 0.5 m, while results in (d)-(f) correspond to a wave amplitude of 1.0 m.

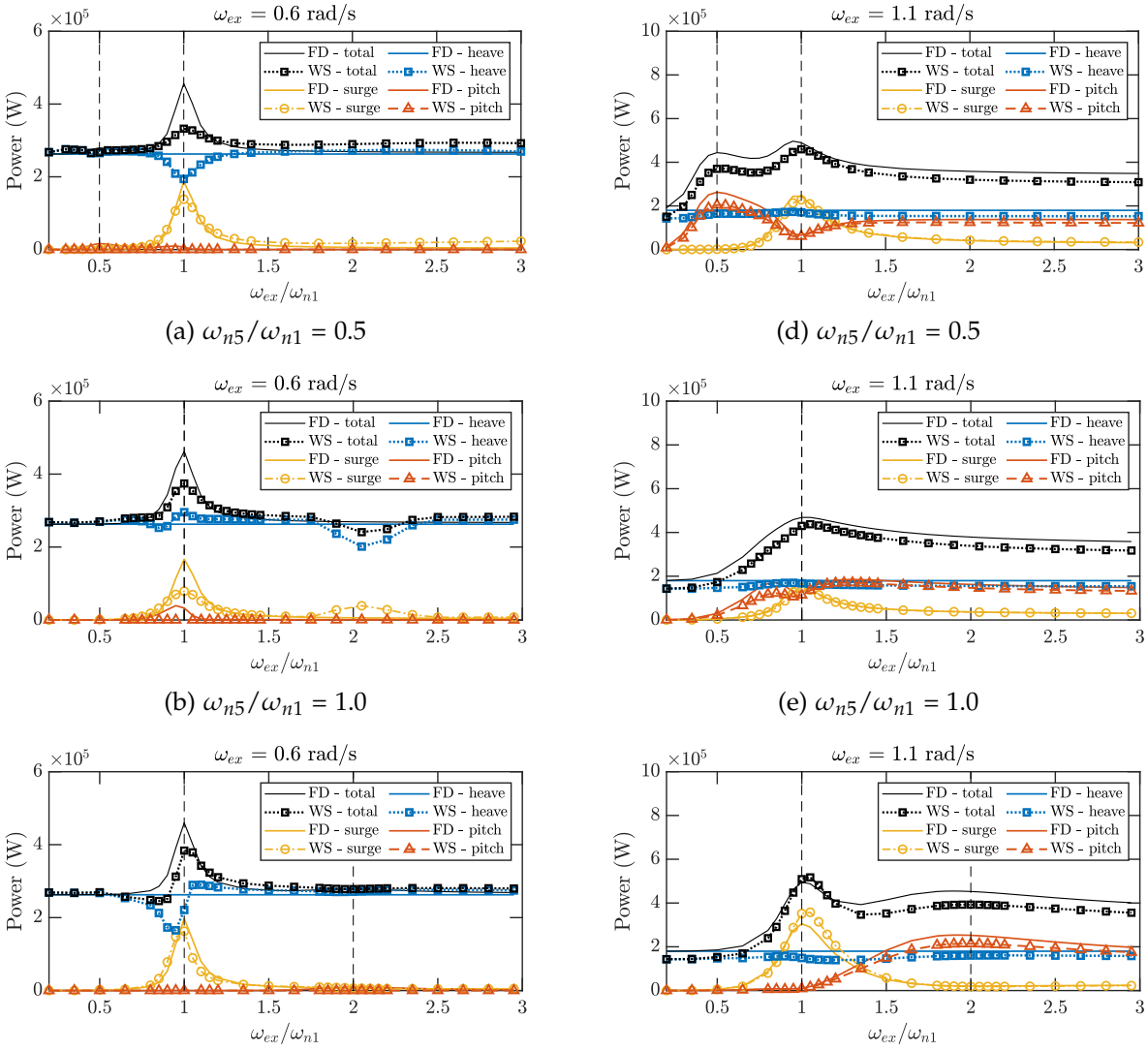

(a) ω_{n5}/ω_{n1} = 0.5

(d) ω_{n5}/ω_{n1} = 0.5

(b) ω_{n5}/ω_{n1} = 1.0

(e) ω_{n5}/ω_{n1} = 1.0

(c) ω_{n5}/ω_{n1} = 2.0

(f) ω_{n5}/ω_{n1} = 2.0

Figure 5.5: Power absorbed by the surge, pitch and heave DOFs, as obtained from the FD (solid lines) and WS (dashed lines) models, for incident wave frequencies ratios of (a)-(c) $\omega_{ex} = 0.6$ rad/s and (d)-(f) $\omega_{ex} = 1.1$ rad/s. The effects of nonlinear hydrodynamic coupling were more significant at the lower frequency of $\omega_{ex} = 0.6$ rad/s compared to 1.1 rad/s, leading to large discrepancies between the linear and nonlinear results.

0.6 rad/s, the power generated from the pitch DOF was negligible in both models. Given that this behaviour was not previously observed in the results shown in Fig. 2, the reduction in pitch power was attributed to the effect of viscous drag, which had been previously ignored in the analysis performed in Section 5.4.

Comparing the linear and nonlinear results, clear differences in the power absorbed were observed from this analysis for $\omega_{ex} = 0.6$ rad/s. At this frequency, when the surge mode was resonant ($w_{ex}/w_{n1} = 1$), the power absorbed by the heave DOF in the WS model was notably reduced for cases $\omega_{n5}/\omega_{n1} = 0.5$ and $\omega_{n5}/\omega_{n1} = 2$. This was a significant difference from the linear results, where the power absorbed in heave was completely independent of the PTO tuning in either surge or pitch. As a result of these nonlinear effects, for the case with $\omega_{n5}/\omega_{n1} = 0.5$, reductions in total power of up to 27% were observed in the WS model compared to the values obtained from the linear FD model. For $\omega_{n5}/\omega_{n1} = 2$, despite the clear drop in heave power the reduction in total power was not as severe, with a 17% difference between the FD and WS results.

For a pitch-surge ratio of $\omega_{n5}/\omega_{n1} = 1$ in Fig. 5.5(b), the heave DOF did not experience a similar reduction in power when both surge and pitch were resonant at the same time. The reduction in power occurred mostly through the surge DOF instead. As a result, the total power achieved in the WS model in this case was reduced by approximately 20% compared to the linear FD model. These results appeared to be consistent with [31], where large reductions in power were also reported for low incident wave frequencies when a cylindrical WEC oscillates in both surge and pitch. Care should therefore be taken when using linear hydrodynamics to design and assess the performance of multi-mode WECs operating at low incident wave frequencies, to avoid overestimating the actual power that can be generated by the device.

5.5.1.2 High frequency response

As demonstrated in Fig. 5.5(d)-(f), for the higher incident wave frequencies, there was a much better match between the FD and WS models. As the wave frequency increased, the relative power absorbed by the pitch DOF also improved. Regarding design of the controller, this analysis made it unequivocally clear that pitch should be tuned to capture energy from higher frequencies for the cylindrical WEC considered in this study.

The power absorbed by the heave DOF obtained from the WS model remained relatively constant regardless of changes to the surge and pitch

natural frequencies. Although slight changes in performance were observed when the surge DOF was resonant, these changes were relatively minor overall. Hence heave may be considered separately from the other two DOFs, as commonly assumed by linear theory, provided that the incident wave frequency is sufficiently high. At ω_{ex} = 1.1 rad/s, there also appeared to be no changes to the total power absorbed caused by nonlinear pitch-surge coupling. This is also consistent with the results in [31], which indicated smaller effects of nonlinear pitch-surge coupling at higher frequencies.

Overall, the results from both the low and high frequency response analysis strongly suggest that all three DOFs should be decoupled in the design of multi-mode WECs. For surge and heave, the results for $\omega_{ex} = 0.6$ rad/s suggest that it may be more advantageous in terms of absorbed power to tune heave to a lower frequency than surge. This is likely due to the higher heave excitation force amplitude at lower frequencies compared to the surge DOF for this WEC geometry (see Fig. 5.13 in Appendix A).

Regarding the pitch DOF, results showed that pitch should be tuned to a higher frequency than surge and heave, to reduce the effects of both viscous drag and nonlinear hydrodynamic coupling. In particular, in the results for ω_{ex} = 0.6 rad/s, when pitch was tuned to the same or a lower natural frequency than surge (Fig. 5.5(a)-(b)), the total power absorbed by the WEC was severely compromised. However, when the pitch was tuned to twice the natural frequency of surge, the reduction in total power was not as significant (Fig. 5.5(c)). Additional investigations were then carried out to further explore the correlation between the tuning of the pitch DOF and the power reductions observed in the nonlinear model, which will be discussed in the following subsection.

5.5.2 Nonlinear motion analysis

The nonlinear WEC response for configurations where the surge DOF was resonant ($\omega_{ex}/\omega_{n1} = 1$) at a wave frequency of ω_{ex} = 0.6 rad/s was then examined in detail. At this point, it was noted that the surge and heave PTO settings were the same ($\omega_{n1} = \omega_{n3} = \omega_{ex}$) across all the pitch-surge natural frequency ratios that were tested. Only the PTO settings of the pitch DOF were different; as a result, the pitch amplitude and phase varied significantly between cases (see Fig. 5.15-5.16 in Appendix B). In the WS model, this would have affected the projected surface area of the WEC and consequently the hydrodynamic forces calculated at different points along its trajectory. Examining the pitch motions, especially in relation to surge and heave, may therefore provide a physical explanation for the nonlinear behaviour obtained

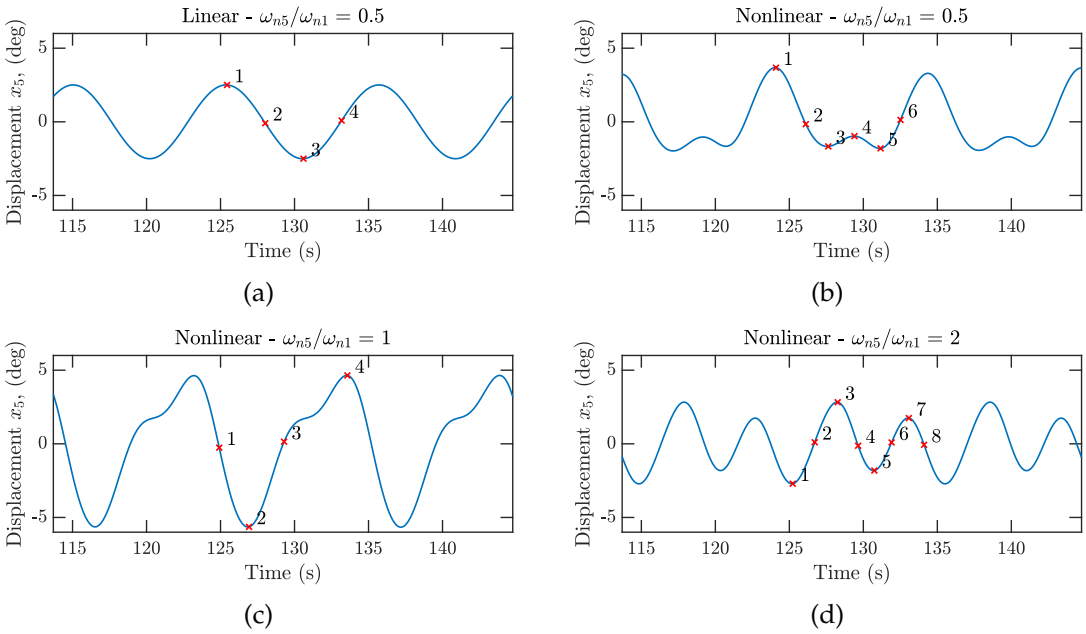

Figure 5.6: Pitch displacement time histories, at $\omega_{ex} = 0.6$ rad/s and $\omega_{ex}/\omega_{n1} = 1$, as obtained from (a) the FD model and (b)-(d) the WS model for different ω_{n5}/ω_{n1} configurations. The pose of the WEC at key points where the magnitude of the pitch displacement was either zero or at its maximum are also indicated and labelled[2].

from the WS model.

Time histories of the pitch displacement were generated and shown in Fig. 5.6 for the results at $\omega_{ex}/\omega_{n1} = 1$, for pitch-surge ratios of $\omega_{n5}/\omega_{n1} = 0.5$, 1 and 2. Key points in the cycle, where the magnitude of the pitch displacement was either zero or a local maximum, were then identified and labelled on corresponding trajectory plots to fully visualise the motion of the WEC in all three planar DOFs, shown in Fig. 5.7. Examples of the linear time history and trajectory for $\omega_{n5}/\omega_{n1} = 0.5$ from the FD model are also shown in these figures to provide a basis for comparison for the nonlinear results. Note that the pitch rotations in the trajectory plots have been exaggerated to better compare the relative pose of the WEC between different points in the cycle.

From a cursory comparison of the linear and nonlinear results in Fig. 5.6, one of the most noticeable differences observed is the strong second harmonic component in the pitch displacement signal obtained from the WS model. By matching the points numbered in Fig. 5.6 with the corresponding WEC

[2]In the published version of this article, the graph labels incorrectly state 'x_3'. This typographic error has been identified and amended here.

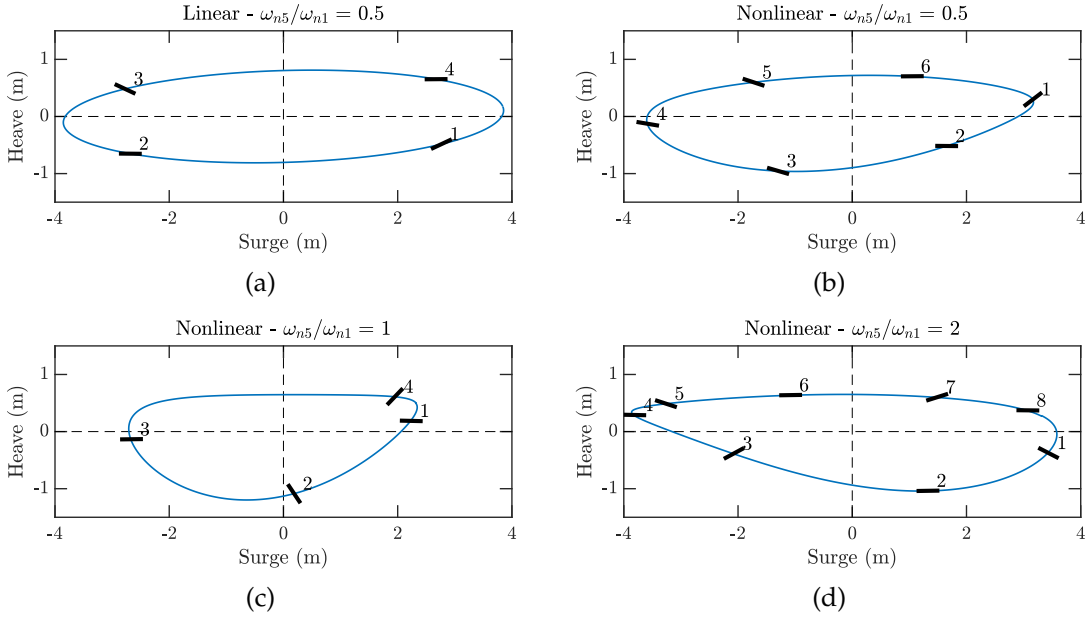

Figure 5.7: Trajectory plots at $\omega_{ex} = 0.6$ rad/s and $\omega_{ex}/\omega_{n1} = 1$, as obtained from (a) the FD model and (b)-(d) the WS model for different ω_{n5}/ω_{n1} configurations. The poses of the WEC at key points, corresponding to those labelled in Fig. 5.6, are also shown. WEC rotations displayed are not to scale.

positions in Fig. 5.7, it was noted that this nonlinear behaviour occurred around the left- and top-most parts of the WEC's trajectory when it moved closer to the free-surface. This suggested that nonlinear free-surface effects may have contributed to the behaviour observed in the WS model. The paths followed by the WEC in the WS results were also slightly flatter on the top half of the trajectory compared to the FD model, further supporting this hypothesis.

Specific differences between each nonlinear case were then considered by analysing the WEC pose at points where surge and heave displacements were close to zero. This is because at instances where $x_j \approx 0$, the magnitude of the velocity would also be closest to its maximum value.

5.5.2.1 Case $\omega_{n5}/\omega_{n1} = 0.5$

In Fig. 5.7(b), it can be seen that the magnitude of the pitch displacement is greatest at the right-most part of the WEC trajectory for this case. Hence, at a point where the heave velocity was significant, both the projected area and horizontal position of the WEC underwent the greatest changes relative to its nominal position. On the left side of the trajectory, the second harmonic

in the pitch displacement signal meant that the projected area of the WEC was reduced twice during the upwards heave stroke. Both noted behaviours would have led to discrepancies between the heave hydrodynamic forces, and consequently the power calculated in the weakly nonlinear WS model compared to the linear model for $\omega_{n5}/\omega_{n1} = 0.5$.

In contrast, the change in WEC pose was not as significant on the top- and bottom-most parts of the trajectory where the surge velocity was greatest. As a result, there was a smaller discrepancy between the two models with regards to the surge power absorbed, as observed in the previous results in Fig. 5.5(a).

5.5.2.2 Case $\omega_{n5}/\omega_{n1} = 1$

It can be seen in Fig. 5.7(c) that the pitch rotation, and consequently the change in WEC pose, was smallest at the left- and right-most parts of the trajectory for this case. Therefore, in this case, the WEC pose was closer to its 'nominal' state during parts of the heave stroke where its velocity was greatest. Hence the linear and nonlinear models showed a closer match in power absorbed from heave.

Conversely, the largest changes to the WEC projected area occurred when the surge velocity was dominant (i.e. when the surge displacement is close to zero near the top and bottom of the trajectory). Furthermore, it was noted that the pitch amplitudes are also greatest for this case. Such a change in the WEC pose would have resulted in significant differences in the WEC hydrodynamics between the linear and nonlinear models, especially in the radiation forces [31]. The added mass and damping coefficients in the radiation force are critical for determining resonance conditions for the WEC; tuning the device according to the linear values may have therefore resulted in the device being off-resonance. This could explain the reduced surge motions and power observed between the linear and nonlinear models for this case.

5.5.2.3 Case $\omega_{n5}/\omega_{n1} = 2$

When the pitch natural frequency was twice that of surge as shown in Fig. 5.6(d), the maximum values of pitch displacement were slightly smaller compared to the previous cases. Furthermore, from Fig. 5.7(d), the change in WEC pose at the most important parts of the heave and surge strokes were also not as large. Hence for this case, the reduction in the nonlinear heave power, specifically at surge resonance ($\omega_{ex}/\omega_{n1} = 1$), was not as severe.

However, note that for $\omega_{n5}/\omega_{n1} = 2$, the maximum drop in heave power actually occurred when the surge and heave DOFs were slightly decoupled. The exact reason for this behaviour was difficult to ascertain due to the significant contribution of the second harmonic in the pitch results close to this point. As previously discussed, the presence of second harmonic in the pitch displacement causes the projected surface area of the WEC to change more frequently. If the phase of the pitch DOF was not ideal, and these rapid changes occurred in the middle of the upward and downward strokes where the heave velocity was high, this could explain the discrepancies in heave power obtained from the two models.

5.6 Recommendations for tuning natural frequencies

From the results presented in previous sections, it is apparent that nonlinear hydrodynamic coupling has a significant and potentially detrimental effect on the power that can be absorbed by the multi-mode WEC. This is an important result due to the fact that, when designing controllers for WECs, it is common to tune the natural frequencies of the device to match the peak or energy frequency of the incident wave [18]. While this may be suitable for single-DOF devices, simply tuning the operating DOFs of a multi-mode WEC in a similar way could potentially lead to large over-estimations of power absorbed. Given these findings, the selection of the most suitable natural frequencies for the surge, heave and pitch DOFs must then be considered.

It is important to note that all previous analysis performed in this paper only considered regular waves. Apart from preventing undesirable effects of nonlinear hydrodynamic coupling, decoupling the surge, heave and pitch DOFs could also potentially increase the broadband power absorption of multi-mode WECs in real-life waves, which contain a spectrum of frequencies. This could reduce the control effort required and increase the power absorbed for a given incident wave spectrum. Estimates for the mean annual power were therefore calculated to investigate the prospective broadband performance of the multi-mode WEC in a real wave site.

5.6.1 Methodology for assessing broadband performance

An outline summarising the methodology used to estimate the potential broadband power that can be absorbed by the multi-mode WEC is shown in Fig. 5.8.

To demonstrate the benefits of decoupling all operational DOFs on broadband performance, two design approaches were compared:

Case 1: All DOFs were tuned to match the peak frequency corresponding to the most probable sea state of the chosen wave site.

Case 2: All DOFs were decoupled, with their natural frequencies tuned to optimal values based on their hydrodynamic coefficients (rather than on wave probability) and also sufficiently far apart to prevent hydrodynamic coupling.

For both cases, the natural frequencies of the device were tuned by adjusting the PTO parameters in each DOF. Note that in this example, wave-to-wave optimal control was not considered. Instead, only a simple causal controller was considered, where the PTO parameters and hence natural frequencies of the surge, heave and pitch DOFs were fixed based on the chosen design approach.

Once the intended wave site and response of the WEC for each case were determined, the average power absorbed by the WEC in a given sea state was then approximated using a similar method described in [3]:

$$\overline{P}_{S,i}(H_s, T_p) = \int_0^\infty S_{\eta,i}(\omega)\overline{p}_S(\omega)d\omega \tag{5.16}$$

where $S_{\eta,i}(\omega)$ is a Pierson-Moskowitz spectrum [25] of the wave elevation for a given sea state with significant wave height H_s and spectral peak wave period T_p, while $\overline{p}_S(\omega)$ is the power response of the WEC in regular waves of unit amplitude (with units of $\mathrm{W/m^2}$). This was calculated for all the possible

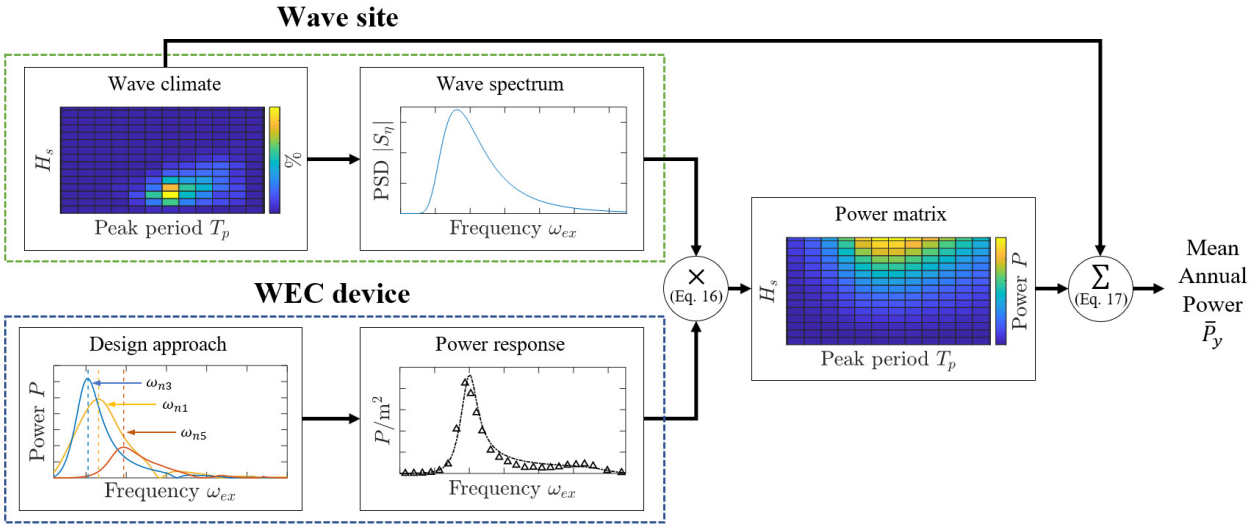

Figure 5.8: Outline of methodology used to assess the mean annual performance of the multi-mode WEC.

sea states in the occurrence matrix of a given wave site to produce a power matrix.

Finally, the average annual power was estimated by multiplying the sea state occurrence matrix with the power matrix [9]:

$$\overline{P}_y = \sum_{i=1}^{N_s} O_i(H_s, T_p) \cdot \overline{P}_{S,i}(H_s, T_p) \tag{5.17}$$

where N_s is the number of sea states considered and O_i is each sea state's probability of occurrence.

5.6.2 Wave site

The intended sea site for the multi-mode WEC was chosen. Given that the WEC considered in this study is inspired by the CETO-6 device, the wave climate near the Albany Test site, Western Australia, for which the device was intended for, was chosen for this analysis. In Fig. 5.9, real time wave data obtained from a buoy deployed close to the test site in Torbay, WA, is shown. From this data, a significant wave height H_s of 2 m and peak period T_p of 12 s ($\omega_p \approx 0.52$ rad/s) was identified as the most probable sea state for this particular site.

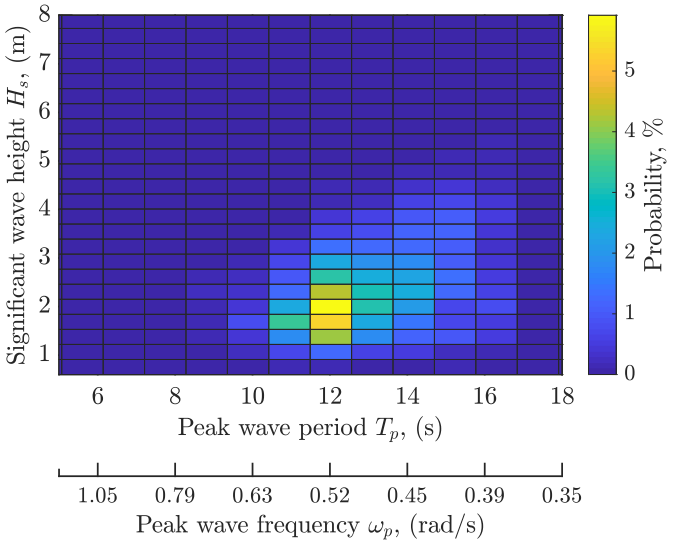

Figure 5.9: Wave climate generated from real wave data from Torbay in Western Australia, which is close to the planned deployment site for the CETO-6 device in Albany.

5.6.3 Power response

To determine the response of the multi-mode WEC, the natural frequencies for the surge, heave and pitch DOFs were defined for each design approach. For case 1, the natural frequency of each DOF were simply set to the most probable peak period identified from Fig. 5.9 ($\omega_{n,j} = 0.52$ rad/s). To guide the initial choice of appropriate natural frequencies for Case 2, a simple linear FD analysis was performed where the maximum power that could be potentially absorbed by each DOF in regular waves at different incident wave frequencies was examined. Each DOF was treated independently and their natural frequencies were simply tuned to match the incident wave as per Eq. (5.15). Results illustrating the maximum power of each DOF are shown in Fig. 5.10.

Among the three DOFs considered, the heave DOF resulted in the maximum power absorbed. This was achieved at a frequency of $\omega_{ex} = 0.52$ rad/s, or $T_p \approx 12$ s, which matches well with the most probable wave period of the wave site identified from Fig. 5.9. For surge, maximum power occurred at a slightly higher frequency of $\omega_{ex} = 0.66$ rad/s, while maximum pitch power was achieved at an even higher frequency of $\omega_{ex} = 0.97$ rad/s. Overall, these frequencies are a suitable choice for Case 2, since the natural frequencies of each DOF will be sufficiently far apart to minimise nonlinear hydrodynamic coupling. The order of natural frequencies, from lowest to highest, also matches with the order recommended in Section 5.5.

The PTO settings in each DOF required to achieve the desired natural frequencies in each case were then fixed and the power absorbed by the WEC

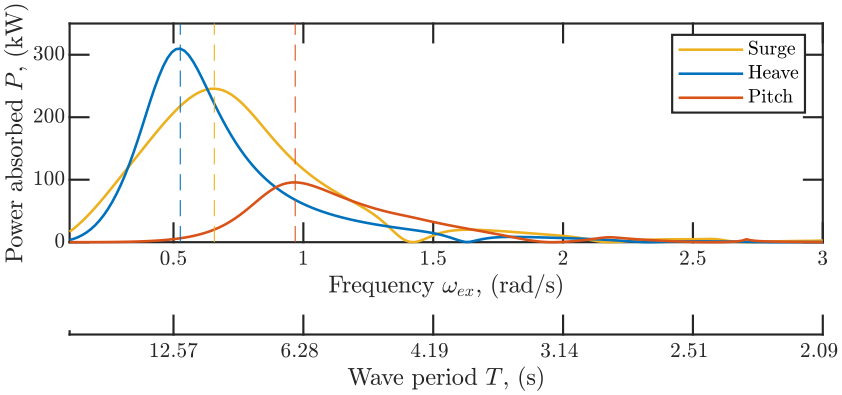

Figure 5.10: Maximum power absorbed by each independent DOF when tuned to match the incident wave for each frequency. From this analysis, the optimal frequencies for each DOF are: $\omega_{n1} = 0.66$ rad/s, $\omega_{n3} = 0.52$ rad/s, $\omega_{n5} = 0.97$ rad/s.

was assessed in regular waves with excitation frequencies ranging from ω_{ex} = 0.2-2 rad/s. The resultant power response for each case in both the FD and WS models are shown and compared in Fig. 5.11.

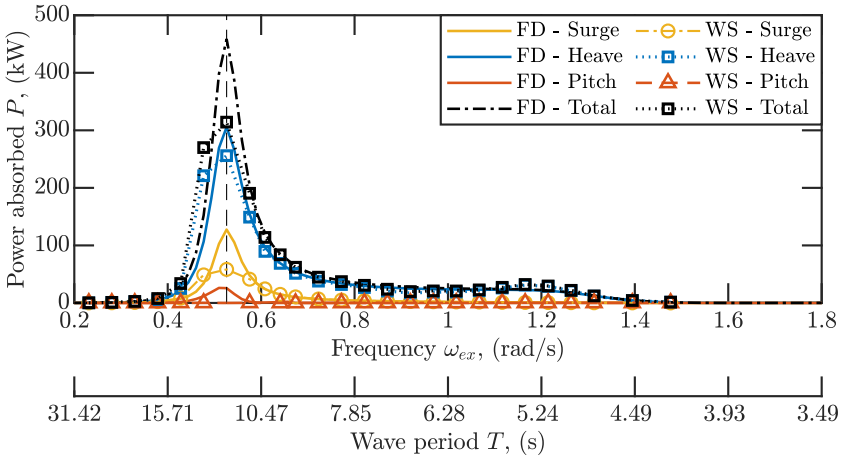

(a)

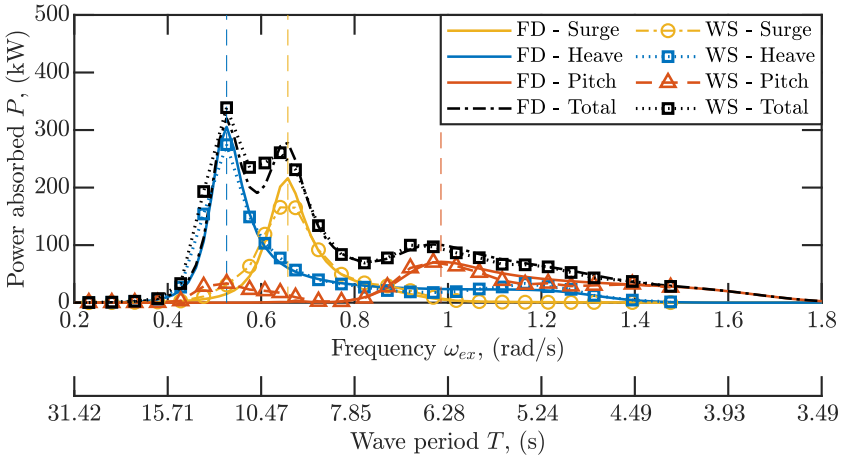

(b)

Figure 5.11: Power response of the WEC in regular waves, for (a) Case 1 where $\omega_{n,j}$ = 0.52 rad/s for all DOFs and (b) Case 2 where $\omega_{n,j}$ were all decoupled and tuned to different frequencies (ω_{n1} = 0.66 rad/s, ω_{n3} = 0.52 rad/s, ω_{n5} = 0.97 rad/s).

The power responses for Case 1 in both the FD and WS models are shown in Fig. 5.11(a). Results for this case confirmed that the pitch DOF was ineffective at absorbing power when tuned to lower frequencies. In the linear FD model, the design for Case 1 resulted in a large peak in power absorbed at the peak wave frequency. However, the value for maximum total power

absorbed was overestimated by 31.5% compared to the WS model. With all three DOFs tuned to the same frequency, the reduction in power was caused primarily by adverse coupling between the surge and pitch DOFs, similar to the behaviour observed in Fig. 5.5(b).

Fig. 5.11(b) illustrates the results for Case 2, where the natural frequencies of each DOF were decoupled and tuned to match their corresponding optimal values found in Fig. 5.10. For this case, the power estimations obtained from the linear FD model showed a better match with the WS model since the DOFs were decoupled. Since the pitch DOF was tuned to a higher frequency, it was able to contribute to power absorption for the WEC. Interestingly, for this case, the WS results also show a slight contribution from the pitch DOF to total power absorbed around $\omega_{ex} = 0.52$ rad/s where the heave DOF was dominant, despite not being tuned for those conditions. This nonlinear coupling between heave and pitch was not observed in the results previously presented in Section 5.5. A possible explanation could be the decreased heave damping between $\omega_{ex} = 0.52$ and 0.6 rad/s.

Comparing Cases 1 and 2, the maximum power absorbed in the linear FD model was much greater at the peak wave frequency in Case 1 compared to Case 2. Therefore, if only regular waves and linear hydrodynamics were considered, the design used for Case 1 may appear to offer better performance. However, from the results obtained in the WS model, where the effects of nonlinear hydrodynamic coupling were included, the maximum power achieved by the WEC in Case 1 was greatly reduced. As a result, Case 2 resulted in better performance in terms of both peak power achieved and absorption bandwidth (defined as the normalised frequency range where the total power absorbed remained within 50% of the peak value), with improvements of approximately 8% and 56%, respectively.

5.6.4 Mean annual power

The wave climate data in Fig. 5.9 and the power response curves were then applied to Eq. (5.16) and Eq. (5.17) to obtain estimates for the mean annual power output of the WEC at the Torbay wave site for both design cases. Example power matrices for Cases 1 and 2, produced using the WS power response curves, are shown in Fig. 5.12. Final estimates for the average annual power generated by both design cases, as obtained from the FD and WS models, are given in Table 5.2.

From this analysis, the performance of the WEC in Case 2 was clearly better in terms of average power absorbed. In Table 5.2, this advantage was already observed in the FD results, with a 14.6% improvement in $\overline{P}_y$ for

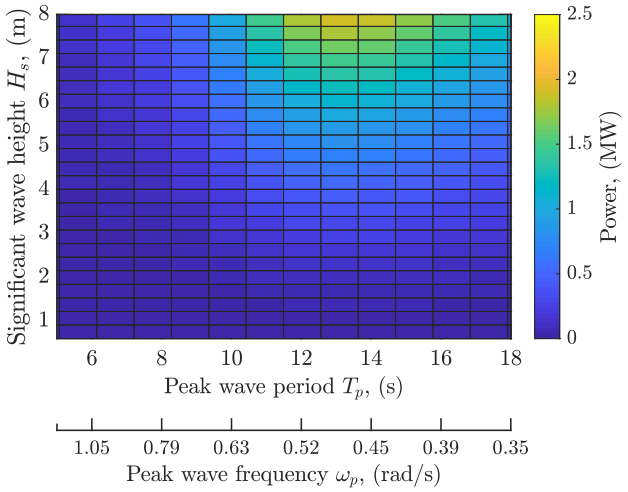

(a)

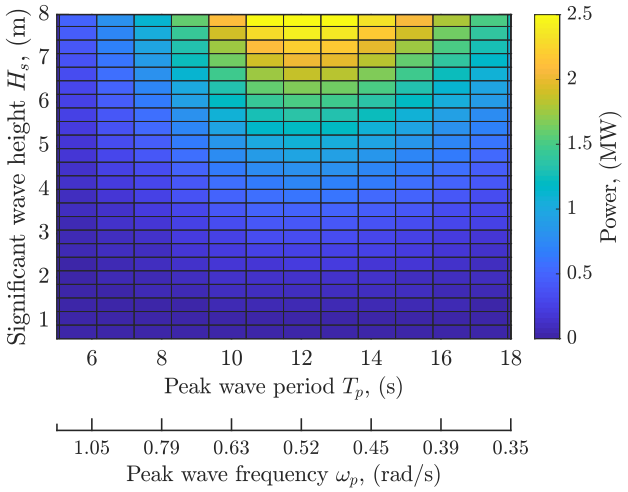

(b)

Figure 5.12: Power matrices of the WEC for (a) Case 1 where $\omega_{n,j} = 0.52$ rad/s for all DOFs and (b) Case 2 where $\omega_{wn,j}$ were decoupled and tuned to different frequencies (ω_{n1} = 0.66 rad/s, ω_{n3} = 0.52 rad/s, ω_{n5} = 0.97 rad/s).

Table 5.2: Comparison of the yearly mean power output between the two different design cases.

Case	Average annual power, $\overline{P}_y$	
	FD	WS
1	173 kW	164 kW
2	198 kW	221 kW

Case 2 compared to Case 1. This advantage was even greater in the WS results when the effects of nonlinear hydrodynamics were included. While the average annual power generated in Case 1 dropped, the power in Case 2 actually increased between the WS and FD models due to contribution of the pitch DOF close to $\omega = 0.52$ rad/s, as previously discussed. Altogether, this led to an increase of 34.6% between the values of $\overline{P}_y$ for Cases 1 and 2 in the WS model.

5.7 Discussion

There were a number of limitations associated with the WS model used in this study which should be noted. In particular, for the WEC operating at resonance, there may have been cases where the small perturbation assumption of the WS approximation was not fully satisfied locally due to large body motions. Although the WS results were still likely to be more accurate than those obtained from linear theory [8, 17], the validity of this assumption should be confirmed through comparisons with fully nonlinear models or experiments. Other additional limitations of the WS model encountered in this study, which could be addressed in future work, included long computational times and problems with handling surface piercing effects.

For this study, viscous drag forces were also implemented using the Morrison equation in both the FD and WS models. Other phenomena related to drag, such as vortex shedding and turbulence were not considered. These effects can be expected to further reduce WEC amplitudes. From a modelling perspective, the reduction in pitch amplitude would result in a closer match between the FD and WS models, since the effect of nonlinear coupling would also be further reduced. Therefore, it may also be valuable to test the multi-mode WEC using CFD in order to fully simulate all of these nonlinear drag effects and their impact on performance.

Given that the primary focus of this paper was specifically on the performance assessment, control and tuning of multi-mode WECs, further analysis of the nonlinear hydrodynamic effects observed in Section 5.5 was not performed. However, with the significant reduction in power observed and relevant implications for multi-mode WECs, more detailed studies focusing on nonlinear hydrodynamics arising from combined surge, heave and pitch motions would be a pertinent area for future work. This could include investigating the impact of nonlinear free-surface effects, such as the existence of trapped modes [19] and other potential interactions between the radiated and incoming waves. Different WEC geometries could also be considered,

which would affect the strength of nonlinear hydrodynamic coupling but also the power absorption efficacy of each DOF.

Although Section 5.6 demonstrated the potential for improved broadband power absorption using a different design approach for multi-mode WECs, simulations involving irregular waves were not performed in order to avoid over-complicating the current study. A complete analysis considering both irregular waves and nonlinear hydrodynamic coupling effects together should be performed in future work in order to confirm the benefits of this design approach.

Further studies could also focus on more detailed optimisation of the natural frequencies for each DOF. However, this will ultimately depend on the specific WEC being considered and requires addressing the challenge of realising these designs in the real-life system. For example, the actual CETO-6 device relies on the use of three tethers for actuation and control, which results in additional coupling between each DOF. Furthermore, the system is under-actuated, meaning that it would be difficult to tune the pitch DOF independently. Other active or passive control mechanisms, such as changing the pitch moment of inertia or shifting the centre of gravity [20], may be required to tune the pitch DOF accordingly. However, this in turn may increase the cost of the system and consequently the levelised cost of electricity of the device. Therefore, from a more general perspective, any future work regarding the real-life actuation multi-mode WECs will also need to consider whether the gains from including multiple DOFs for power absorption can justify the increase in complexity in the control design.

5.8 Conclusion

The effect of fully linear and weakly nonlinear hydrodynamic coupling between the surge, heave and pitch DOFs on the performance of a multi-mode WEC with spring-damper control and a submerged cylindrical buoy was investigated in this study. It was found that the effects of the weakly nonlinear hydrodynamics on performance were most apparent when the incident wave frequency was low. For the WEC system studied in this paper, nonlinear coupling between DOFs at an incident wave frequency of ω_{ex} = 0.6 rad/s led to reductions in power absorbed of up to 27% in the weakly nonlinear WS model, compared to the FD model. The reductions in power were attributed predominantly to the relative phases between each DOF, especially pitch. The greatest discrepancies were observed for cases where pitching motions caused notable changes to the projected area of the WEC

compared to its equilibrium position.

As a result, it was recommended to decouple the surge, heave and pitch DOFs as much as possible when designing multi-mode WECs. Additionally, for the cylindrical WEC considered in this study, it was further recommended to tune the pitch DOF to higher natural frequencies to avoid the effects of viscous drag. A higher natural frequency in pitch also resulted in a more favourable phase relationship between the three DOFs, and consequently less power lost through nonlinear hydrodynamic coupling.

Two potential design cases were then compared where the natural frequencies of each DOF were: (1) all tuned to match the most probable peak wave frequency and (2) decoupled and fixed at different frequencies to reduce the effects of hydrodynamic coupling. From the resultant power response curves alone, the linear FD results suggested greater power absorbed for Case 1. However, this advantage disappeared when nonlinear hydrodynamic coupling effects were included. As a result, decoupling the surge, heave and pitch DOFs according to Case 2 resulted in similar power absorbed but with a larger absorption bandwidth. The average annual power generated by the WEC for both cases was also estimated to compare the potential broadband performance. From this analysis, the performance of the device in Case 2 was clearly superior, especially from the nonlinear results which suggested an improvement in average power of over 30% compared to Case 1 for the WEC considered in this paper.

Overall, the results of this analysis highlight the importance of selecting appropriate natural frequencies in the design of multi-mode WECs. In addition to reducing the effects of nonlinear hydrodynamic coupling, the potential for increasing the power absorption of the device in real seas was also identified. However, further analysis involving both irregular waves and nonlinear hydrodynamics is required to confirm the benefits of the proposed multi-mode WEC design strategy. More detailed controller designs will also need to address the challenge of decoupling and tuning each DOF in real WEC designs, especially in the case of under-actuated systems.

Acknowledgements

This research was supported by an Australian Government Research Training Program (RTP) Scholarship. The numerical WS_CN model used in this study was developed by École Centrale de Nantes and shared with the University of Adelaide for wave energy research. This work was also supported with supercomputing resources provided by the Phoenix HPC service at the

University of Adelaide.

Appendix 5.A Linear hydrodynamic coefficients

In this study, the excitation force and radiation coefficients used in the linear FD model were determined using analytical expressions [14, 15]. Values of the linear amplitude $|F_{\text{exc}}|$ and phase $\angle F_{\text{exc}}$ used to calculate the excitation force in the FD hydrodynamic model are shown in Fig. 5.13 for a range of wave frequencies. Likewise, for the radiation force calculations, the individual matrix elements for the added mass and radiation damping coefficients are given in Fig. 5.14. Note that due to reciprocity relation, $A_{\text{rad},15} = A_{\text{rad},51}$ and $B_{\text{rad},15} = B_{\text{rad},51}$ [10].

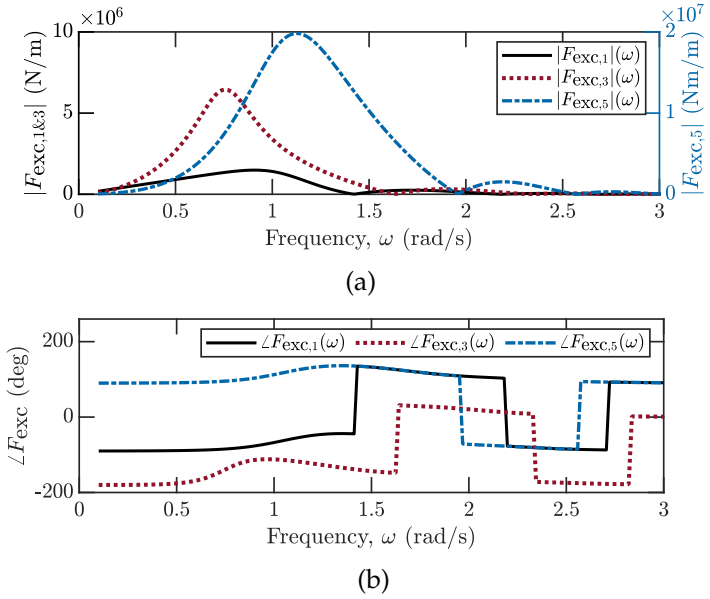

Figure 5.13: Surge and heave excitation force and pitch excitation moment (a) amplitudes and (b) phases.

Appendix 5.B Nonlinear amplitude and phase

The velocity amplitudes and phases of each DOF were also compared between the FD and WS models, shown in Fig. 5.15-5.16. Note that results for velocity were shown instead of displacement, given the important relationship between WEC velocity and excitation force when assessing power. To extract the velocity amplitudes and phases of the dynamic signal obtained from the WS model, a simple least mean squares method was used. It was assumed

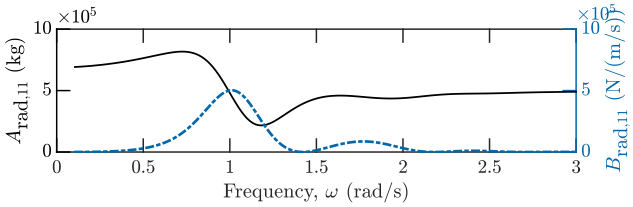

(a) Surge-surge

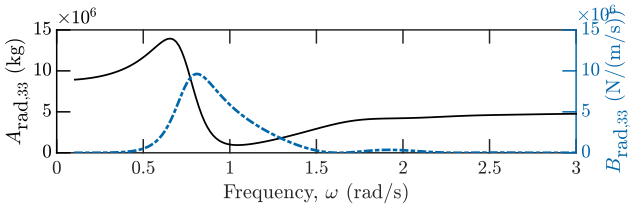

(b) Heave-heave

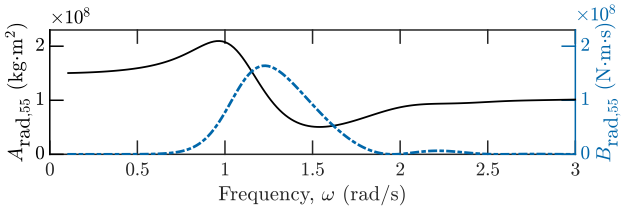

(c) Pitch-pitch

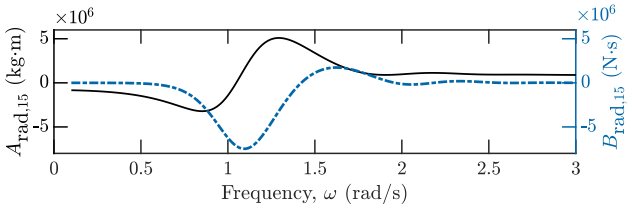

(d) Surge-pitch

Figure 5.14: Added mass and radiation damping coefficients.

that the obtained WS signal could be approximated using a series expansion [1]:

$$\dot{x}(t) = \sum_i a_i \cos(\omega_i t) + b_i \cos(\omega_i t) \tag{5.B.1}$$

where a_i and b_i are the unknown coefficients of the ith frequency component, which were computed by minimising the sum of the squared errors between the approximation and the original dynamic signal from the WS model. These coefficients were then used to determine the magnitude and phase at of the signals at each natural frequency ratio. In Fig. 5.15, the amplitudes of the first and second harmonic are shown in the results for $\omega_{ex} = 0.6$ rad/s.

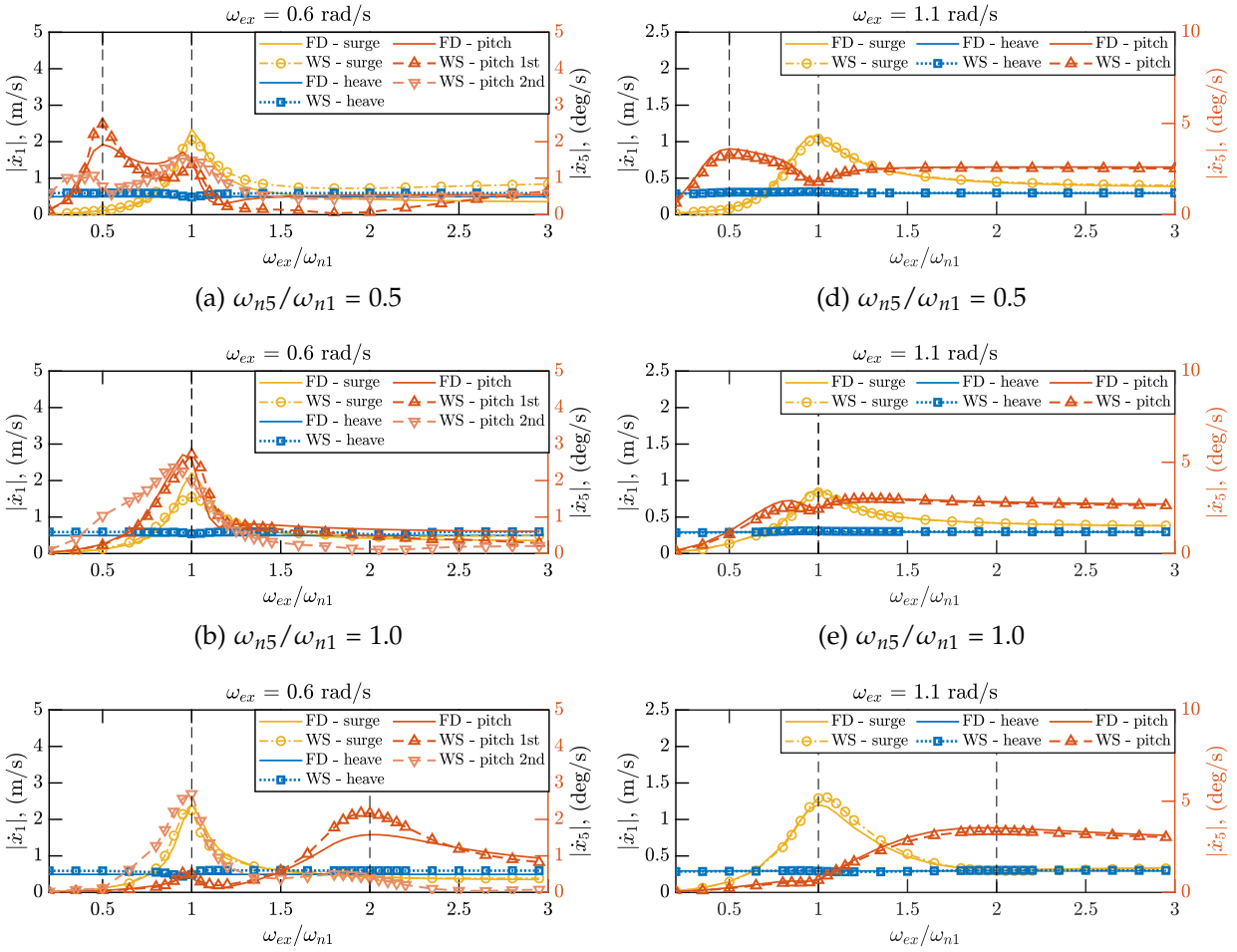

(a) ω_{n5}/ω_{n1} = 0.5 (d) ω_{n5}/ω_{n1} = 0.5

(b) ω_{n5}/ω_{n1} = 1.0 (e) ω_{n5}/ω_{n1} = 1.0

(c) ω_{n5}/ω_{n1} = 2.0 (f) ω_{n5}/ω_{n1} = 2.0

Figure 5.15: Amplitudes of the surge, heave and pitch DOF at various incident wave frequencies, as obtained from the FD and WS models for pitch-surge natural frequency ratios of (a)-(c) 0.5, (d)-(f) 1.0 and (g)-(i) 2.0.

For $\omega_{ex} = 1.1$ rad/s, the second harmonic was not as significant, so only the first harmonic amplitude is displayed. For the phases in Fig. 5.16, only the fundamental frequency component is shown, since this is the most important for determining the total average power that can be absorbed by the device.

It was noted that for $\omega_{ex} = 1.1$ rad/s, a noticeable phase offset was observed between the FD and WS models, as seen in Fig. 5.16. However, the same offset was present between the phases of the excitation force obtained from models as well. Therefore, since this phase differential was identical, the power calculations should not be affected and were still comparable between the two models.

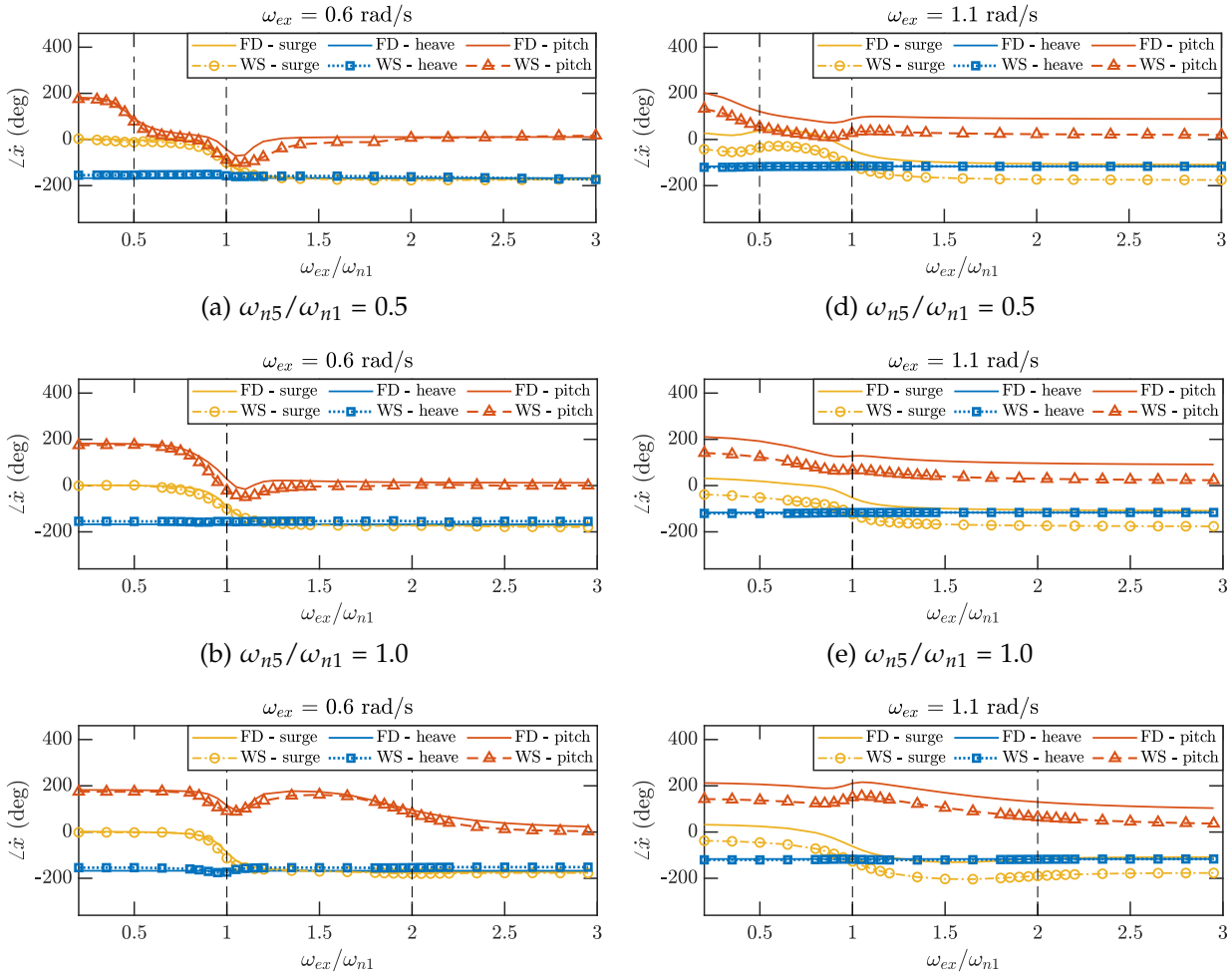

(a) ω_{n5}/ω_{n1} = 0.5 (d) ω_{n5}/ω_{n1} = 0.5

(b) ω_{n5}/ω_{n1} = 1.0 (e) ω_{n5}/ω_{n1} = 1.0

(c) ω_{n5}/ω_{n1} = 2.0 (f) ω_{n5}/ω_{n1} = 2.0

Figure 5.16: Phases of the surge, heave and pitch DOF at various incident wave frequencies, as obtained from the FD and WS models for pitch-surge natural frequency ratios of (a)-(c) 0.5, (d)-(f) 1.0 and (g)-(i) 2.0.

References

[1] Abdelkhalik, O., Zou, S., Robinett, R. D., Bacelli, G., Wilson, D. G., Coe, R. and Korde, U. (2017). "Multiresonant feedback control of a three-degree-of-freedom wave energy converter". In: *IEEE Transactions on Sustainable Energy* 8.4, pp. 1518–1527.

[2] Alves, M. (Jan. 2016). "Frequency-Domain Models". In: *Numerical Modelling of Wave Energy Converters*. Academic Press, pp. 11–30.

[3] Babarit, A, Wendt, F, Yu, Y.-H. and Weber, J (2017). "Investigation on the energy absorption performance of a fixed-bottom pressure-

differential wave energy converter". In: *Applied Ocean Research* 65, pp. 90–101.

[4] Carnegie Clean Energy (2020). *CETO Technology - Carnegie Clean Energy*. URL: https://www.carnegiece.com/ceto-technology/.

[5] Coe, R., Bacelli, G., Spencer, S. J., Forbush, D. and Dullea, K. (2019). *MASK3 for Advanced WEC Dynamics and Controls*. Tech. rep.

[6] Coe, R. G., Bacelli, G., Wilson, D. G., Abdelkhalik, O., Korde, U. A. and Robinett III, R. D. (2017). "A comparison of control strategies for wave energy converters". In: *International Journal of Marine Energy* 20, pp. 45–63.

[7] Ding, B., Sergiienko, N., Meng, F., Cazzolato, B., Hardy, P. and Arjomandi, M. (Jan. 2019a). "The application of modal analysis to the design of multi-mode point absorber wave energy converters". In: *Ocean Engineering* 171, pp. 603–618.

[8] Ding, B., Wuillaume, P, Meng, F., Babarit, A., Schubert, B., Sergiienko, N. Y. and Cazzolato, B. S. (2019b). "Comparison of wave-body interaction modelling methods for the study of reactively controlled point absorber wave energy converter". In: *Proceedings of the 34th International Workshop on Water Waves and Floating Bodies*. Newcastle.

[9] Fàbregas Flavià, F, Babarit, A and Clément, A. H. (2017). "On the numerical modeling and optimization of a bottom-referenced heave-buoy array of wave energy converters". In: *International Journal of Marine Energy* 19, pp. 1–15.

[10] Falnes, J. (2002). *Ocean waves and oscillating systems: Linear interactions including wave-energy extraction*. Cambridge University Press, p. 220.

[11] Folley, M., Whittaker, T. and Hoff, J. van't (2007). "The design of small seabed-mounted bottom-hinged wave energy converters". In: *Proceedings of the 7th European Wave and Tidal Energy Conference EWTEC*. Porto, Portugal.

[12] Hannan, M. A., Bai, W and Ang, K. K. (Mar. 2014). "Modeling of fully nonlinear wave radiation by submerged moving structures using the higher order boundary element method". In: *Journal of Marine Science and Application* 13.1, pp. 1–10.

[13] Hoerner, S. F. (1965). *Fluid-dynamic drag: practical information on aerodynamic drag and hydrodynamic resistance*. Hoerner Fluid Dynamics.

[14] Jiang, S.-C., Gou, Y. and Teng, B. (May 2014a). "Water wave radiation problem by a submerged cylinder". In: *Journal of Engineering Mechanics* 140.5, p. 6014003.

[15] Jiang, S.-C., Gou, Y., Teng, B. and Ning, D.-Z. (Jan. 2014b). "Analytical solution of a wave diffraction problem on a submerged cylinder". In: *Journal of Engineering Mechanics* 140.1, pp. 225–232.

[16] Korde, U. A., Lyu, J., Robinett, R. D., Wilson, D. G., Bacelli, G. and Abdelkhalik, O. (2017). "Constrained near-optimal control of a wave energy converter in three oscillation modes". In: *Applied Ocean Research* 69, pp. 126–137.

[17] Letournel, L., Chauvigné, C., Gelly, B., Babarit, A., Ducrozet, G. and Ferrant, P. (2018). "Weakly nonlinear modeling of submerged wave energy converters". In: *Applied Ocean Research* 75, pp. 201–222.

[18] Li, B, Macpherson, D. E. and Shek, J. K. H. (2011). "Direct drive wave energy converter control in irregular waves". In: *IET Conference on Renewable Power Generation (RPG 2011)*, pp. 1–6.

[19] McCauley, G., Wolgamot, H., Orszaghova, J. and Draper, S. (2018). "Linear hydrodynamic modelling of arrays of submerged oscillating cylinders". In: *Applied Ocean Research* 81, pp. 1–14.

[20] Meng, F., Ding, B., Cazzolato, B. and Arjomandi, M. (Jan. 2019). "Modal analysis of a submerged spherical point absorber with asymmetric mass distribution". In: *Renewable Energy* 130, pp. 223–237.

[21] Mofor, L., Goldsmith, J. and Jones, F. (2014). *Ocean Energy: Technology Readiness, Patents, Deployment Status and Outlook*. Tech. rep. August, p. 76.

[22] Morison, J., Johnson, J. and Schaaf, S. (1950). "The force exerted by surface waves on piles". In: *Journal of Petroleum Technology* 2.05, pp. 149–154.

[23] Pawlowski, J. S. and Bass, D. W. (1991). *A theoretical and numerical model of ship motions in heavy seas*. Tech. rep.

[24] Pichard, A., Wale, C. and Rafiee, A. (2019). "Techno-economical tools for WEC scale optimisation". In: *Proceedings of the 13th European Wave and Tidal Energy Conference EWTEC*. Naples, Italy.

[25] Pierson, W. J. and Moskowitz, L. (1964). "A proposed spectral form for fully developed wind seas based on the similarity theory of S. A. Kitaigorodskii". In: *Journal of Geophysical Research* 69.24, pp. 5181–5190.

[26] Ringwood, J. V., Bacelli, G. and Fusco, F. (2014). "Energy-maximizing control of wave-energy converters: The development of control system technology to optimize their operation". In: *IEEE Control Systems* 34.5, pp. 30–55.

[27] Sergiienko, N. Y., Cazzolato, B. S., Arjomandi, M, Ding, B and Silva, L. S. P. da (2019). "Considerations on the control design for a three-

tether wave energy converter". In: *Ocean Engineering* 183, pp. 469–477.

[28] Sergiienko, N. Y., Cazzolato, B. S., Ding, B, Hardy, P and Arjomandi, M (2017). "Performance comparison of the floating and fully submerged quasi- point absorber wave energy converters". In: *Renewable Energy* 108, pp. 425–437.

[29] Sergiienko, N. Y., Cazzolato, B. S., Ding, B. and Arjomandi, M. (2016). "Three-tether axisymmetric wave energy converter: estimation of energy delivery". In: *Proceedings of the 3rd Asian Wave and Tidal Energy Conference AWTEC*. Singapore: Singapore: Research Publishing, pp. 163–171.

[30] Terra, G. M., Berg, W. J. van de and Maas, L. R. M. (2005). "Experimental verification of Lorentz' linearization procedure for quadratic friction". In: *Fluid Dynamics Research* 36.3, pp. 175–188.

[31] Tran, N., Sergiienko, N. Y., Cazzolato, B. S., Ding, B., Ghayesh, M. H. and Arjomandi, M. (2020). "The impact of pitch-surge coupling on the performance of a submerged cylindrical wave energy converter". In: *Applied Ocean Research* 104, p. 102377.

[32] Wendt, F., Nielsen, K., Yu, Y.-H., Bingham, H., Eskilsson, C., Kramer, M., Babarit, A., Bunnik, T., Costello, R., Crowley, S., Gendron, B., Giorgi, G., Giorgi, S., Girardin, S., Greaves, D., Heras, P., Hoffman, J., Islam, H., Jakobsen, K.-R., Janson, C.-E., Jansson, J., Kim, H. Y., Kim, J.-S., Kim, K.-H., Kurniawan, A., Leoni, M., Mathai, T., Nam, B.-W., Park, S., Rajagopalan, K., Ransley, E., Read, R., Ringwood, J. V., Rodrigues, J. M., Rosenthal, B., Roy, A., Ruehl, K., Schofield, P., Sheng, W., Shiri, A., Thomas, S., Touzon, I. and Yasutaka, I. (2019). "Ocean energy systems wave energy modelling task: modelling, verification and validation of wave energy converters". In: *Journal of Marine Science and Engineering* 7.11, p. 379.

[33] Wendt, F., Yu, Y.-H., Nielsen, K., Ruehl, K., Bunnik, T., Touzón, I., Nam, B. W., Kim, J., Kim, K.-H., Janson, C.-E., Jakobsen, K.-R., Crowley, S., Vega, L., Rajagopalan, K., Mathai, T., Greaves, D., Ransley, E., Lamont-Kane, P., Sheng, W and Hoffman, J. (Aug. 2017). "International Energy Agency Ocean Energy Systems task 10 wave energy converter modeling verification and validation". In: *Proceedings of the 12th European Wave and Tidal Energy Conference EWTEC*.

[34] Wuillaume, P.-Y. (Jan. 2019). "Numerical simulation of installation operations for offshore wind farms". PhD thesis. École Centrale de Nantes.

[35] Wuillaume, P.-Y., Babarit, A., Rongère, F., Lynch, M., Combourieu, A. and Ferrant, P. (June 2018). "Comparison between experiments and a multibody weakly nonlinear potential flow approach for modelling of marine pperations". In: *ASME 2018 37th International Conference on Offshore Mechanics and Arctic Engineering*. Madrid, Spain.

[36] Yavuz, H. (July 2011). "On control of a pitching and surging wave energy converter". In: *International Journal of Green Energy* 8.5, pp. 555–584.

Chapter 6

Design considerations for a three-tethered WEC with nonlinear coupling between modes

To this point, all the analysis has been focused on fully-actuated systems with independent control in all hydrodynamic modes. This was necessary to isolate the effect of nonlinear hydrodynamic coupling on the system, which in the previous chapter was found to negatively impact power when all three hydrodynamic modes were tuned to the same natural frequency. It was therefore recommended for the surge, heave and pitch modes to be tuned to different frequencies in such a system, to avoid compromising the total power absorbed as well as potentially improving broadband performance in irregular waves. However, the assumption of fully independent control may not be reflective of many real-world devices which are often under-actuated.

The behaviour of the coupled hydrodynamic modes in an under-actuated three-tethered multi-mode WEC is therefore considered in this chapter, as shown in Figure 1.2(c). Here, the hydrodynamic modes are coupled not only through the nonlinear hydrodynamic forces, but also through geometric nonlinearities arising from the tether arrangement. This analysis is therefore intended to build upon the knowledge previously established in Chapter 5, which considered the effect of coupling due to hydrodynamic nonlinearities only. To this end, a Time-Domain (TD) model is also developed in addition to the fully linearised potential flow and weakly-nonlinear WS models used in Chapters 4 and 5 to study the under-actuated WEC system. While the WS model includes both geometric and hydrodynamic nonlinearities, the

TD model can be used to observe and distinguish between the effects of geometric nonlinearities on the system exclusively.

The focus of this analysis is retained on the surge, heave and pitch modes, in order to make the problem more tractable without the complication of the other orthogonal DOFs and to allow a better comparison with the study previously presented in Chapter 5. Sensitivity studies are performed in this chapter to analyse the influence of various aspects of the three-tethered WEC design, such as the tether arrangement and mass distribution, on the power absorbed and nonlinear response of the converter, while addressing the following research question: *What design parameters can be implemented to passively tune the hydrodynamic modes in a nonlinear, under-actuated WEC device?*

This chapter is based on the following manuscript submitted for review, with a number of additional changes based on examiner comments:
Tran, N., Sergiienko, N. Y., Cazzolato, B. S., Ghayesh, M. H. and Arjomandi, M. (2022). "Design considerations for a three-tethered point absorber wave energy converter with nonlinear coupling between hydrodynamic modes". In: *Ocean Engineering* 254, p. 111351

Statement of Authorship

Title of Paper	Design considerations for a three-tethered point absorber wave energy converter with nonlinear coupling between hydrodynamic modes
Publication Status	☐ Published ☐ Accepted for Publication ☑ Submitted for Publication ☐ Unpublished and Unsubmitted w ork w ritten in manuscript style
Publication Details	Tran, N., Sergiienko, N. Y., Cazzolato, B. S., Ghayesh, M. H. and Arjomandi, M. (2022). "Design considerations for a three-tethered point absorber wave energy converter with nonlinear coupling between hydrodynamic modes", Submitted to *Ocean Engineering*.

Principal Author

Name of Principal Author (Candidate)	Ngan Tran
Contribution to the Paper	Developed ideas and concepts, conducted literature review Performed modelling • Developed a weak-scatterer (WS) model of the three-tethered WEC using the WS_CN code • Developed a fully linearised model of the system based on hydrodynamic parameters obtained using potential flow solver NEMOH • Developed a time-domain model in Simulink to study effect of geometric nonlinearities on the system • Verified all models in linear conditions with small wave amplitudes and body motions • Performed sensitivity studies varying the WEC design parameters in both regular and irregular waves using all three models • Conducted modal analysis to study resonance behaviour of the system Analysed results • Collected and stored data from simulations • Post processed data using Matlab • Analysed and compared results between all three models, generated plots • Used simulation results to generate trajectory plots to visualise WEC motion • Identified common trends in the obtained results between the different modelling approaches, wave scenarios and WEC design parameter combinations Writing • Wrote first full draft of manuscript • Applied comments and feedback provided by co-authors • Acted as corresponding author
Overall percentage (%)	85%
Certification:	This paper reports on original research I conducted during the period of my Higher Degree by Research candidature and is not subject to any obligations or contractual agreements with a third party that would constrain its inclusion in this thesis. I am the primary author of this paper.
Signature	Date: 01/12/21

Co-Author Contributions

By signing the Statement of Authorship, each author certifies that:

i. the candidate's stated contribution to the publication is accurate (as detailed above);

ii. permission is granted for the candidate in include the publication in the thesis; and

iii. the sum of all co-author contributions is equal to 100% less the candidate's stated contribution.

Name of Co-Author	Nataliia Y. Sergiienko		
Contribution to the Paper	Supervised the work, participated in developing ideas and concepts, helped analyse and interpret results, derived equation to approximate optimal tether angle, provided revision of manuscript		
Signature		Date	07/12/21

Name of Co-Author	Benjamin S. Cazzolato		
Contribution to the Paper	Supervised the work, participated in developing ideas and concepts, helped analyse and interpret results, provided revision of manuscript		
Signature		Date	01/12/21

Name of Co-Author	Mergen H. Ghayesh		
Contribution to the Paper	Supervised work, provided revision of manuscript		
Signature		Date	22/12/2021

Name of Co-Author	Maziar Arjomandi		
Contribution to the Paper	Supervised work, provided revision of manuscript		
Signature		Date	7/12/2021

Design considerations for a three-tethered point absorber wave energy converter with nonlinear coupling between hydrodynamic modes

N. Tran, N. Y. Sergiienko, B. S. Cazzolato, M.H. Ghayesh, M. Arjomandi

Abstract

Multi-mode Wave Energy Converters (WECs) are designed to harvest energy simultaneously from multiple hydrodynamic modes, thereby maximising power absorption. The behaviour of each operational mode must be carefully considered, given that hydrodynamic and geometric coupling between modes can lead to severe reductions in power if improperly designed. This study aims to investigate how the design of a planar three-tethered WEC can be used to tune the behaviour of the surge, heave and pitch hydrodynamic modes to achieve maximum power absorption. The effect of various design parameters, namely the power take-off control parameters, tether angles, tether attachment points, centre of gravity and rotational moment of inertia, on the performance of a WEC subjected to both geometric and hydrodynamic nonlinearities was investigated. Results indicated that, to absorb the most power in regular waves, the tether configuration should be adjusted such that two of its rigid body modes are resonant with the incident wave. For this WEC, these rigid body modes should contain predominantly surge and heave motions, since the contribution to power from pitch is relatively minimal. Geometric nonlinearities associated with the tether arrangement were found to cause sub-harmonic excitations which severely compromised device performance. The detrimental effect of these sub-harmonic excitations was further exacerbated when nonlinear hydrodynamics were considered, leading to greater losses of power. In irregular waves, surge and heave remained the primary absorption modes for power, although the optimal design was more strongly driven by performance in surge. Overall, maximum power was achieved when the WEC was tuned according to the dominant excitation frequency in surge, and when all three tethers were attached close to one another on the bottom of the buoy.

6.1 Introduction

Despite the numerous Wave Energy Converter (WEC) prototypes proposed over the years, there is still no convergence on the best design. An emerging

category of point absorber designs are multi-mode converters, which are capable of absorbing power from multiple hydrodynamic modes simultaneously. Compared to an axisymmetric Point-Absorber (PA) WEC operating in heave only, a multi-mode WEC can potentially harvest up to three times more power from incoming waves [9].

In this paper, the term '*multi-mode converter*' is used to refer to devices that are designed to harvest power from several hydrodynamic modes (i.e. surge, heave or pitch) simultaneously. It is also necessary to note that these *hydrodynamic modes* are distinct from a device's *rigid body modes* of vibration, which may result from the Power Take-Off (PTO), mooring configuration or the design of the WEC itself (e.g. hinged multi-body devices). Devices with only one dominant hydrodynamic mode for power absorption (e.g. heave) are not included in the category of '*multi-mode converters*' as defined here, irrespective of the number of rigid body modes or their ability to move in multiple directions at once.

When developing multi-mode WECs, it is necessary to consider the effect of each hydrodynamic mode on the total power absorption efficiency of the device. However, this can prove challenging due to the coupled interactions between hydrodynamic modes. As a result, it is not sufficient to simply employ the design methodologies typically used for generic single-DOF converters, as this could potentially lead to sub-optimal performance [36, 45]. It is therefore necessary to carefully consider both the controller and geometric design of the device itself when developing multi-mode WECs, since these aspects can significantly influence the coupled dynamics of the system.

Regarding the design of the controller specifically, several researchers have attempted to address the multi-Degree-of-Freedom (DOF) control of WECs operating in the surge, heave and pitch modes simultaneously. In an early study, Yavuz [51] considered the active control of a floating WEC, and suggested that coupling between the surge and pitch modes could potentially be used to improve the performance of the device. Control of a planar three-DOF floating WEC was also considered in a later study by Abdelkhalik et al. [2] who, in contrast to Yavuz, recommended only using either surge or pitch for power absorption. Energy could instead be shifted from one mode to the other through their coupled dynamics, allowing the system to absorb the same amount of power as when both surge and pitch were active simultaneously, while also reducing the number of actuators required. Various other studies have also considered the Multiple-Input Multiple-Output (MIMO) control of similar floating multi-DOF WEC devices [1, 20, 52], including experimental testing in a more realistic ocean environment by

Coe et al. [5]. However, while the controllers in these studies were designed to take into account coupling between hydrodynamic modes, the significance of this coupling on performance was not examined. Furthermore, all of the aforementioned studies also assumed fully-actuated devices capable of independent control in all hydrodynamic modes.

For under-actuated devices with more complex actuator systems, separate studies by Sergiienko et al. [36, 41] and Hillis et al. [14] have also attempted to apply MIMO velocity tracking control strategies to multi-tethered systems based on the CETO-6 and WaveSub WECs, respectively. However, like most controllers that have been developed specifically for multi-mode WECs, the strategies developed in these studies were designed under the assumption of linear hydrodynamics. This is an important consideration, given that control strategies developed based on linear hydrodynamic models have consistently led to over-estimations of power when compared to results from higher fidelity models [6].

Apart from the controller, the geometric design and actuation systems of the WEC can also influence the behaviour of each hydrodynamic mode relative to one another. While many studies have addressed the geometric optimisation of wave energy converters [12, 13], studies focused on the design of multi-mode converters specifically are comparatively limited. A number of studies have attempted to optimise the shape of the buoy used in multi-mode WECs, such as the CETO-6 [25, 42], Triton WEC [34] and CECO [33] devices, in order to improve the power absorbed by at least two different modes simultaneously. Aside from the shape of the buoy, there are various other aspects of the device design that can also have an effect on its performance. For example, Sergiienko et al. [37] demonstrated how the buoy aspect ratio and tether angles in a multi-mode cylindrical WEC with three tethers arranged in a 'tripod' configuration, similar to the CETO-6 device, can be adjusted to achieve a greater power absorption from either surge or heave. In another study, Fararggiana et al. [10] applied a genetic algorithm to determine the ideal values for various device parameters, such as the floater spacing and PTO settings, in an attempt to minimise the levelised cost of electricity of the WaveSub device. In a study by Meng et al. [22], the location of an offset mass was used as a design variable to modify the response of a multi-mode asymmetric spherical point absorber. Improvements in power were observed for mass offset configurations which facilitated coupled motions between the surge and heave modes.

Overall, most studies indicate that surge and heave are the most effective hydrodynamic modes for power absorption in multi-mode WECs, whereas the effect of the pitch mode is often neglected. This is partly due to the

geometries considered - if the buoy is spherical or sufficiently small, the influence of pitch on the device response is expected to be relatively minimal overall. However, for other geometries or larger WECs, pitch motions can significantly influence the behaviour in surge and heave due to hydrodynamic coupling between modes. This was demonstrated in a study by Sergiienko et al. [36], who considered the MIMO control of a submerged cylindrical WEC. While the controller was designed to optimise the heave and surge motions, hydrodynamic coupling effects with pitch were neglected. As a result, up to 15% of the total power was lost through the pitch mode.

The effect of coupling between modes on performance can become even more apparent when nonlinear hydrodynamic forces are considered. Using a weakly nonlinear numerical model, Tran et al. [45, 46] studied the nonlinear hydrodynamic coupling caused by changes to the projected area of a cylindrical WEC due to large pitching motions. Results indicated that nonlinear hydrodynamic coupling can severely compromise performance if the operational DOFs in a multi-mode system are not correctly tuned, especially in cases where large pitch motions are also present. It is therefore critical to consider methods of minimising the influence of coupling with pitch in the design and control of multi-mode WECs, especially since it is often difficult to restrain pitch in practice.

The motivation of this study is to provide insight into the application of geometric design for passive tuning of the surge, heave and pitch hydrodynamic modes in a three-tethered cylindrical WEC. The WEC design is influenced by Carnegie Clean Energy's CETO-6 device, consisting of a flat cylindrical buoy and three tethers which allow the device to harvest energy from surge, heave and pitch simultaneously. This study also aims to identify the impact of various system nonlinearities on the performance of this multi-mode WEC, namely those caused by the tether arrangement and hydrodynamic coupling.

The paper is organised as follows. Details pertaining to modelling of the system, such as the WEC dimensions and equations of motion, are provided in Section 6.2. The sensitivity of the WEC performance to different design parameters in regular waves is analysed using a fully linearised model in Section 6.3. Section 6.4 then introduces geometric and hydrodynamic nonlinearities to the system in order to determine their effects on the overall performance of the multi-mode WEC. The performance of the multi-mode WEC in irregular waves is considered in Section 6.5. The paper is concluded in Section 6.6.

6.2 Wave energy converter model

This section describes the multi-mode WEC system and numerical models which were considered in this study. Three numerical modelling approaches were used to analyse the performance of the multi-mode WEC:

(1) A fully linearised Frequency Domain (FD) model,

(2) Time Domain (TD) modelling implemented in Simulink/ MATLAB,

(3) A weakly nonlinear potential flow model based on the Weak-Scatterer (WS) approximation [28].

These modelling approaches were used to study and distinguish between the effects of the two key nonlinearities considered in this work: (1) geometric nonlinearities due to the tether system and (2) hydrodynamic nonlinearities caused by the changes in the instantaneous position of the WEC due to large amplitude motions. The TD model was used to observe the effects of geometric nonlinearities on the system alone, while the WS model included both geometric and hydrodynamic nonlinearities. The key assumptions and equations relevant to each modelling approach will be discussed in the following subsections.

6.2.1 System description

The multi-mode system investigated in this study consists of a fully submerged, disk-like WEC with a three-tether mooring configuration, as illustrated in Fig. 6.1. In addition to anchoring the buoy to the sea floor, each inclined tether is also connected to a PTO unit, allowing the WEC to harvest energy from surge, heave and pitch motions simultaneously.

The constant parameters of the WEC used in this study are given in Table 6.1, which are based on design parameters previously proposed for Carnegie Clean Energy's full-scale CETO-6 device [32]. Based on its dimensions, the device can be classified as a quasi-PA type WEC [44]. Due to the large pitch amplitudes considered in this study, a relatively deep submergence depth of d_s = 6.5 m (taken from the centre of the buoy) was used in the analysis to prevent the WEC from breaking the free-surface and resulting in an invalidation of the assumptions of the WS model. This depth is also consistent with the value used in [45, 46], which allows for more direct comparisons to be drawn between the results of this analysis and those reported in the aforementioned studies.

Table 6.1: WEC parameters.

Parameter	Notation	Value
Radius	a	12.5 m
Height	H	5 m
Mass	m	1.99 $\times 10^6$ kg
Water depth	d	30 m
Submergence depth	d_s	6.5 m

For the preliminary analysis, it was assumed that the buoy was excited by linear, monochromatic plane waves travelling purely in the positive x-direction. Irregular waves were then introduced and discussed in Section 6.5. Only planar motions in the xz-plane were considered, denoted by the position vector $\mathbf{x} = [x_1\ x_3\ x_5]^\mathsf{T}$. The subscripts 1, 3 and 5 refer to the surge, heave and pitch hydrodynamic modes, respectively. For this WEC design, it is assumed that the rotary PTOs allow sufficiently large extensions of tethers and hence displacement constraints were not included in this study. This assumption also allows nonlinear behaviours of the WEC to be more clearly identified. However, depending on the design of the real-life device, the power delivered in practice may be lower than the values reported here.

Each tether is connected to a PTO unit, which is modelled as a spring-damper system that generates a force proportional to the tether displacement and velocity. Two main parameters were used to define the geometry of the tethers: the tether inclination angle α and the horizontal tether attachment location on the buoy hull x_{TA}. In this study, it was assumed that the PTO parameters, tether angles and attachment point locations were identical for

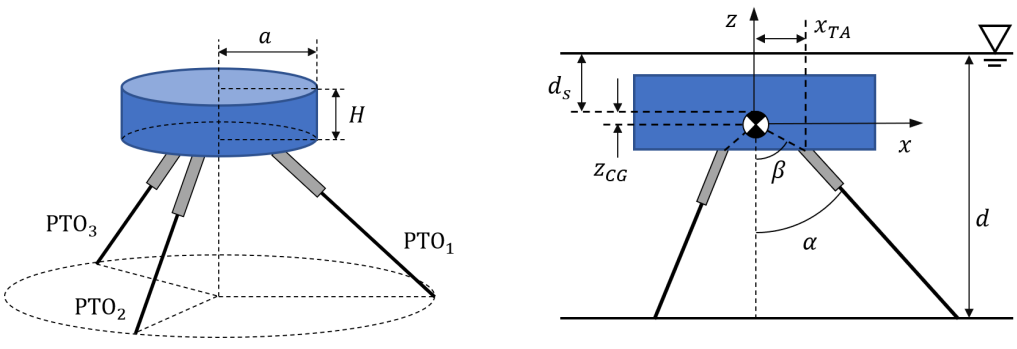

(a) (b)

Figure 6.1: Schematic of the three-tether WEC: (a) 3D view and (b) front view (xz-plane). Not to scale.

all three tethers. The vertical position offset between the centre of gravity and the geometric centre of the buoy was also investigated and is denoted by z_{CG}. Horizontal position offsets of the centre of gravity were not considered in this study. From the values of x_{TA} and z_{CG}, the angle between the centre of gravity and tether attachment points can also be calculated, denoted by β.

6.2.2 Equations of motion

Assuming an incident wave travelling along the positive x-direction, the equation describing the dynamic motion of the WEC in the planar surge, heave and pitch modes can be written as:

$$\mathbf{M}\ddot{\mathbf{x}}(t) = \mathbf{F}_{\text{buoy}}(t) + \mathbf{F}_{\text{visc}}(t) + \mathbf{F}_{\text{PTO}}(t) + \mathbf{F}_{\text{hyd}}(t)\,, \tag{6.2.1}$$

where $\mathbf{M}$ is the mass matrix and $\ddot{\mathbf{x}}$ is the acceleration at the centre of gravity of the buoy. The main forces acting on the buoy, $\mathbf{F}_{\text{buoy}}$, $\mathbf{F}_{\text{visc}}$, $\mathbf{F}_{\text{PTO}}$ and $\mathbf{F}_{\text{hyd}}$ are the buoyancy, viscous, PTO and hydrodynamic (excitation and radiation) forces, respectively.

The vector $\mathbf{F}_{\text{buoy}}$ consists of the buoyancy force in heave and a moment in pitch generated by the offset between the centre of gravity and the centre of buoyancy:

$$\mathbf{F}_{\text{buoy}}(t) = \begin{bmatrix} 0 \\ (\rho V - m)g \\ (\rho V - m)g z_{CG} \sin(x_5) \end{bmatrix}, \tag{6.2.2}$$

where ρ is the density of water, V and m are the volume and mass of the buoy, respectively, and g is the acceleration due to gravity. The buoy is positively buoyant, with the PTO and tether systems providing the tension required to keep the device fully submerged.

The viscous drag force in surge and heave can be modelled based on the Morison equation [24], while the pitch damping moment due to viscous effects can be calculated from the product of drag force and moment lever from the pitch axis [16, 17]:

$$\mathbf{F}_{\text{visc}}(t) = \begin{bmatrix} -\frac{1}{2}\rho C_{Dx} A_x |\dot{x}_1 - \dot{x}_{f,1}|(\dot{x}_1 - \dot{x}_{f,1}) \\ -\frac{1}{2}\rho C_{Dz} A_z |\dot{x}_3 - \dot{x}_{f,3}|(\dot{x}_3 - \dot{x}_{f,3}) \\ -\frac{1}{2}\rho C_{Dxz} D^4 D |\dot{x}_5| \dot{x}_5 \end{bmatrix}, \tag{6.2.3}$$

where C_{Dx}, C_{Dz}, C_{Dxz} are the viscous drag coefficients in surge, heave and pitch, respectively. A_x and A_z denote the cross-sectional areas of the buoy in surge and heave, respectively, while $D = 2a$ is the diameter of the buoy.

The buoy velocity in the j-th hydrodynamic mode is denoted by $\dot{x}_j$, while the undisturbed fluid particle velocity in surge and heave at the position of the geometric centre of the buoy is denoted as $\dot{x}_{f,1}$ and $\dot{x}_{f,3}$, respectively. The viscous drag effects were considered independently in each hydrodynamic mode, assuming fixed cross-sectional areas. The viscous drag coefficients in surge, heave and pitch respectively were taken as $C_{Dx} = 1$, $C_{Dz} = 1.2$ and $C_{Dxz} = 0.2$, based on published results from [15, 31].

In the linear FD model, the nonlinear quadratic terms in Eq. (6.2.3) were approximated using a Lorentz linearisation approach [11, 23, 43]. Therefore, in the FD model and for each wave height condition, the viscous drag forces can alternatively be modelled as:

$$\hat{\mathbf{F}}_{\text{visc}}(\omega) = -\mathbf{B}_{\text{visc}}(\omega)\hat{\mathbf{u}}(\omega)\,, \tag{6.2.4}$$

where ^ denotes the complex amplitude, $\hat{\mathbf{u}}$ is the velocity of the buoy in the frequency domain and $\mathbf{B}_{\text{visc}}$ is the matrix containing the linearised viscous damping coefficients.

6.2.3 PTO and power absorption

The full nonlinear equations for the tether forces have been previously derived in [40, 41] for a three-tethered WEC, hence only the key points will be outlined here.

It is assumed in this study that the PTO system does not contain any hard-stop motion constraints. The total PTO force acting along the i-th tether is therefore modelled as [3]:

$$F_{\text{tether},i}(t) = C_{\text{PTO}} - B_{\text{PTO}}\Delta\dot{\ell}_i(t) - K_{\text{PTO}}\Delta\ell_i(t)\,, \tag{6.2.5}$$

where the damping and stiffness coefficients applied to each tether are denoted B_{PTO} and K_{PTO}, respectively. It is also assumed that all the tethers remain taut ($F_{\text{tether,i}} > 0$) throughout the operation of the device. The term C_{PTO} is a constant force that counteracts the buoyancy force experienced by the WEC in an undisturbed position, given by:

$$C_{\text{PTO}} = -\frac{(\rho V - m)g}{3\cos\alpha}\,. \tag{6.2.6}$$

The change in the length of the i-th tether is denoted $\Delta\ell_i$. The rate of change of the tether length can be mapped from the WEC velocities in the Cartesian coordinate frame using the inverse kinematic Jacobian [37]:

$$\dot{\mathbf{q}}(t) = \mathbf{J}^{-1}(t)\dot{\mathbf{x}}(t)\,, \tag{6.2.7}$$

where $\mathbf{q}$ is a vector containing the tether length variables $\mathbf{q} = [\ell_1\ \ell_2\ \ell_3]^\mathsf{T}$ and $\mathbf{J}^{-1}$ is the inverse kinematic Jacobian.

Since the instantaneous tether length and inverse kinematic Jacobian are both position-dependent, the PTO force acting on the WEC is therefore nonlinear. The full nonlinear tether forces are included in both the TD and WS models. Through the 'small angle' approximation, the linearised tether forces can also be calculated in the FD model using the WEC motions in the Cartesian coordinate frame:

$$\hat{\mathbf{F}}_{\text{PTO}}(\omega) = -\mathbf{K}_t\hat{\mathbf{x}}(\omega) - \mathbf{B}_t\hat{\mathbf{u}}(\omega)\,, \tag{6.2.8}$$

where $\mathbf{K}_t$ and $\mathbf{B}_t$ can be found in [35].

The total instantaneous power absorbed by the system is determined by summing the mechanical power dissipated by the PTO dampers along each tether:

$$P(t) = B_{\text{PTO}}\sum_{i=1}^{3}\left(\Delta\dot{\ell}_i(t)\right)^2. \tag{6.2.9}$$

In the FD model, Eq. (6.2.9) can be re-written to give the time-averaged power absorbed by the WEC [9]:

$$\overline{P} = \frac{1}{2}B_{\text{PTO}}\sum_{i=1}^{3}\left|\Delta\hat{\dot{\ell}}_i\right|^2, \tag{6.2.10}$$

where $\Delta\hat{\dot{\ell}}_i$ can be calculated using the inverse kinematic Jacobian at the nominal position of the buoy.

6.2.4 Hydrodynamic modelling

The FD and TD models used in this study both employ linear hydrodynamic coefficients calculated from semi-analytical equations [18, 19], which have been previously validated against results from a higher-order boundary element method. These equations can be used to find the excitation and radiation forces acting on the WEC about its equilibrium position. The values used to model the excitation force $\mathbf{F}_{\text{exc}}$, added mass matrix $\mathbf{A}$ and radiation damping matrix $\mathbf{B}$, can be found in Appendix 6.A.

For the TD simulations, Eq. (6.2.1) was implemented in Simulink/MATLAB. The ode45 solver was used with a time step of $\Delta t = 0.01$ s and total simulation time of $300 \times T$, where T is the period of the incident wave. The transient response in the first $15 \times T$ was omitted in the analysis. The Marine Systems Simulator toolbox [29] was used to obtain a state space representation

of the convolution integrals for the radiation forces. Values of the infinite-frequency added mass were obtained using the boundary element method solver NEMOH [4].

To capture the effects of nonlinear hydrodynamic coupling between modes, a weakly-nonlinear potential flow model based on the WS approximation [28] was used. The code for the WS numerical model used in this study was developed by École Centrale de Nantes (ECN) [21]. This model also performs simulations in the time domain; however, the instantaneous hydrodynamic forces are calculated using the position of the WEC at each time step. It is noted that nonlinearities related to surface piercing and wave breaking effects cannot be captured using this model and are therefore considered outside the scope of this study.

Justification for the use of the WS modelling approach was provided previously in [45], while more detail about the mathematical theory and assumptions of the WS model can be found in [21, 49, 50]. A more detailed comparison of the key differences between the WS, linear potential flow and CFD models with regards to WEC applications can also be found in [8]. Validation of the ECN WS code used in this study against other available hydrodynamic models and experimental data has also been performed in [48] and [47], respectively.

All three models were further verified for the three-tethered case used in this study by comparing results from linear cases with a small wave amplitude of $A_w = 0.1$ m. A very good match was achieved across all three models for these cases. Mesh and time step convergences were also checked for the WS model, as detailed in Appendix 6.B. A value of $\Delta dx = \lambda/250$ (where λ is the wavelength of the incoming wave) was used for the smallest mesh elements on the free-surface above the cylinder in the WS model. For the time step, a value of $\Delta t = T/300$ was used. The cylindrical body was meshed using approximately 4000 panels, while 2800 to 3200 panels were used for the free-surface mesh depending on the incident wavelength.

6.3 Sensitivity study of the linear model

The sensitivity of the WEC performance to various design parameters was first examined using the linear FD model. Five main design parameters were initially considered as part of the sensitivity study. The selected design parameters were the PTO stiffness K_{PTO}, the tether attachment angle α, the horizontal position of the tether attachment points on the bottom of the buoy x_{TA}, the vertical position of the centre of gravity z_{CG} and the rotational

Table 6.2: Design parameters used in the sensitivity study.

Order	Design parameter	Notation	Unit	Min	Max	Nominal
1	PTO stiffness	K_{PTO}	N/m	5×10^5	5×10^7	N/A
2	Tether angle	α	deg	0	85	28.3
3	Tether attachment point	x_{TA}	m	0	12.5	0.53
4	Centre of gravity position	z_{CG}	m	-2.5	2.5	0
5	Pitch moment of inertia	I_{yy}	kg·m^2	1.07×10^3	3.11×10^8	8.19×10^7

moment of inertia in the pitch axis I_{yy}. The design parameters are listed in Table 6.2, along with the upper, lower and nominal values considered for each parameter.

For most design parameters, the minimum and maximum values were constrained by the physical dimensions of the device (e.g. buoy radius and height). The PTO stiffness was constrained to values between 0.1-10$\rho g \pi a^2$ (where $\rho g \pi a^2$ is a normalisation factor based on the hydrostatic stiffness of an equivalent floating buoy). For the pitch moment of inertia I_{yy}, the nominal value was taken as the moment of inertia for a solid cylinder with evenly distributed mass. The lower limit was defined as the moment of inertia if all the WEC mass was theoretically concentrated in a sphere of radius 0.1 m at the centre of the buoy. The upper limit of the moment of inertia occurs when all the WEC mass is distributed in a ring along the outer radius of the buoy. The nominal values for K_{PTO}, α and x_{TA} were determined during the analysis process, with more details given in the following subsection.

6.3.1 Power absorbed

A systematic grid search was used to obtain a holistic picture of the sensitivity of the WEC performance across the range of parameters listed in Table 6.2. To reduce computational costs and better characterise the search space, the analysis was limited to pairs of grid searches. In other words, for each possible pair of design parameters, the power absorbed by the WEC was determined as these two parameters were varied, while all other parameters were kept constant at the nominal values given in Table 6.2. An exception to this arrangement was the grid search where K_{PTO} and α were the pair of parameters being varied. In this case, the value of x_{TA} was adjusted such that $\alpha = \beta$ for all values of α. The PTO damping value B_{PTO} was optimised at every point in the grid search, such that it maximised the power that could be absorbed by the WEC for all cases considered. Further information regarding the optimal PTO damping values is given in Appendix 6.C. The PTO stiffness

K_{PTO} was also optimised for all grid search points, with the exception of cases where it was one of the design parameters being varied. The design parameter pairs were investigated sequentially according to the order given in Table 6.2, hence the nominal values of α and x_{TA} were chosen based on optimal configurations from previous tests.

The full sensitivity analysis was performed for regular waves with an amplitude of $A_w = 0.5$ m across a range of frequencies of $\omega_{ex} = 0.5$-1.0 rad/s. These excitation frequencies were considered based on the expected

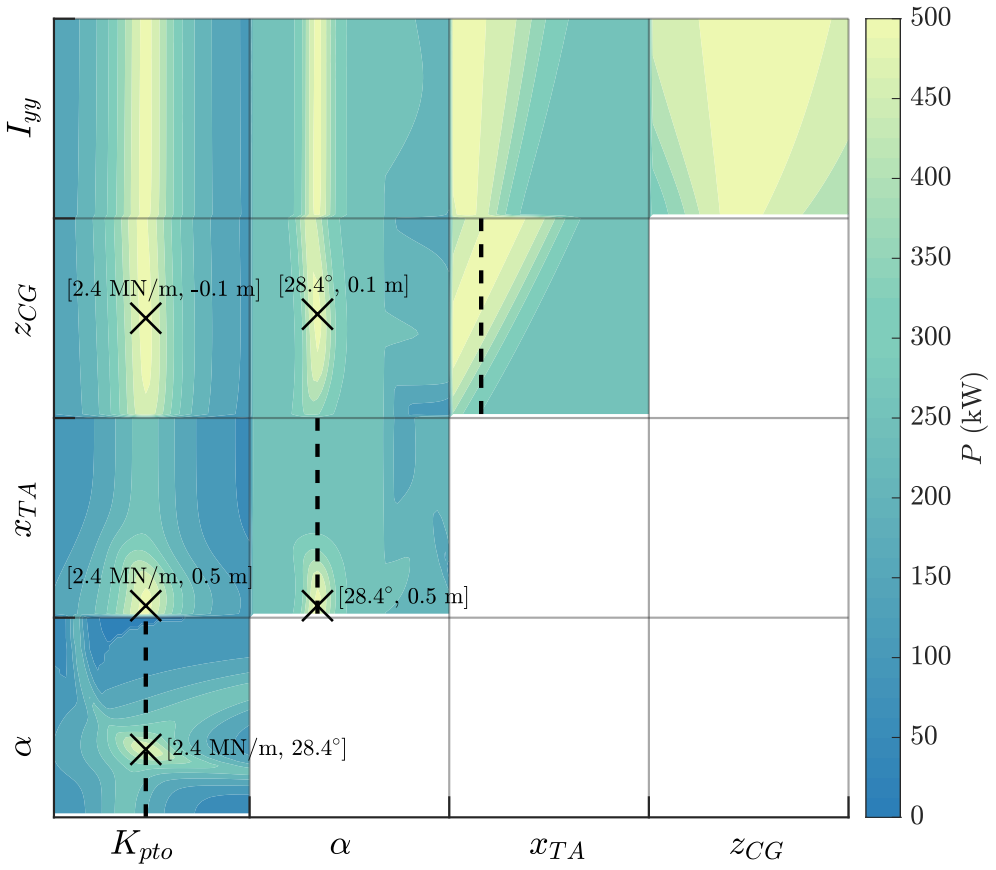

Figure 6.2: Sensitivity matrix showing the change in total power absorbed by the WEC as the design parameters are varied. Results are from the linear FD model assuming regular waves with frequency $\omega_{ex} = 0.6$ rad/s and amplitude $A_w = 0.5$ m. Unique parameter pairs that resulted in maximum power are also indicated by a cross in the figure. The dashed lines indicate sections of the results where more detailed power and modal analysis was conducted.

operating range of the actual CETO-6 device. The grid search results for waves with an excitation frequency of $\omega_{ex} = 0.6$ rad/s are displayed in the matrix shown in Fig. 6.2. Whilst not presented here, the trends identified across the full range of frequencies are reflected in this figure.

From this analysis, K_{PTO}, α and x_{TA} were identified as the parameters that had the greatest effect on the power absorbed by the WEC. Unsurprisingly, when K_{PTO} was not properly optimised, there were cases where the power absorption capability of the device dropped to only 3% of the maximum total power. The device was far from resonance in these cases, hence the phase optimality conditions between the wave excitation force and device velocity could not be fulfilled. For the tether angle α, assuming K_{PTO} was optimised and all other parameters were kept constant, power reductions of up to 53% were observed when this parameter deviated significantly from its optimal value. Similarly, assuming optimal K_{PTO} and α, sub-optimal locations of x_{TA} could result in decreases of up to 47% of the total maximum power.

Regarding the centre of gravity location z_{CG}, its optimal position appeared to be dependent on the tether attachment point location x_{TA}. If x_{TA} was already optimised, there was minimal benefit in shifting z_{CG} from its nominal value. In fact, changing z_{CG} was more likely to result in losses to power instead, with up to a 37% reduction in the maximum total power when the centre of gravity was shifted to the bottom of the buoy. Finally, out of all the design parameters considered, the WEC performance appeared to be least affected by the pitch rotational moment of inertia I_{yy}. When all other parameters were optimised, adjusting this value only resulted in a 1% difference in total power.

While Fig. 6.2 gives an indication of the overall sensitivity of the total absorbed power to the design parameters, the effect of these parameters on each hydrodynamic mode individually is not as obvious. Additional analysis was therefore conducted to explore the effect of each key design parameter on the power absorbed by each hydrodynamic mode in greater detail.

6.3.2 Contribution of hydrodynamic modes to power

The total power absorbed by the WEC was then decomposed into the power absorbed from each of the heave, surge and pitch modes individually. The contribution of each mode, given an incident wave with $\omega_{ex} = 0.6$ rad/s and $A_w = 0.5$ m, is shown in Fig. 6.3 for varying values of α, x_{TA} and z_{CG}. For clarity, only relevant slices of the full results, indicated by the dashed lines in Fig. 6.2, are displayed and analysed here. In Fig. 6.3(a), the effect of α on the power absorbed by each hydrodynamic mode is shown (with

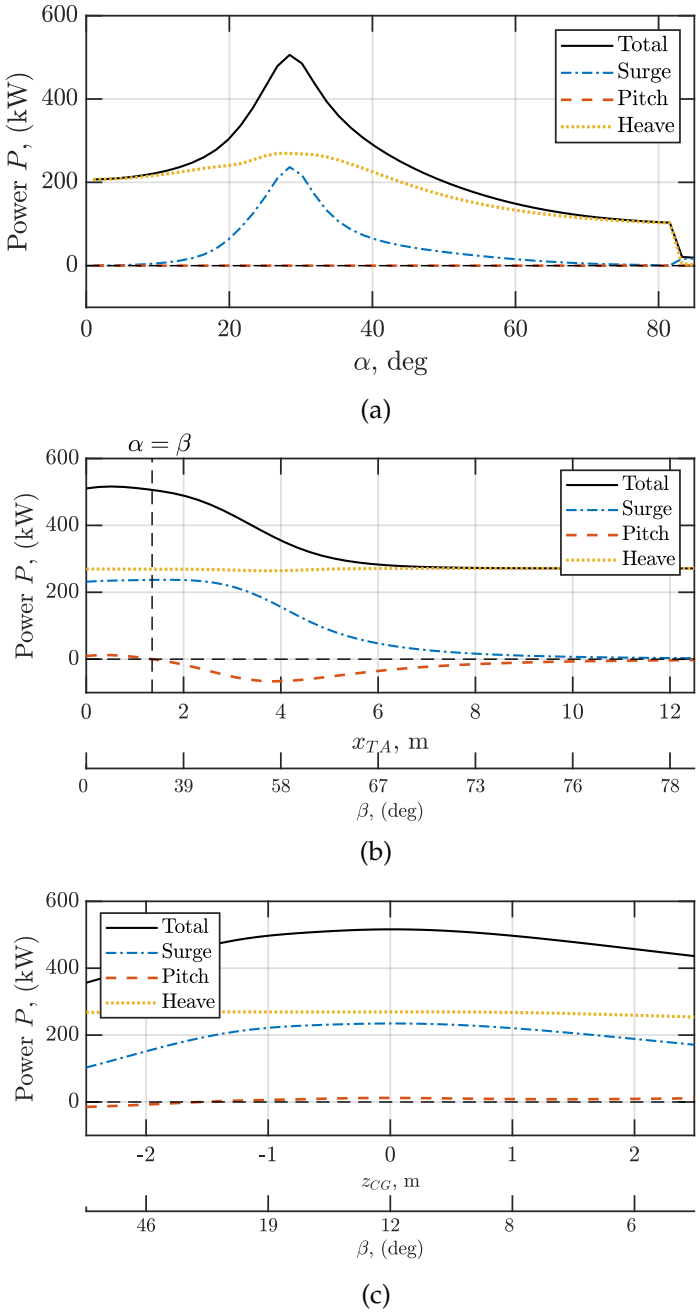

Figure 6.3: Contribution of each hydrodynamic mode to power in the linear FD model as the (a) tether inclination angle α, (b) tether attachment point location x_{TA} and (c) centre of gravity position z_{CG} is varied. Heave and surge are the primary modes of power absorption.

$\alpha = \beta$, as was the case in the grid search). The stiffness parameter K_{PTO} in this plot corresponds to the optimal value resulting in maximum power as identified from the grid search ($K_{\text{PTO}} = 2.4$ MN/m). Fig. 6.3(b) illustrates the effect of x_{TA} on power, with a constant tether angle of $\alpha = 28.3°$. The corresponding value of β is also displayed on the graph. In this plot, both K_{PTO} and B_{PTO} were optimised for all values of x_{TA} shown. In Fig. 6.3(c), the power absorbed by the WEC with different z_{CG} locations is shown, given a fixed tether inclination of $\alpha = 28.3°$ and tether attachment location of $x_{TA} =$ 0.53 m.

From the results shown in Fig. 6.3, it is clear that heave and surge are the main hydrodynamic modes for power absorption. In contrast, pitch does not contribute much to power overall, and in some configurations even results in reductions to the total power, which is consistent with the results of a previous study by Sergiienko et al. [36]. Although slight contributions to power from pitch were observed in some configurations, this gain was relatively minimal overall; hence, one can conclude that avoiding the potential losses from pitch should be the main focus when tuning the design parameters of the device.

Out of the design parameters considered, the tether angle α was particularly important as it determined the relative effectiveness of the surge and heave modes for power absorption (as previous identified by Sergiienko et al. [37]). In fact, apart from the PTO stiffness K_{PTO}, the tether angle was the only other parameter that had a noticeable effect on response of the heave mode. At very small tether angles, the WEC behaves similar to a single-tethered heaving point absorber, which consequently limits the power absorption ability of the surge mode. In contrast, heave becomes relatively less effective at very large tether angles. It is noted that power absorbed by surge appeared to be more sensitive to the tether angle than the power in heave. Overall, a total maximum power of 506 kW was achieved for a tether angle of $\alpha =$ 28.4°, which corresponds roughly to a 2.5 times increase compared to the case at $\alpha = 0°$ when only heave was contributing to power. This is close to the three-fold increase in power predicted by linear theory for an axisymmetric point absorber [9]. The slight reduction compared to the theoretical limit is due to the inclusion of viscous drag and is consistent with previous studies using linear hydrodynamic models.

The tether attachment location x_{TA} was also an important parameter due to its influence on the surge and pitch modes. Greater power was absorbed when the tether attachment distance from the axis of symmetry was small, with maximum power achieved at $x_{TA} = 0.5$m. Larger tether attachment distances resulted in poorer performance, with the power dropping quickly beyond $x_{TA} > 3$ m. The results therefore suggest that for this WEC geometry,

the tethers should be attached very close to one another on the bottom of the buoy.

Compared to previous studies featuring similar three-tethered cylindrical geometries these results differ from the findings reported in [39], but are in agreement with the results presented in [42]. This can be attributed to the shape of the buoys used in these studies. While the former study featured a taller buoy with a larger a/H aspect ratio, the findings in the latter study corresponded to a flatter cylinder similar to the one used in this paper. The shape of the WEC affects the hydrodynamic parameters - specifically the added mass - which in turn affects the natural frequency of the system, which will be discussed in more detail in the following subsection. Although the power absorbed by surge and pitch modes was also affected by the centre of gravity offset, the sensitivity to this parameter was not as significant as the tether attachment location.

Having identified the main modes for power absorption, the resonance behaviour of the WEC was then considered to further explain the distribution of power between the three hydrodynamic modes, and to determine how the overall system should be tuned for improved performance.

6.3.3 Modal analysis

Since the buoy considered in this study is fully submerged, the only stiffness provided to the WEC is through the tethers and PTO machineries [38]. Hence, by adjusting these parameters, the resonance behaviour and natural frequencies of the system can be controlled. The resonance behaviour of the system and its rigid body modes can be investigated by examining the eigenvalue problem:

$$(\mathbf{M} + \mathbf{A}(\omega))^{-1}\mathbf{K}_t - \omega_{ni}^2\mathbf{I} = \mathbf{0} \tag{6.3.1}$$

where $\mathbf{I}$ is the identity matrix. The eigenvectors obtained from this analysis denote the mode shapes of the system, while the square roots of the eigenvalues are the natural frequencies of each rigid body mode ω_{ni} ($i = 1,...,3$).

Due to the additional geometric coupling introduced by the tether arrangement, it is not possible to consider the resonance behaviour of the surge, heave and pitch modes independently. Instead, the system's rigid body modes of vibration (not to be confused with the hydrodynamic modes) must be considered instead. A graphical representation of the planar rigid body modes of the system are shown in Fig. 6.4. Modes 1 and 2 both feature motions in surge and pitch but can differ in terms of the relative amplitudes

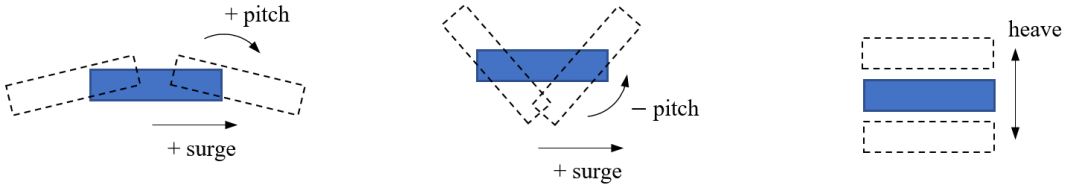

(a) Mode 1 (b) Mode 2 (c) Mode 3

Figure 6.4: Graphical representation of the planar rigid body modes of the three-tethered WEC obtained from the linear eigen analysis.

and phases of surge and pitch in each rigid body mode. The natural frequencies of Modes 1 and 2 are also separate, so the overall buoy motion in surge and pitch will depend on which mode is being excited by the incident waves. Note that the visualisations shown in Fig. 6.4 are representative only. The relative phases between surge and pitch may vary between Modes 1 and 2 depending on the design parameters. However, the important detail to note is that in most cases, Mode 1 is more surge dominant, while Mode 2 contains relatively larger pitch motions. Mode 3 involves heave motions almost exclusively.

The natural frequencies of the rigid body modes for various design parameter combinations are shown in Fig. 6.5. Similar to the analysis presented in Section 6.3.2, the results shown here also correspond to the configurations indicated by the dashed lines in Fig. 6.2, with $\omega_{ex} = 0.6$ rad/s and $A_w = 0.5$ m. By examining Fig. 6.3 and Fig. 6.5 together, it can be seen that in the cases with the most power absorbed, the natural frequencies of Modes 1 and 3 were equal to the incident wave frequency. This is consistent with the modal analysis of a three-tethered WEC performed in a previous study by Ding et al. [7]. Using this conclusion, and ignoring the coupling between surge and pitch, an approximate expression for the optimal tether angle α_{opt} can be found for the case where $\alpha = \beta$:

$$\alpha_{\text{opt}} \approx \tan^{-1} \sqrt{2 \times \frac{m + A_{11}(\omega_{ex})}{m + A_{33}(\omega_{ex})}}. \tag{6.3.2}$$

where A_{jj} are elements of the added mass matrix $\mathbf{A}$. For cases where $\alpha \neq \beta$, it is difficult to obtain a simple expression for the optimal design parameters due to strong coupling between the surge and pitch modes.

The distribution of power between the three hydrodynamic modes displayed in Fig. 6.3 can also be explained by inspecting the natural frequencies of each rigid body mode in greater detail. In Fig. 6.3(a), the tether angle α resulting in maximum total power absorbed also corresponds to the angle where

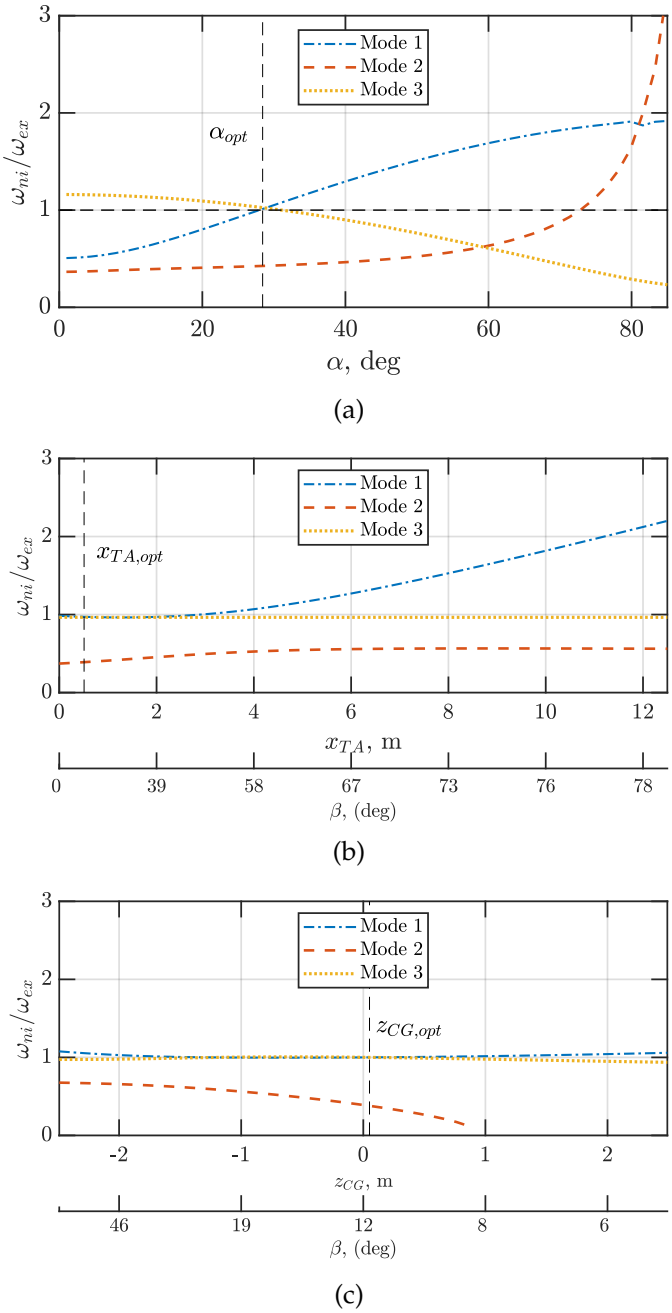

Figure 6.5: Natural frequencies of the planar rigid body modes as the (a) tether inclination angle α, (b) tether attachment point location x_{TA} and (c) centre of gravity position z_{CG} is varied. Optimal parameters resulting in maximum power absorbed are also indicated on the plots.

$\omega_{n1} = \omega_{n3} = \omega_{ex}$, as demonstrated in Fig. 6.5(a). The reduction in power absorbed by surge with increased tether attachment distances in Fig. 6.3(b) can be explained by the fact that the natural frequency of Mode 1 breaks away from ω_{ex} for $x_{TA} > 3$m in Fig. 6.5(b). Regarding the centre of gravity location, it can be seen in Fig. 6.5(c) that the natural frequencies of Modes 1 and 3 do not change much with z_{CG}; consequently, the power absorbed by the WEC system is not as sensitive to this design parameter as α and x_{TA}. Although not shown here, these results also explain why the system is relatively insensitive to the pitch moment of inertia I_{yy}. Of the three rigid body modes, only the pitch dominant Mode 2 is strongly affected by I_{yy}, hence its impact on the response of the WEC is relatively limited.

As indicated earlier, the trends discussed here for $\omega_{ex} = 0.6$ rad/s were also consistent across the full range of incident wave frequencies analysed. This is demonstrated in Fig. 6.6, which shows the natural frequencies of rigid body modes 1, 2 and 3 corresponding to the optimal WEC configurations resulting in the maximum power absorbed at each incident wave frequency. These optimal configurations were determined for each incident wave frequency using a similar grid search method as outlined in Section 6.3.1. A dashed line is also plotted to indicate where $\omega_{n_i} = \omega_{ex}$. Overall, it can be seen that the natural frequencies of Modes 1 and 3 generally remain close to the vicinity of ω_{ex} for the range of wave frequencies considered. It is noted that for $\omega_{ex} > 0.8$ rad/s, the natural frequencies of Modes 1 and 3 began to diverge slightly from ω_{ex}. This can be explained by examining Eq. (6.3.1). The added mass values are frequency dependent, so in cases where $\omega_{ex} > 0.8$ rad/s, there exists no design parameter combinations such that $\omega_{n_1} = \omega_{n_3} = \omega_{ex}$.

From this linear analysis, it can be concluded that the multi-mode WEC

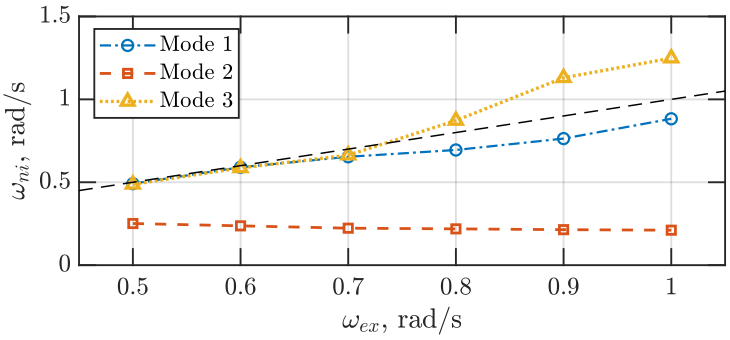

Figure 6.6: Optimal natural frequencies of the three-tethered WEC planar rigid body modes across a range of incident wave frequencies. The dashed line indicates where $\omega_{n_i} = \omega_{ex}$.

should be tuned such that the natural frequency of two of its rigid body modes are similar to the incident wave frequency to achieve maximum power absorption. Additionally, these rigid body modes should contain primarily surge and heave motions, as these are the hydrodynamic modes that contribute most to power. Overall, these results support the findings previously reported in [7, 36] for similar three-tether mooring systems.

6.4 Effect of nonlinear forces on performance

In this section, nonlinear forces are introduced and their resultant impact on the performance of the multi-mode WEC is analysed.

Sections of the sensitivity study, as marked by the dotted lines in Fig. 6.2, were reproduced in the TD and WS models using the same design parameter values as those used in the linear FD analysis in Section 6.3.2 (including PTO stiffness and damping). From this, the total power absorbed is compared between all three models in Fig. 6.7 for various tether angles and attachment point locations. It was found that varying the location of the centre of gravity did not lead to any divergent behaviour in the TD or WS models, so results corresponding to this case are not shown here. The power absorbed by each individual hydrodynamic mode is also compared between the different models in Fig. 6.8. All results displayed in these figures are for regular incident waves with a frequency of $\omega_{ex} = 0.6$ rad/s and amplitude $A_w = 0.5$ m.

From Figs. 6.7 and 6.8, it can be seen that the optimal values for α and x_{TA} remained approximately the same in all three models. It can hence be concluded that even with the inclusion of geometric and hydrodynamic nonlinearities, the natural frequencies of the rigid body modes corresponding to surge and heave should both be tuned to match the incident wave frequencies. This result is in contrast to the findings reported in [46], which stated that the natural frequencies of the surge, heave and pitch modes should all be decoupled for improved multi-mode performance when hydrodynamic nonlinearities were present.

The reason for this discrepancy can be attributed to the behaviour of pitch in the current study. For the analysis in [46], independent control was assumed, meaning that the only coupling between modes was through the hydrodynamic interactions. Due to the strong hydrodynamic coupling between surge and pitch, resonances in surge also resulted in high pitch amplitudes, which consequently affected the projected surface area and power absorbed in heave. In the current paper, the system was modally

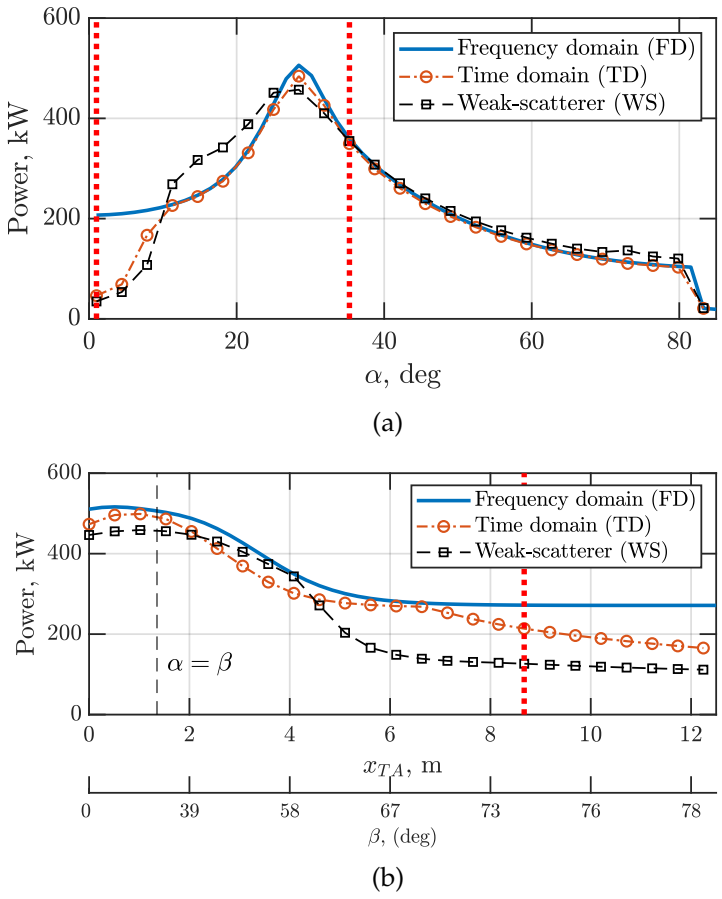

Figure 6.7: Comparison of total power absorbed by the WEC from all three models as the (a) tether inclination angle α and (b) tether attachment point location x_{TA} is varied. All results are for regular waves with frequency $\omega_{ex} = 0.6$ rad/s and amplitude $A_w = 0.5$ m. The thick, red dotted lines indicate configurations where the WEC trajectory was also analysed, as presented in Fig. 6.9

driven due to the geometric coupling from the tethers and PTOs. The pitch motion was therefore limited by the arrangement of the tethers in the surge dominant mode, so even when this mode was resonant, the pitch amplitude remained small. Having both the surge and heave modes simultaneously resonant was therefore acceptable in this case, since the power in heave was not adversely affected by nonlinear hydrodynamic coupling with pitch.

Conversely, when α and x_{TA} deviated from their optimal values in Figs. 6.7 and 6.8, the performance of the WEC in the three models became significantly different due to the introduction of nonlinear forces. Large discrepancies

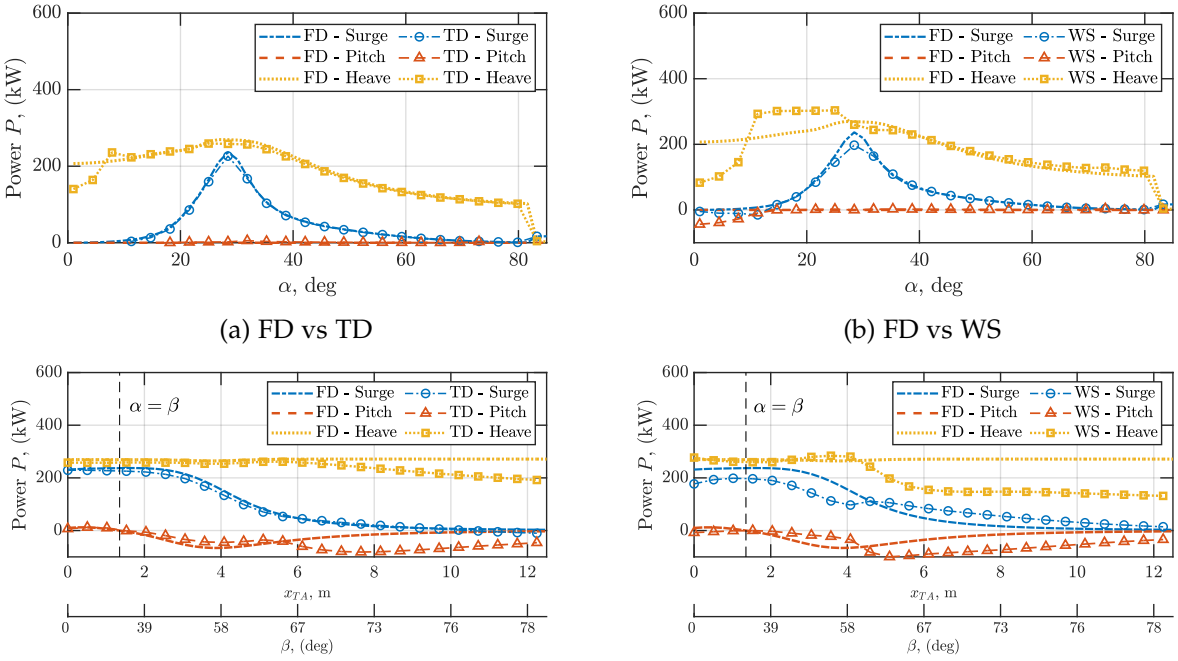

(a) FD vs TD

(b) FD vs WS

(c) FD vs TD

(d) FD vs WS

Figure 6.8: Comparison of power absorbed by each hydrodynamic mode in the different WEC models as the (a)-(b) tether inclination angle α and (c)-(d) tether attachment point location x_{TA} is varied. For clarity, the left-hand plots compare the FD and TD results while the right-hand plots compare the FD and WS results.

were observed for cases where the tether angle was small ($\alpha < 10°$) and when the location of the tether attachment points on the buoy hull were far apart ($x_{TA} > 4$m).

To investigate the causes for the discrepancies between the models, the trajectory of the buoy was plotted for certain configurations where large differences in the results were observed. These configurations of interest are marked by a dotted line in Fig. 6.7, and the trajectory of the WEC at these points as obtained from TD and WS models are shown in Fig. 6.9. The WEC pose at evenly distributed points in time throughout its orbit is also illustrated on the trajectory plots. Note that the WEC pitch rotations shown in these plots have been exaggerated to provide a clearer visualisation of the motion in pitch. Out of the trajectories shown, Fig. 6.9(b) and (e) are representative of 'typical' orbits obtained in cases where the WEC behaviour was consistent across all three models. In the other cases shown, the significant effect of nonlinearities on the dynamics of the system is clearly evident from the trajectory plots.

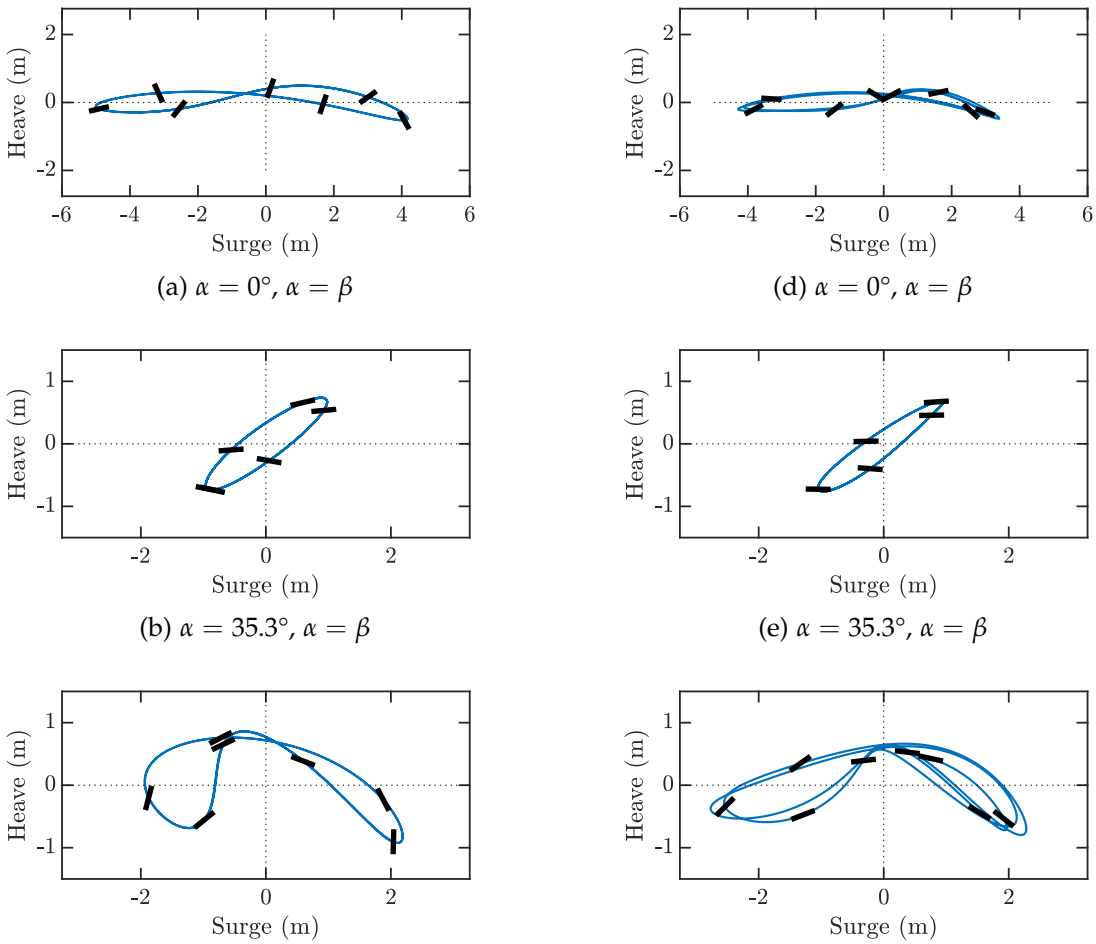

(a) $\alpha = 0°$, $\alpha = \beta$ (d) $\alpha = 0°$, $\alpha = \beta$

(b) $\alpha = 35.3°$, $\alpha = \beta$ (e) $\alpha = 35.3°$, $\alpha = \beta$

(c) $\alpha = 28.3°$, $x_{TA} = 8.7$ m (f) $\alpha = 28.3°$, $x_{TA} = 8.7$ m

Figure 6.9: Trajectory of the WEC as obtained from the (a)-(c) TD and (d)-(f) WS models for various tether configurations where discrepancies with the FD model were observed. Trajectories shown in (b) and (e) illustrate the 'typical' motions in cases where consistent behaviour was obtained across all three models. Note that the WEC rotation is not to scale.

The subsequent discussions will address the effects of geometric and hydrodynamic nonlinearities separately, in order to distinguish how each influences the dynamic behaviour of the system.

6.4.1 Geometric nonlinearities

Given that the discrepancies in power were observed in both the TD and WS models, it can be inferred that geometric nonlinearities associated with the

tether arrangement were the main cause for the large divergence from the linear FD results (rather than hydrodynamic nonlinearities).

From the trajectory plots, it can be seen that the period of the surge and pitch motions in the divergent cases are twice as long as the heave period. Referring back to the natural frequencies in Fig. 6.5, it can be seen that for these configurations, the natural frequency of Mode 2 is approximately half the incident wave frequency. From this, it can be deduced that the divergent behaviour observed in the TD and WS models was caused by sub-harmonic excitations of this rigid body mode.

Furthermore, it is noted that in these configurations, the natural frequency of Mode 1 is also far from incident wave frequency. Since both Modes 1 and 2 contain surge and pitch motions, the dominant mode will determine the overall response of the WEC in these two hydrodynamic DOFs. If Mode 1 is resonant, surge and pitch will oscillate at the fundamental frequency, leading to similar behaviour as predicted by the linear FD model. However, when $\alpha < 10°$ or $x_{TA} > 3.5$ m, Mode 1 moves away from resonance. Mode 2 therefore becomes the dominant mode for surge and pitch motions, resulting in the sub-harmonic behaviour observed in the TD and WS models.

The role of Mode 1 on the onset of this sub-harmonic behaviour can be observed most clearly in the results when the tether attachment location was varied. In Fig. 6.5(b), the natural frequency of Mode 1 begins to break away from the incident wave frequency around $x_{TA} \approx 3.5$ m. The power absorbed by the WEC in the TD and WS models also began to diverge from the FD results beyond this point, as seen in Fig. 6.8(c)-(d). The influence of Mode 1 also can also explain why sub-harmonic excitations were not observed for the results with varying centre of gravity. For all values of z_{CG} shown in Fig. 6.5(c), Mode 1 was close to resonance with the incident wave, which prevented the Mode 2 from being sub-harmonically excited.

A possible explanation for the sub-harmonic behaviour observed could be the occurrence of parametric instabilities, such as those reported by Orszaghova et al. [26, 27]. For regular waves, parametric excitation of a given mode has been shown to occur when the natural frequency was within a range around half the exciting frequency (with higher frequency 'instability branches' present as well), with the range depending on the damping and amplitude of parametric excitation. If so, this could mean that at sufficiently high wave amplitudes, the excitation of Mode 2 may potentially dominate the system response even in cases where Mode 1 is close to resonance.

Regarding power, since the motion amplitudes and phases were significantly disparate with those obtained the linear FD model, it is unsurprising that the cases with sub-harmonic excitations resulted in very different es-

timates of power across all three models. The optimal amplitude and phase requirements for maximum power absorption could no longer be achieved in the TD and WS models, greatly reducing the power absorption efficacy of the system as observed in Fig. 6.8. The reduction in power was greater in the WS model due to the effect of hydrodynamic nonlinearities, which will be discussed further in the following subsection. With regards to the tuning of the system, what can be concluded from this analysis is that if neither Mode 1 or 2 is resonant then it is critical to ensure that neither mode is tuned to a sub-harmonic of the system as well to avoid compromising the power absorption efficacy of the device. Imposing physical motion constraints such tether extension limits, which were not included in this study, could also potentially aid in suppressing the impact of this nonlinear behaviour on the WEC performance.

6.4.2 Hydrodynamic nonlinearities

The effect of nonlinear hydrodynamic coupling, caused by large changes in the instantaneous position of the WEC relative to its nominal position, was then considered. Given the flat shape of the buoy, its projected surface area can change significantly when the pitch amplitude is large. Consequently, the instantaneous hydrodynamic forces in both surge and heave are also affected, resulting in enhanced nonlinear hydrodynamic coupling between all three planar modes. This nonlinear coupling has been shown to be detrimental to performance [45, 46] and hence must be considered in the design of this multi-mode WEC.

Overall, the inclusion of nonlinear hydrodynamic forces exacerbated the effects of the geometric nonlinearities on performance. This is most evident by comparing the power absorbed in heave between the TD and WS models in Fig. 6.8. The significant reductions in power can be explained by observing key points in WS trajectories displayed in Fig. 6.9 (d) and (f). Of particular importance are points where the heave displacements are close to zero (i.e. where the velocity of the WEC in heave is also greatest). In Fig. 6.9 (d) and (f), as a result of the sub-harmonic excitations, it can be seen that the instantaneous position of the WEC in both surge and pitch were significantly shifted relative to its nominal position at these points. Additionally, the projected surface area of WEC in heave was noticeably reduced due to the relatively high pitch rotation in these instances. Consequently, the heave excitation force acting on the WEC would also have been smaller in the WS model compared to the values calculated from the linear hydrodynamic models. As a result, the reduction in total power absorbed was even greater

in the WS model compared to the TD model. These results are consistent with the findings reported in [46].

The presence of hydrodynamic nonlinearities also appeared to make the system more susceptible to sub-harmonic excitations. Examining the TD results in Fig. 6.8(a) and (c), as well as the natural frequencies of the system in Fig. 6.5, it can be seen that the sub-harmonic excitations only began to significantly affect the response of the system after the natural frequency of Mode 1 had shifted sufficiently far away from the incident wave frequency. In contrast, the performance of the WEC in the WS model in Fig. 6.8(b) and (d) began to diverge away from the linear FD results even when the difference in frequencies was much smaller. Tuning the natural frequencies of the three-tethered WEC in reality may therefore require greater care than what linear hydrodynamic models would suggest, since even small inaccuracies could result in large deviations in the expected behaviour.

There were also a number of additional observations which were unique to the WS results. In Fig. 6.7(a), it can be seen that for a range of tether angles α, the power absorbed in the WS model was greater than the values obtained from the FD and TD models. From Fig. 6.7(b), this appeared to be due to an increase in power absorbed from the heave mode specifically. A possible explanation could be that the nonlinear hydrodynamic forces in the WS model were such that the heave amplitude or phase were closer to the optimal values in these cases. It can also be seen that the trajectories obtained from the WS model in Fig. 6.9(d) and (f) demonstrated slight chaotic behaviour, although the overall shape of the orbits remained similar to those obtained from the TD model.

It was noted that the results shown here were for a relatively moderate wave amplitude of 0.5 m. At higher amplitudes, it is possible that sub-harmonic motions could occur for a greater range of WEC configurations than reported here, given that nonlinear behaviour is more likely to occur with increasing wave amplitude. The chaotic behaviour observed in the WS results could also potentially become more prominent with increased wave amplitude.

6.5 Irregular wave analysis

The performance of the WEC was also analysed in irregular waves. In a previous study, it was suggested that passively tuning the operational modes of a multi-mode WEC to different natural frequencies could potentially lead to improved performance in broadband waves [46]. However, this assumed

idealised controllers that were capable of tuning each hydrodynamic mode independently. The current analysis therefore aims to determine whether increasing the broadband performance through multi-resonance tuning is possible with the under-actuated three-tether configuration, which has very little control authority over pitch.

The irregular wave analysis presented in this section was performed using the TD model, since the WS model used in this study does not accept irregular waves. From Section 6.4, it was determined that geometric nonlinearities were the primary cause of the sub-harmonic behaviour which led to large divergences from the linear FD results, while hydrodynamic nonlinearties mainly augmented its effects. The TD model was therefore considered sufficient for this analysis, since these geometric nonlinearities can already be observed using this model.

Results showing the variation in total power absorbed by the WEC in irregular waves with different tether angle and attachment point locations is shown in Fig. 6.10. The irregular wave time-series used in this analysis was generated using the Pierson-Moskowitz wave spectrum [30], assuming a wave elevation peak frequency of $\omega_p^\eta = 0.6$ rad/s (corresponding to a peak period of $T_p = 10.3$ s) and significant wave height of $H_s = 2$ m. These wave parameters were chosen to allow for a more direct comparison with

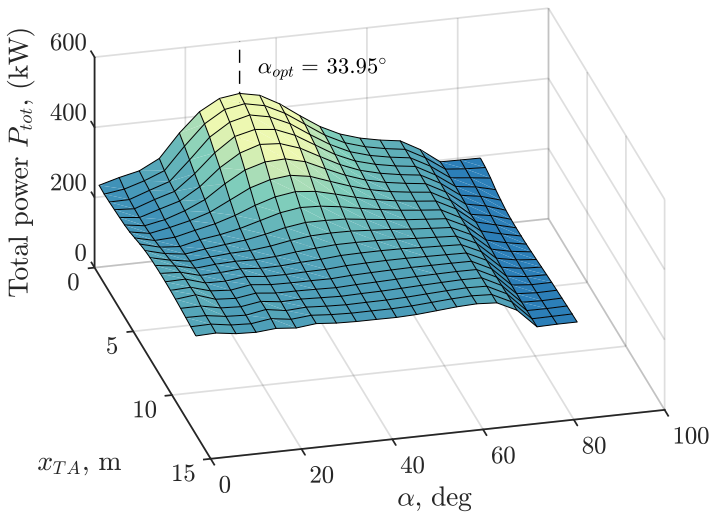

Figure 6.10: Power absorbed by the WEC in irregular waves with peak frequency $\omega_p^\eta = 0.6$ rad/s ($T_p = 10.3$ s) and significant wave height $H_s = 2$ m, as the tether angle α and tether attachment point position x_{TA} is varied. The optimal tether angle for power absorption is higher than in regular waves.

the results presented in the previous sections. The values of K_{PTO} and B_{PTO} were also optimised for each tether angle and attachment point configuration shown in Fig. 6.10.

It was observed that the optimal tether angle, $\alpha_{opt} = 33.95°$, for maximum power absorbed by the WEC in irregular waves was slightly higher than the values obtained previously for regular waves by approximately 5°. Regarding the tether attachment location x_{TA}, the outcomes obtained for the irregular wave analysis remained consistent with the findings from the previous sections. For the three-tethered WEC considered in this study, attaching all three tethers close to one another at the bottom of the buoy consistently resulted in the most power absorbed by the device. The effect of the centre of gravity and pitch moment of inertia was also investigated in irregular waves; however, no noteworthy differences in behaviour were observed compared to the results already presented for regular waves.

A subset of the results shown in Fig. 6.10 was selected for further analysis of the different hydrodynamic and rigid body modes of the system. The contribution of each hydrodynamic mode to the total power absorbed in irregular waves at various tether angles with a fixed tether attachment point of $x_{TA} = 0$ m is displayed in Fig. 6.11(a). The corresponding natural frequencies of the rigid body modes of the system is shown in Fig. 6.11(b). Note that the natural frequencies of the rigid body modes shown here are approximate values only, which were calculated by considering the linear added mass values corresponding to the peak incident frequency of the wave.

From the results shown in Fig. 6.11(a), it appeared that the heave power absorbed by the WEC in irregular waves was relatively insensitive to the tether angle. Consequently, the design became more strongly driven by the performance in surge. Furthermore, in Fig. 6.11(b) it can be seen that unlike in regular waves of a similar excitation frequency, the natural frequencies of Modes 1 and 3 were not equal to the peak wave frequency in the configuration with optimal α. This can be explained by examining the dominant frequency of the excitation force signal.

For submerged WECs, the dominant frequency of the excitation force is not equal to the peak frequency of the wave elevation [41]. This is demonstrated in Fig. 6.12 for the sea state of $\omega_p^\eta = 0.6$ rad/s ($T_p = 10.3$ s) and $H_s = 2$ m. The wave elevation spectrum is denoted S_η, while $\left|H_{Fe_j,\eta}\right|$ is used to denote the magnitude of the response function of the excitation loads for an incident wave with amplitude $A_w = 1$ m. The subscript j is used to denote the hydrodynamic mode. From this, the resultant spectrum of the excitation force can be determined by $S_{Fe_j}(\omega) = |H_{Fe_j,\eta}(\omega)|^2 S_\eta(\omega)$.

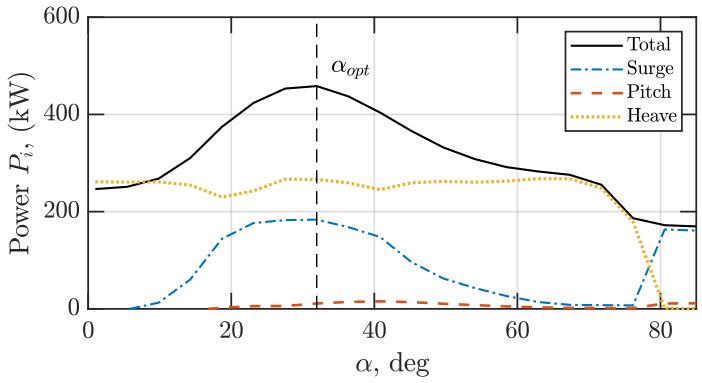

(a)

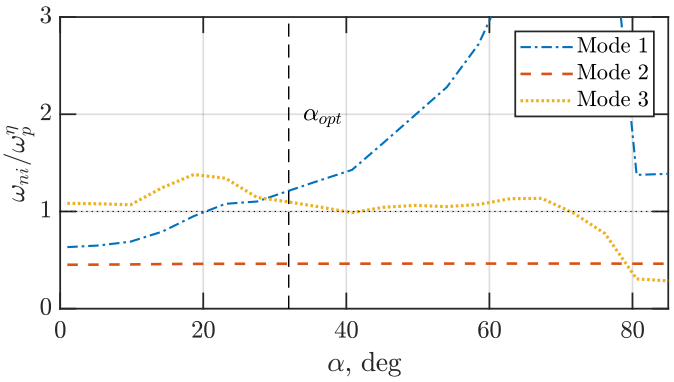

(b)

Figure 6.11: Results from the irregular wave analysis with a constant tether attachment location of $x_{TA} = 0$ m, showing the change in (a) power absorbed from each hydrodynamic mode and (b) approximate natural frequencies of each rigid body mode, as the tether angle α is varied. The peak frequency is $\omega_p^\eta = 0.6$ rad/s ($T_p = 10.3$ s) and significant wave height is $H_s = 2$ m.

It can be seen in Fig. 6.12 that the peak excitation force frequency $\omega_p^{Fe_j}$ is greater than the peak frequency of the incident waves for all hydrodynamic modes. Essentially, this means that the peak in the submerged WEC oscillations will occur at a higher frequency relative to the peak in the incoming wave spectrum. The natural frequencies of the WEC may therefore need to be tuned to match the dominant frequency of the excitation force, rather than the peak frequency of the wave spectrum.

To corroborate these findings, further tests were conducted in different sea states with varying peak wave frequencies. The optimal design parameters of the three-tethered WEC were determined for each sea state. The natural frequencies of the rigid body modes of the WEC in each of these optimal

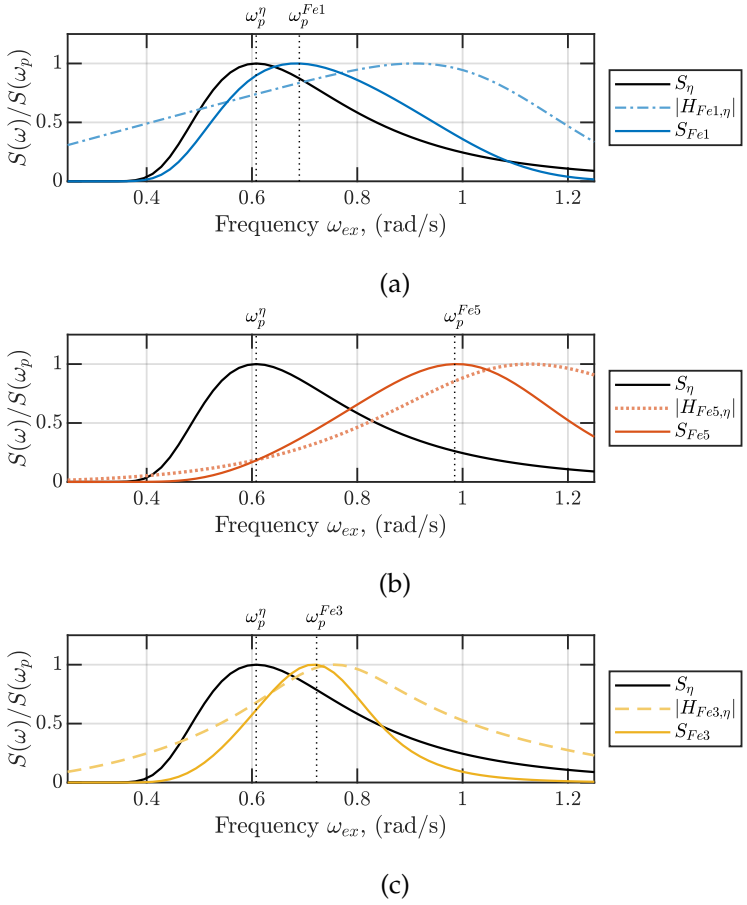

Figure 6.12: Dominant frequency of the excitation loads in (a) surge, (b) pitch and (c) heave for waves with $\omega_p^\eta = 0.6$ rad/s ($T_p = 10.3$ s).

configurations are plotted against the peak wave frequency in Fig. 6.13. The dominant frequency of the excitation force or moment in the corresponding hydrodynamic mode is also illustrated in the plots. It can be seen that the optimal design consistently favours the dominant excitation force in surge. It can therefore be concluded that for maximum power absorption in irregular waves, the design of the three-tethered WEC should focus on tuning the natural frequency of the rigid body mode which is most surge dominant to match with the corresponding dominant excitation frequency.

6.6 Conclusion

In this study, tuning of the planar hydrodynamic modes through the geometric design of a multi-mode WEC was investigated. Sensitivity studies using a

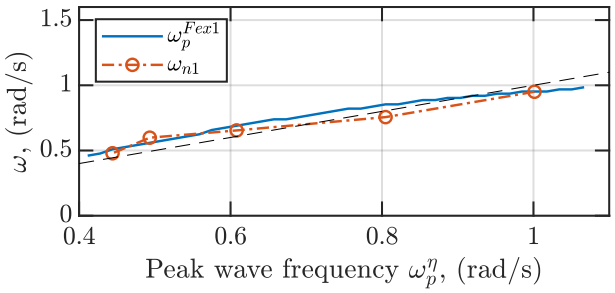

(a) Surge, Mode 1

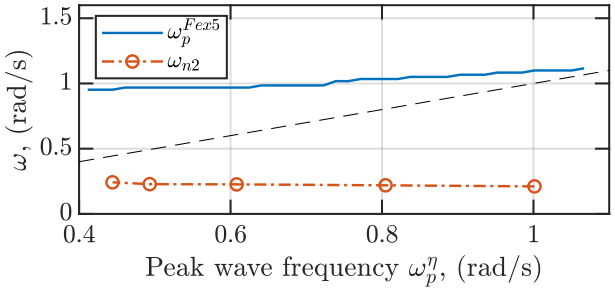

(b) Pitch, Mode 2

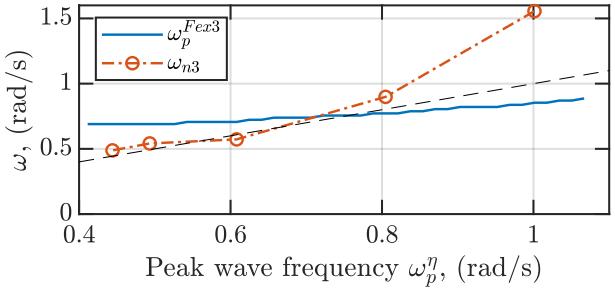

(c) Heave, Mode 3

Figure 6.13: Natural frequencies of the planar rigid body modes, calculated using the optimal design parameters of the three-tethered WEC in irregular waves with various peak wave frequencies. The dominant excitation frequency in surge, pitch and heave across the range of peak wave frequencies is also illustrated. The black dashed line indicates where $\omega_p^\eta = \omega$. The optimal design parameters should be tuned such that the natural frequency of Mode 1 matches the dominant excitation in surge.

linear FD model demonstrated that, other than the PTO stiffness, the tether angle and tether attachment location on the bottom of the buoy hull were the most critical design parameters in determining the total power that could be absorbed by the system. Conversely, adjusting the location of centre of gravity and the pitch moment of inertia resulted in little benefit to the total absorbed power.

To increase the total power absorbed, it was determined that the tether angle and tether attachment location should be adjusted so that the system has two (out of three) planar rigid body modes tuned approximately to the incident wave frequency and thus contributing to power absorption. These active rigid body modes should also contain primarily surge and heave motions. In irregular waves, the optimal design parameters became more dependent on the performance of the surge mode. Furthermore, the rigid body mode responsible for surge motions should be tuned to match the peak excitation force of the surge mode rather than the peak incident wave frequency. With these tuning considerations, it was determined that for the three-tethered WEC considered in this study, the best design in terms of total absorbed power required all three tethers to be attached close to one another on the bottom of the buoy.

When geometric and hydrodynamic nonlinearities were considered, the optimal tether angle and attachment point locations remained approximately the same. However, for certain sub-optimal design parameter combinations, it was found that geometric nonlinearties caused by the tether forces resulted in sub-harmonic excitations which severely diminished the performance of the WEC. The losses in power due to these sub-harmonic excitations were even greater when nonlinear hydrodynamic effects were considered. Therefore, the three-tethered WEC design should also avoid configurations where the dominant rigid body mode for surge and pitch motions is a sub-harmonic of the incident wave.

From this study, it is clear that coupling between hydrodynamic modes due to geometric design and nonlinear hydrodynamic interactions should be an important consideration in the design and control of multi-mode WECs. Ignoring such coupling effects can lead to unexpected nonlinear behaviour which may significantly compromise performance. Conversely, careful selection of effective design parameters can prevent the occurrence of such detrimental coupling effects, and lead to improved resonance behaviour and power absorption in these devices.

Acknowledgements

This research was supported by an Australian Government Research Training Program (RTP) Scholarship. The numerical WS_CN model used in this study was developed by École Centrale de Nantes and shared with the University of Adelaide for wave energy research. In particular, the authors would like to thank Pierre-Yves Wuillaume of École Centrale de Nantes and Boyin Ding of the University of Adelaide for their assistance with the WS modelling. This work was also supported with supercomputing resources provided by the Phoenix HPC service at the University of Adelaide.

Appendix 6.A Linear hydrodynamic coefficients

In this study, the excitation force and radiation coefficients used in the linear FD model were determined using semi-analytical expressions [18, 19]. To ensure convergent results, the number of eigenfunction expansions used to obtain the hydrodynamic coefficients was set to 40. Values of the linear amplitude $|F_{\text{exc}}|$ and phase $\angle F_{\text{exc}}$ used to calculate the excitation force in the FD hydrodynamic model are shown in Fig. 6.14 for a range of wave frequencies. Likewise, for the radiation force calculations, the individual matrix elements for the added mass and radiation damping coefficients are given in Fig. 6.15. Note that due to reciprocity relation, $A_{15} = A_{51}$ and $B_{15} = B_{51}$ [9].

Appendix 6.B Weak-scatterer convergence tests

Convergence tests were performed in order to determine suitable sizes for the mesh elements and time steps for the WS model. From these tests, it was found that the three most important simulation settings with regards to the accuracy of the results were:

- Δdx_2 - mesh element size on the body of the WEC,
- Δdx_3 - mesh element size on the free surface directly above the WEC,
- Δdt - simulation time step.

The impact of these simulation parameters on the displacement values obtained from the WS model are shown in Fig. 6.16. The computation times taken to complete 220 s of simulation are also displayed on the graphs. The terms λ and T used in the graphs refer to the wavelength and period of the incident wave, respectively. The wave conditions used in the convergence tests were identical to the verification tests, with constant wave amplitude

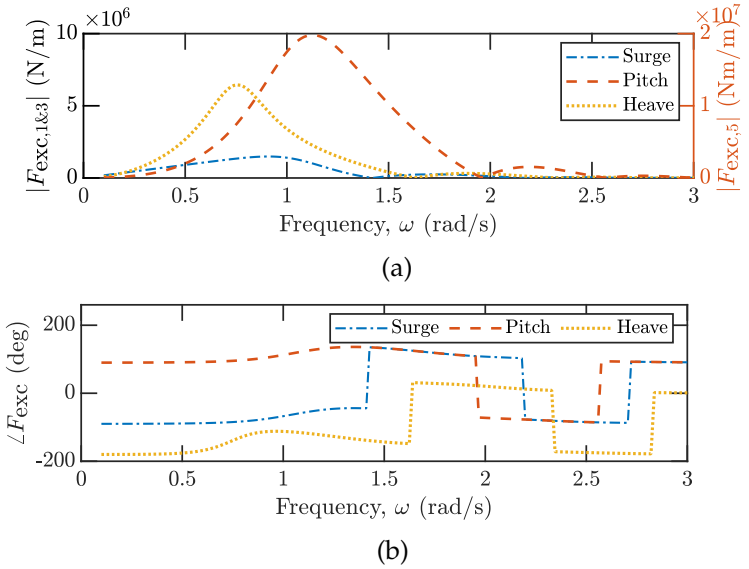

Figure 6.14: Surge and heave excitation force and pitch excitation moment (a) amplitudes and (b) phases.

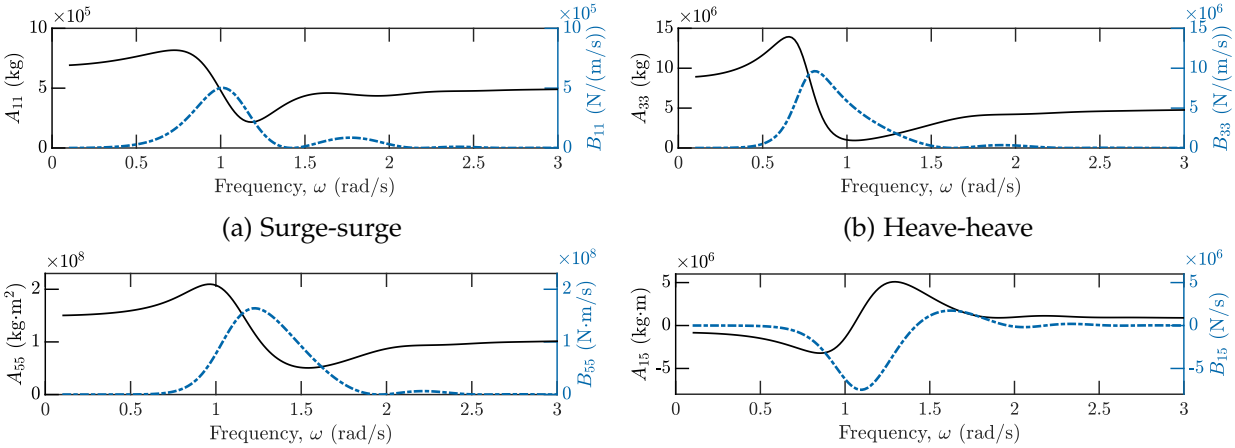

Figure 6.15: Added mass and radiation damping coefficients.

$A_w = 0.1$ m and off-resonance PTO settings. Convergences were also checked for a range of frequencies, although only results corresponding to $\omega_{ex} = 0.6$ rad/s are shown here in Fig. 6.16. The dashed lines plotted on the graphs also indicate the WEC displacement values obtained from the FD model.

From these convergence tests, it can be seen that the WS displacement values were most sensitive to Δdx_3, which can be observed most clearly in Figs. 6.16(c)-(d). The smallest mesh size was therefore set to $\Delta dx = \lambda/250$,

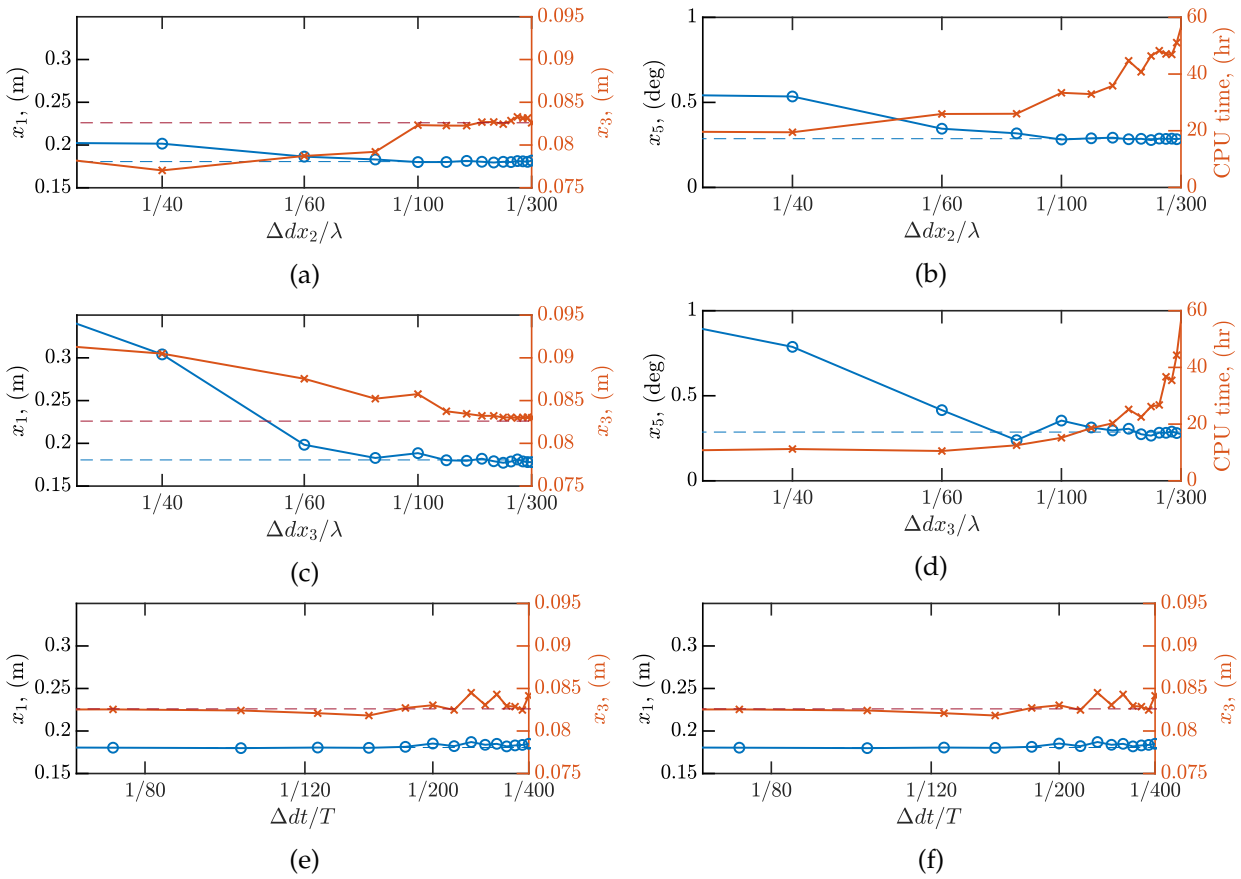

Figure 6.16: Examples of mesh convergence tests showing the effect of (a)-(b) Δdx_2, (c)-(d) $\Delta dx3$ and (e)-(f) Δt on the WEC displacement values obtained from the WS model for an incident wave frequency of $\omega_{ex} = 0.6$ rad/s. Wave conditions were identical to the verification tests, with constant wave amplitude $A_w = 0.1$ m and non-resonant PTO settings. The dashed lines indicate the displacement values obtained from the FD model.

as a compromise between modelling accuracy and computation time. The time step value of $\Delta t = T/300$ was chosen based on the convergence results shown in Fig. 6.16(f) for the pitch displacement.

Appendix 6.C Optimal PTO damping

As discussed in Section 6.3, the PTO damping values were optimised for all design configurations tested. Graphs illustrating a section of the optimal PTO damping values as calculated from the FD model are given in Fig. 6.17. These results also correspond to the cases indicated by the dashed lines displayed in Fig. 6.2. Due to computational constraints, these optimal PTO damping

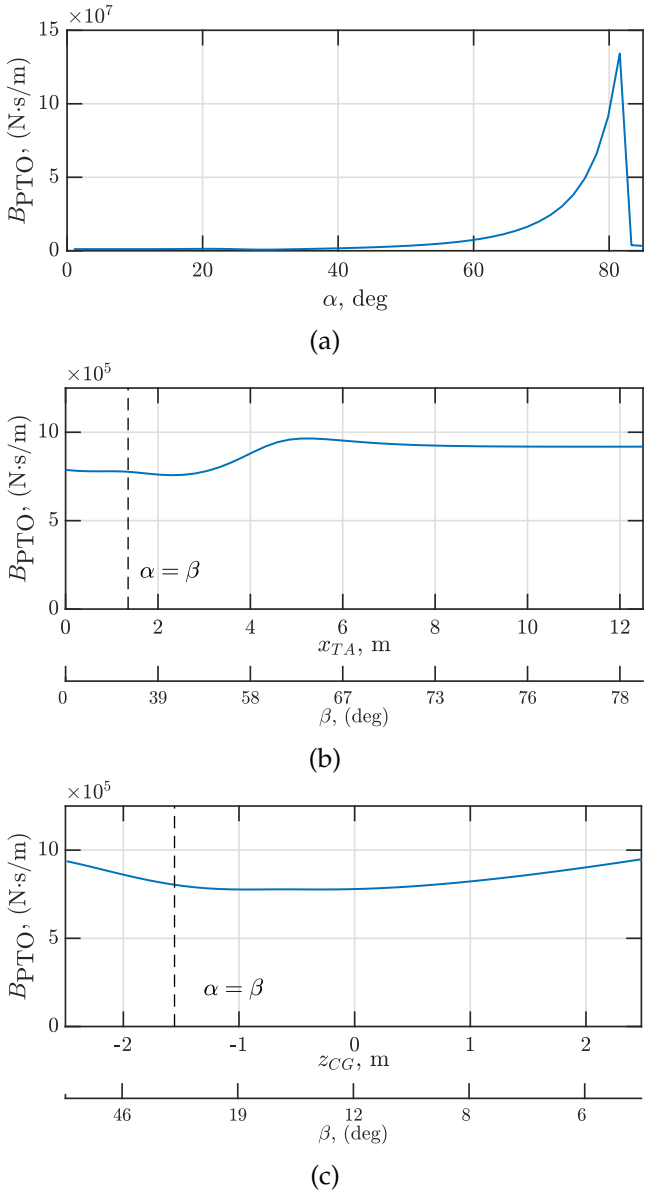

Figure 6.17: Optimised PTO damping values calculated from the linear FD model as the (a) tether inclination angle α, (b) tether attachment point location x_{TA} and (c) centre of gravity position z_{CG} is varied.

values were also used in the TD and WS simulations. It is possible that increased PTO damping may suppress the occurrence of the sub-harmonic excitations seen in Section 6.4, although such a configuration would still result in sub-optimal power absorbed compared to the linear estimates from the FD model.

References

[1] Abdelkhalik, O. and Zou, S. (2018). "Control of Wave Energy Converters Using A Simple Dynamic Model". In: *IEEE Transactions on Sustainable Energy* 10.2, pp. 579–585.

[2] Abdelkhalik, O., Zou, S., Robinett, R. D., Bacelli, G., Wilson, D. G., Coe, R. and Korde, U. (2017). "Multiresonant feedback control of a three-degree-of-freedom wave energy converter". In: *IEEE Transactions on Sustainable Energy* 8.4, pp. 1518–1527.

[3] Babarit, A, Hals, J, Muliawan, M. J., Kurniawan, A, Moan, T and Krokstad, J (2011). *Numerical estimation of energy delivery from a selection of wave energy converters*. Tech. rep., pp. 1–37.

[4] Babarit, A. (Jan. 2014). *NEMOH user manual*. École Centrale de Nantes.

[5] Coe, R., Bacelli, G., Spencer, S. J., Forbush, D. and Dullea, K. (2019). *MASK3 for Advanced WEC Dynamics and Controls*. Tech. rep.

[6] Davidson, J, Genest, R and Ringwood, J. V. (2018). "Adaptive control of a wave energy converter". In: *IEEE Transactions on Sustainable Energy* 9.4, pp. 1588–1595.

[7] Ding, B., Sergiienko, N., Meng, F., Cazzolato, B., Hardy, P. and Arjomandi, M. (Jan. 2019a). "The application of modal analysis to the design of multi-mode point absorber wave energy converters". In: *Ocean Engineering* 171, pp. 603–618.

[8] Ding, B., Wuillaume, P, Meng, F., Babarit, A., Schubert, B., Sergiienko, N. Y. and Cazzolato, B. S. (2019b). "Comparison of wave-body interaction modelling methods for the study of reactively controlled point absorber wave energy converter". In: *Proceedings of the 34th International Workshop on Water Waves and Floating Bodies*. Newcastle.

[9] Falnes, J. (2002). *Ocean waves and oscillating systems: Linear interactions including wave-energy extraction*. Cambridge University Press, p. 220.

[10] Faraggiana, E, Whitlam, C, Chapman, J, Hillis, A, Roesner, J, Hann, M, Greaves, D, Yu, Y.-H., Ruehl, K, Masters, I, Foster, G and Stockman, G (2020). "Computational modelling and experimental tank testing of the multi float WaveSub under regular wave forcing". In: *Renewable Energy* 152, pp. 892–909.

[11] Folley, M., Whittaker, T. and Hoff, J. van't (2007). "The design of small seabed-mounted bottom-hinged wave energy converters". In: *Proceedings of the 7th European Wave and Tidal Energy Conference EWTEC*. Porto, Portugal.

[12] Garcia-Teruel, A and Forehand, D. I. M. (2021). "A review of geometry optimisation of wave energy converters". In: *Renewable and Sustainable Energy Reviews* 139, p. 110593.

[13] Guo, B. and Ringwood, J. V. (2021). "Geometric optimisation of wave energy conversion devices: A survey". In: *Applied Energy* 297, p. 117100.

[14] Hillis, A. J., Whitlam, C, Brask, A, Chapman, J and Plummer, A. R. (2020). "Active control for multi-degree-of-freedom wave energy converters with load limiting". In: *Renewable Energy* 159, pp. 1177–1187.

[15] Hoerner, S. F. (1965). *Fluid-dynamic drag: practical information on aerodynamic drag and hydrodynamic resistance*. Hoerner Fluid Dynamics.

[16] Ikeda, Y., Himeno, Y. and Tanaka, N (1978). "Components of roll damping of ship at forward speed". In: *Journal of the Society of Naval Architects of Japan* 1978, pp. 113–125.

[17] International Towing Tank Conference (ITTC) (2011). *Numerical Estimation of Roll Damping*. Tech. rep. Zurich, Switzerland: International Towing Tank Conference.

[18] Jiang, S.-C., Gou, Y. and Teng, B. (May 2014a). "Water wave radiation problem by a submerged cylinder". In: *Journal of Engineering Mechanics* 140.5, p. 6014003.

[19] Jiang, S.-C., Gou, Y., Teng, B. and Ning, D.-Z. (Jan. 2014b). "Analytical solution of a wave diffraction problem on a submerged cylinder". In: *Journal of Engineering Mechanics* 140.1, pp. 225–232.

[20] Korde, U. A., Lyu, J., Robinett, R. D., Wilson, D. G., Bacelli, G. and Abdelkhalik, O. (2017). "Constrained near-optimal control of a wave energy converter in three oscillation modes". In: *Applied Ocean Research* 69, pp. 126–137.

[21] Letournel, L., Chauvigné, C., Gelly, B., Babarit, A., Ducrozet, G. and Ferrant, P. (2018). "Weakly nonlinear modeling of submerged wave energy converters". In: *Applied Ocean Research* 75, pp. 201–222.

[22] Meng, F., Cazzolato, B., Li, Y., Ding, B., Sergiienko, N. and Arjomandi, M. (2019a). "A sensitivity study on the effect of mass distribution of a single-tether spherical point absorber". In: *Renewable Energy* 141, pp. 583–595.

[23] Meng, F., Ding, B., Cazzolato, B. and Arjomandi, M. (Jan. 2019b). "Modal analysis of a submerged spherical point absorber with asymmetric mass distribution". In: *Renewable Energy* 130, pp. 223–237.

[24] Morison, J., Johnson, J. and Schaaf, S. (1950). "The force exerted by surface waves on piles". In: *Journal of Petroleum Technology* 2.05, pp. 149–154.

[25] Neshat, M., Sergiienko, N. Y., Mirjalili, S., Majidi Nezhad, M., Piras, G. and Astiaso Garcia, D. (2021). "Multi-mode wave energy converter design optimisation using an improved moth flame optimisation algorithm". In: *Energies* 14.13.

[26] Orszaghova, J., Wolgamot, H., Draper, S., Eatock Taylor, R., Taylor, P. H. and Rafiee, A. (2019). "Transverse motion instability of a submerged moored buoy". In: *Proceedings of the Royal Society A: Mathematical, Physical and Engineering Sciences* 475.2221, p. 20180459.

[27] Orszaghova, J., Wolgamot, H., Draper, S., Taylor, P. H. and Rafiee, A. (2020). "Onset and limiting amplitude of yaw instability of a submerged three-tethered buoy". In: *Proceedings of the Royal Society A: Mathematical, Physical and Engineering Sciences* 476.2235, p. 20190762.

[28] Pawlowski, J. S. and Bass, D. W. (1991). *A theoretical and numerical model of ship motions in heavy seas*. Tech. rep.

[29] Perez, T. and Fossen, T. I. (2009). "A Matlab toolbox for parametric identification of radiation-force models of ships and offshore structures". In: *Modeling, Identification and Control* 30.1, pp. 1–15.

[30] Pierson, W. J. and Moskowitz, L. (1964). "A proposed spectral form for fully developed wind seas based on the similarity theory of S. A. Kitaigorodskii". In: *Journal of Geophysical Research* 69.24, pp. 5181–5190.

[31] Rafiee, A. and Fiévez, J. (2015). "Numerical prediction of extreme loads on the CETO wave energy converter". In: *Proceedings of the 11th European Wave and Tidal Energy Conference EWTEC*. Nantes, France.

[32] Rafiee, A. and Valizadeh, A. (2018). *Multi-moored CETO and results from Plymouth 2018 test campaign*. Tech. rep. Carnegie Clean Energy.

[33] Rodríguez, C. A., Rosa-Santos, P. and Taveira-Pinto, F. (2020). "Hydrodynamic optimization of the geometry of a sloped-motion wave energy converter". In: *Ocean Engineering* 199, p. 107046.

[34] Rosenberg, B. J. and Mundon, T. R. (2016). "Numerical and physical modeling of a flexibly-connected two-body wave energy converter". In: *Proceedings of the 4th Marine Energy Technology Symposium*. Washington D.C., USA, pp. 5–8.

[35] Scruggs, J. T., Lattanzio, S. M., Taflanidis, A. A. and Cassidy, I. L. (2013). "Optimal causal control of a wave energy converter in a random sea". In: *Applied Ocean Research* 42, pp. 1–15.

[36] Sergiienko, N. Y., Cazzolato, B. S., Arjomandi, M, Ding, B and Silva, L. S. P. da (2019). "Considerations on the control design for a three-tether wave energy converter". In: *Ocean Engineering* 183, pp. 469–477.

[37] Sergiienko, N. Y., Cazzolato, B. S., Ding, B and Arjomandi, M (2016a). "An optimal arrangement of mooring lines for the three-tether submerged point-absorbing wave energy converter". In: *Renewable Energy* 93, pp. 27–37.

[38] Sergiienko, N. Y., Cazzolato, B. S., Ding, B, Hardy, P and Arjomandi, M (2017a). "Performance comparison of the floating and fully submerged quasi- point absorber wave energy converters". In: *Renewable Energy* 108, pp. 425–437.

[39] Sergiienko, N. Y., Rafiee, A, Cazzolato, B. S., Ding, B and Arjomandi, M (2018). "Feasibility study of the three-tether axisymmetric wave energy converter". In: *Ocean Engineering* 150, pp. 221–233.

[40] Sergiienko, N. Y., Cazzolato, B. S., Ding, B. and Arjomandi, M. (2016b). "Three-tether axisymmetric wave energy converter: estimation of energy delivery". In: *Proceedings of the 3rd Asian Wave and Tidal Energy Conference AWTEC*. Singapore: Singapore: Research Publishing, pp. 163–171.

[41] Sergiienko, N. Y., Cazzolato, B. S., Hardy, P., Arjomandi, M. and Ding, B. (2017b). "Internal-model-based velocity tracking control of a submerged three-tether wave energy converter". In: *Proceedings of the 12th European Wave and Tidal Energy Conference EWTEC*, pp. 1–8.

[42] Sergiienko, N. Y., Neshat, M., Silva, L. S. P. da, Alexander, B. and Wagner, M. (2020). "Design optimisation of a multi-mode wave energy converter". In: *ASME 2020 39th International Conference on Ocean, Offshore & Arctic Engineering*. Vol. 9. International Conference on Offshore Mechanics and Arctic Engineering.

[43] Terra, G. M., Berg, W. J. van de and Maas, L. R. M. (2005). "Experimental verification of Lorentz' linearization procedure for quadratic friction". In: *Fluid Dynamics Research* 36.3, pp. 175–188.

[44] Todalshaug, J. H. (Dec. 2013). "Practical limits to the power that can be captured from ocean waves by oscillating bodies". In: *International Journal of Marine Energy* 3-4, e70–e81.

[45] Tran, N., Sergiienko, N. Y., Cazzolato, B. S., Ding, B., Ghayesh, M. H. and Arjomandi, M. (2020). "The impact of pitch-surge coupling on the performance of a submerged cylindrical wave energy converter". In: *Applied Ocean Research* 104, p. 102377.

[46] Tran, N., Sergiienko, N. Y., Cazzolato, B. S., Ding, B., Wuillaume, P.-Y., Ghayesh, M. H. and Arjomandi, M. (2021). "On the importance of nonlinear hydrodynamics and resonance frequencies on power production in multi-mode WECs". In: *Applied Ocean Research* 117, p. 102924.

[47] Wendt, F., Nielsen, K., Yu, Y.-H., Bingham, H., Eskilsson, C., Kramer, M., Babarit, A., Bunnik, T., Costello, R., Crowley, S., Gendron, B., Giorgi, G., Giorgi, S., Girardin, S., Greaves, D., Heras, P., Hoffman, J., Islam, H., Jakobsen, K.-R., Janson, C.-E., Jansson, J., Kim, H. Y., Kim, J.-S., Kim, K.-H., Kurniawan, A., Leoni, M., Mathai, T., Nam, B.-W., Park, S., Rajagopalan, K., Ransley, E., Read, R., Ringwood, J. V., Rodrigues, J. M., Rosenthal, B., Roy, A., Ruehl, K., Schofield, P., Sheng, W., Shiri, A., Thomas, S., Touzon, I. and Yasutaka, I. (2019). "Ocean energy systems wave energy modelling task: modelling, verification and validation of wave energy converters". In: *Journal of Marine Science and Engineering* 7.11, p. 379.

[48] Wendt, F., Yu, Y.-H., Nielsen, K., Ruehl, K., Bunnik, T., Touzón, I., Nam, B. W., Kim, J., Kim, K.-H., Janson, C.-E., Jakobsen, K.-R., Crowley, S., Vega, L., Rajagopalan, K., Mathai, T., Greaves, D., Ransley, E., Lamont-Kane, P., Sheng, W and Hoffman, J. (Aug. 2017). "International Energy Agency Ocean Energy Systems task 10 wave energy converter modeling verification and validation". In: *Proceedings of the 12th European Wave and Tidal Energy Conference EWTEC*.

[49] Wuillaume, P.-Y. (Jan. 2019). "Numerical simulation of installation operations for offshore wind farms". PhD thesis. École Centrale de Nantes.

[50] Wuillaume, P.-Y., Babarit, A., Rongère, F., Lynch, M., Combourieu, A. and Ferrant, P. (June 2018). "Comparison between experiments and a multibody weakly nonlinear potential flow approach for modelling of marine pperations". In: *ASME 2018 37th International Conference on Offshore Mechanics and Arctic Engineering*. Madrid, Spain.

[51] Yavuz, H. (July 2011). "On control of a pitching and surging wave energy converter". In: *International Journal of Green Energy* 8.5, pp. 555–584.

[52] Zou, S., Abdelkhalik, O., Robinett, R., Korde, U., Bacelli, G., Wilson, D. and Coe, R. (2017). "Model Predictive Control of parametric excited pitch-surge modes in wave energy converters". In: *International Journal of Marine Energy* 19, pp. 32–46.

Chapter 7

Conclusion

7.1 Overall conclusions

The overarching aim of this Thesis is to develop an understanding of the impact of nonlinear coupling between hydrodynamic modes on the performance of a submerged multi-mode, quasi-point absorber WEC with a flat cylindrical geometry. This WEC is capable of utilising multiple hydrodynamic modes for improved power absorption, but can also be susceptible to nonlinear coupling effects when the device oscillates in surge, heave and pitch simultaneously. Fully linearised and weakly nonlinear hydrodynamic models were utilised to determine the importance of this nonlinear coupling on the power absorption efficacy, control and design of the multi-mode converter. To develop the fundamental understanding of the various aspects in the full multi-mode system, the WEC was initially modelled as a simplified system with idealised control, before progressing onto a more complex case with spring-damper control, and finally to a more realistic under-actuated system featuring three inclined tethers for control and power take-off.

Initially, it was necessary to identify the importance of nonlinear hydrodynamic forces acting on a WEC device when it oscillates in multiple hydrodynamic modes simultaneously. To this end, a fully idealised multi-mode WEC model with kinematic control was initially considered in Chapter 4, wherein the pitch and surge motions could be explicitly defined. Comparisons between a fully linear and weakly nonlinear model revealed that pitch had a much greater impact on the performance of the multi-mode WEC when nonlinear coupling effects were considered. Noticeable nonlinearities were observed in the hydrodynamic forces, including changes to both amplitude and phase, when the device oscillated simultaneously in both surge and pitch. As a result, the power absorbed in the nonlinear model was significantly

reduced compared to estimates obtained from the linear model. Additionally, the control requirements for maximum power increased with the inclusion of nonlinear hydrodynamics, necessitating finer tuning of both the surge and pitch phases, whereas this was not necessary in the linear model.

For the next stage of this work, the kinematic control assumption was replaced with independent spring-damper control in Chapter 5, and nonlinear hydrodynamic interactions with heave were also added. While the case with kinematic control in Chapter 4 allowed the optimal WEC motion amplitudes and phases to be defined at any frequency, with spring-damper control this is only possible through optimally setting the resistance and reactance at one frequency. However, when the surge, heave and pitch modes were all tuned to match the incident wave frequency, under the effects of nonlinear coupling between hydrodynamic modes, losses of up to 27% of the total power absorbed were observed between the fully linearised and weakly nonlinear models. The losses were attributed to the large pitch amplitudes in these cases, which led to notable changes in the projected area of the WEC compared to its equilibrium position. As a result, it was therefore recommended to decouple and tune these modes to different natural frequencies in multi-mode WECs where the design does not limit large pitch amplitudes. Preliminary analysis in irregular waves suggested that this tuning approach may also potentially improve broadband power absorption by up to 30% in real seas, compared to a case where all the hydrodynamic modes were simply tuned to match the peak wave frequency.

The last step of this research involved analysing the effect of both geometric and hydrodynamic nonlinearities on the coupling between modes in an under-actuated, three-tethered WEC device. Assuming fully optimised PTO parameters, it was found in Chapter 6 that the device was most sensitive to the arrangement of the tethers, while parameters related to the mass distribution were not as critical for optimal performance. In contrast to the previous study presented in Chapter 5, it was found that maximum power was achieved when both the surge and heave dominant rigid body modes were tuned close to the incident wave frequency. This was true even with the inclusion of nonlinear hydrodynamic forces and irregular waves, since the pitch amplitudes became limited by the addition of geometric coupling through the tether arrangement. However, in certain cases where the tether design parameters deviated from their optimal values, sub-harmonic excitations caused by geometric nonlinearities could significantly decrease performance compared to the fully linearised model, an effect which was further exacerbated by the large pitch amplitudes and nonlinear hydrodynamic forces.

Overall, these findings demonstrate that interactions between hydrodynamic modes, whether from the geometric design or nonlinear hydrodynamic forces, should be an important consideration in the development of multi-mode WECs. The phases of each hydrodynamic mode, not only relative to the incident wave but also between each other, play a critical role in determining the power absorption of the device. While kinematic control permitted perfectly setting the phase at any frequency, spring damper control only allowed this at resonance, and the three-tether case made this very difficult due to under-actuation and additional geometric coupling between modes. Therefore, selecting appropriate design parameters and natural frequencies of the system should be considered to attain the optimal phase conditions and improve device performance. The importance of the pitch mode in larger multi-mode WECs with non-spherical geometries is also highlighted in this research. Even in cases where it is not designed to contribute to power absorption, neglecting its interactions with the other modes can potentially lead to significant overestimations of power, especially when relying solely on fully linearised hydrodynamic models for performance assessment. In conclusion, the pitch amplitude should be limited as much as possible in the operation of such WECs to avoid compromising power absorption due to nonlinear coupling between hydrodynamic modes. In practice, this can be achieved through decoupling the hydrodynamic modes altogether, or through careful design of the WEC device itself, such as through the PTO and mooring systems.

7.2 Original contributions

The main contributions of this research to the field of wave energy are listed as follows:

1. demonstrating the importance of coupling effects with the pitch mode in multi-mode quasi-point absorber WEC systems, in particular nonlinear effects arising from the change in the projected surface area with large pitch amplitudes,

2. application of a weakly nonlinear hydrodynamic model based on the weak-scatterer approximation for high-fidelity performance assessment and optimisation of a multi-mode converter,

3. determining the effect of nonlinear hydrodynamic forces and coupling on the power production of multi-mode WECs which oscillate in multiple directions simultaneously,

4. proposing alternate approaches to the tuning of multi-mode systems in order to both reduce nonlinear coupling effects and maximise power production,

5. demonstrating the potential for increased broadband power absorption in a multi-mode WEC through decoupling the hydrodynamic modes,

6. identifying the key design parameters which drive the performance and resonance behaviour of an under-actuated three-tethered system,

7. identifying the effects of sub-harmonic excitations arising from the tether arrangement on the power absorption and nonlinear hydrodynamic forces experienced by a three-tethered WEC.

7.3 Recommendations for future work

The work performed in this Thesis is intended to provide a general understanding of multi-mode WEC systems and a number of important nonlinear effects which may impact their performance. Opportunities for future work could therefore involve extending the knowledge developed in this Thesis to more focused studies which consider specific nonlinear forces or different WEC designs.

Extended nonlinear hydrodynamic force analysis

Since the work performed in this Thesis is focused specifically on the WEC performance resulting from nonlinear hydrodynamic effects, detailed analysis of the various forces themselves were considered outside the scope of the project. Future work could therefore involve examining these nonlinear forces in greater detail, including:

- developing simplified or analytical methods for calculating the nonlinear radiation forces acting on bodies oscillating in multiple directions simultaneously, including harmonics and changes to the hydrodynamic coefficients, such as those observed in Chapter 4. This could also have potential uses for other marine applications which feature bodies moving in such a manner, such as in the case of ships and cargo handling operations at sea,

- identifying the importance of other possible nonlinear free-surface effects, such as trapped modes, which could have affected the nonlinear WEC trajectories observed in Chapter 5. Additionally, given the close

proximity of the WEC to the free-surface in these trajectories, potential wave breaking effects on performance may also be a relevant topic for future work,

- more dedicated investigations of real flow aspects related to viscous drag, such as implementing orientation dependent drag coefficients or projected areas for calculating drag forces. Turbulent flow effects could also be investigated, although CFD may be required since this cannot be fully simulated using the potential flow models applied in this work.

Improvements to the weak-scatterer model

There were a number of limitations associated with the WS model used in this Thesis which should be noted. Most notably, while the potential broadband power absorption of multi-mode WECs in real seas was explored in Chapters 5 and 6, this analysis was not performed using the WS model, which currently does not have the capability to simulate irregular waves. This functionality could therefore be incorporated into the WS model to allow for more complete analyses involving both irregular waves and nonlinear hydrodynamic coupling effects at the same time. Other relevant aspects of the WS model which could be addressed include further improvements to the computation times, or adding in capabilities for handling surface piercing effects so that WECs with shallower submergence depths can be modelled. This could also allow for investigations involving more strongly nonlinear regimes, to determine whether the conclusions from this study would still be relevant when other significant nonlinear forces dominate.

Multi-mode design optimisation

Due to the long computational times required by the WS model, only rudimentary optimisation processes were applied when analysing the multi-mode WEC systems in this Thesis. As previously discussed, simplified hydrodynamic models which can still capture the effect of the relevant nonlinear hydrodynamic forces, or improvements to the WS computation times, may allow for more sophisticated optimisation methods to be applied for the design and control of these devices. More complex optimisations permitting all six hydrodynamic modes could also be explored, especially in the case of the three-tethered arrangement where the yaw mode has been known to couple with many DOFs and result in parametric excitations. Different WEC geometries could also be explored and optimised, including hybrid designs

with off-shore wind turbines to further improve the economic viability of these wave devices.

Laboratory scale experiments

As discussed in Section 3.4.1, there may have been cases where the small perturbation assumption of the WS approximation was not fully satisfied locally due to large body motions, such as when the WEC was operating near resonance. While the WS model has been validated against experimental data for single-DOF systems oscillating in one mode only, experiments featuring WECs oscillating in many directions at once should also be performed to fully validate the models used in this Thesis and to demonstrate the importance of nonlinear hydrodynamic coupling effects on multi-mode WECs in practice. Extreme loads and very nonlinear cases involving large surge and pitch displacement amplitudes could also be tested, again to explore how well the conclusions of this research would hold in such conditions.

Appendix A

The effect of nonlinear pitch-surge coupling on multi-DOF submerged WECs

This appendix consists of the published conference paper:
Tran, N., Sergiienko, N. Y., Cazzolato, B. S., Ghayesh, M. H. and Arjomandi, M. (Oct. 2020). "The effect of nonlinear pitch-surge coupling on the performance of multi-DOF submerged WECs". In: ***Proceedings of the 30th International Ocean and Polar Engineering Conference*****, pp. 144–151.**

This paper may be considered a preliminary study to Chapter 4, involving early studies on the effect of nonlinear pitch-surge hydrodynamic forces acting on a submerged, flat cylindrical and multi-mode WEC.

Statement of Authorship

Title of Paper	The effect of nonlinear pitch-surge coupling on the performance of multi-DOF submerged WECs
Publication Status	☑ Published ☐ Accepted for Publication ☐ Submitted for Publication ☐ Unpublished and Unsubmitted work written in manuscript style
Publication Details	Tran, N., Sergiienko, N. Y., Cazzolato, B. S., Ghayesh, M. H. and Arjomandi, M. (Oct. 2020). "The effect of nonlinear pitch-surge coupling on the performance of multi-DOF submerged WECs". In: *Proceedings of the 30th International Ocean and Polar Engineering Conference*, pp. 144–151.

Principal Author

Name of Principal Author (Candidate)	Ngan Tran		
Contribution to the Paper	Developed ideas and concepts, conducted literature review Performed modelling • Developed weak-scatterer (WS) model of the multi-mode WEC using WS_CN code • Developed fully linearised model of the system based on hydrodynamic parameters obtained using potential flow solver NEMOH • Systematically varied the surge and pitch velocities to study effect on power • Performed radiation-only simulations in the WS model to obtain the nonlinear hydrodynamic forces Interpreted results • Collected and stored data from simulations • Post processed data using Matlab • Applied processes to extract the nonlinear radiation coefficients • Analysed and compared results between the linear and WS models • Generation of plots to visualise results Writing • Wrote first full draft of manuscript • Applied comments and feedback provided by co-authors • Acted as corresponding author • Revised manuscript following review		
Overall percentage (%)	85%		
Certification:	This paper reports on original research I conducted during the period of my Higher Degree by Research candidature and is not subject to any obligations or contractual agreements with a third party that would constrain its inclusion in this thesis. I am the primary author of this paper.		
Signature		Date	01/12/21

Co-Author Contributions

By signing the Statement of Authorship, each author certifies that:

i. the candidate's stated contribution to the publication is accurate (as detailed above);

ii. permission is granted for the candidate in include the publication in the thesis; and

iii. the sum of all co-author contributions is equal to 100% less the candidate's stated contribution.

Name of Co-Author	Nataliia Y. Sergiienko		
Contribution to the Paper	Supervised the work, participated in developing ideas and concepts, shaped research and direction of manuscript, provided parts of code for modelling, helped analyse and interpret results, provided revision of manuscript		
Signature		Date	07/12/21

Name of Co-Author	Benjamin S. Cazzolato		
Contribution to the Paper	Supervised the work, participated in developing ideas and concepts, encouraged to pe, helped analyse and interpret results, provided revision of manuscript		
Signature		Date	01/12/21

Name of Co-Author	Mergen H. Ghayesh		
Contribution to the Paper	Supervised work, provided revision of manuscript		
Signature		Date	22/12/2021

Name of Co-Author	Maziar Arjomandi		
Contribution to the Paper	Supervised work, helped in developing ideas, provided revision of manuscript		
Signature		Date	7/12/2021